

# Properties and application spectrum of cast porous implants made of Ti-6Al-7Nb in coated and uncoated conditions

TEODOLITO GUILLEN GIRON



## **TEODOLITO GUILLEN GIRON**

Properties and application spectrum of cast porous implants made of Ti-6Al-7Nb in coated and uncoated conditions

Bibliografische Information der Deutschen Nationalbibliothek  
Die Deutsche Nationalbibliothek verzeichnet diese Publikation in der Deutschen Nationalbibliografie; detaillierte bibliografische Daten sind im Internet über <http://dnb.d-nb.de> abrufbar.

Zugl.: Siegen, Univ., Diss., 2012

Herausgeber:  
Prof. Dr.-Ing. habil. H.-J. Christ  
Lehrstuhl für Materialkunde und Werkstoffprüfung  
Institut für Werkstofftechnik  
Paul-Bonatz-Str. 9-11  
Universität Siegen  
D-57068 Siegen

© Copyright Teodolito Guillén Girón 2012  
© Copyright Lehrstuhl für Materialkunde und Werkstoffprüfung,  
Universität Siegen 2012  
Alle Rechte vorbehalten, auch das des auszugsweisen Nachdruckes,  
der auszugsweisen oder vollständigen Wiedergabe, der Speicherung  
in Datenverarbeitungsanlagen und das der Übersetzung.

URN:nbn:de:hbz:467-6738  
ISSN 2193-5114

# Properties and application spectrum of cast porous implants made of Ti-6Al-7Nb in coated and uncoated conditions

DISSERTATION

zur Erlangung des Grades eines Doktors  
der Ingenieurwissenschaften

vorgelegt von

M.Sc. Teodolito Guillén Girón  
aus Costa Rica

eingereicht bei der Naturwissenschaftlich-Technischen Fakultät  
der Universität Siegen

Referent: Prof. Dr.-Ing. habil. H.-J. Christ

Korreferent: Prof. Dr.-Ing. habil. U. Krupp

Tag der mündlichen Prüfung: 02.11.2012



## **Acknowledgements**

This thesis is the result of my activities at the research group of Materialkunde und Werkstoffprüfung (LMW) at the Universität Siegen, Germany. I would like to express my sincere and immense gratitude in all respects to my thesis advisor and head of LMW Professor Dr.-Ing. habil. Hans-Jürgen Christ for his wonderful guidance and tremendous support at every stage of this work. It was really a great honour to learn from his wide knowledge and supervision.

I would next like to extend my sincerely thanks to Professor Dr.-Ing. habil. Ulrich Krupp of the faculty of Engineering and Computer Science at the University of Applied Science Osnabrück for the coordination of this project as well as for his support, corrections and advices. I would also like to thank Professor Dr.-Ing. Claus-Peter Fritzen and Professor Dr.-Ing. PD Kerstin Weinberg for accepting to be my examiners.

My special appreciation to Dr.-Ing. Arne Ohrndorf for his tremendous guidance, feedback, corrections and for his friendship. He support and advice me from my first day in Germany until the end of my work in LMW, I cannot express in words my gratitude for that. My hearty thanks to all my colleagues at the LMW at the Universität Siegen especially to Dr.-Ing Slava Gorr, Lisa Häbel, Dr.-Ing Steffen Burk, M.Sc. Ravisankar Naraparaju, Dipl.-Ing. Andrei Grigorescu, M.Sc. Lin Wang, Dipl.-Ing. Christian Freitag, Dipl.-Ing. Ken Wackermann, Dipl.-Ing. Christian Stöcker and Dipl.-Ing. Ali El-Chaikh for their friendships and support in the hard times. I will always remember their great friendship and assistance during my stay in this research group. My deeply gratitude to Dipl.-Ing. Wolfgang Kramer for his friendship and technical support and to Marlies Mockenhaupt for her help and support during my stay in the LMW. I like to thank Dr. Sanjib Majumdar for his corrections of this thesis. Furthermore, thanks to Christian Schroder and Mathias Vogel those contribute with their student works to improve the quality of this work.

The help by all the colleagues of the MEDFOAM project is greatly appreciated. Specially, I would like to thank to Dipl.-Ing. Katrin Hagemann of the RWTH Aachen, Dr. rer. nat. Ute Ploska of the Bundesanstalt für Materialforschung und -prüfung (BAM) Berlin and Dr. med. vet. Ursula Sommer of the Justus-Liebig-Universität Gießen, Germany for their feedback and support.

Special thanks also to Prof. Dr. Jie Tong, Dr. Gianluca Tozzi, Dr. Qinghang Zhang of the Mechanical Behaviour of Materials research group of the University of Portsmouth, UK.

## Acknowledgements

Their collaboration and support in the understanding of the mechanical properties of cancellous bone are highly appreciated. Additionally, I would like to thank the support of the personal of the Ingenieurbüro F. Braun (Zerstörungsfreie Werkstoffprüfungen) Freudenberg, Germany for the X-ray examination of the sheep bones.

This work would not have been possible without the help of my family members and friends. They encouraged me in every aspect during the period of this work. Finally, I would like to dedicate this dissertation to my parents: Mercedes Lucia Jiron Melgar and Bertilo Guillén Henriquez as well as to my sister and brothers.

Siegen, November 2012

Teodolito Guillén Girón

# Content

<b>Symbols and abbreviations.....</b>	<b>VI</b>
<b>1 Introduction.....</b>	<b>1</b>
<b>2 Theoretical background.....</b>	<b>5</b>
2.1 Cancellous bones.....	5
2.1.1 Bone tissue.....	5
2.1.2 Cancellous bone structure.....	6
2.1.3 Mechanical properties of cancellous bones.....	8
2.1.4 Degenerative diseases of cancellous bones.....	12
2.2 Requirements for a biomaterial.....	14
2.2.1 Design and mechanical properties.....	14
2.2.2 Biocompatibility and osseointegration.....	16
2.2.3 Corrosion resistance behaviour of biomaterials.....	19
2.2.4 Surface modification of biomaterials: Coatings.....	22
2.3 Titanium and its alloys as implant materials.....	25
2.3.1 Manufacturing of Ti implants - Casting process.....	28
2.3.2 Defects in cast Ti-alloy implants.....	30
2.4 Engineering cellular solids in medical applications.....	36
2.4.1 Open-cell metallic foams in medicine.....	39
2.4.2 Manufacturing processes of open-cell metallic foams.....	40
2.4.3 Mechanical properties of open-cell metallic foams.....	43
<b>3 Materials and experimental methods.....</b>	<b>50</b>
3.1 Preparation of the bone samples.....	50
3.1.1 Rat bone.....	50
3.1.2 Ovine bone.....	51
3.1.3 Bovine bones.....	52
3.2 Ti-6Al-7Nb material.....	53
3.3 Fabrication of the specimens.....	54
3.3.1 Cast Ti-6Al-7Nb plates, grid-shape and sponge samples.....	55
3.3.2 Porous Ti-6Al-7Nb implants.....	56

## Content

3.3.3 Open-cell AlSi7Mg foam.....	56
3.4 Microstructure and surface modification.....	57
3.4.1 Heat treatment.....	57
3.4.2 Pickling process.....	57
3.4.3 Reaction layer coatings.....	58
3.5 Mechanical testing.....	58
3.5.1 Monotonic bending.....	59
3.5.2 Corrosion-cyclic bending analysis of the reaction layer .....	59
3.5.3 Fretting analysis of the reaction layer.....	60
3.5.3 Compression test.....	60
3.6 In-vivo investigation.....	63
3.6.1 Implantation of porous Ti-6Al-7Nb implants in rats.....	63
3.6.2 Implantation of porous Ti-6Al-7Nb implants in sheep.....	63
3.6.3 Post-operative biomechanical testing.....	64
3.7 Morphological and analytical studies.....	66
<b>4 Results.....</b>	<b>67</b>
4.1 Compression behaviour of the cancellous bones and open-cell foam.....	67
4.1.1 Compression behaviour of the ovine cancellous bone.....	67
4.1.2 Compression behaviour of the bovine cancellous bone.....	69
4.1.3 Compression behaviour of an open-cell metallic foam.....	71
4.2 Characterization of the cast Ti-6Al-7Nb material.....	73
4.2.1 Microstructural analysis.....	74
4.2.2 Removal of the $\alpha$ -case.....	76
4.2.3 Effect of heat treatment and pickling on the mechanical properties of the cast Ti-6Al-7Nb samples .....	79
4.2.4 Cast Ti-6Al-7Nb porous implants.....	82
4.3 Characterization of calcium titanate reaction layer.....	86
4.3.1 Corrosion-bending behaviour of the reaction layer.....	88
4.3.2 Fretting behaviour of the reaction layer.....	91
4.4 Post-operative biomechanical analysis.....	92
4.4.1 Post-operative biomechanical analysis of the rat implants.....	92
4.4.2 Post-operative biomechanical analysis of the ovine implants.....	95

<b>5 Discussion.....</b>	<b>101</b>
5.1 Comparison of the mechanical properties of the cancellous bone and open-cell metallic foam.....	101
5.2 Cast Ti-6Al-7Nb as implant material.....	104
5.2.1 Microstructure and mechanical properties of the cast Ti-6Al-7Nb material.....	104
5.2.2 Cast Ti-6Al-7Nb porous implants.....	110
5.3 Properties of CaTiO <sub>3</sub> reaction layer on cast Ti-6Al-7Nb material.....	112
5.4 Biomechanical response of porous Ti-6Al-7Nb implants in animal experiments.....	116
5.4.1 Biomechanical response of porous Ti-6Al-7Nb implants in rats.....	117
5.4.2 Biomechanical response of porous Ti-6Al-7Nb implants in sheep.....	121
<b>Summary.....</b>	<b>127</b>
<b>Appendices.....</b>	<b>131</b>
<b>References.....</b>	<b>135</b>

## Symbols and abbreviations

### Latin symbols

$C_1, C_2, C_3$	Geometry constants for cellular materials defined by Gibson and Ashby
E	Young's modulus
$E^*$	Young's modulus of a open-cell foam
$E_s$	Young's modulus of the solid which make a strut
F	Force
$F_x$	Longitudinal force during push-out test
$F_y$	Lateral force during push-out test
$h$	Height of a cell strut in a honeycomb defined by Gibson and Ashby
HV	Vickers microhardness
I	Moment of inertia
$l$	Length of the cell strut
$M_p$	Plastic moment
n	Number of samples
pH	Measure of the acidity or basicity of an aqueous solution
R	Stress ratio
$R_a$	Arithmetic average of the absolute roughness
$R_{max}$	Maximum roughness
$t$	Thickness of the cell strut
$t^2$	Cross-sectional area of a cell strut

**Greek symbols**

$\delta$	Bending deflection
$\varepsilon$	Strain
$\varepsilon_D$	Densification strain
$\theta$	Angle of a cell strut in a honeycomb defined by Gibson and Ashby
$\mu\text{CT}$	Micro-computed tomography
$\rho^*$	Density of the cellular material
$\rho_r$	Relative density
$1 - \rho_r$	Porosity
$\rho_s$	Density of the solid
$\sigma$	Stress
$\sigma_{cr}^*$	Brittle crushing strength
$\sigma_{el}^*$	Elastic collapse stress defined by Gibson and Ashby
$\sigma_{fs}^*$	Rupture strength defined by Gibson and Ashby
$\sigma_{pl}^*$	Plastic collapse stress
$\sigma_{ult}$	Ultimate strength
$\sigma_y$	Yield strength
$\sigma_{ys}$	Yield strength of the solid which make the strut

## Symbols and Abbreviations

### Abbreviations

bcc	Body centered cubic
BSE	Back scattering electron
BSP	Bone sialoprotein
Ca-Ti	Calcium titanate
CE	Counting electrode
CP	Commercially pure
cph	Closed packed hexagonal
CVD	Chemical vapour deposition
DIN	Deutsches Institut für Normung
EBS	Electron back-scattered diffraction
ECM	Extracellular matrix
HA	Hydroxyapatite
HD	High density
HDI	High-density inclusions
HIP	Hot isostatic pressing
LD	Low density
LDI	Low-density inclusion
LOF	Weld lack-of-fusion
MD	Medium density
MTD	Main trabecular direction
OCP	Open-circuit potential
OPN	Osteopontin
PLGA	Poly (lactic-co-glycolic)
PMMA	Polymethyl metha acrylate
ppi	Pores per inch
ppm	Parts-per-million
PSR	Pseudo saturation region
PTFE	Polymer-poly tetra fluorethylene
RE	Reference electrode
rpm	Revolutions per minute
SB	Salt bath
SBF	Simulated body fluid
SCE	Saturated calomel electrode

SD	Standard deviation
SE	Secondary electron
SEM	Scanning electron microscope
TAT	Tensile adhesion test
Tb.Sp	Trabeculae spacing
Tb.Th.	Trabeculae thickness
UHMWPE	Ultra-high-molecular-weight polyethylene
WE	Working electrode
XRD	X-ray diffraction
ZTA	Zirconia toughened alumina

## Symbols and Abbreviations

# 1 Introduction

Materials used for orthopaedic implants should possess excellent biocompatibility, superior corrosion resistance in body environment, excellent combination of high strength and low Young's modulus, high fatigue resistance, high wear resistance, high ductility and be without cytotoxicity [1, 2]. For decades, fully dense alloys of cobalt-chromium, titanium, tantalum and stainless steel have been used to replace bone in prosthetic implants. These materials have demonstrated excellent biocompatibility and corrosion resistance but their Young's modulus are substantially higher than that of the bone they replace, leading to stress shielding: a reduction in stress in the remaining bone, which can lead to bone resorption and loosening of the implant [3, 4].

The study of the mechanical behaviour of cancellous bone is important to design appropriated orthopaedic implants. Patients with osteoporosis show an increment of fractures on bones. These fractures are due in part to a reduction in the amount of cancellous bone density. The understanding of the relationship between cancellous bone density and strength helps in predicting when the risk of a fracture has become high and it may help to design an implant that can substitute the damaged bone section. For example, most of the bone replaced by an artificial hip is cancellous; an improved analysis of the structure-property relationships for cancellous bone allows the design of orthopaedic implants with properties that more closely match those of the bone they replace [3].

To solve this problem, in the last years the use of engineering cellular solids has been increased. The cellular solids have a large volume fraction of interconnected pores to facilitate cell migration and transport of nutrients and regulatory factors e.g. cell adhesion peptides, growth factors, hormones [3, 5]. Additionally, cellular solids can be made from a large variety of materials, such polymers, ceramics and metals which results in implants with diverse structural and mechanical properties. Particularly, metal foams offer a number of advantages over solid metals. A variety of processing routes allow control over the relative density, cell size and the fraction of open and closed cells. Control over the relative density of the foam allows matching of the foam and bone Young's modulus [6].

Implant fixation enhanced by porous structures is still under intensive study, after more than 30 years of development [7]. The main problem to overcome is the necessity to balance different properties: average mechanical strength to resist the applied load, a relatively low Young's modulus to prevent stress shielding phenomena, controlled single pore dimensions to stimulate both mineral and collagen osseointegration, an overall porosity to guarantee

## Introduction

interconnection between different pores, corrosion resistance under stress conditions and good biocompatibility [8].

Titanium and its alloys are excellent candidates to be used as implants. They have outstanding biocompatibilities, high corrosion resistance, high strength and low Young's modulus. Especially, commercially pure titanium (CP-Ti) and Ti-6Al-4V have been widely used for manufacturing of implants. However, CP-Ti has low strength which makes it unsuitable for orthopaedic implants. Ti-6Al-4V alloy possesses superior mechanical properties than the CP-Ti which makes it the most commonly used alloy for orthopaedic implants. Unfortunately, the vanadium ions released from the Ti-6Al-4V became suspected to be in long-term toxic to the human body [9-11]. That can be solved by substituting Ti-6Al-4V by the Ti-6Al-7Nb alloy which is also an  $\alpha+\beta$  alloy and has similar mechanical properties than the Ti-6Al-4V. Contrary to vanadium, the element niobium is considered as a vital class element [10, 12].

Porous titanium implants can be manufactured by various techniques such as controlled powder sintering [13], solid-state foaming by superplastic expansion of argon-filled pores [14], as well as by selective electron beam melting and precision casting methods [15, 16]. There is a tendency to use precision-cast methods to fabricated open-cell structures based on Ti-alloys, since the metallurgical quality of casting was continuously improved during the last years. However, the use of cast titanium in biomedical applications has been restrained by inherent casting problems. Molten titanium is extremely reactive with elements such a nitrogen and oxygen as well as with the casting investment elements [17-19]. The high affinity of titanium to oxygen in combination with a high solubility results in the quick formation of titanium oxides and an oxygen-enriched surface layer in the base metal. Additionally, reactions with the mold material may cause the formation of embrittling phases, e.g.,  $Ti_3Al$ . The brittle surface layer on titanium alloys has been termed  $\alpha$ -case layer. Since  $\alpha$ -case deteriorates strongly the mechanical properties of the material by promoting crack formation under static or cyclic loading conditions [9, 17, 19], attention has to be paid to avoid  $\alpha$ -case formation by vacuum metallurgy or to remove the embrittling layer either mechanically or chemically, e.g., by acid pickling (cf. [18]).

The investigations reported in this dissertation are part of an interdisciplinary work between the Gießerei-Institut der RWTH Aachen, the Bundesanstalt für Materialforschung und -prüfung (BAM) Berlin, the Labor für Metallkunde und Werkstoffanalytik of Hochschule Osnabrück, the Labor für Experimentelle Unfallchirurgie of the Justus-Liebig-Universität Gießen and the Institut für Werkstofftechnik of the Universtät Siegen. Particularly, the work

carried out in the Universität Siegen was financially supported by the Deutsche Forschungsgemeinschaft (DFG) under the grant No. Ch92/38. The aim of this work is the characterization of precision-cast porous Ti-6Al-7Nb implants coated with a CaTiO<sub>3</sub> reaction layer. In order to analyse the biocompatibility properties of the cast Ti-6Al-7Nb implants and the influence of the reaction layer in the osseointegration process, in-vitro and in-vivo biomechanical analyses were carried out using rats and sheep in the framework of the joint project. These animals were chosen due to their metabolism, cancellous bone structure, cost and availability, transferability of information as well as ethical and social implications.

To evaluate the biological fixation and to analyse the biomechanical behaviour of the porous implants, they were inserted in “defects” created in the cancellous bone area of the distal femoral metaphyses of rats and sheep. After a recovering time of 30 days in rats and 6 months in sheep, the implants were extracted from the bone by using a push-out test. This test allows an accurate and reliable evaluation of the uni-axial strength of the bone that grows around and inside the implants. Additionally, the deformation behaviour rate during the push-out test can be controlled permitting an optimal evaluation of the biomechanical characteristics of osseointegrated implants.

This dissertation is subdivided in seven chapters: introduction, theoretical background, materials and methods, results, discussion, summary and appendices. The section 2.1 describes the cancellous bone which is a natural cellular solid with extraordinary structural and mechanical properties, and it was the inspiration of the porous implants used in this work. The structure, mechanical properties, and degenerative diseases of cancellous bone are explained to understand the optimal properties that an implant should possess in order to substitute a damaged cancellous bone section. The requisites that a biomaterial should fulfil before to be used in the body are analysed in section 2.2 focusing on orthopaedic implants. Titanium and its alloys are described in section 2.3 as outstanding materials for orthopaedic applications. Therefore, their properties and manufacturing processes with focus in the casting process to fabricate cellular structures are explained. In section 2.4 the properties of engineering open-cell structures used in medical applications are introduced.

Chapter 3 describes the bones and metallic samples used in this work and their preparation for the experiments that include microstructural analysis, mechanical testing and the in-vitro biomechanical analysis after the euthanasia of the rats and sheep. The results obtained during the experiments are reported in chapter 4 which is subdivided in 4 sections: Section 4.1 describes the compression behaviour of the bovine and ovine cancellous bones and the compression behaviour of 45ppi open-cell AlSi7Mg foam samples. Bovine and ovine bones

## Introduction

were used to understand the behaviour of cancellous bone of big animals under compressive loading conditions. The open-cell AlSi7Mg foam has similar structure and morphology to those of the ovine and bovine bones. The results obtained with the cancellous bone and foam samples are important to understand and compare the mechanical response of these materials with those of the Ti-6Al-7Nb porous implants. Section 4.2 deals with the results obtained by microstructural and mechanical characterization of the cast Ti-6Al-7Nb porous implants. The chemical and mechanical properties of the titanate reaction layer are depicted in section 4.3. The post-operative biomechanical results obtained with the rat and ovine implants are described in section 4.4.

In chapter 5 results are thoroughly discussed against the background of the information available in the literature. Finally the main highlights are summarized in chapter 6. Clinical information of the animals before and after the implantation and euthanasia as well as the complete lists of push-out test data are listed in the appendices.

## 2 Theoretical background

### 2.1 Cancellous bones

#### 2.1.1 Bone tissue

Bones fulfil mechanical, biological and chemical functions in the body of a vertebrate. Bones are responsible for the movement and support of the body as well as the protection of various organs. Inside bones, red and white blood cells are produced and they store important mineral for the body. Bones come in a variety of shapes and have a complex internal and external structure [20, 21]. Macroscopically they can be subdivided as hollow or long bones (femur, tibia, fibula, etc.), flat bones (ilium, sacrum, scapula, etc.), irregular bones (vertebrae, sacrum, maxilla, etc.), short bones, and sesamoid bones [22]. The mechanical properties of the bone material depend on the properties of its components phases, and the structural relationship between them at the various levels of hierarchical structural organization [23-25]. Figure 2.1 shows the different levels and structures. The level 1 corresponds to the macrostructure. In this level bones are subdivided in cancellous or trabecular (spongy bone) and cortical bone (compact bone). The level 2 is the microstructural level. In this level the bones are building of harvesian system, osteons and single trabeculae. This level is followed by the sub-microstructural level (level 3). Lamellae, wovens are the principal constituents of the bones at the level 3. The level 4 correspond to the nanostructure. Bones at this level are made of fibrillar collagen and embedded material. Finally, the sub-nanostructural level of the bones corresponds to the molecular structure of constituent elements, such as mineral, collagen, and non-collagenous organic proteins [24, 26, 27].

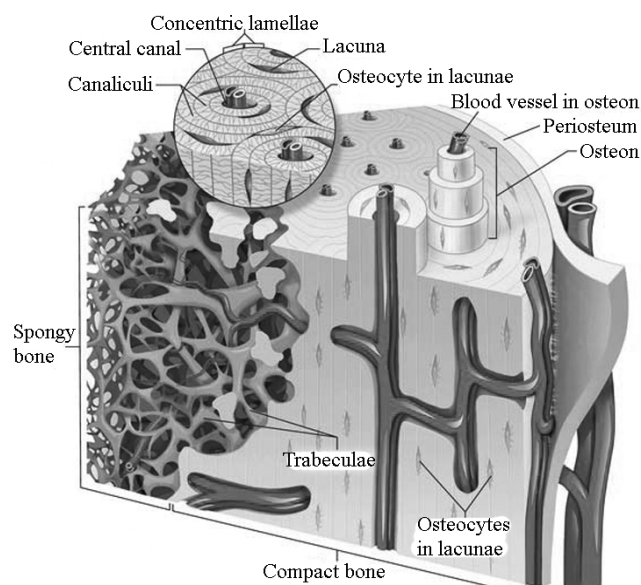


Figure 2.1: Schematic representation of the bone structure [28]

## Theoretical background

Different mechanical properties are reported for these structural levels. For instance, the Young's modulus of large tensile cortical specimens has been found to be in the range of 14-20 GPa [29]. On the other hand, the Young's modulus of micro-bending cortical specimens was about 5.4 GPa [30]. It has also been found that the modulus of the osteon lamellar bone measured by nanoindentation was approximately 22 GPa [31].

Apart from the differing structural architecture, the tissue composition is almost similar in the cortical and cancellous bone. It consists of approximately 65% of a mineral and 35% of an organic phase. The mineral component is built of hydroxyapatite [HA;  $\text{Ca}_{10}(\text{PO}_4)_6(\text{OH})_2$ ], carbonate, citrate, magnesium and fluoride. Collagen type 1 organised in helix-like fibres forms about 90% of the organic matrix proteins. The other components are non-collagenous proteins and water [32].

The cortical and cancellous bone are distinguished by their degree of porosity or density [33, 34]. The true differentiation comes from the histological evaluation of the microstructure of the tissue. In general, the cancellous bone material is much more active metabolically and it remodels more often than cortical bone. Therefore, even though cancellous and cortical bone may be composed of the same kind of material, the maturation of the cortical bone material may alter the mechanical properties at the microstructure level [24].

The mechanical properties of cortical bone are influenced by the porosity, the mineralisation level and the organization of the solid matrix [35, 36]. The values of the mechanical properties at the macrostructural level vary from one bone to another as well as within different regions of the same bone. It has been found that the mechanical properties of human cortical bone from tibia, femur, and humerus vary between subjects, although the density is the same. The Young's modulus in the longitudinal direction is not very different between the various types of cortical bone. However, the modulus varies greater along the length of a whole bone than around its circumference [24, 37, 38].

### **2.1.2 Cancellous bone structure**

Cancellous bone, also termed as trabecular bone, is a tissue with foam-like structure [34]. This bone type exists at the end of the long bones, in the vertebrae (irregular bones), and in the core of shell-like bones such as the skull and the pelvis [3].

The cancellous bone of human adults is made primarily of lamellae or fragments of Haversian. In young mammals it may be made of woven or parallel-fibered bone [27]. The structure of trabecular bone varies in three ways: in its fine-scale structure, in its large-scale structure, and in its porosity. At the fine scale, cancellous bone is usually made of lamellar

bone. At the first look, the cancellous bone consists of randomly oriented cylindrical (rod-like) struts, about  $100\ \mu\text{m}$  in diameter, each extending for about 1 mm before making a connection with one or more other struts [27, 39].

Figure 2.2 shows that the pattern of cylindrical struts can vary by little plates. Low-density trabecular bone has a rod-like (struts) structure (Figure 2.2a). As the density increases, the foam structure becomes more like perforated plates (Figure 2.2b). The amount of variation between rod- or plate-like structure ranges from cancellous bone in which there is just an occasional plate among the struts to cancellous bone in which there is just an occasional strut among the plates. In many cancellous bones the plates or struts may be considerably longer up to several millimeters. The longer plates or struts are not randomly oriented instead they are preferentially aligned in one direction called main trabecular direction (MTD). That led to higher level of anisotropy along the bones [3, 39, 40].

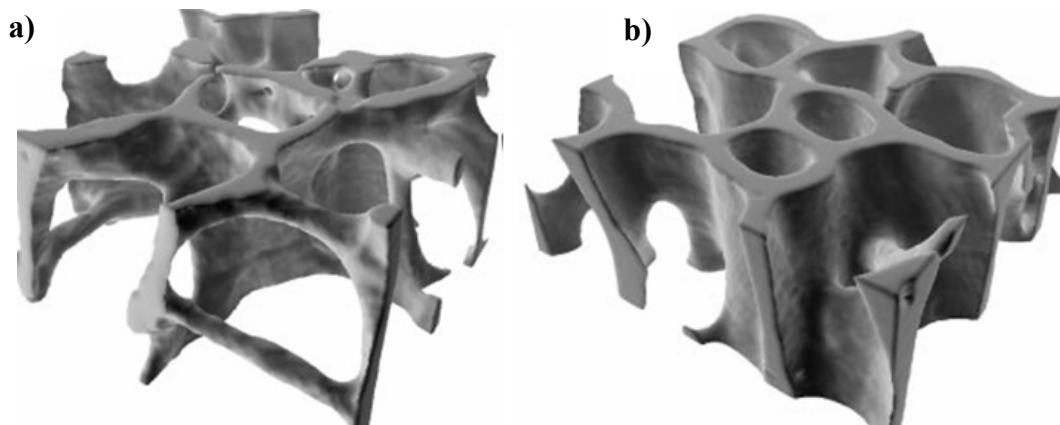


Figure 2.2: a) rod-like trabecular bone, b) plate-like trabecular bone [41]

The type of bone made of cylindrical struts has no preferred orientation and is usually found deep in bones away from any loaded surface. On the other hand, the more oriented type is made of many sheets and is found just underneath loaded surfaces particularly where the pattern of stress is reasonably constant [27, 42].

The porosity of cancellous bone is the proportion of the total volume that is not occupied by bone tissue. Usually it is filled with marrow, whereas in birds there may be gas. The porosity varies from being effectively complete, where there is only the occasional tentative strut sticking into the marrow cavity, until approximately 50%. If the porosity is less than about 50%, then cancellous bone becomes difficult to distinguish from compact bone with many holes in it. However, the change from compact to cancellous bone is usually clear and takes place over a small distance [27].

Bones grow in response to mechanical loading, and there is substantial evidence that the trabeculae are oriented in the direction of the main stresses [27, 43]. That can be observed in

## Theoretical background

trabecular bone in human vertebrae. They are loaded primarily along the length of the spine and from the constraint of the cortical shell, in other words radially. Therefore, most vertebral trabeculae are oriented roughly in the longitudinal or transverse directions [44]. It is generally accepted that the density of trabecular bone depends on the magnitude of the stresses that it experiences, while the microstructural anisotropy depends on the ratio and the direction of the main stresses [3].

### **2.1.3 Mechanical properties of cancellous bones**

Cancellous bones are made up of individual trabeculae, each with its own stiffness. At the same time the trabeculae build a structure that has its own unique stiffness, which is the stiffness of each trabecula and the stiffness of the trabecular structure [45]. In the past it was assumed that individual trabeculae, single osteons, and a thin cortical shell had the same mechanical properties as those of large cortical bone specimens regardless of their type or size [24, 46]. However, many investigators produced values for the Young's modulus of individual trabeculae, single osteons, and a thin cortical shell that were considerably less than that for the whole bone [30, 45, 47]. Most biomechanical studies of cancellous bone concentrate on structural properties because the material properties of trabeculae are difficult to measure.

Cancellous bone possesses various anisotropies depending on the specific anatomical site [34, 48, 49]. The tissue structure has been shown to vary from nearly transverse isotropic (for example in human vertebra) to orthotropic e.g. human calcaneus [40, 50].

The structure of trabecular bone changes due to reductions in bone mass during aging. It has been found in previous work that there is a 50% reduction in the relative density of vertebral trabecular bone between 20 and 80 years of age [51]. The trabeculae initially are thin and then they grow until the thickness reaches a critical dimension. When this happens, they resorb entirely reducing the connectivity of the structure [52]. Resorption of the trabeculae has a dramatic effect on the Young's modulus and strength of cancellous bone [44, 53-55].

Numerous animal models have become a reliable basis for research on aetiology and pathogenesis, and they enable scientists to develop new treatment strategies. So far, there has been no animal model available which can satisfactorily answer the orthopaedic and surgical questions related to osteosynthesis materials and fracture healing treatments for bones subject to osteoporosis. An adequate size of the animal bones used for the tests is mandatory in order to allow any transfer of knowledge to the human medicine field [56]. Bovine and ovine

trabecular bone specimens were used as they provide an appropriate large animal model for analysis of the mechanical behaviour of bone [49, 57-64]. Table 2.1 shows the Young's modulus and compressive strength of cancellous bone for different anatomic sites, ages and animal models.

Table 2.1: Mean values of Young's modulus and ultimate strength of various cancellous bones

Anatomic site	Age	Young's modulus (MPa)	Ultimate compressive strength (MPa)
Human vertebra [65]	87 years	67±45	2.4 ± 1.6
Human proximal tibia [66]	82 years	445±257	5.3 ± 2.9
Human proximal femur [67]	85 years	441±271	6.8 ± 4.8
Human femur head [40]	65 years	2730±1060	18 ± 6.4
Human calcaneus [50]	Not reported	68±84	1.4 ± 1.3
Bovine proximal tibia [68]	Not reported	2380±777	24 ± 8.3
Bovine femurs [69]	Not reported	310±161	15.74 ± 9.59
Bovine calf lumbar sacral [70]	Not reported	173±97	7.1 ± 3.0
Ovine lumbar vertebra [62]	Not reported	261±53	27.61 ± 8.02
Ovine proximal tibia [63]	36 months	869±224	16.6 ± 3.4
Ovine femur neck [71]	Not reported	Not reported	3.15 ± 0.337

The Young's modulus and failure stress of trabecular bone depends primarily on apparent density, which is the product of volume fraction and trabecular tissue density. However, the precise form of this relationship remains controversial [41]. It appears that most of the controversy stems from the dependence of this relationship on anatomic site and loading direction [72-74], and from the imprecision introduced by ignoring anisotropy and end-artifact effects in the mechanical tests [40, 72, 75].

Data for the Young's modulus and strength of different materials present in nature are plotted in Figure 2.3. The trabecular bones are subdivided in: low density (LD), medium density (MD), and high density (HD). Both strength and Young's modulus vary largely with the variation of density of the trabecular bone.

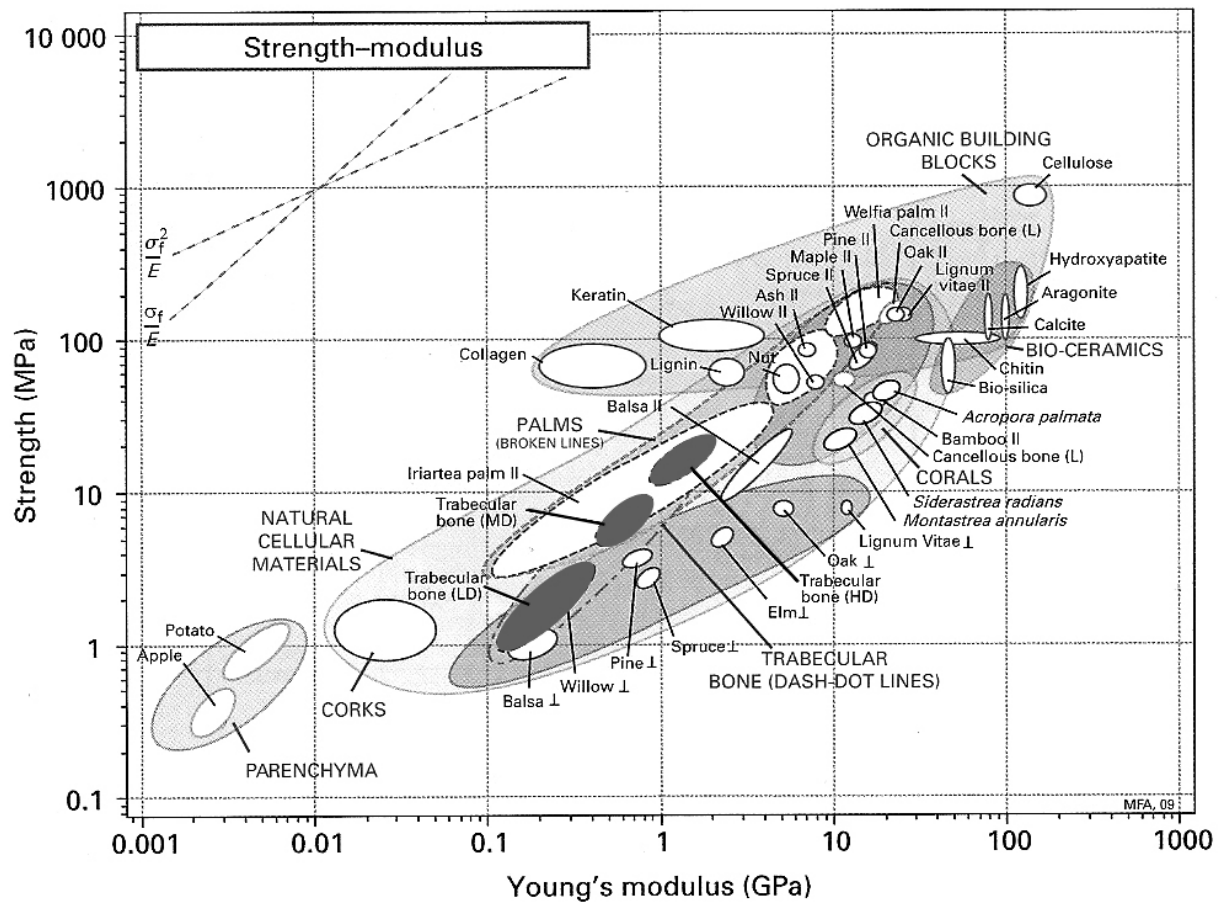


Figure 2.3: Strength-Young's modulus chart for natural cellular material [3]

### Compression behaviour

The stress-strain curve of cancellous bone in compression follows similar behaviour as other cellular solids. In Figure 2.4 it is possible to distinguish three regions of behaviour: an initial linear portion, a plateau of almost constant stress, and a final increasingly steep region. Each of these regions has a distinct mechanism of deformation associated with the density [34]. At small strains the behaviour is linear elastic. In cells with asymmetric structure, the rod or plates intersect at each other's mid-points, causing elastic bending of the cell walls [76]. In cells with columnar structure, the rod or plate-like trabeculae stack one on the top of the other, and deformation in the longitudinal direction is driven by axial compression of the cell walls [77]. In the transverse direction, the cells do not align, and the deformation is governed by bending the same as in asymmetric cells. At sufficiently high strains, the cell fails by buckling, by plastic yielding or by brittle fracture. If the trabeculae have a high ratio of length to thickness, failure is caused by elastic buckling both in wet and dry specimens. But at lower ratios, the wet specimens yield plastically while the dry samples fracture in a brittle manner [78].

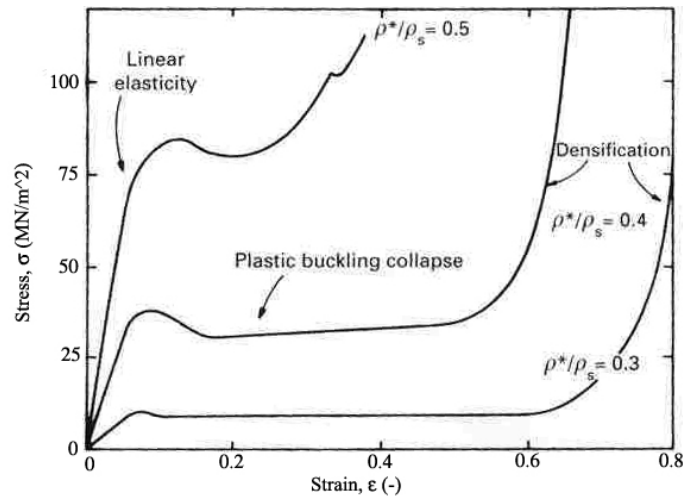


Figure 2.4: Compressive stress-strain curve of cancellous bone for different relative densities of wet trabecular bone [3]

Failure progresses at a roughly constant load until the cells close up sufficiently for the cell walls to touch. When this occurs, the resistance to load increases giving rise to the final steep portion of the stress-strain curve. As the density of the trabecular bone increases, the cell walls become thicker and consequently the Young's modulus and strength of the cellular structure increase. The strain at which the cell walls touch decreases, reducing the length of the plateau regime [34].

### ***Fatigue and creep behaviour***

Cyclic deformation of cancellous bone varies depending on the anatomic position, density, etc., but it shows common deformation mechanisms [49, 57, 60, 79]. An increasing residual strain (cyclic creep) which causes a shift of the hysteresis loops along the strain axis and an increase of the nonlinearity of the hysteresis loops have been observed [79]. Some suggest that cyclic creep plays an important role in the deformation of cancellous bones under fatigue loading conditions [57, 59, 79], whilst Moore et al. [61] seem to believe otherwise, i.e. creep does not contribute to fatigue in trabecular bones.

Figure 2.5 shows the main phases of the cyclic deformation behaviour. They may be classified as deformation in the transient region, the pseudo saturation region (PSR), defined failure and catastrophic failure [32, 57, 60, 80].

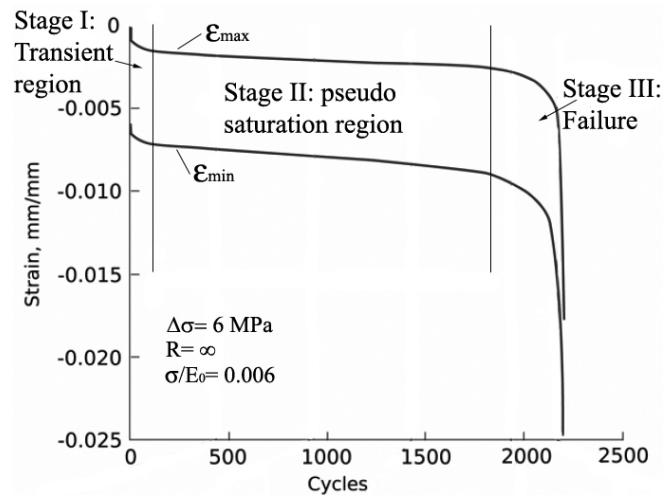


Figure 2.5: Strain evolution as a function of numbers of cycles of bovine cancellous bone [79]

Creep failure of trabecular bone plays an important role in the loosening of hip prostheses and in the etiology of spine fracture [81-83]. An understanding of the creep behaviour of trabecular bone may therefore have clinical relevance if it can be related to these etiologies. For example, it may be possible that cyclic creep damage, like fatigue damage, decreases the strength of whole bones [84]. Damage to trabecular bone tissue caused by cyclic creep may also have biological relevance if bone remodelling is induced to repair this damage [58].

The mechanical properties of cancellous bones are of interest in understanding how it behaves in both healthy and diseased states [3]. This knowledge is necessary to investigate treatment options for bone diseases like osteoporosis. In elderly patients with osteoporosis, the mass of bone in the body decreases over the time to such an extent that fractures can occur under loads that, in healthy people, would be considered normal. Such fractures are common in the vertebrae, hip and wrist. A reason of these fractures is the reduction in the amount of trabecular bone in these areas [32, 51].

#### 2.1.4 Degenerative diseases of cancellous bones

Bone growth occurs during the first twenty years of life followed by a period of consolidation during which time an individual's peak bone mass is reached. Bone has the property of renewing itself throughout adult life and is never metabolically at rest [85]. Throughout life, females have lower bone mass than males but with advancing age this difference widens. Over a lifetime a female will lose approximately 35% of their peak cortical bone and approximately 50% of their cancellous bone, while a male will lose approximately three quarters of this amount [86]. For cancellous bone the rate of loss ranges from  $1 \pm 3\%$  per year in women and is approximately 1.2% in men. The loss rate of cortical bone is lower at

$0.3\pm 0.5\%$  per year. Temporary accelerated rates may be experienced by postmenopausal women [85, 87, 88].

Aging-related bone diseases are comprised of three major classes: the erosion of the joints or osteoarthritis; an increase in bone resorption leading to osteoporosis, a low bone mass disease with high risk of fracture; and metastatic bone disease that relates to breast cancer in women or prostate cancer in men [89]. Osteoarthritis and osteoporosis are the most frequent degenerative diseases of the skeleton. They are also the most frequent degenerative diseases observed in developed countries [89, 90]. Figure 2.6 shows the effect of the osteoarthritis, and osteoporosis in the compressive strain-stress curve of a trabecular human cuboid bone.

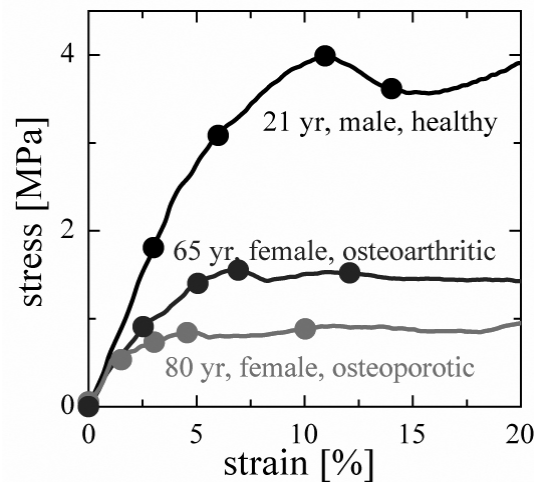


Figure 2.6: Effect of osteoarthritis, and osteoporosis in the compressive strain-stress curve of a trabecular human cuboid bone [91]

Osteoporosis is a health problem of clinical relevance that recognizes many different pathogenetic factors [92, 93]. Structural modifications related to osteoporosis mainly affect cancellous bone, but cortical bone also is compromised with the reduction of cross-sectional area because of the endosteal resorption and medullary expansion [94, 95]. Osteoporotic patients develop pathologic fractures mainly affecting the hip, spine, and wrist, but the incidence of fracture also increases at many other sites, necessitating the greater use of plates, pins screws, and arthroplasties in osteoporotic bones [96].

Trabecular bone may play a role in osteoarthritis, which is thought to be related to a breakdown in the lubrication process at joints. The distribution forces acting across a joint is directly related to the mechanical properties of the underlying trabecular bone, so changes in its structure (and hence properties) may change the distribution of the forces and cause

damage to the lubrication system [3]. The ability to accurately assess the bone quality in-vivo is essential for improving the diagnostic and therapeutic goals for bone loss from such varied etiologies as osteoporosis, microgravity, bed rest, or stress shielding from an implant [97].

Most of the bone replaced by an artificial hip is trabecular; therefore a better understanding of the structure-properties relationships for trabecular bone allows a better design of implants with properties that more closely match those of the bone they replace. The mismatch of properties between current implants and surrounding bone is thought to be one of the reasons of implant failure [3].

### **2.2 Requirements for a biomaterial**

Biomaterials are artificial or natural materials, used for making of structures or implants, to replace the lost or diseased biological structure to restore its form and function. The biomaterial helps in improving the quality of life and longevity of human beings. The field of biomaterials has shown rapid growth to keep with the demands of an aging population [4]. Biomaterials are used in different parts of the human body such as artificial valves in the heart, stents in blood vessels, replacement implants in shoulders, knees, hips, elbows, ears and orodental structures [98]. Particularly, the number of implants used for spinal, hip and knee replacements are extremely high. In the previous chapter, it was described that the human joints suffer from degenerative diseases such as osteoporosis and osteoarthritis generating pain and loss of function. The degenerative diseases lead to degradation of the mechanical properties of the bone due to excessive loading or absence of normal biological self-healing process. Artificial biomaterials are the solutions for these problems, as surgical implantation of these materials of appropriate shapes helps in restoring the function of the damaged tissues.

The design and selection of biomaterials depend on the intended medical application. Development of new biomaterials is an interdisciplinary effort and it often requires a collaborative effort between materials scientists, engineers, pathologists and clinicians [4].

#### **2.2.1 Design and mechanical properties**

Biomaterials are used either to regenerate the tissues (tissue engineering scaffolds) or to substitute tissues in the body e.g. implants. The goal of tissue engineering is to generate diseased or damaged tissues by providing a scaffold that mimics the body's own extracellular matrix (ECM). Scaffolds for the regeneration of a wide range of tissues, e.g. orthopaedic, cardiovascular, nervous, gastrointestinal, urogenital, are currently being developed [3]. Tissue

engineered scaffolds should fulfil a number of requirements. The material must be biocompatible and it is desired that these materials degrade over time because they lose strength as they age [99, 100]. The degraded scaffold should be replaced by the restored host tissue. It must also promote cell attachment, proliferation, migration, differentiation and production of native ECM [3].

Materials used for hip and knee implants are examples of bone substitute materials. The materials used for orthopedic implants especially for load bearing applications should possess excellent biocompatibility, superior corrosion resistance in body environment, excellent combination of high strength and low modulus, high fatigue strength, high creep strength, toughness and wear resistance, high ductility and be without cytotoxicity [1, 2, 101]. Presently, the materials used for these applications are mostly 316L stainless steel, cobalt chromium alloys, and titanium-based alloys. They are sometimes coated with a porous sintered metal or ceramic to increase bone ingrowths into the implant.

The mechanical properties decide the type of material that will be selected for a specific application. Some of the properties that are of prime importance are hardness, tensile strength, modulus and elongation [4]. The response of the material to repeated cyclic loads or strains is determined by the fatigue strength of the material and this property determines the long-term success of the implant subjected to cyclic loading. If an implant fractures due to inadequate strength or mismatch in mechanical properties between the bone and implant, then this is referred as biomechanical incompatibility. The material that replaces a part or the complete bone is expected to have a modulus equivalent to that of bone. The current implant materials have higher stiffness than bone, and thus the implant transfers the major part of the load, resulting in bone resorption around the implant that finally lead to implant loosening. This biomechanical incompatibility that leads to death of bone cells is called “stress shielding effect” [102]. Thus a material with excellent combination of high strength and low modulus closer to bone has to be used for implantation to avoid loosening of implants and longer service period to avoid revision surgery. Figure 2.7 shows a comparison between the mechanical properties of bone and various biomedical materials.

## Theoretical background

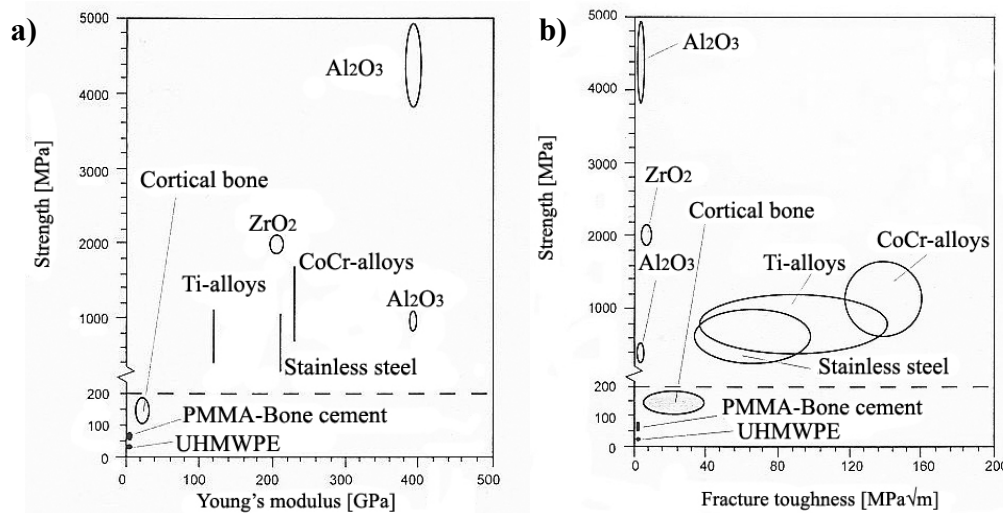


Figure 2.7: Comparison of the mechanical properties of different biomaterials used in orthopaedic implants: a) strength vs. Young's modulus and b) strength vs. fracture toughness [103]

A very important factor for the success of an implant is the fixation between the prosthesis and the bone. A good bone-implant fixation is necessary to have a pain free joint. When the bone-implant interface starts to fail, a soft fibrous tissue grows at the interface that allows more relative motion between the implant and the bone under loading. This leads to migration of the implant and causes pain to the patient. After a certain period the pain becomes intolerable and the implant must be replaced. There are a number of factors that may contribute to aseptic or mechanical loosening. Among these factors are bone necrosis (death) in the interface of bone-implant, mechanical damage done during surgery, wear debris, and mechanical loosening from fatigue at the interface. The last two factors are mechanical in nature and can be accounted for in implant design [104, 105]. It is therefore necessary to put particular attention to the design of the implant in order to avoid these problems and to induce the ingrowth of bone tissue in the implant.

### 2.2.2 Biocompatibility and osseointegration

The material used for the implant is expected to be highly non-toxic and should not cause any inflammatory or allergic reaction in the human body. The success of the biomaterial is mainly dependent on the reaction of the human body to the implant, and this measures the biocompatibility of a material [101]. The two main factors that influence the biocompatibility of a material are the host response induced by the biomaterial and the material's degradation in the body environment. Based on the response of the human body biomaterials can be biotolerant, bioactive or/and bioreabsorbable. Biotolerant are those materials that respond with the formation of thin connective tissue capsule (0.1 to 10  $\mu\text{m}$ ) and the capsule does not

adhere to the implant surface. Example of biotolerant materials are polymer-poly tetra fluorethylene (PTFE), polymethyl metha acralyte (PMMA), titanium, cobalt-chromium, etc. Bioactive materials response in the body with the formation of bony tissue around the implant and they strongly integrate with the implant surface. Examples of bioactive materials are bioglass, synthetic calcium phosphate including hydroxyapatite (HA), etc. Finally, the bioreabsorbable materials are those that after some time in the body are replaced by autologous tissue. Examples of these materials are polyactic acid, polyglycolic polymers as well as processed bone graft, composites of all tissue extracts, proteins and support system [4]. Bioactive materials are highly preferred as they give rise to high integration with surrounding bone, however, biotolerant implants are also accepted for implant manufacturing.

When implants are exposed to human tissues and fluids, several reactions take place between the host and the implant material and these reactions dictate the acceptability of these materials by our immune system. Figure 2.8 shows a schematic representation of the response of the human bone to an implant at different time intervals and the various reactions occurring on the surface.

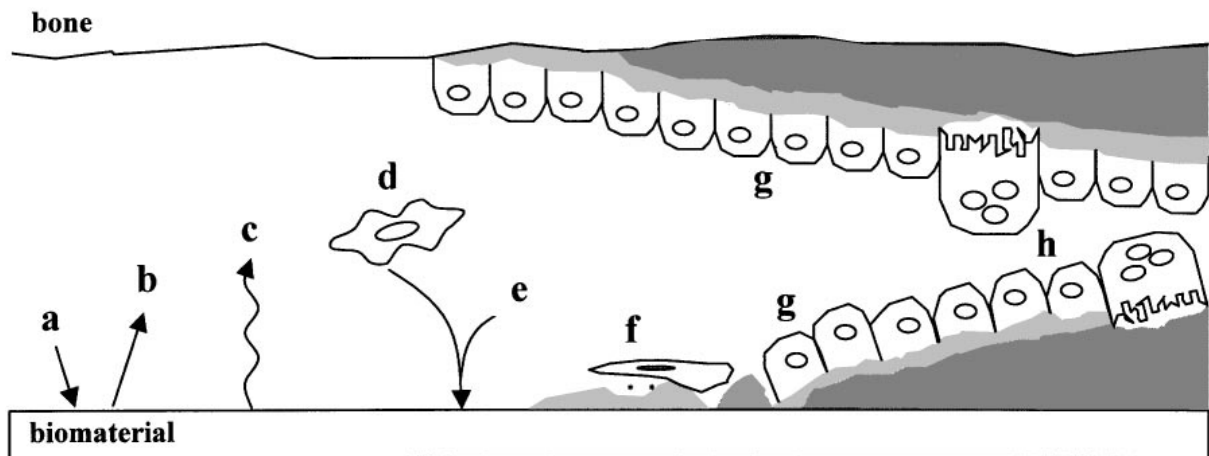


Figure 2.8: Representation of events at the bone-implant interface: a) Protein adsorption from blood and tissue fluids, b) protein desorption, c) surface changes and material release, d) inflammatory and connective tissue cells approach the implant, e) possible targeted release of matrix proteins and selected adsorption of proteins such as BSP (Bone sialoprotein) and OPN (Osteopontin), f) formation of *lamina limitans* and adhesion of osteogenic cells, g) bone deposition on both the exposed bone and implant surfaces, h) remodelling of newly formed bone [106]

The events at the bone-implant can be separated in two components: the response of the host to the implant and the behaviour of the biomaterial in the host [107]. The biomaterial response begins almost immediately after the implantation with the adsorption of proteins. These proteins first come from blood and tissue fluids at the wound site and later from cellular activity in the periprosthetic region. Once on the surface, proteins can desorb (native

## Theoretical background

or denatured, intact or fragmented) or remain to mediate tissue-implant interactions [108, 109]. Some authors believe that the nature of this *conditioning film* deposited on biomaterials is responsible for the host response [106]. Additionally, it is necessary to put attention on the surfaces changes that occur in the biomaterial. One of these changes is the oxidation of metallic implants. This topic will be described in details in the next section.

On the other hand, the host response to implants placed in bone involves a series of cell and matrix events, ideally culminating in intimate apposition of bone to biomaterial, i.e., osseointegration. For this intimate contact to occur, gaps between bone and implant must be filled, and bone damaged during preparation of the implant site must be repaired [106]. During this time, unfavorable conditions e.g. premature loading leading to micromotion, will disrupt the newly forming tissue, leading to formation of a fibrous tissue capsule around an implant [110-112]. This unfavourable reaction of the body is principally due to the conditions of the biomaterial surface, since the first contact of the body is with the surface of the implant. The specific interactions determine the path and speed of the healing process and the long-term integration of the bone-implant interface. Both the chemical composition on the surface and the surface topography are important in bone contacting implants. They regulate the type and the degree of the interactions that take place at the interface. Examples of these interactions are the adsorption of ions and biomolecules such as proteins, formation of calcium phosphate layers, and the interaction with different types of cells e.g. macrophages, bone marrow cells and osteoblasts. Therefore, the nature of the initial interface that is developed between an artificial material and the attached tissue determines the ultimate success or failure of the materials. Tissue-biomaterial compatibility is the most important issue to be considered for the implant success [4].

In addition to the biomaterial and biological events, the biomechanics of the bone-implant interface must be studied. There, the presence of a cement line/*lamina limitans* at the interface between bone and implant, similar to that between mineralized matrices or bone cells and mineralized matrix, need to be considered. These cement lines are believed to be weak points because mechanical failure of bone are frequently localized at these sections [113]. Consequently, the strength of the interface tissue-implant is expected to be significantly inferior to the intrinsic strength of the bone [106]. Another factor that must be considered is that the excessive interfacial micromotion during bone healing is detrimental to osseointegration [112]. It is possible that the relative motion between bone and implant damages the *fibrin network* and new vasculature that are part of the early bone healing process, consequently rerouting the healing response into repair by scar tissue [106].

Considering the complexity of the tissue-implant interface, it is necessary to study the mechanical loading altering the interface responses with in-vivo and in-vitro tests.

The mechanical characteristics of the bone-implant interface can be evaluated with different techniques such as e.g. removal torque [114], tensile pull-out [115], push-in [116] and push-out [117, 118] tests. The anatomical position and the type of implant need to be considered in the selection of one of these techniques. For example, the removal torque is commonly used to measure the osseointegration of screwed implants. Pull-out test is utilized to measure the uni-axial strength and in order to control the deformation rate of the bone-implant interface. Similar advantages offer the push-in and push-out test, but additionally the push-out test allows an accurate analysis of the shear strength without the interference of the tensile component. Consequently, it produces a stress analysis more reliably directed at the bone-implant interface [118].

### **2.2.3 Corrosion resistance behaviour of biomaterials**

Metals and alloys are subjected to corrosion when they are in contact with the body fluids. The reason is that the body environment is very aggressive owing to the presence of chloride ions and proteins [4]. Figure 2.9 shows the relationship of the biocompatibility (discussed above) and the polarization resistance of metals (common technique in the corrosion monitoring). In this figure it is possible to observe that the best combination of biocompatibility and high corrosion resistance are achieved by Ti-alloys, Ta-alloys, Co-Cr alloys and the 316L stainless steel. These materials react with the blood and other body fluids and develop very thin and stable oxide films. These films are passive in nature and protect the metals against further corrosion as long as the integrity of the films is maintained [9, 119]. Nevertheless, on these biomaterials still electrochemical changes occur in the physiological environment. For example, depending on the method of sterilization, commercially pure Ti implants have an oxide thickness of 2-6 nm before implantation [120]. Films on implants retrieved from human tissues are two to three times thicker [119, 121].

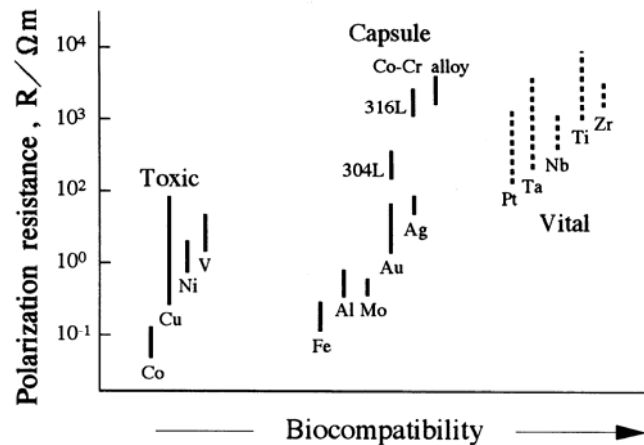


Figure 2.9: Relationship between polarization resistance and biocompatibility of pure metals, Co–Cr alloy and stainless steels [122]

Surface analytical studies show that the chemical composition of the oxide film of Ti-alloys and stainless steel changes due to the presence of Ca, P, and S [119, 120]. Continued oxide growth reflects ongoing electrochemical events at the tissue-implant interface. Another consequence of these events is the release of metal ions into tissues [123]. This corrosion by-products accumulates locally, but it also spreads systemically. As consequence, elevated metal contents have been detected both in periprosthetic tissues [124, 125] and in serum and urine of patients with implants [126, 127]. For example, metal levels of up to 21 ppm Ti, 10.5 ppm Al, and 1 ppm V around Ti-6Al-4V and up to 2 ppm Co, 12.5 ppm Cr, and 1.5 ppm Mo around Co-Cr-Mo have been measured in the fibrous membrane encapsulating implants [124, 125]. Trace metals are essential for health, but they can also be toxic [128] or cause hypersensitivity reactions [129]. In-vitro studies have revealed that metal ions, even at sublethal doses, interfere with differentiation of osteoblasts and osteoclasts. It remains to be determined if these effects on bone cells also occur in-vivo [106, 130-132].

The corrosion resistance of the passive film depends on the alloying elements and their oxides formed. In addition, the corrosion resistance is affected by the physiological conditions of the body. For example, the pH of the body may vary from 3.5 to 9 depending on the condition of the area around the implant, e.g., if the area is wounded or infected [4].

Some forms of corrosion that can occur are crevice, pitting, fretting, etc. (Figure 2.10). Crevice attack refers to corrosion at shielded sites such as screw/plate interface and under washers. This is often observed in 316L and REX stainless steel as well as in other passive alloys in the presence of chlorides [4, 133]. Pitting corrosion is a common problem with 304 SS implants. This corrosion of the implants is more predominant in the oral cavity due to the greater availability of oxygen and acidic food stuffs in the environment [134]. Most of the orthopaedic implants are subjected to low frequency loads that may lead to corrosion fatigue.

Even simple walking results in a hip implant being subjected to a cyclic loading at about 1 Hz. Fatigue corrosion resistance of titanium is almost independent of the pH value while the fatigue corrosion strength of stainless steel declines below pH 4 [135]. Fretting corrosion is very common in all load bearing metallic orthopedic implants. Fretting occurs at the bone-stems interface, the stem-cement interface and on the interface of modular connection between implant components. The generation of ionic and particulate debris through fracture and abrasion of the metal oxide protective layers and their deposition in the local tissue has caused clinical concern [4].

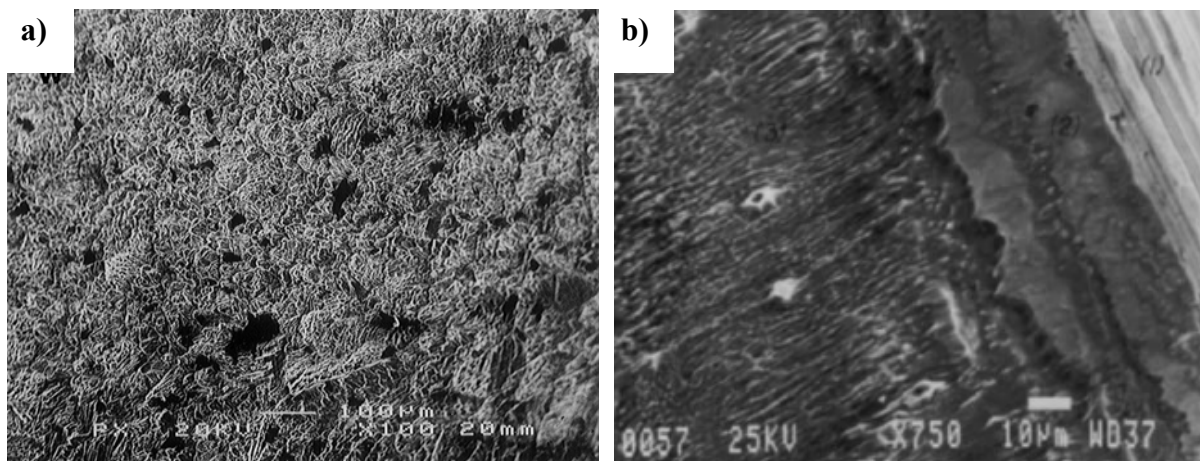


Figure 2.10: a) Pitting corrosion in a welded REX 734 stainless-steel orthopaedic implant [136], b) Fretting-corroded region of a wrought CoCrMo head on a forged titanium-stem retrieved after 33 months [137]

Corrosion behaviour of a given metal in an electrolytic medium can be evaluated by using different techniques e.g. polarization curve to observe the development and breakdown of the passivation layer of biomaterials [10], electrochemical noise to study local corrosion as crevice or pitting [138], potentiostatically controlled current to analyse the fatigue induced surface damage [139]. The free corrosion potential or the open-circuit potential has been used to observe the influence of the surface damage on the steady-state corrosion potential [140-143]. Figure 2.11 shows the open-circuit potential (OCP) of different biomaterials in a simulated body fluid (SBF). It is observed that at certain time, the alloys achieve a steady-state potential which indicate the complete formation of the passive layer. The behaviour of this steady-state potential can be changed when the metal is exposed under monotonic and cyclic loading conditions. For example, fatigue induces changes of the specimen surface e.g. slip bands, intrusions, extrusions or microcracks. Consequently, negative potential peaks are produced due to the more negative equilibrium potential of the alloys in the non-oxidized state as compared to the oxidized form [142].

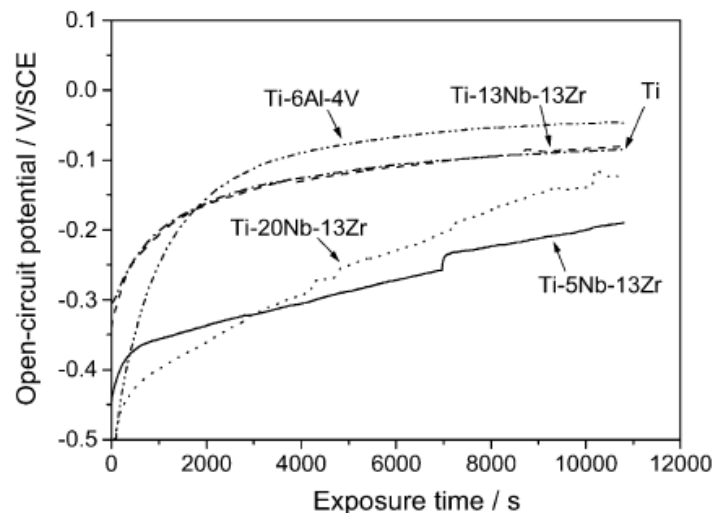


Figure 2.11: Variation of OCP with exposure time for CP-Ti, Ti-6Al-4V, and Ti-xNb-13Zr alloys in Ringer's solution at 37°C [143]

#### 2.2.4 Surface modification of biomaterials: Coatings

Long-term performance of surgical implants is often restricted by their surface properties. Biomaterials such as 316L stainless steel or titanium and its alloys have poor tribological properties such as low wear resistance which lead to a reduced service life of the implant. In order to achieve high osseointegration, the surface chemistry, surface topography, surface roughness and mainly the surface energy of the implants must be improved [4, 144].

Modification of the implant surface can be classified in physicochemical, morphological or biochemical [106]. The physicochemical methods are those that alter the surface energy, surface charge and surface composition with the aim of improving the bone-implant interface. Examples are: glow discharge to increase surface free energy in order to improve tissue adhesion [145], electrostatic interactions charge the surface to being conducive to tissue integration [146] and coatings with e.g. calcium phosphate due to their chemical similarities to bone mineral [147].

Morphological methods are referred to the alterations in surface morphology, topography and roughness in order to influence cell and tissue responses to implants [106]. Examples of these methods include sand blasting, etching, ion sputtering of solids, and inclusively porous coatings with suitable surface roughness and controlled surface topography (Figure 2.12).

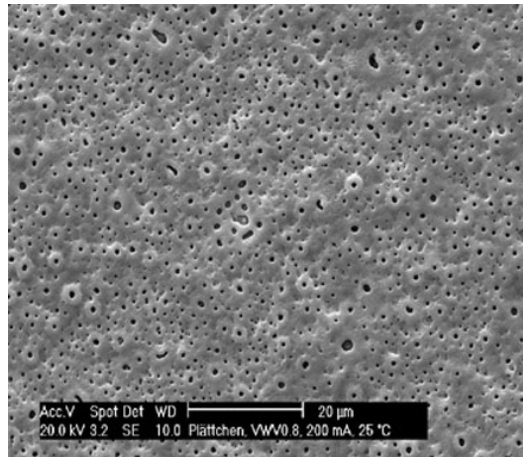


Figure 2.12: Titanium implant with porous coating based on calcium phosphate[148]

Finally, biochemical methods of surface modification offer an alternative or adjunct to physicochemical and morphological methods. Biochemical surface modification endeavors to utilize current understanding of the biology and biochemistry of cellular function and differentiation. The goal of biochemical surface modification is to immobilize proteins, enzymes, or peptides on biomaterials for the purpose of inducing specific cell and tissue responses or, in other words, to control the tissue-implant interface with molecules delivered directly to the interface. This method has some similarities with some physicochemical methods. Nevertheless, in contrast to e.g. calcium phosphate coatings, biochemical surface modification utilizes critical organic components of bone to affect tissue response [106].

Among the different surface treatments there is a tendency to prefer the morphological modifications as well as the physicochemical methods with coatings based on bioactive materials. Surface machining, grit and sand blasting as well as polishing and etching methods have shown to enhance cell growth, improving the interlocking of the bone tissue with the surface area of the implant [111, 149]. These surface treatments induce the formation of the passive oxides e.g.  $\text{TiO}_2$  in titanium alloys,  $\text{Cr}_2\text{O}_3$  in 316L stainless steel and hence they induce osseointegration on the implants [150, 151]. Additionally, it is possible to increase the range of biocompatibility by depositing thicker passive layers or by covering it with bioactive coating. Common coatings are: porous calcium phosphate, nano-ceramic particles, HA (Hydroxyapatite), oxide coatings, etc. [4, 111]. These coatings can be produced by anodizing [152], salt baths [153] as well as by physical deposition methods like ion implantation [154] and plasma spray coating [155]. In addition thermo-chemical surface treatments such as nitriding, carburization and boriding have been used to improve the surface hardness of the implants [4]. Figure 2.13 shows the early cell proliferation after different times of cell cultivation in titanium implants with different surface treatments.

## Theoretical background

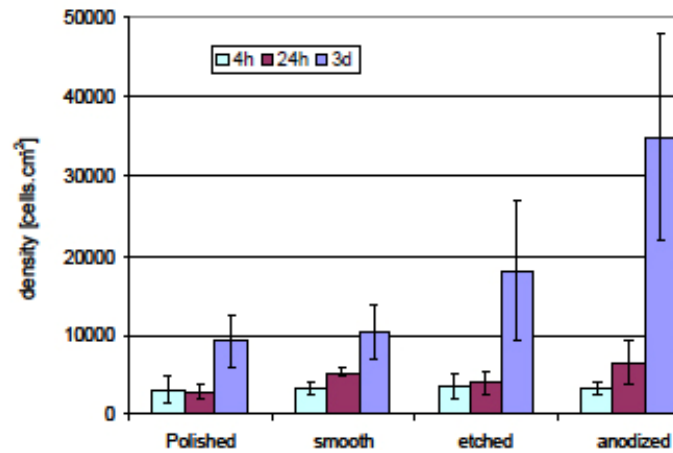


Figure 2.13: Cell density on polished, smooth, etched and anodized surfaces of titanium implants, after 4 hours, 24 hours, 3 days [152]

Investigations of coatings have been concentrated in the deposition processes, biocompatibility and biological reactions on the surface of the coatings. However, the mechanical behaviour of the coating on the implants must always be under consideration. The ideal coating for orthopaedic implants would be one with optimal porosity, strong cohesive strength, good adhesion to the substrate and a high degree of crystallinity [156]. For example, it is well known that the Young's modulus of plasma sprayed coatings e.g. HA is usually much lower than its corresponding bulk value. This can be attributed to the presence of pores and microcracks inside the coating. Young's modulus of coatings is essential in predicting the residual stress levels present inside the coatings and in determining their fatigue behaviour under cyclic loading [157].

Various in-vivo studies have found that failure mainly occurs at the metal/coating interface [158-160]. The longer the period of implantation, the higher is the probability of failure at this interface (since the strength of the bone/coating interface tends to increase with time during the early stages of the post-operative recovery). Therefore, any anticipated long-term benefit is expected to depend on the adhesive and cohesive integrity of the coating, which are strongly dependent on microstructure of the coatings [157].

Another factor that might affect the mechanical behaviour of the coating is the manufacturing process used. For instance, coatings deposited by ion implantation and plasma spray may cause interfacial separation under repeated loading conditions. Surface treatment techniques that operate at high temperatures e.g. nitriding, carburization and boriding usually cause a torsion or twist of the substrate [4].

The adhesion of coatings on metal substrates is frequently determined by the tensile adhesion test (TAT). The TAT is implemented by manufacturing a specimen which consists

of a coating deposited onto a cylindrical bar. A complementary uncoated plug is then affixed (with e.g. epoxy glue) to the coated sample so that a tensile force may be directly applied to the coating [161]. This test has been regarded as semi-quantitative at best and useful only for ranking purposes. The main problem associated with this test is that failure depends on the distribution of the flaws present at the specimen edge, which results in a wide scatter for the strength values obtained. In addition, there is a danger of significant penetration of adhesive (usually epoxy) into the coatings or even down to the interface if they are thin [157]. Therefore, it is recommended to use micro-analyses that combine a fine observation with SEM, XRD, etc, with the study of the coating behaviour under monotonic and cyclic loading conditions.

### **2.3 Titanium and its alloys as implant materials**

Amongst the materials available for implant applications, the selection of titanium-based materials is due to the combination of their outstanding characteristics such as high strength, low density, high immunity to corrosion, complete inertness to body environment, enhanced biocompatibility, low modulus and high capacity to join with bone and other tissues [4, 162]. Titanium is found to be well tolerated and nearly an inert material in the human body environment. In an optimal situation titanium is capable of osseointegration with bone [163]. Titanium and its alloys form a very stable passive layer of  $\text{TiO}_2$  on its surface and provide superior biocompatibility. Even if the passive layer is damaged, the layer is immediately rebuilt. The nature of the oxide film that protects the metal substrate from corrosion and its physicochemical properties such as crystallinity, impurity segregation, etc. are of particular importance in the selection of titanium as implant material [4].

At low temperatures, titanium has a hexagonal crystal structure which is commonly known as  $\alpha$ . Above  $883^\circ\text{C}$ , Ti has a body centered cubic structure (bcc) termed as  $\beta$ . The  $\alpha$  to  $\beta$  transformation temperature (known as  $\beta$  transus) of pure titanium is changed based on the nature of the alloying elements [4]. Alloying elements such as Al, O, N, etc. tend to stabilize the  $\alpha$  phase (called alpha stabilizers) and the addition of these elements increases the beta transus temperature. Aluminium is the most important  $\alpha$  stabilizer and is therefore present in many titanium alloys. On the other hand, elements that stabilize  $\beta$  phase are known as beta stabilizers (V, Mo, Nb, Fe, Cr, etc.) and the addition of these elements decreases the  $\beta$  transus temperature [4, 9]. Figure 2.14 shows the effect of the Al, V and Nb on the stabilization of the  $\alpha$  and  $\beta$  phases.

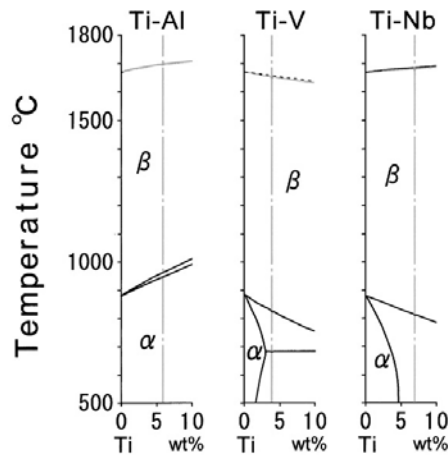


Figure 2.14: Section of phase diagrams of binary titanium systems: Ti-Al, Ti-V and Ti-Nb [164]

The  $\alpha$  and  $\beta$  phases form the basis for normally accepted classification of titanium alloys. Alloys having only  $\alpha$  stabilizer and consisting entirely of  $\alpha$  phase are known as  $\alpha$  alloys. Alloys containing 1-2% of  $\beta$  stabilizers and about 5-10% of  $\beta$  phase are termed as near  $\alpha$  alloys. Alloys containing higher amounts of  $\beta$  stabilizers which results in 10-30% of  $\beta$  phase in the microstructure are known as  $\alpha+\beta$  alloys. Alloys with still higher  $\beta$  stabilizers where  $\beta$  phase can be retained by fast cooling are known as metastable  $\beta$  alloys. These alloys decompose to  $\alpha+\beta$  on aging. Most of the biomedical titanium alloys belong to  $\alpha+\beta$  or metastable  $\beta$  class [4].

$\beta$  transus temperature plays a central role in evolution of microstructure and is of great technological importance in determining heat treatment and processing schedule. The alloys processed or heat treated above the  $\beta$  transus temperature result in acicular or lamellar structure and are typically known as  $\beta$  treated structure. When these alloys are mechanically processed below the  $\beta$  transus and heat treated in  $\alpha+\beta$  phase region, the microstructure consists of a mixture of equiaxed  $\alpha$  and  $\beta$  phases. Depending upon the alloy chemistry, heat treatment temperatures and cooling rate, volume fraction of equiaxed  $\alpha$  and nature of  $\beta$  phases may change. In faster cooled structures, transformed  $\beta$  phase may constitute martensite or  $\alpha$  laths along with the retained  $\beta$ , while on slow cooling the transformed  $\beta$  phase may entirely be retained  $\beta$ . [4, 9, 165]. Figure 2.15 shows various types of microstructures of Ti alloys depending of the process route and heat treatment applied to them.

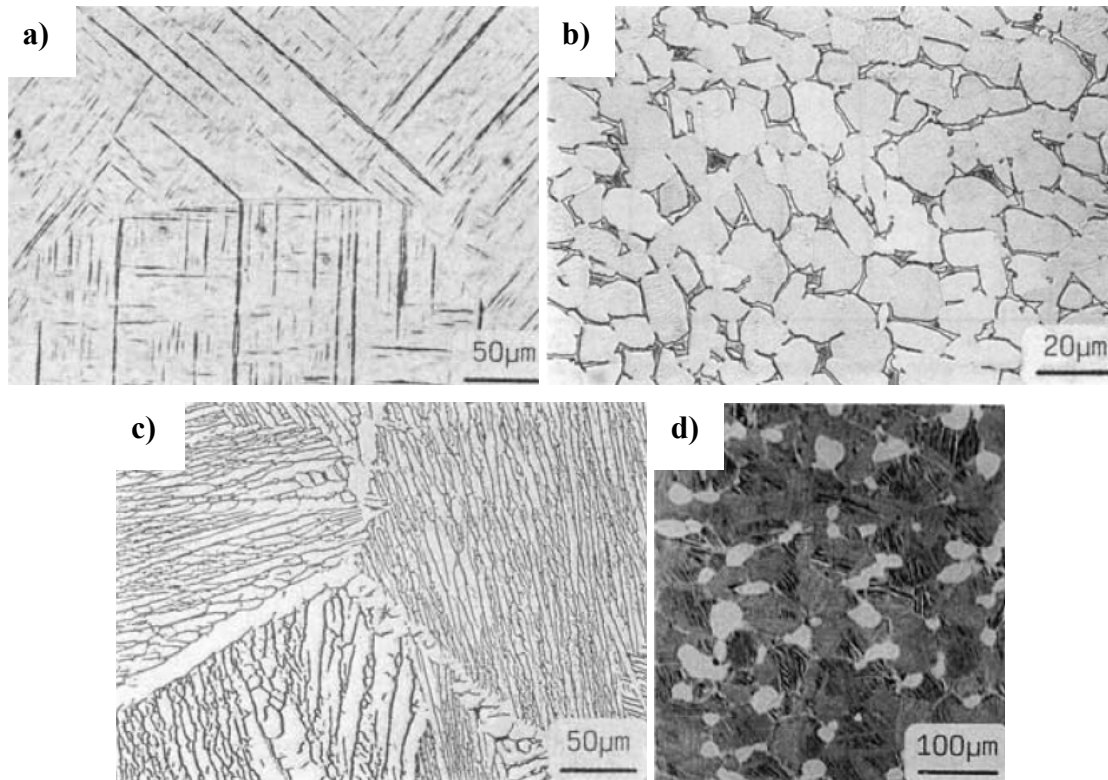


Figure 2.15: a) Acicular martensite in Ti-6Al-4V quenched from  $\beta$  phase field, b) fully equiaxed microstructure of a Ti-6242, c) lamellar  $\alpha + \beta$  microstructure in Ti-6Al-4V slowly cooled from the  $\beta$  phase field, d) Bi-modal microstructure of a IMI 834 [9]

The Ti-6Al-4V (Ti64) alloy is the most commonly used  $\alpha + \beta$  titanium biomedical alloy. Ti64 offers an excellent corrosion resistance and biocompatibility, however long-term performance of this alloy has raised some concerns due to release of aluminium and vanadium. Both Al and V ions released from the Ti64 alloy are found to be associated with long-term health problems, such as Alzheimer disease, neuropathy and osteomalacia [166]. In addition, vanadium present at the surface of the implant may be transported with the blood and accumulated in kidneys and liver [12, 167]. That is undesirable because vanadium is toxic both in the elemental state and as oxide  $V_2O_5$  [168, 169]. An interesting alternative to solve this problem is the replacement of vanadium with niobium in an  $\alpha + \beta$  titanium alloy type. Ti-6Al-7Nb (Ti67) alloy has similar properties compared to Ti64. However, contrary to vanadium the element niobium is considered as a vital class element [10]. Nb has a stabilizing effect on the oxide film of Ti based alloys [170]. The addition of Nb enhances passivation and also resistance to dissolution by decreasing the concentration of anion vacancies. The enhanced corrosion resistance is due to the formation of Nb rich oxide which is highly stable in the body environment [4].

Ti alloys have lower Young's modulus varying from 55 to 116 GPa compared to other implant materials e.g. 316L stainless steel (193 GPa) and Co-Cr alloys (240 GPa).

## Theoretical background

Nevertheless, it is still greater than that of bone. Figure 2.16 shows the Young's modulus of the most used bio-titanium alloys. It has been searched for different methods to further reduce the Young's modulus of titanium and its alloys without compromising the strength of the implant. One possibility is to change the designs of the implant e.g. making porous structures [171]. Another possibility is to change the alloy composition in order to retain a single phase  $\beta$  microstructure on rapidly cooling from high temperatures. Previous authors have shown that Nb, Zr, Mo, and Ta are the most suitable alloying elements that can be added to decrease the modulus of elasticity of bcc Ti without compromising the strength [172]. It has been observed that addition of these alloying elements up to certain weight percentage decreases the modulus, beyond which increase in modulus is noted which is due to  $\omega$  phase formation and precipitation of  $\alpha$  on aging [4, 173].

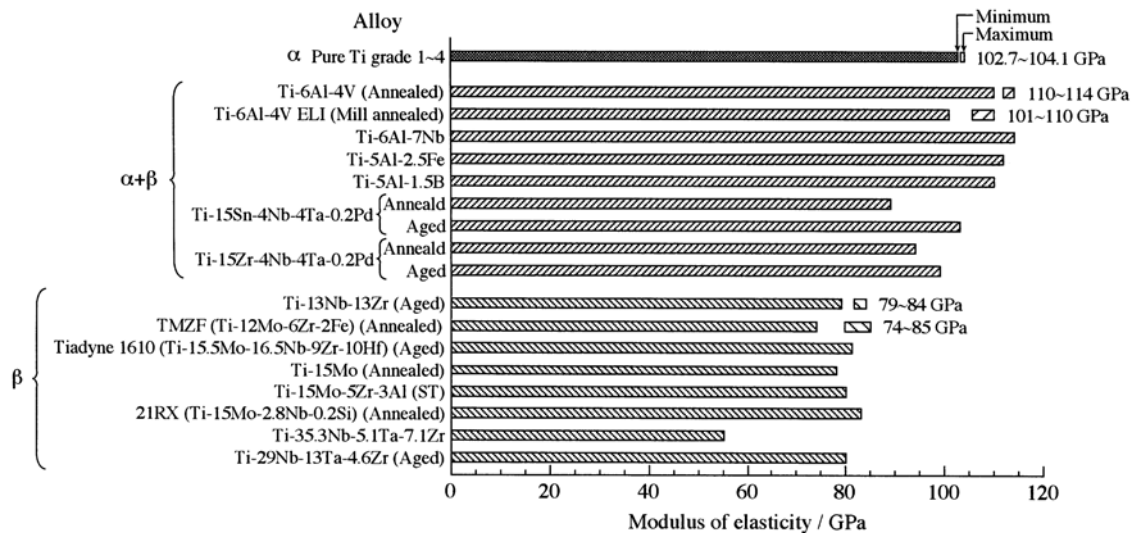


Figure 2.16: Elastic modulus of various Ti- alloys used as biomaterials [174]

### 2.3.1 Manufacturing of Ti implants - Casting process

The selection of a manufacturing process for Ti implants depends upon different aspects e.g. complexity of the implant, cost, final mechanical properties, etc. For example, during the manufacturing of a part by forging, the microstructure and the mechanical properties can be modified over a wide range by thermomechanical treatments which can be easily incorporated into the processing scheme of the part [175]. In the past, forging as well as machining were intensely used to manufacture implants. Nowadays, the necessity to use implants with very complicated shapes in restorative dentistry and orthopaedics has been observed. In the fabrication of devices with complex shapes that requires great accuracy, the methods such as precision casting [164, 176], electron and laser beam melting [16, 177], powder metallurgy [13], etc. are used.

Precision casting has attracted an increasing interest due to the relative reduction of the overall cost and material. In addition, the mechanical properties of the cast Ti-alloy implants can be controlled by controlling their microstructures [175].

In precision casting of titanium many variables must be taken into account. Titanium alloys have high melting points and excessive reactivity of the melt with crucibles and moulds, therefore melting and pouring of titanium alloys have to be performed under vacuum or inert atmosphere [178]. A standard method to produce precision-cast parts is by vacuum-arc melting and centrifugal casting in a lost-wax mould made from materials that will not react with the molten titanium alloy [179].

Figure 2.17 shows a schematic representation of a centrifugal casting machine used to produce precision-cast Ti products. This machine uses an electrode to melt the ingot into the mould. A special attention should be placed in how the metal flows into a mould and the completeness of casting in order to guarantee the success of the cast piece. The centrifugal force must be high enough to fill the complete product.

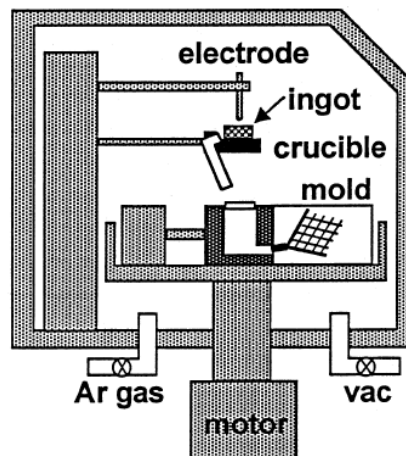


Figure 2.17: Schematic representation of the centrifugal titanium casting machine [180]

The production technique of investment moulds for titanium casting is similar to the production of investment moulds for ferrous and superalloys castings [181] except for some very important differences. The major difference is in the investment slurry formulation. Due to the reactivity of the molten titanium, a special attention to the chemical composition of ceramic moulds must be paid. For these reasons, the conventional ceramic moulds of zirconium silicate or alumina/silica are not suitable. Moulds made of such materials result in titanium castings having unacceptable surface finish, high microporosity, and nonuniform microstructure. That can cause a deterioration of the mechanical properties of the cast parts [178, 179]. To avoid these problems, it is necessary to employ a combination of melting,

moulding with investment moulds of special high-stable refractories and suitable heat-treating practices [178, 182, 183].

### 2.3.2 Defects in cast Ti-alloy implants

#### *Non-uniform microstructure*

The typical microstructure of cast Ti-alloys is fully lamellar with coarse  $\beta$  grain size. In the microstructure of conventional cast Ti-alloys such as Ti-6Al-4V or Ti-6242, parallel  $\alpha$  and  $\beta$  lamellae are aligned within one colony which indicates that parallel plates belong to the same Burgers relationship [184]. That permits an easy slip transfer across  $\alpha$ - $\beta$  phase boundaries and consequently the colony size determines the effective slip length. The size and the density of  $\alpha$  and  $\beta$  lamellae in these colonies as well as the slip length affect the mechanical properties of the cast part [9, 175].

Previous authors have identified that the cross sectional structure of a cast-Ti can consist of three zones. An outer and undesired reaction layer called  *$\alpha$ -case*. This layer is followed by a coarse *acicular* structure that is made of plate-like  $\alpha$ -Ti crystals. The core of the samples usually is a fine  $\beta$ -Ti plate structure called *bulk microstructure* [185]. The structure and thickness of these layers can vary with the influence of the investment material, cooling rate, mould temperature, casting volume and the thickness of the cast part [17, 175, 185]. For example, the higher the mould temperature and the larger the cast volume, the thicker is each layer and the coarser are the acicular grains [17]. As consequence, the mechanical properties of the cast part will be affected. It has been reported that in complex cast parts with lamellar structure the yield stress in thicker sections is lower than in thinner sections [175]. That can be explained due to the increase of the colony size and thickness of the  $\alpha$ -laths of thicker sections. Previous theoretical work based on fuzzy logic neural networks has been conducted to show the mechanical properties and functional dependency on the Ti microstructure [186]. Figure 2.18 shows that the increment of the lath thickness and the colony size induce to decrease the yield strength in a Ti-64 alloy.

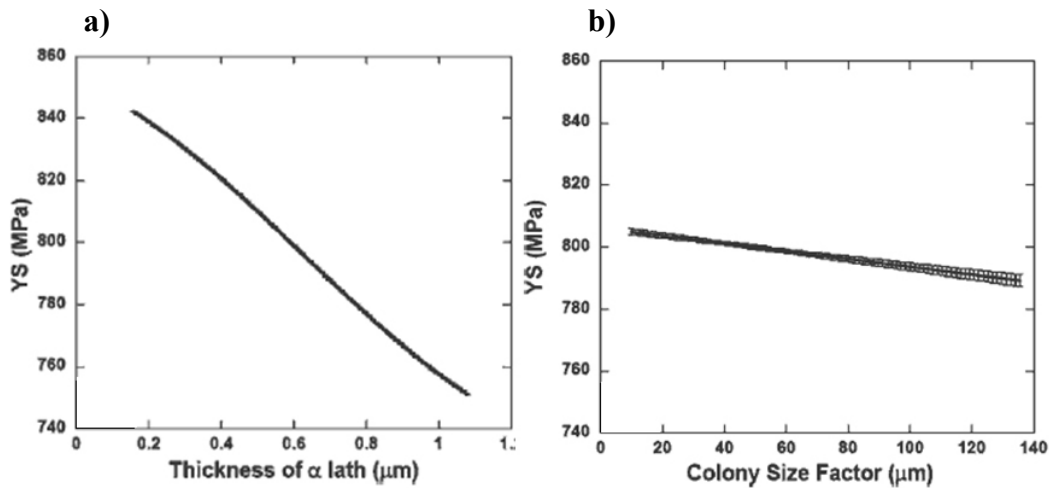


Figure 2.18: Variation of the yield strength of a Ti67 alloy with: a) the thickness of the lath and with the b) colony scale factor [186]

The lamellar structure of cast Ti-alloys can be modified with heat treatments e.g. quenching, hot isostatic pressing (HIP), etc. The design of these heat treatments is based on the fact that the slip length has a strong influence on the mechanical properties [175]. Heat treatments in the  $\alpha + \beta$  phase field induce a decrease of the  $\alpha$ -phase, which indicate that the width of the  $\beta$  lamellae increases at the expenses of the  $\alpha$  lamellae. An appropriate cooling rate permits that the widened  $\beta$  lamellae are hardened by the precipitation of very fine  $\alpha$  lamellae in different orientations. Microstructures containing modified  $\beta$  lamellae are called bi-lamellar structures [9, 175].

Cast prostheses with complex shapes usually are heat treated with HIP and aging treatment in order to eliminate subsurface casting flaws [187]. This heat treatment comprises of  $\beta$  solutionizing step. This step is included to eliminate any effect on the microstructure and properties arising from differential cooling rates upon HIPing. Then different cooling rates can be used to homogenise and to produce a microstructure with small  $\alpha - \beta$  platelet colonies and a tortuous morphology. Figure 2.19 shows the effect of the cooling rate on lamellar microstructure of a Ti-6242. Hot isostatic pressing is done to close internal shrinkage. This treatment produces a satisfactory ductility and improves the fatigue resistance two times higher than the cast part without HIP. Hot isostatic pressing had permitted the growth of Ti-cast parts in fatigue limited applications [9, 187]. For more complicated geometries with thin sections the HIP process must be avoided in order to reduce the risk of cracks and failure of the implant.

## Theoretical background

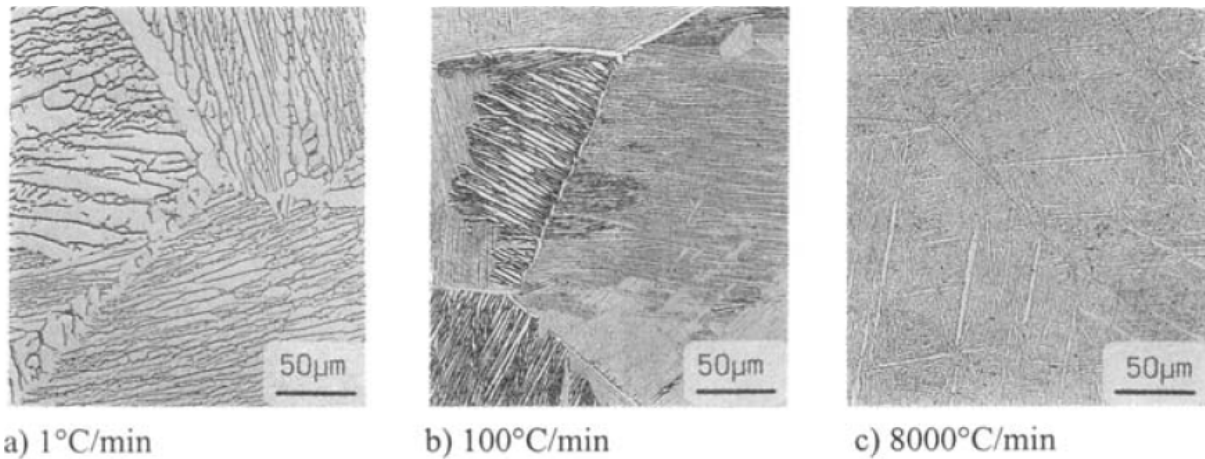


Figure 2.19: Effect of cooling rate from the  $\beta$  phase field on lamellar microstructures of a Ti-6242 [9]

### *$\alpha$ -Case*

Titanium is an inherently difficult metal to cast because of its high melting point (1670°C), and its strong affinity to carbon and gases such as oxygen, hydrogen and nitrogen. Molten titanium is extremely reactive with investment materials based on SiO<sub>2</sub>-phosphate, Al<sub>2</sub>O<sub>3</sub>, ZrO<sub>2</sub>, ZrSiO<sub>2</sub> and CaO [18, 188, 189]. The reaction between Ti and the elements of the mould results in the formation of hard and brittle layers, termed as  $\alpha$ -case (Figure 2.20).

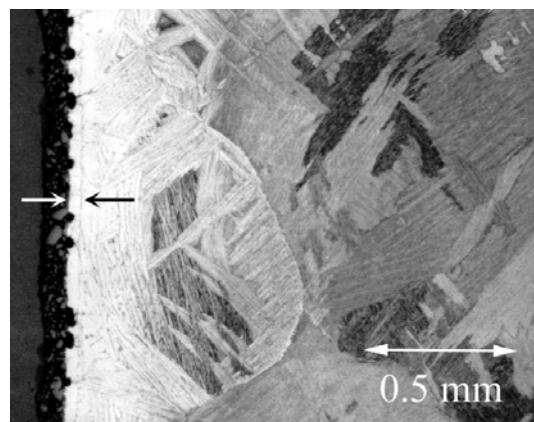


Figure 2.20: Micrograph of a cast Ti sample: arrows show the  $\alpha$ -case thickness [190]

$\alpha$ -Case can be formed by the local increase in oxygen content in the metal near the surface. This increment in oxygen promotes the formation of an oxygen-rich Ti hexagonal solid solution at temperatures where the bulk alloy would be single-phase  $\beta$  and also alters the  $\alpha/\beta$  structure near the surface during cooling to room temperature [190]. Some authors have described the  $\alpha$ -case in parts made with moulds based on Al<sub>2</sub>O<sub>3</sub> as a combination of TiO<sub>2</sub> and intermetallic Ti<sub>3</sub>Al phases [189]. Because of its high content of oxygen, the alpha case is mechanically hard and brittle, and this can cause a serious reduction in performance of the metal, especially in fatigue [191]. For example, tensile testing of Ti castings revealed that

microcracks formed readily in the  $\alpha$ -case and the growth of these microcracks caused ultimate fracture and determined the tensile ductility of Ti castings [192]. In general, a large  $\alpha$ -case can lower the fatigue strength and tensile ductility because of larger microcracks in the  $\alpha$ -case [193].

Many studies of the  $\alpha$ -case involved characterization of the microhardness in this layer as a function of distance from the surface in order to establish the depth of the  $\alpha$ -case [194-196]. Previous work has reported alpha-case thickness in the range of 50-500  $\mu\text{m}$  [190]. It has been shown that using wedge-shaped casting specimens the  $\alpha$ -case thickness increases with increasing wedge thickness for CP-Ti, Ti-6Al-4V and Ti-6Al-7Nb [195, 196]. In dental and prostheses with thin sections the  $\alpha$ -case can be a significant fraction of the thickness or cross-sectional area of the product.

In order to avoid or eliminate the undesired  $\alpha$ -case, various methods can be used. To avoid  $\alpha$ -case formation, expensive mould coatings such as  $\text{ZrO}_2$ , and  $\text{Y}_2\text{O}_3$  have been adopted since their oxides formation occurs at standard energy changes with more negative values than  $\text{TiO}_2$  [197]. Consequently, minimal reaction between the mould wall and liquid Ti into the mould is expected [196]. Disadvantage of this method is the high cost of these coatings and therefore it becomes unattractive when a low-cost casting process is desired.

The  $\alpha$ -case can be removed using mechanical methods such as grinding, sand-blasting, etc. or by chemical methods like acid pickling [198, 199]. The method selected to eliminate the  $\alpha$ -case must take into account the shape and dimensions of the cast part as well as the depth of the  $\alpha$ -case layer. For example, chemical milling is utilized to eliminate the  $\alpha$ -case of cast specimens with very complex geometries [198]. On the other hand, if the Ti-cast part is too large and extended surface areas are present, it is better to remove the  $\alpha$ -case by mechanical methods.

### ***Porosities and Voids***

Metal contamination or inappropriate sprue designs may lead to formation of shrink, gas bubbles, or weld lack-of-fusion cavities. These defects react with the molten titanium and produce porosities in the cast parts [200, 201]. Three principal phenomena can cause high internal porosity in titanium casting: (1) When the suctioning pressure is too high because of a large pressure difference between the casting chamber and the mould chamber, gas is introduced into the flowing melt; (2) if the speed of the flowing molten metal stream is too high then it results in gas incorporation in the cast part; and (3) when the wettability of the surface of the mould is too high for the molten titanium, the metal flow becomes intermittent;

## Theoretical background

the metal poured first travels too quickly to the end of the mould, immediately solidifying, and the metal following the first pour cannot catch-up [185, 188]. It has been found that laminar rather than turbulent flow can be beneficial for the casting of mesh patterns using a pressure casting machine [202]. Shrink voids result from the reduction in volume as the molten metal solidifies and contracts. Gas pores can develop if gases (such as hydrogen) liberated by the solidifying metal, or from the mould wall, do not escape prior to passage of the solidification front. Consequently, the entrapped gas forms bubbles in the casting [200].

Weld lack-of-fusion (LOF) cavities may develop during weld repair of the casting and so are not truly casting defects. They are generated during post-casting foundry processing and do contribute to the defect population. They are typically due to poor surface preparation or inadequate heat delivered in the weld pool [200].

The presence of undesirable porosity deteriorates the mechanical properties of titanium casting. Previous authors have observed that the tensile strength and elongation of the cast CP-Ti samples decrease as the internal porosities increase [185]. Most of these samples fractured at large centrally located pores.

Low internal porosity can be obtained by producing a smooth metal flow with little Ar gas following the metal into the mould cavity. This technique avoids the inadequate mould filling that affects the porosity of the cast part and produces better escape possibilities for the gases trapped in the mould [203]. Shrink void defects can be minimized by sound gating practices to insure a source of molten filler metal to move the shrink out of the part envelope [200].

### ***Inclusions***

Inclusions are exogenous solids defects in titanium casting and occur as two main types: low-density inclusion (LDI), e.g. hard- $\alpha$ , and high-density inclusions which appear as ceramic shell and tungsten (Figure 2.21). The inclusions are typified by a core of Ti-O or Ti-N phases (often, with  $Ti_3Al$ ) surrounded by porous, embrittled  $\alpha$ -Ti phase. [200, 204].

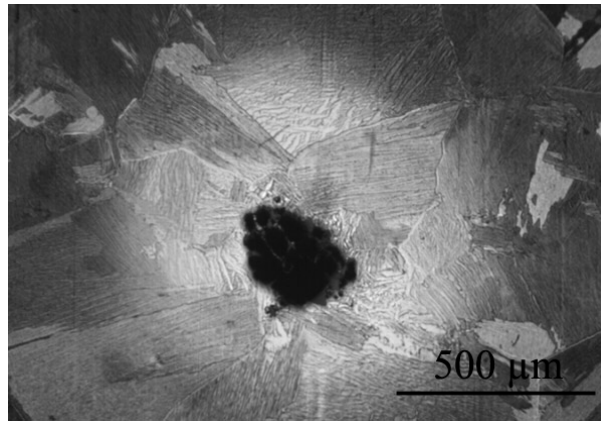


Figure 2.21: Ceramic shell inclusions in titanium investment casting [200]

The so-called low-density inclusions (LDI), e.g. hard- $\alpha$  inclusions, create big problems. They originate in a number of different ways, but the principal source of the most troublesome variety, with high nitrogen contents, is in the original manufacture of titanium sponge. The formation mechanism of these inclusions is identical to the mechanism followed by the formation of the  $\alpha$ -case. The form of the inclusions is one in which there is extensive local stabilisation of the  $\alpha$ -phase generally by nitrogen although some combination of nitrogen, oxygen and carbon may also be present in certain cases. The stabilized phase is very brittle and after mechanical working normally contains cracks and also may retain some porosity from the original sponge structure [204].

The HDI inclusions can arise from: (1) contamination of the scrap fraction of the raw materials used in machine-tool tips made from cobalt-bonded tungsten carbide; (2) accidental inclusion of heavy metal scrap such as incandescent light filaments, ball-point pens and thermocouple scrap; (3) heavy metal component of incorrectly-prepared master alloy; (4) use of incorrectly formulated alloy mixes including the addition of heavy metal pieces which are too large to dissolve and homogenize in the vacuum-arc-remelting processing [204].

The applications of Ti-alloys as implant material have shown outstanding increase in the last decade. Modern and high-quality casting techniques have improved the properties of the Ti-implant. However, to improve the mechanical interaction between implant and bone, implants with better designs and structures must be developed. Recently, there has been increasing interest in the use of metal foams in orthopaedic implants [6, 205]. These materials have low Young's modulus, structures that allow tissue ingrowth, high specific surface area that promote the delivery of biological factors such as cells, genes, proteins and growth factors.

## 2.4 Engineering cellular solids in medical applications

Cellular structures extend a range of properties available to the engineer. These properties depend on the material from which they are made e.g. ceramics, polymers or metals. Cellular solids have physical, mechanical and thermal properties which are measured by the same methods as those used for fully dense solids. The low densities permit the design of light and stiff components such as sandwich panels and large portable structures. The low stiffness makes foams ideal for a wide range of cushioning applications; for example elastomeric foams are the standard materials for seating. The low strengths and large compressive strains of foams make them attractive for energy-absorbing applications [206]. The combination of these properties has favoured cellular materials for orthopaedic research and testing purposes [3, 207]. Figure 2.22 shows the mechanical properties of engineering materials, including cellular materials, commonly used in medical applications.

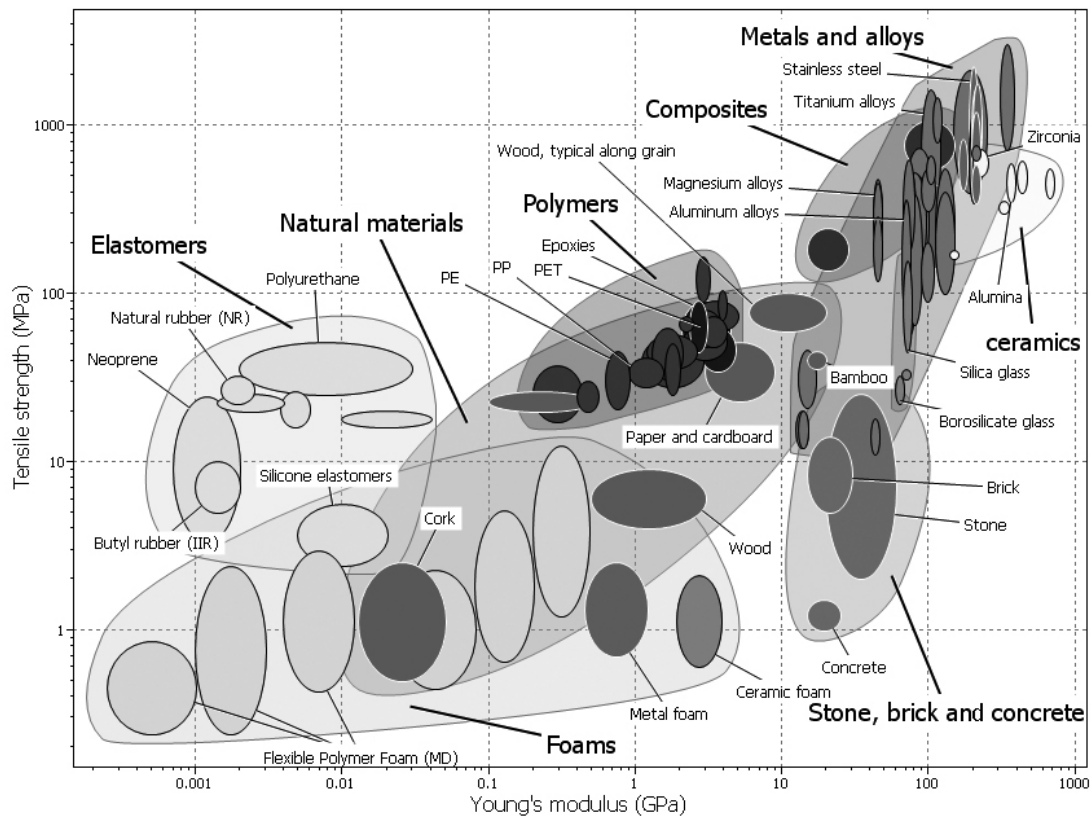


Figure 2.22: Young modulus vs. tensile strength of engineering materials [3]

The properties of the cellular solids depend on the bulk properties and the relative density, the distribution of the material and the architecture of the cellular solid [208, 209]. The most important property of a cellular solid is its relative density  $\rho^* / \rho_s$ , which is the relationship between the density of the cellular material  $\rho^*$  divided by that of the solid from

which the cell walls are made,  $\rho_s$  [209]. Special ultra-low-density foams can be made with a relative density as low as 0.001. Polymeric foams used for cushioning, packaging and insulation have relative densities which are usually between 0.05 and 0.2; cork is about 0.14; and most softwoods are between 0.15 and 0.40. It is generally accepted that the true cellular solids have relative densities less than 0.3. As the relative density increases, the cell walls or struts thicken and the pore spaces shrink; above about 0.3 there is a transition from a cellular structure to one which is better thought of as a solid containing isolated pores [3, 206, 208, 209].

Cellular materials can be divided into closed-cell foams and open-cell sponges (Figure 2.23). When the pores in the foam are sealed between them, it is called closed-cell, and in contrary, when the pores form an interconnecting network, the material is called open-cell foam. In order to make a comparison between cancellous bone and engineering cellular materials, it can be said that closed-cell foam follow similar shapes as plate like cancellous bone (Figure 2.2). Perhaps with the only difference that in cancellous bone the pores are always interconnected between each other, that doesn't occurs in all closed-cell foams [34]. On the other hand, open-cell foams show extreme similarities with the architecture of the rod-like cancellous bone [3, 34, 207].

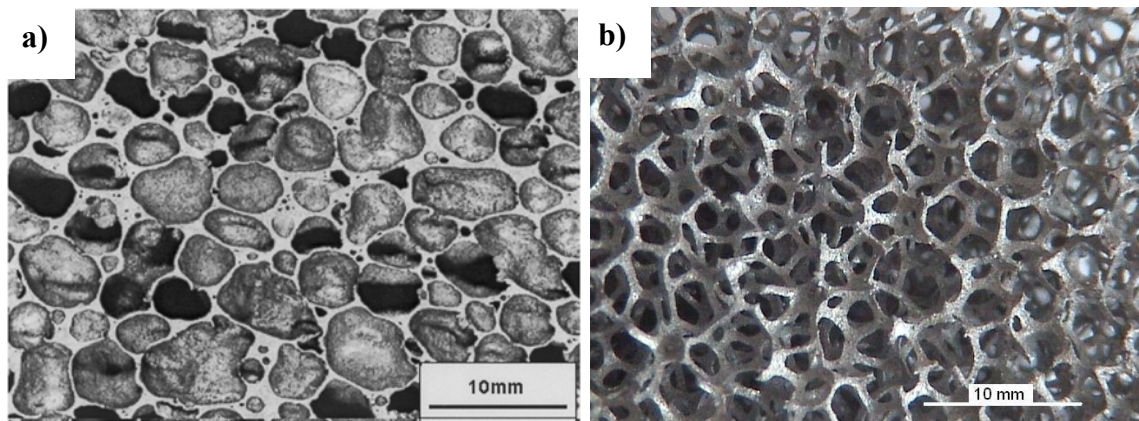


Figure 2.23: a) closed-cell foam [210], b) open-cell foam

In this work particular attention is placed to the open-cell foams as orthopaedic implants and as analogue cancellous bone material for in-vitro studies. The aims of using open-cell foams as implant material are two: favouring bone ingrowth into the cell pores and offer Young's moduli closer to that of the bone they replace. Previous studies have found that bone ingrowth is optimized in cellular materials with pore size in the range of 50-400  $\mu\text{m}$  [6]. Implants with Young's modulus closer to bones avoid stress shielding: a reduction in stress in the remaining bone, which can lead to bone resorption and loosening of the implant. This is especially critical in load-bearing such as implant for joint replacement [49].

## Theoretical background

The open-cell foam structure consists of little columns or beams forming a network that can be approximated by a bcc lattice of space-filling tetrakaidecahedral cell structure. The cells are randomly orientated and they show better homogeneity in size and shape than in the closed-cell foams [208, 211].

On broad lines the open-cell foams can be considered almost isotropic, meaning that their structure and their properties have no directionality. On the other hand, natural cellular solids e.g. wood, cork, bone, etc. are rarely so [208]. In section 2.1.2 it was observed that the structural anisotropy of bones depends on the ratio and direction of the main stresses, meaning that the bone shows higher strength in the main trabecular direction (MTD) than e.g. perpendicular to that direction. Open-cell foams do not present this characteristic, permitting the use of foams as implant in different directions inside the bone without altering the Young's modulus and strength of the implant. Open-cell ceramics, polymer and metallic foams can be found in medical applications.

### *Ceramics foams in medicine*

Ceramic materials used in medicine are calcium phosphate, aluminium oxide, zirconium oxide as well as bioactive glasses and glass ceramics. These materials have been used for long time in medicine as full materials but in the last years the implementation of calcium phosphates,  $\text{Al}_2\text{O}_3$  and  $\text{ZrO}_2$  as foam structures has been increased specially in dental implants and vertebral bone replacement [21].

Porous  $\text{Al}_2\text{O}_3$  scaffold coated with tricalcium phosphate (TCP) have been already used to improve the osteosynthesis, biocompatibility and the interaction of the implant surface with the bone material. Clinical research has shown excellent growth and propagation of bone cell in the interconnecting porous surface of these implants [212].

$\text{ZrO}_2$  and its composites exhibit higher mechanical properties compared to  $\text{Al}_2\text{O}_3$ . Researchers have successfully fabricated porous  $\text{ZrO}_2$  parts for biomedical applications [5, 213]. However,  $\text{ZrO}_2$  has the limitation that it could not bond directly to bone nor conduct bone ingrowth into the pore channels. Therefore, these implants need to be coated or incorporated as second phases with biocompatible materials. The HA (hydroxyapatite) coatings on bioinert materials were reported to have advantages in surgical applications due to the rapid fixation and bonding to bones as well as uniform ingrowth at the interface [158, 214]. However, incorporating the  $\text{ZrO}_2$  implant with HA coating produces reactions between the  $\text{ZrO}_2$  and the HA, they can reduce the mechanical properties and degrade the biocompatibility of the material [215].

Zirconia toughened alumina (ZTA) has been regarded as the next generation orthopedic graft material due to its excellent mechanical properties, wear resistance and biocompatibility. Porous ZTA ceramics with good interconnectivity can potentially be used as bone grafts for load-bearing applications. Due to the bio-inertness of alumina and zirconia ceramics, surface bioactivation of the ZTA foams was carried out in order to improve their bioactivity [216].

### ***Polymeric foams in medicine***

Applications of polymeric materials for clinical purposes have been strongly increased in the last years. That is basically due to their reduced prices and easy workability. From these materials it is possible to elaborate short and long-term implants e.g. artificial blood vessels, heart valves and catheters. Beyond these applications, different bone replacement materials are developed from polymers based on natural and synthetic materials [21].

A big challenge is the development of foamed materials based on natural, biodegradable and reabsorbable polymeric materials. A novel processing technology has been reported for creating a biodegradable polymer scaffold that mimics the architecture of trabecular bone and that supports bone growth throughout its volume [217].

Researchers have generated porous Poly (lactic-co-glycolic) (PLGA) foams, those include solvent casting-particulate leaching, fibre weaving, and phase separation [218]. Although, PLGA foams with porosities as high as 95% and cell sizes ranging from 20 to 500  $\mu\text{m}$  have been reported, big drawback to these techniques is that they utilize organic solvents in the fabrication process. Residues of organic solvents left in the polymer after processing may be harmful to the transplanted cells and can inactivate many biologically active factors e.g. growth factors [219].

#### **2.4.1 Open-cell metallic foams in medicine**

Recently, there has been increasing interest in the use of metal foams in orthopaedic implants [6, 205]. Initially, foams were used for coating of prosthetic devices, similar to porous sintered beads, but there is also interest in their potential for broader use e.g. replacement for vertebral bodies. Nearly all the work to date has focused in open-cell foams made from tantalum and Ta alloys, and intermetallics of titanium, as they have already been demonstrated to have excellent biocompatibility and corrosion resistance. Particularly, titanium has the advantage that its Young's modulus is approximately half that of other orthopaedics metals e.g. cobalt-chromium and stainless steel alloys [3].

## Theoretical background

Porous tantalum implants have been increasingly used in the last years. Figure 2.24 shows a tantalum foam with porosity of 75-80%. These foams are typically made with cell sizes between 400 and 600  $\mu\text{m}$ , which is suited for the bone ingrowth [6]. Tantalum foams have the disadvantage that they form a surface oxide,  $\text{Ta}_2\text{O}_5$ , which does not form bond with the bone. However, tantalum foam can be coated with an apatite layer that does bond to bone [220].

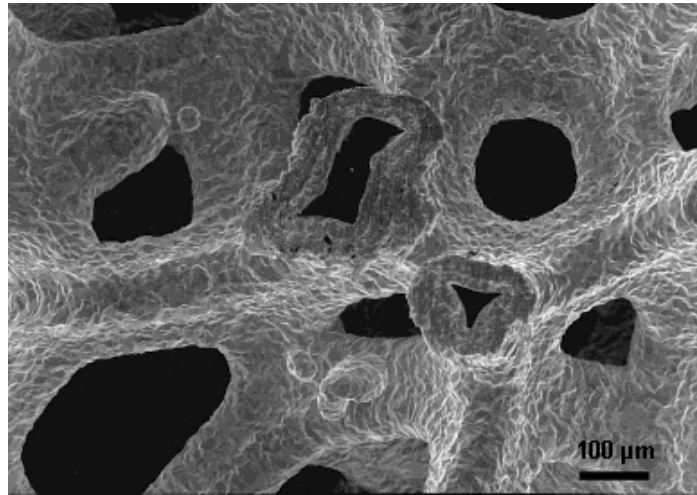


Figure 2.24: SEM micrograph of a tantalum foam [221]

Foams of titanium alloys have enormous potential for orthopaedic and load bearing implants application [8, 16, 222]. Cell size of the titanium foams used for implant varies from 100 to 800  $\mu\text{m}$  depending on the fabrication method. Relative densities have been observed to range from 0.2 to 0.65. Consequently, a big variation on the mechanical properties of the foams can be expected reflecting the variation of microstructure obtained from different manufacturing processes [3].

Implant fixation enhanced by porous structures is still under intensive study, even after more than 30 years of development [7]. The main problem to overcome is the necessity to balance different properties. It is necessary to increase the average mechanical strength to resist the applied load and reduce the Young's modulus to prevent stress shielding phenomena. The single pore dimensions should be controlled to stimulate both mineral and collagen osteointegration. Additionally, an adequate porosity to assure the proper interconnection between different pores and bone, high corrosion resistance under stress conditions and good biocompatibility are needed [8].

### 2.4.2 Manufacturing processes of open-cell metallic foams

The most common fabrication method to produce open-cell metal foams is by replication. This process involves the use of a template which possesses the desired structure to be

foamed. Different structures can be used as templates to fabricate metal foams: polymer foams that are first opened by special treatment, reticulated vitreous carbon, loose or sintered bulks of inorganic or organic granular metals, hollow spheres and regular polymer structures [223].

The template is then replaced by the desired metal. This process can be carried out by coating the template with metal vapour, electroplating, or investment casting. For example, tantalum foam can be manufactured by chemical vapour deposition (CVD) process, slurry infiltration, sintering as well as by fugitive phase method, foaming agents, expansion of argon gas, freeze casting, selective laser melting and by self-propagating high temperature synthesis [3, 221].

Open-cell titanium structures are manufactured by a number of different techniques, e.g. controlled powder sintering [13], solid-state foaming by superplastic expansion of argon-filled pores [14], as well as by selective electron beam melting and precision casting methods [15, 16].

In this work, the precision casting method has been adopted and is of particular importance. Therefore, this method is explained in details. Figure 2.25 shows a schematical description of the casting method to produce open-cell metallic foams. An open-cell polymer foam template with the desired porosity, cell size and strut thickness is first selected. This is coated with a mould casting slurry (ceramic powder) which is then dried and embedded in casting sand. The mould is then baked both to harden the casting material and to decompose (and evaporate) the polymer template, leaving behind a negative image of the foam. This mould is subsequently filled with a metal alloy and allowed to cool [224].

## Theoretical background

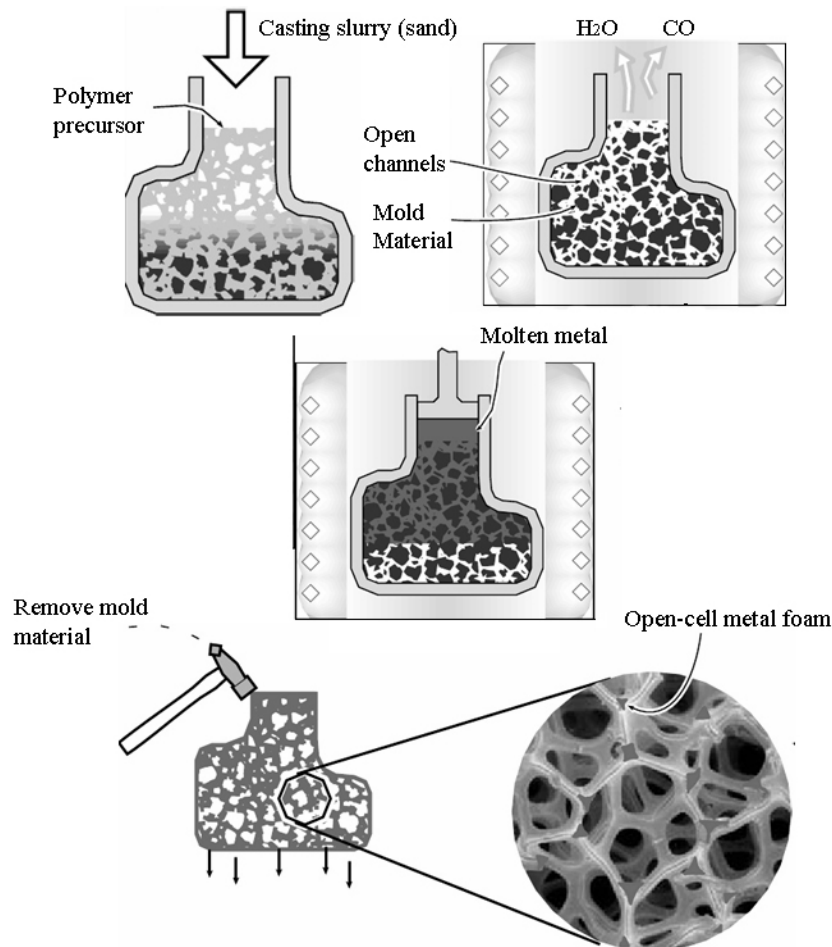


Figure 2.25: Investment casting method used to manufacture open-cell foams [224]

The use of a moderate pressure during melt infiltration can overcome the resistance to flow of some liquid alloys. That is particularly important for metals that are difficult to cast e.g. titanium alloys. After solidification and cooling, the mould materials are removed leaving behind the metal equivalent of the original polymer foam [225]. In a variant of this process, the precursor structure is assembled from injection-moulded polymeric or wax lattices. The lattice structure is coated with a casting slurry and fired, burning out and leaving a negative image mould. Metal is cast or pressure-cast into the mould using conventional investment casting techniques [224].

Precision casting process has been used in the manufacturing of: Aluminium, magnesium, nickel-chromium, stainless steel, and copper foams [224]. The advantages of the precision casting are in the great variety of structure parameters that can be produced. Furthermore, the increasing of the availability of precision-cast foams in these varieties of structures and steadily decreasing production costs open new applications for cellular materials [226].

### 2.4.3 Mechanical properties of open-cell metallic foams

The structural behaviour of a foam depends principally on its relative density  $\rho^* / \rho_s$ . The fraction of pore space in the foam is termed as *porosity* defined by  $1 - \rho^* / \rho_s$ . At first sight one might think that the cell size should be an important parameter, and sometimes it is, but most mechanical and thermal properties depend only weakly on cell size. Cell shape matters much more e.g. when the cells are equiaxed the properties are isotropic, but when the cells are slightly elongated or flattened the properties depend on direction. In addition, the three dimensional topology of the foams is an important factor that requires special attention. This structure in which the cell struts have random orientations in space is complex to analyse and usually this structure is simplified using a two-dimensional model to describe the properties of the foams [209]. All these properties are crucial to understand the mechanical properties. Among the principal mechanical properties of the foams compression and compressive fatigue behaviour are of particular interest in the analysis of the open-cell foams as implant materials.

#### *Compression behaviour*

Figure 2.26 shows a schematic stress-strain behaviour of open-cell and closed-cell metallic foams during compression. The foams under compressive loads are characterized by three regimes. The first region is a linear elastic regime (Figure 2.26, point (1)), corresponding to cell edge bending or face stretching. The Young's modulus of the foam is usually measured in this regime since the initial loading appears to be elastic. Nevertheless, the initial loading curve is not straight, and its slope is less than the true modulus, because some cells yield at very low loads. The real Young's modulus  $E$ , is best measured dynamically or by loading the foam into the plastic range, then unloading and determining  $E$  from the unloading slope [208, 224]. For this reason, a compression test standard has been developed for metallic foams that permits more accurate measurements of  $E$  [227].

After the first stress maxima, crushing of cell struts within a localized deformation band leads to a pronounced decrease in the stress level. During further compression the stress increases again, until reaching a state, where massive plastic buckling of the cell struts keeps the stress at a constant value. Once a critical deformation is exceeded, collapse of the respective band leads once more to a stress decrease. This process of deformation-band formation and collapse is repeated throughout the plateau regime (Figure 2.26, point (2)) of the stress-strain curve. In the stress plateau, the principal deformation mechanism is the

## Theoretical background

plastic yielding or brittle crushing, depending on the nature of the solid from which the foam is made. Finally, when the complete cellular structure is collapsed, further deformation leads to the densification of sponge and a strong stress increase (3) [208, 211]. This behaviour is similar to the behaviour analysed for bones in chapter 2.1.2 (Figure 2.4).

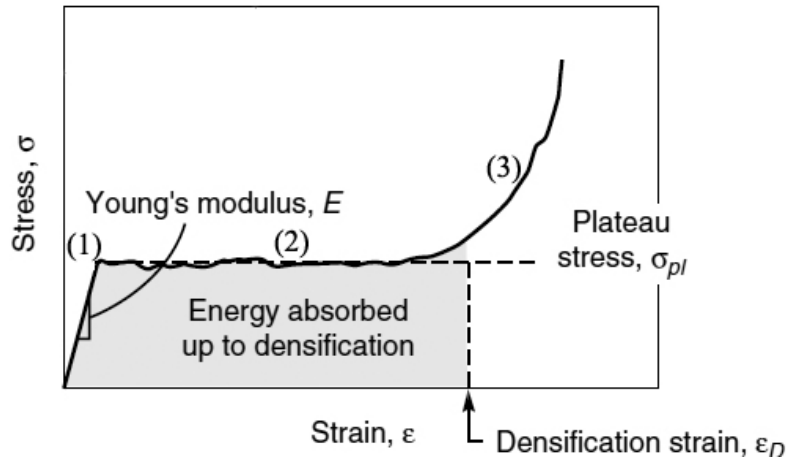


Figure 2.26: Schematic representation of the compression strain-stress curve of a metallic foam [224]

In order to analyse the deformation behaviour of the foams, it can be simplified by using two-dimensional honeycomb cell models (Figure 2.27a) or with a cubic cell model (Figure 2.27b). A hexagonal or honeycomb network is a good starting point because the modes of deformation correspond to those of three-dimensional foams [208]. The geometry of foams is much more complicated than that of honeycombs but the mechanisms by which foams deform and fail are similar to those in hexagonal structure. Figure 2.27b shows a cubic cell model used commonly in literature to analyse the mechanism of deformation and failure of open-cell foams. The results obtained with this model can be used for any cell geometry so long as the mode of deformation or failure is the same that the studied foam [3].

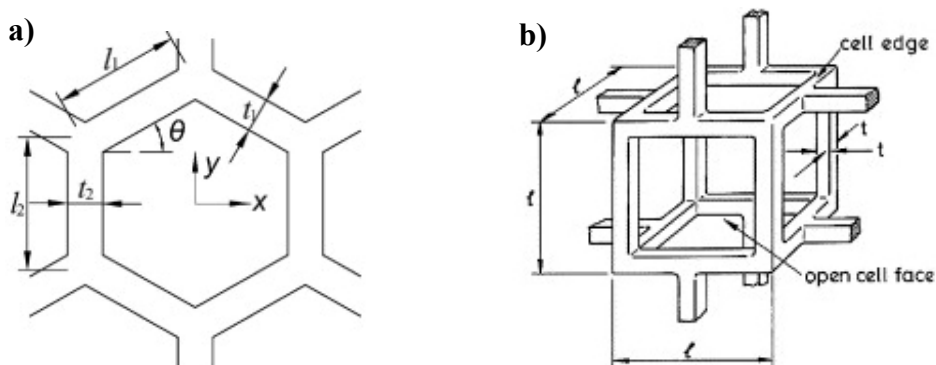


Figure 2.27: a) Honeycomb cell model, b) 3-D model of an open-cell foam [3]

In the linear elastic regime, low-density open-cell foams deform primarily by bending of the cell edges. The Young's modulus,  $E^*$ , can be estimated as follows: Figure 2.28a shows

that under a transverse load,  $F$ , the bending deflection,  $\delta$ , of a strut of length,  $l$ , and cross-sectional area proportional to  $t^2$ , is given by

$$\delta \propto Fl^3 / E_s I \quad (2.1)$$

where  $E_s$  is the Young's modulus of the solid and  $I$  is the moment of inertia and  $I \propto t^4$ .

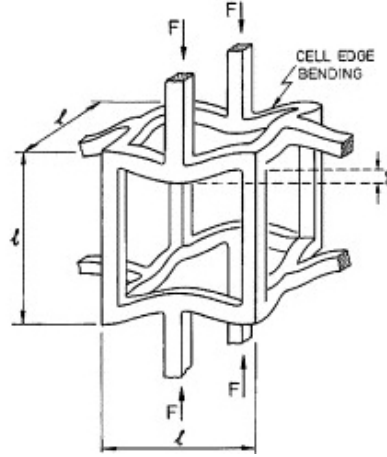


Figure 2.28: Linear elastic strut bending of an open-cell foam model [3]

The stress acting on the cell is proportional to  $F/l^2$  and the strain is proportional to  $\delta/l$ , giving

$$E^* / E_s \propto (t/l)^4 \quad (2.2)$$

The relative density of any open-cell foam,  $\rho^* / \rho_s$ , is proportional to the square of the ratio of the strut thickness to length,  $t/l$ , so that

$$E^* / E_s \propto C_1 (\rho^* / \rho_s)^2 \quad (2.3)$$

The analysis gives the dependence of the Young's modulus on the solid modulus and the relative density, and combines all of the constants of proportionality related to the cell geometry into a single constant,  $C_1$  [3]. By fitting equation 2.3 to data, it was found that  $C_1 \sim 1$  [209]. A structural analysis of a tetrakaidecahedral unit cell model with edges with plateau borders found that  $C_1 = 0.98$  [228].

The cells in open-cell foams can collapse by buckling, plastic yielding or by brittle crushing (Figure 2.29), depending on the nature of the cell strut material. Highly plastic foams can be compressed at high strain values without failure. The deformation is still recoverable, but is nonlinear. That is caused by elastic buckling of the columns or beams which make up the cell edges [229] (Figure 2.29a). The elastic collapse stress in an open-cell foam is proportional to the Euler buckling load divided by  $l^2$ :

$$\sigma_{el}^* / E_s \propto C_2 (\rho^* / \rho_s)^2 \quad (2.4)$$

## Theoretical background

Fitting equation 2.4 to data gives  $C_2 \sim 0.05$  [209]. Structural analysis of a tetrakaidecahedral unit cell gives  $C_2 \sim 0.1-0.18$ , depending on the cross-section of the edges, for loading in one direction; loading normal to the square faces does not produce buckling [230].

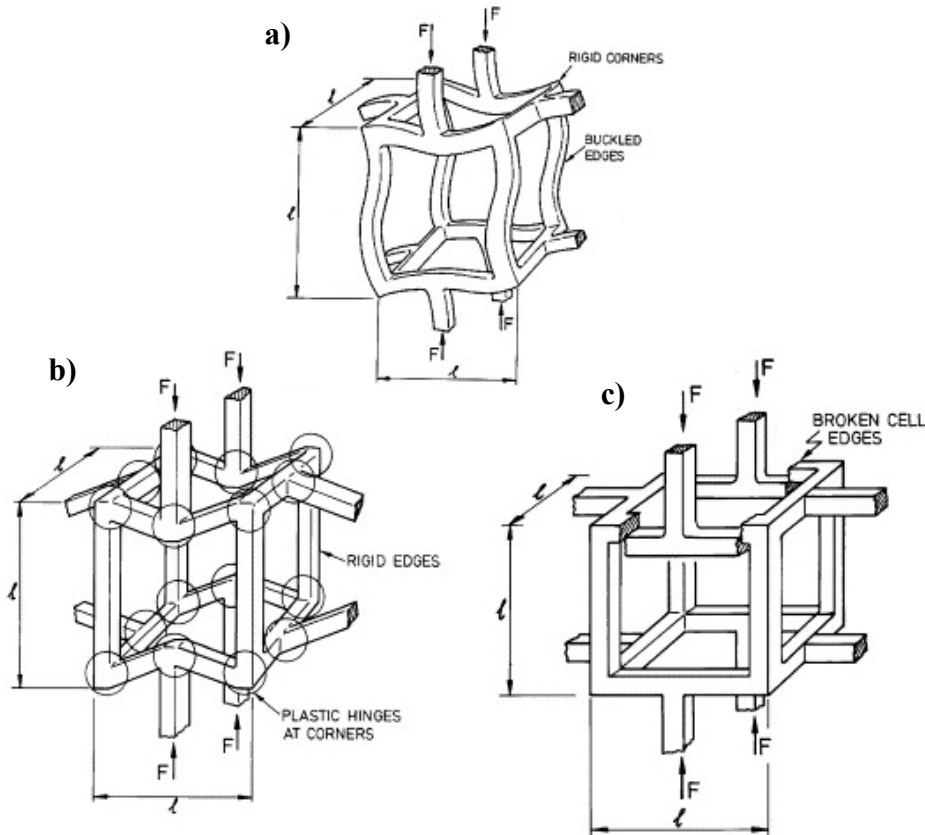


Figure 2.29: Dimensional analysis of cell collapse in an open-cell foam by a) buckling, b) plastic yielding and c) brittle fracture [3]

If the cell-strut material is ductile which holds for most metals (depending of the manufacturing process), then the foam as whole shows ductile behaviour. The plastic collapse stress,  $\sigma_{pl}^*$ , is found by equating the applied moment,  $M$ , in a strut from a transverse force,  $F$ , to the “plastic moment”,  $M_p$ , required to form plastic hinges (Figure 2.29b):

$$M \propto Fl \propto \sigma_{pl}^* l^3 \quad (2.5)$$

$$M_p \propto \sigma_{ys}^* t^3 \quad (2.6)$$

giving

$$\sigma_{pl}^* / \sigma_{ys} \propto (t/l)^3 \propto C_3 (\rho^* / \rho_s)^{3/2} \quad (2.7)$$

for an open-cell foam, where  $\sigma_{ys}$  is the yield strength of the solid cell strut material. Fitting equation 2.7 to data gives  $C_3 \sim 0.3$  [209]. In the yielding of ductile foams the fully plastic moment of the cell wall is exceeded, giving large deformation at an almost constant stress.

The brittle crushing strength,  $\sigma_{cr}^*$ , is found in similar manner, with (Figure 2.29c):

$$\sigma_{cr}^* / \sigma_{fs} \propto C_4 (\rho^* / \rho_s)^{3/2} \quad (2.8)$$

where  $\sigma_{fs}$  is the “rupture strength” of the solid cell strut material. The rupture strength of an elastic beam is the maximum surface stress at the instant of failure by bending [208]. Fitting equation 2.8 to data gives  $C_4 \sim 0.2$  [209]. Brittle foams collapse by crushing in compression [231]. Figure 2.29c shows that the low crushing strength of the foam limits the loads that can be applied to it. In the crushing of a brittle foam, the “rupture strength” of the cell walls is exceeded leading to fracture.

Another factor that may affect the deformation behaviour is the homogeneity of the foam. Poor homogeneity introduces localised deformation by the formation of deformation bands leading to cell collapsing. With increasing homogeneity the deformation of the foam structure becomes more uniform due to the more uniform distribution of the stresses [232].

### ***Compressive fatigue behaviour***

Like monotonic loading conditions, the mechanical behaviour of foams under fatigue depends on their ductility and homogeneity [233]. Previous works have shown that cyclic loading of cellular metals leads to cyclic creep and depends strongly on the stress ratio R. The increasing residual strain (cyclic creep) causes a shift of the hysteresis loops along the strain axis and an increase of the nonlinearity of the hysteresis loops [79]. Compression-compression testing ( $R > 1$ ) results in sudden collapses of localized deformation bands after a certain number of cycles [211, 234]. Under compressive fatigue loading, metallic foams undergo progressive crushing, and can achieve large strains prior to densification [235-237].

The compressive fatigue behaviour of foams involves an initial transition period. Then large plastic strains gradually develop and the material behaves in a quasi-ductile manner. Ashby et al. have described the mechanisms that occurs in compression-compression fatigue as a combination of distributed cracking of cell walls and edges, and cyclic ratcheting under non-zero mean stress [224]. Both mechanisms lead to the progressive crushing of cells. Three types of deformation pattern have been developed:

- Type I behaviour: Uniform strain accumulates throughout the foam, with no evidence of crush band development. This fatigue response is the analogue of uniform compressive straining in monotonic loading. This mechanism has been observed for open-cell aluminium foam e.g. Duocel (Figure 2.30).

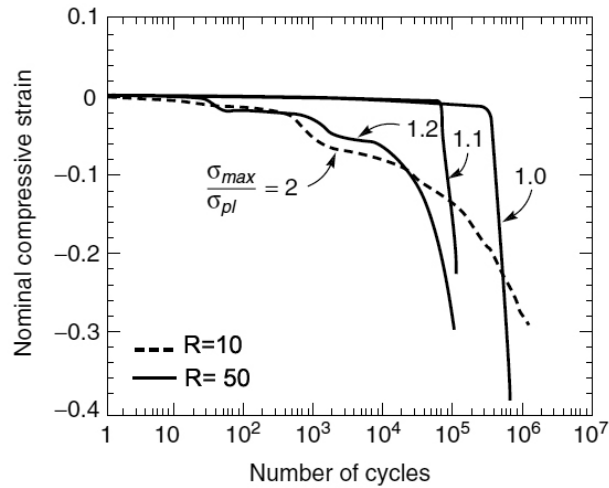


Figure 2.30: Progressive shortening behaviour in compression-compression fatigue for a Duocel Al-6101-T6 foam of relative density 0.08 [224]

- Type II behaviour. A single crush band forms and broadens with increasing fatigue cycles, as sketched in Figure 2.31a. Eventually, the crush band consumes the specimen and some additional shortening occurs in a spatially uniform manner. Type II behaviour has been observed for closed-cell foams e.g. Alulight.
- Type III behaviour: Crush bands form at random non-adjacent sites, causing strain to accumulate as sketched in Figure 2.31b. A crush band first forms at site (1), the weakest section of the foam. The average normal strain in the band increases to a saturated value of about 30% nominal strain, and then a new crush band forms elsewhere (sites (2) and (3)), as it is sometimes observed in monotonic tests. Type III has been observed for closed-cell foams e.g. Alporas, Alcan.

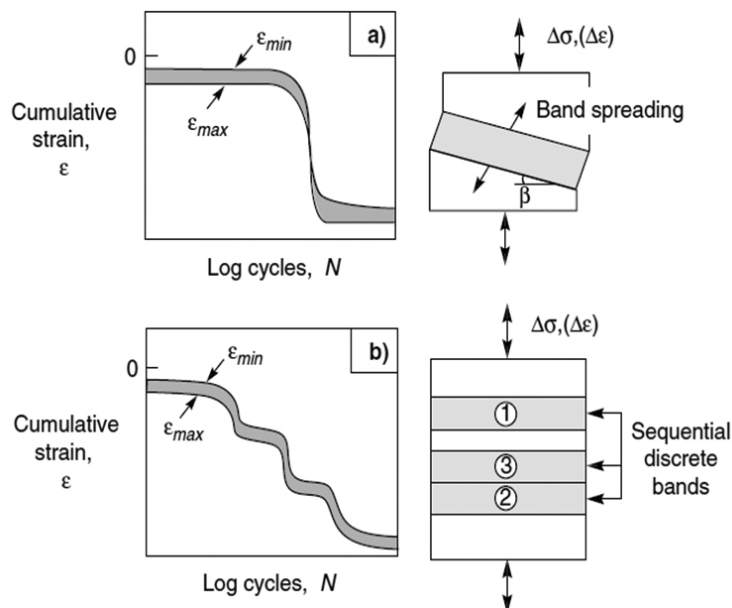


Figure 2.31: Typical behaviours in compression-compression fatigue of metallic foams at a fixed stress range: a) Progressive shortening by broadening of a single crush band with increasing cycles, b) sequential formation of crush bands [224]

The behaviour of open-cell foams shows that large compressive strains are achieved in a progressive manner. It can be anticipated that this high ductility endows the foams with notch insensitivity in compression-compression fatigue [224] (Figure 2.30). In open-cell foams, fatigue cracks propagate across cell edges, so that at the end of the test, tetragonal joints fall out of the foams. The resulting disconnection of the foam structure gives rise to a collapse band [236, 238]

### 3 Materials and experimental methods

#### 3.1 Preparation of the bone samples

Ovine, bovine and rat bones were used in this study to analyse the structure and mechanical properties of animal cancellous bones. Morphological analysis was focused on the rat and ovine cancellous bones. The analysis of the mechanical properties of big animal models was one of the principal aims of this work. Due to specimen limitations, few samples of ovine cancellous bones for the compression test were received. To solve this deficiency of cancellous bone samples, bovine bones were utilized to test big animal bones under compressive loading conditions. The understanding of the morphological and mechanical properties of the cancellous bone was important for the design and manufacture of the porous implant used in rats and sheep. The implantation was carried out in rat and sheep and after a period of recovery the animals were sacrificed in order to perform the post operative bio-mechanical studies at the implant-bone interface.

##### 3.1.1 Rat bone

The rat bones were obtained from the Labor für Experimentelle Unfallchirurgie, JLU Gießen. Due to the small dimensions of the rat bone, analyses were focused on the morphological structure of the cancellous bone for indentifying the osseointegration process in the implant-bone interface by using bio-mechanical testing. The bones were studied at the distal femoral metaphysis (Figure 3.1a). Figure 3.1b shows that the structure of the rat cancellous bone at the distal femoral metaphysis is rod-like with a trabeculae spacing (Tb.Sp.) of  $234\pm 131\ \mu\text{m}$  and a trabeculae thickness (Tb.Th.) of  $90\pm 78\ \mu\text{m}$ .

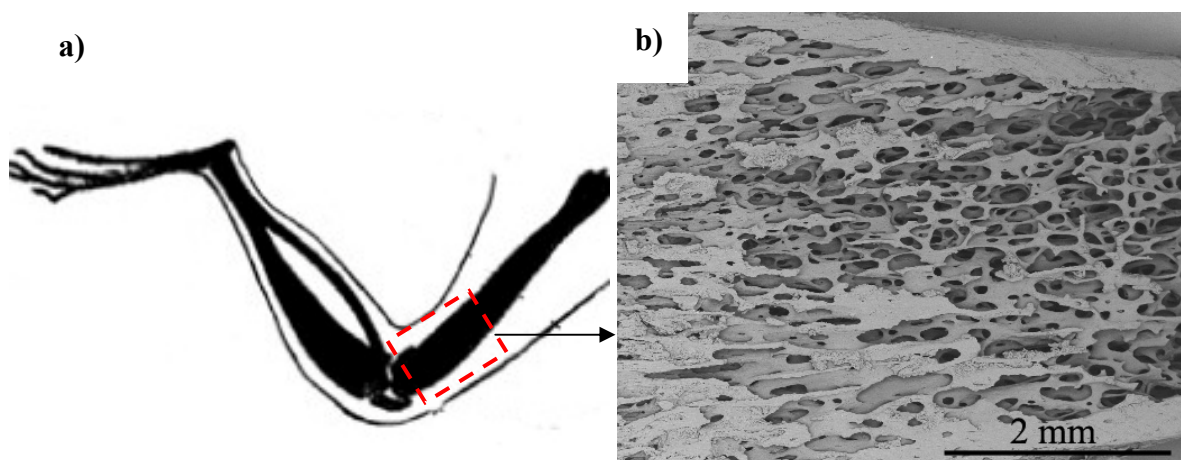


Figure 3.1: a) Position of the extracted rat bone (modified from [239]), b) SEM micrograph of cancellous rat bone at the distal femoral metaphysis

For the morphology analysis, the distal femoral metaphysis of rats that did not survive the implantation were extracted. The complete extracted metaphysis was then carefully laterally cut with a diamond saw and ground with an abrasive SiC paper of grit size 220 in order to reach the desired internal cancellous bone structure. The prepared bone samples were stored in Ringer's solution for 24 hr at 4°C. Subsequently, the bone samples receive a special preparation for the SEM analysis (details in section 3.7). The operation procedure and preparation of the rat bone specimens used for the post-operative biomechanical testing are described in section 3.6.

### 3.1.2 Ovine bone

The ovine bones were also obtained from the JLU Gießen. Morphology, compression behaviour and biomechanical properties after the implantation were studied at the distal femoral metaphysis (Figure 3.2a). Figure 3.2b shows the structure of the cancellous ovine bone at the distal femoral metaphysis which is a plate like structure with Tb.Sp. varying from 520 to 7670  $\mu\text{m}$  and a plate thickness of  $163 \pm 50 \mu\text{m}$ .

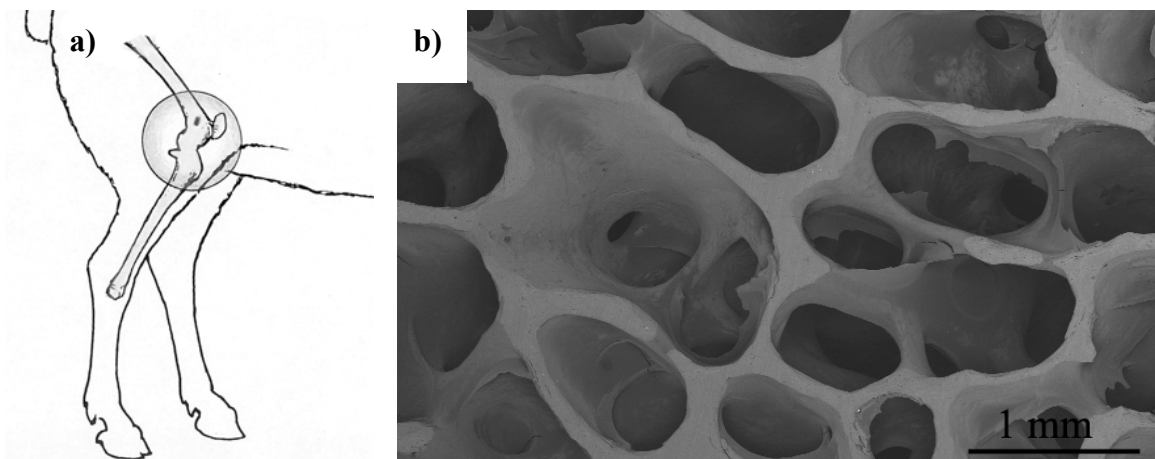


Figure 3.2: a) Position of the extracted ovine bone samples (modified from [240], b) SEM micrograph of cancellous ovine bone at the distal femoral metaphysis

Cancellous bone samples used for the morphological analysis and compression test were obtained before the positioning of the implants in the sheep. Cylindrical samples with diameter of 10 mm and 15 mm in length were harvested from the distal femoral metaphysis of the sheep (Figure 3.2a). Between the extraction and the testing, the samples were kept frozen [241] and then they were stored in a Ringer's solution for approximately 24h at 4°C before testing. The bone samples used for the morphological analysis were specially prepared for the SEM studies (details in section 3.7).

Figure 3.3 shows the schematic of the ovine distal femoral metaphysis with the position of interest for compression test samples. The samples were extracted perpendicular to the MTD (Main trabecular direction) which was the position occupied by the implants (Figure 3.3a). Ovine bone samples were also tested along the MTD to study the behaviour of the bone in the main stress direction (Figure 3.3b). Main trabecular direction was obtained after analyzing the cancellous bone structure with a computed tomography (CT) in Access Technology GmbH, Aachen, Germany and by comparison with corresponding literature [97, 242-244]. Compression test protocol is described in section 3.5.3. The operation procedure and preparation of the ovine bone specimens used for the post-operative biomechanical testing are described in section 3.6.

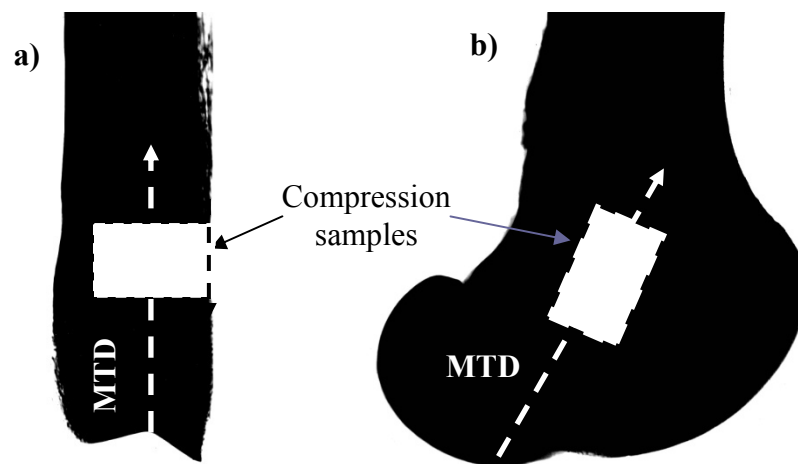


Figure 3.3: a) Lateral schematic of the ovine distal femoral metaphysis with the position of the compression sample oriented perpendicular to the MTD, b) frontal schematic of the ovine distal femoral metaphysis with the position of the compression sample oriented along the MTD

### 3.1.3 Bovine bones

Bovine cancellous bones were obtained from the University of Portsmouth (UK). Cancellous bone samples were harvested from fresh bovine iliac crest (Figure 3.4a). Slices of approximately 19 mm in length were prepared using a diamond saw. Cylinders with a diameter of 8 mm were then extracted from the iliac crest slices by a milling drill. There was no preferential orientation of the specimens with respect to the trabecular network. After the extraction, the bovine bone samples were kept frozen and before testing they were stored in

a Ringer's solution for approximately 24h at 4 °C. Cancellous bovine bone at this position is of rod like structure with a Tb.Sp. of  $807 \pm 213 \mu\text{m}$  and a Tb.Th. of  $142 \pm 35 \mu\text{m}$  (Figure 3.4 b). These samples were then used for the compression test (section 3.5.3) and the results were compared with those obtained on the ovine cancellous bone.

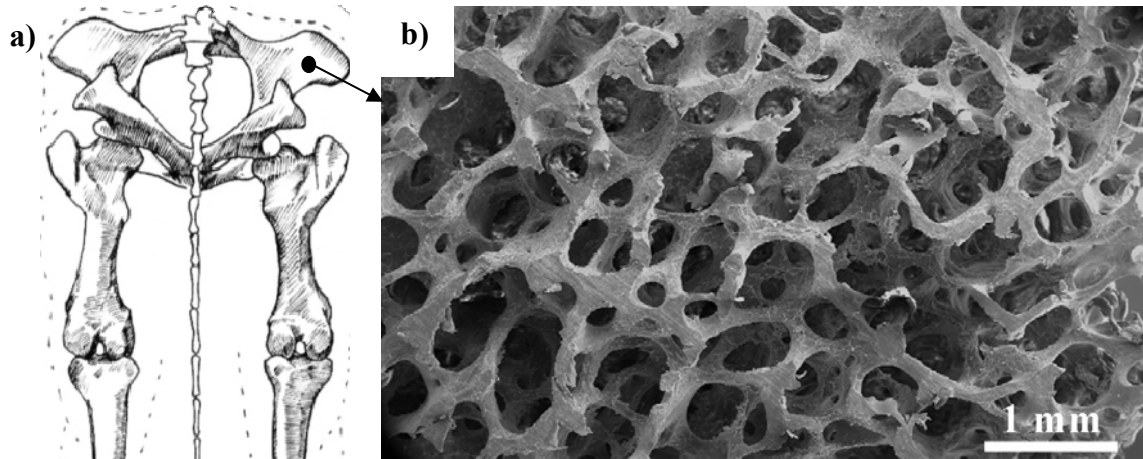


Figure 3.4: a) Position of the extracted bovine bone samples (modified from [245], b) SEM micrograph of cancellous bovine bones at the iliac crest

### 3.2 Ti-6Al-7Nb material

The material selected for the manufacturing of the porous implants was a Ti-6Al-7Nb (ISO 5832-11) alloy. Table 3.1 shows the chemical analysis of the Ti67 alloy according to the TIMET Savoie S.A. data specifications.

Table 3.1: Chemical composition of the Ti-6Al-7Nb alloy (weight percent)

Element	Al	Nb	Fe	Ta	C	O	N
Min	5.50	6.50					
Max	6.50	7.50	0.25	0.50	0.08	0.20	0.05

Ti67 ingots were hot rolled, annealed at 700°C for 1 hr and cooled at air. Figure 3.5 shows the microstructure of a Ti67 ingot. The microstructure consisted of fine globular  $\alpha$ -grains (dark areas, average diameter 10  $\mu\text{m}$ ) with the  $\beta$ -phase (bright spots) located in  $\alpha$ -grain boundaries at triple junctions.

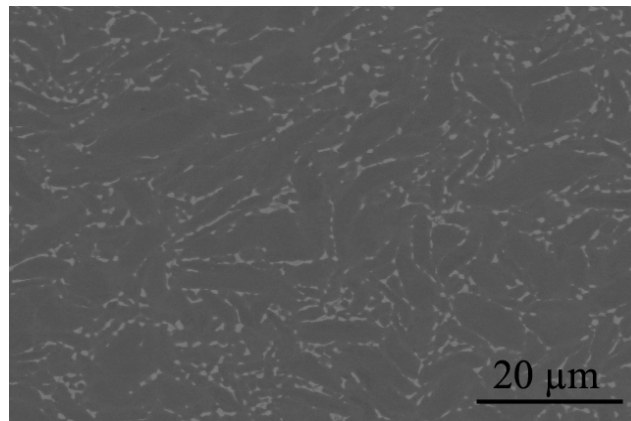


Figure 3.5: Globular microstructure of rolled Ti-6Al-7Nb ingot

### 3.3 Fabrication of the specimens

Ti-6Al-7Nb implants used in this study were manufactured using precision casting at the Gießerei Institut in the RWTH Aachen University. The samples were fabricated by reproducing polyurethane templates which possess the desired final geometry of the samples. The polymer templates were filled with a mould casting slurry (invest Ti-T) based on  $MgO + Al_2O_3 + CaO$  which was then baked to harden the casting material. During the baking process, the polymer template was burning out and the subsequently free space left by the template removal was filled with the Ti-6Al-7Nb melt alloy with a centrifugal casting machine (TiCast Super R, SelecCast) which is shown in Figure 3.6. The casting machine has a small electric-arc furnace that produce a drop of molten metal lying on a skull of solid material, saving the melt from contaminations of the graphite crucible. While melting the ingot material, the plate on which the mould was fixed was accelerated to a final velocity of 3000 rpm to assure the complete filling of the mould. Casting of the Ti67 parts was carried under an inert argon atmosphere at approx. 250 torr.

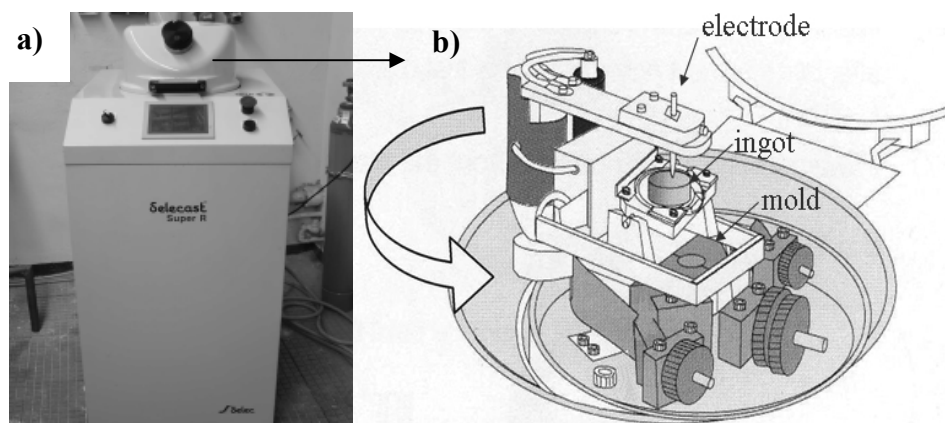
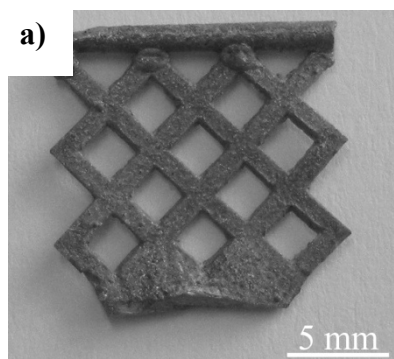


Figure 3.6: a) Centrifugal casting machine, b) schematic of the casting chamber

Technical limitations in the production of Ti67 specimens lead to the fabrication of open-cell structures with unsatisfactory porosities and dimensions for the mechanical testing. For example, the standard DIN 50134 suggests the use of a foam sample with at least 10 pores in every testing direction of the compression test [246]. In addition, to compare the mechanical properties of metallic structures with those of the cancellous bones it was desired to have similar morphology and sample dimensions of bones and foams (8 mm of diameter by 19 mm in length). Therefore, mechanical response of open-cell structures under monotonic loading conditions was carried out with 45ppi open-cell AlSi7Mg foam samples. This foam was precision cast by m-pore GmbH in Dresden, Germany.

### 3.3.1 Cast Ti-6Al-7Nb plates, grid-shape and sponge samples

Grid-shape samples with dimensions of  $13 \times 14 \times 0.5 \text{ mm}^3$ , rectangular specimens with dimensions of  $10 \times 10 \times 1 \text{ mm}^3$  and sponge specimens with dimensions of  $10 \times 30 \times 10 \text{ mm}^3$  as shown in Figure 3.7 were used for roughness measurement, metallography, corrosion test, cyclic bending, coating layer analysis and compression test. The three types of samples were utilized to understand and optimize the surface and mechanical properties of the porous implants. Grid samples were used as 2D models in order to analyse in detail the behaviour of the porous materials under localized bending loads. Rectangular samples were used to observe the effect of the mold material on the surface and microstructure of the cast Ti67 samples as well as to analyse the corrosion properties of this material. Both of these sample types were used to optimize the pickling and heat treatment processes used to remove the  $\alpha$ -case and homogenize the microstructure of the cast samples. Finally, the sponge samples were used to observe the compression behaviour of the cast open-cell Ti67 structure.



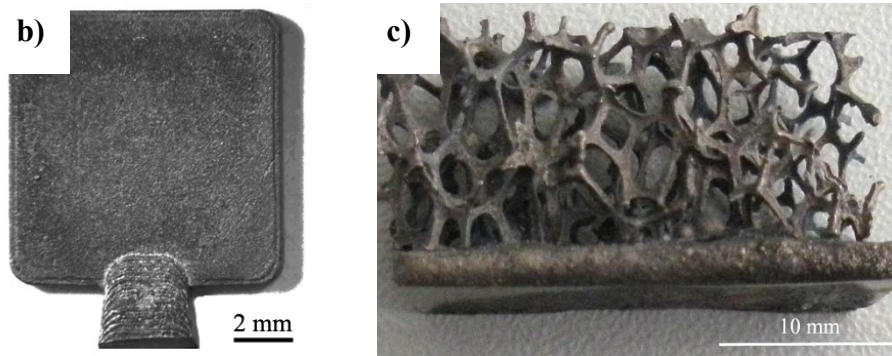


Figure 3.7: a) Grid-shaped specimen, b) plate sample and c) cast Ti67 sponge

### 3.3.2 Porous Ti-6Al-7Nb implants

Figure 3.8 shows the porous implants used for the rats and sheep operations. Rat implants were cylinders with external diameter of  $3.0\pm 0.2$  mm and  $3.5\pm 0.3$  mm in length (Figure 3.6a). These cylinders had 4 holes of approx. 1 mm of diameter located on the lateral surface and interconnected with a fifth hole on the bottom of the implant. The ovine implants were initially cast with an external diameter of  $10.5\pm 1$  mm, internal diameter of  $8.6\pm 0.4$  mm and  $12.5\pm 1$  mm in length (Figure 3.6b). In order to obtain an externally perfect cylinder, the specimens were then mechanical milled to a diameter of 9.7 mm. The inner position of the cylinder consisted of porous structure with cell spacing of  $1674\pm 704$   $\mu\text{m}$  and strut thickness of  $595\pm 205$   $\mu\text{m}$ .

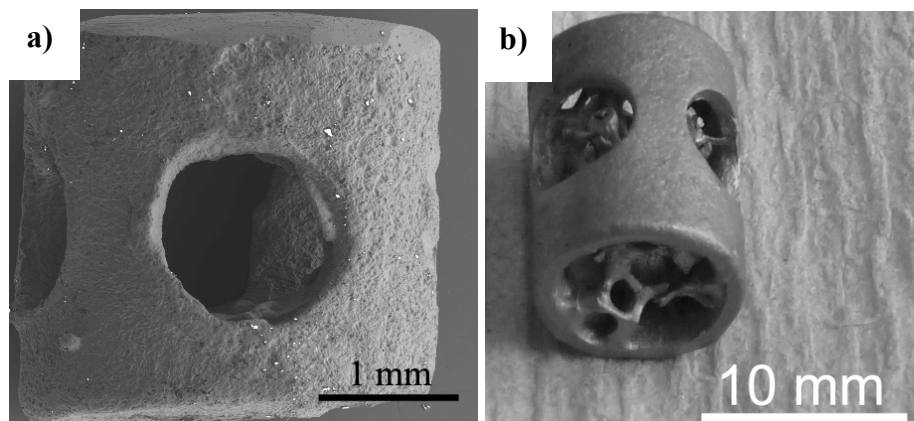


Figure 3.8: a) Rat implant, b) ovine porous implant

### 3.3.3 Open-cell AlSi7Mg foam

The AlSi7Mg foam was used to study the deformation mechanisms occurring in the compression test of metallic foams and compared the results with those of the cancellous bones. This analysis was useful to understand the deformation behaviour of the porous

Ti-6Al-7Nb implants. Figure 3.9 shows the 45ppi open-cell AlSi7Mg foam (density  $\rho^* \approx 0.25 \text{ g cm}^{-3}$ , relative density  $\rho_r \approx 11\%$ ). The foam samples were cut into cubic shape by using an ATM Brillant 220 machine and a Buehler grinding system. The samples were then gently ground to the final dimensions of 8 mm of diameter and 19 mm of length. AlSi7Mg foam exhibit a cell spacing of  $1.783 \pm 0.448 \text{ mm}$  and a strut thickness of  $0.142 \pm 0.02 \text{ mm}$ .

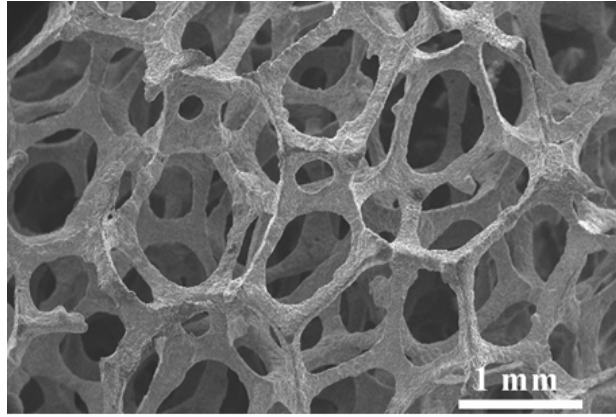


Figure 3.9: Structure of 45ppi open-cell AlSi7Mg foam

### 3.4 Microstructure and surface modification

#### 3.4.1 Heat treatment

The cast Ti67 samples were heat treated in order to achieve homogeneous microstructure. Annealing at  $1060^\circ\text{C}$  and  $870^\circ\text{C}$  for 1 hr, and aging at  $600^\circ\text{C}$  for 4 hr were used to study the effect of the heat treatments on the mechanical behaviour of the cast Ti67 samples. The treatments were carried out in a Nabertherm N21/M furnace under inert argon atmosphere. The effect of the heat treatment on the microstructure of the grid-shaped, rectangular samples and Ti67 sponge samples were analysed by Vickers hardness testing. The heat treatment process was combined with an acid milling process with the aim of improving of the ductility of the cast Ti-6Al-7Nb porous implants.

#### 3.4.2 Pickling process

For this study, cast Ti67 rectangular, grid samples and porous implants were used. The surfaces of the samples were attacked with acid etching or pickling to remove the brittle  $\alpha$ -case. Prior to pickling, the samples were ultrasonically cleaned in ethanol for 10 min to remove any residues of the investment material from the surface. For the pickling process, an acid mixture of 70%  $\text{HNO}_3$  + 10 % HF and distilled water was used inside of an ultrasonic

cleaning device at a temperature between 30-40°C. The effect of ultrasonic vibration in the pickling process was registered by a self-designed LabVIEW-based software. This program measures the open-circuit potential (OCP) between the sample and an Ag/AgCl electrode in the pickling bath with and without ultrasonic vibration. A gravimetric method was used to quantify the loss of material during the pickling process. For this purpose the pickling treatment was stopped every 10 min to measure the mass of the samples with a precision balance of type Sartorius CP124S having a resolution of 0.1 mg.

### 3.4.3 Reaction layer coatings

After pickling, the samples were coated with calcium titanate reaction layer at the Bundesanstalt für Materialforschung und -prüfung (BAM) Berlin. Coatings were used to observe their effect in the osseointegration process. For this purpose, grid-shaped and plate samples were coated in different salt baths which are described in Table 3.2. The surface and thickness of the coatings SBI, SBII, SBIII and SBIV were characterized using SEM. The performance of the coatings was evaluated using cyclic bending and fretting testing in Ringer's solution.

Table 3.2: Chemical composition of the different salt baths studied in this work

Code	Composition [Mol-%]			Temperature [°C]
	Ca(NO <sub>3</sub> ) <sub>2</sub>	NaNO <sub>3</sub>	KNO <sub>3</sub>	
SBI	46	27	27	350
SBII	50	50	-	410
SBIII	60	40	-	450
SBIV	75	25	-	510

### 3.5 Mechanical testing

Mechanical tests were carried out to understand and improve the mechanical properties of the Ti-6Al-7Nb implants. These tests include:

- (1) bending test to analyse the effect of the heat treatments and of removing the  $\alpha$ -case in grid-shaped samples,
- (2) cyclic bending and fretting tests combined with corrosion analysis to monitor the coating layer behaviour on grid-shaped and plate samples and

(3) compression behaviour analysis of ovine and bovine cancellous bone as well as the Ti67 porous implants and the AlSi7Mg foam.

### 3.5.1 Monotonic bending

Monotonic bending tests were performed in a self-constructed bending system (Figure 3.10) in a servohydraulic MTS810 testing machine with a displacement rate of 0.05 mm/sec. This test was designed to analyse the effect of pickling and heat treatment on the mechanical properties of the cast Ti67 material. The test was carried out on grid-shaped samples until they failed. The forces were registered with a ME KD24S (200N) load cell. A distance of 5 mm between the gripping system and a sharp indenter was used to assure bending of the grid sample.

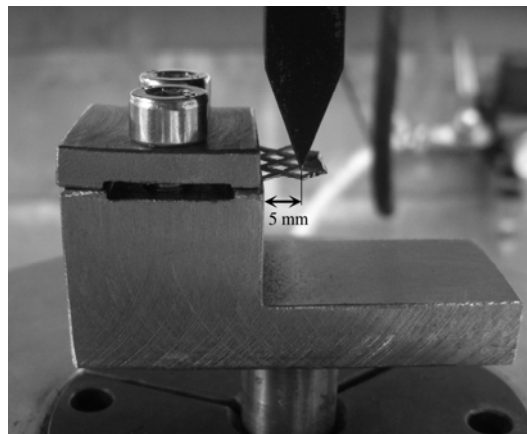


Figure 3.10: Monotonic bending system for grid-shaped samples

### 3.5.2 Corrosion-cyclic bending analysis of the reaction layer

Mechanical behaviour of the reaction layer was tested by cyclic bending tests in a corrosive atmosphere. Cyclic bending tests of grid-shaped samples were performed under load control (-2 to -15 N) at 5 Hz using the ME KD24S load cell.

The reaction layers on the Ti67 samples were analysed during the mechanical tests by measuring the open-circuit potential (OCP). The OCP signal was monitored by a self-designed LabView-based software. This program measured the differential potential between the sample (working electrode, WE) and an Argenthal Ag/AgCl electrode (reference electrode, RE) in Ringer's solution as electrolyte. In order to keep a constant current (0.3 mA) between the working electrode and the counter electrode (CE, cast Ti67), a Wenking potentiostat / galvanostat (70 TS1) was used. Figure 3.11 shows the complete corrosion system used for the cyclic bending test.

## Materials and experimental methods

To improve the accuracy in the measurement of the OCP, the cable connections of the RE, CE, and WE were isolated and then the electrodes were carefully positioned following the suggestion of Leinenbach et al. [141]. The proper positioning of the electrodes reduced the travelling distance of the ions during the oxidation between the electrodes and therefore reduces the errors in the measurement of the open-circuit potential.

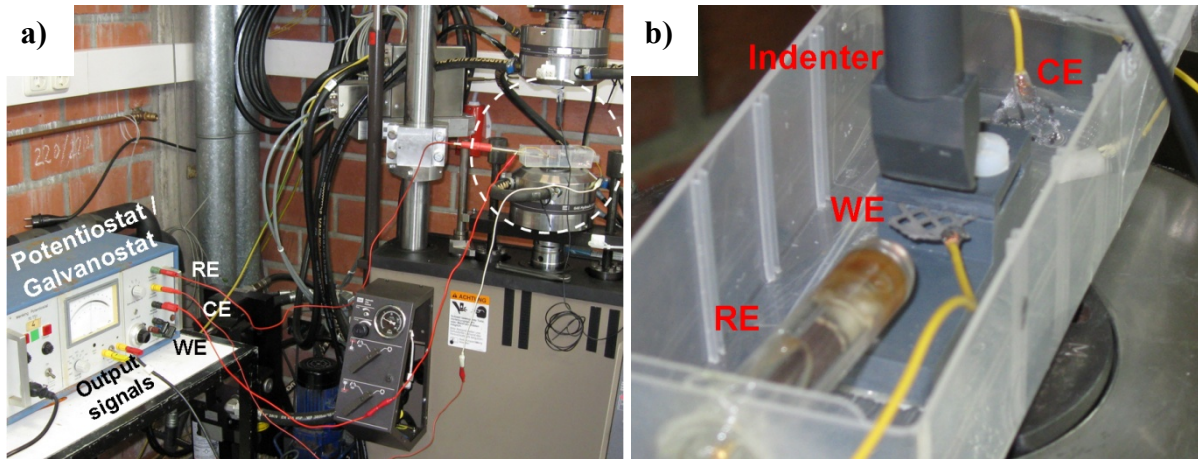


Figure 3.11: a) Corrosion system used in the cyclic bending, b) detail of the corrosion-testing chamber

### 3.5.3 Fretting analysis of the reaction layer

The corrosion-cyclic bending analysis of the reaction layers was complemented with a fretting test to observe the behaviour of the coatings under friction loads. Coated rectangular samples were fixed in a self designed cyclic friction system (Figure 3.12). The coating of the samples were fretted with a force of 1.5 N using a titanium sphere with a diameter of 3 mm which was connected to a ME KD24S (200 N) load cell. The samples were tested for 200 cycles with a displacement amplitude of  $\pm 4$  mm and a frequency of 3Hz. After the mechanical tests, the coating on the samples were analysed by SEM.

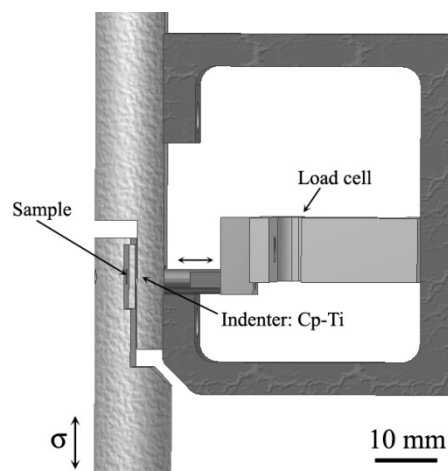


Figure 3.12: Fretting system

### 3.5.4 Compression test

Ovine and bovine cancellous bones as well as the ovine porous implants and the 45ppi open-cell AlSi7Mg foam were used for the compression tests. The AlSi7Mg foam and the bovine bone samples were tested without any preferential direction. The ovine implant and ovine bone samples were tested in two directions: parallel and perpendicular to the MTD.

Compression testing was carried out on a MTS 810 servo-hydraulic testing system under displacement control. The measured mechanical properties were reported to be influenced by the experimental procedures [72] and the specimen geometry [75, 247]. Hence, efforts were made to minimize the test variables. Custom-made end-caps were manufactured from hardened steel. The ends of each cylindrical specimen were then embedded about 3 mm into the end-caps with acrylic cold mounting resin (DuroCit powder, Struers A/S) to minimise the end artifacts [247]. A custom-made aligning system was also used to ensure the alignment of the sample with the loading axis. The length of the cylinders after fixation was approximately 13 mm, thus achieving an aspect ratio of 1.625:1 for the AlSi7Mg foam and bovine bone, a ratio of 1.3:1 for the ovine bone and a ratio of 1.2:1 for the ovine implants. These aspect ratios are close to the range of 1.5 to 2 recommended by DIN 50134 [246] for compressive testing of metallic cellular materials and are not far from the ratio of 2:1 suggested by Keaveny et al. [247] for testing of bones. Strain measurements were performed using a 15 mm gauge-length extensometer (Sandner EXA R15-5X) attached to the end-caps [72]. The elastic modulus, yield stress and ultimate strength were determined. The experimental set-up used for the mechanical testing is shown in Figure 3.13. Due to the dimensions of the ovine bone and ovine implant samples, the system in Figure 3.13 was slightly modified with an end-cap diameter of 10 mm and an end-cap depth of 1 mm.

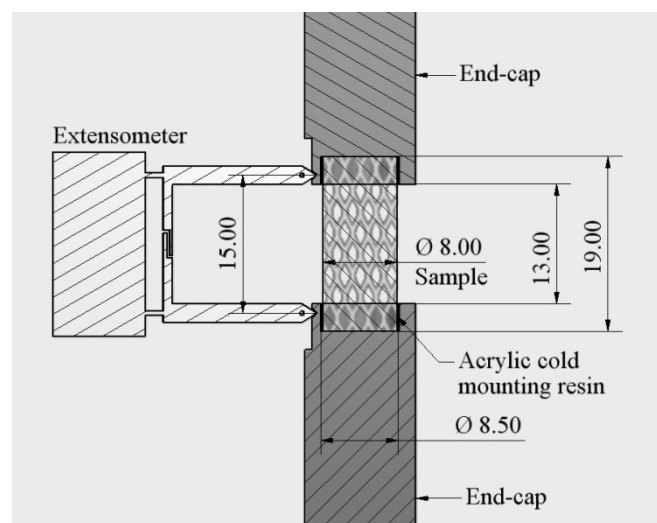


Figure 3.13: Schematic of the experimental set-up

## Materials and experimental methods

Tests were carried out following the test standard for cellular metals (DIN 50134) [246]. Preliminary compression tests were carried out at a constant strain rate of 0.01/s on the foam (n=5), ovine bone samples (n=3), bovine bone samples (n=5), and ovine implants (n=3) to assess the mechanical properties, including  $R_{20}$ ,  $R_{70}$  (20% and 70% of the compressive strength, respectively) and ultimate compressive strength ( $\sigma_{ult}$ ). The tests were then carried out at an initial strain rate of 0.001/s starting from a preload of approximately 2% of the  $\sigma_{ult}$  until  $R_{70}$  was reached. The load was then reduced until  $R_{20}$  was reached at a strain rate of 1/s. Finally, the samples were re-loaded from  $R_{20}$  until failure at a strain rate of 0.01/s. The ultimate compressive strength was defined as the maximum stress reached during the first cells deformation [248, 249]. The test standard was slightly modified for the testing of bones, where  $R_{40}$  was used instead of  $R_{70}$ . The elastic modulus was measured directly from the unloading linear stress-strain relationship between  $R_{70}$  ( $R_{40}$  for the bones) and  $R_{20}$ . The yield stress was determined using the 0.2% offset method [68]. For the compression test, 10 samples of bovine bones, 5 samples of ovine bones, 7 samples of the AlSi7Mg foam and 5 samples of the ovine implants were used.

The compressive deformation behaviour and the failure mode of bovine cancellous bone and AlSi7Mg foam were studied with an in-situ micromechanical loading stage installed in a 3D real time  $\mu$ CT imaging system (CT X-Ray Inspection System, X-Tek Systems Ltd). This study was carried out at the Mechanical Behaviour of Materials Laboratory of the University of Portsmouth. Foam and bone samples were step-wise compressed in a novel custom-made (Deben Ltd, UK) loading stage equipped with a 3 kN load cell inside a  $\mu$ CT chamber (Figure 3.14). The samples (n=4 for each material) were compressed in the loading stage at a constant strain rate of 0.01/s. The strain was kept constant whilst the samples were  $\mu$ CT imaged at four points of the stress-strain curve: 0% strain, yield,  $\sigma_{ult}$ , and at 10% strain (plastically deformed).

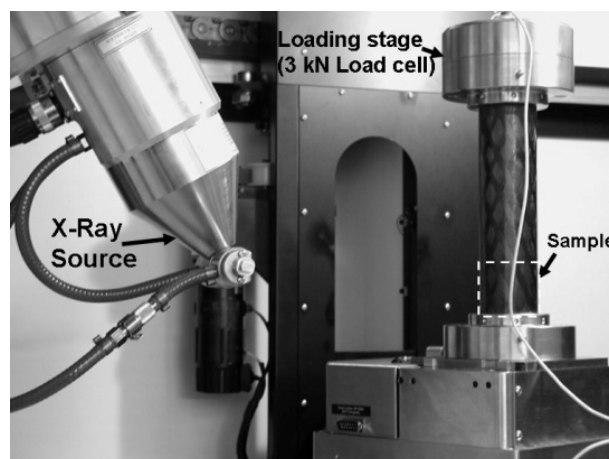


Figure 3.14:  $\mu$ CT system with loading stage

The scanner settings used in the  $\mu$ CT were 55 kV-130  $\mu$ A for bovine cancellous bone and 60 kV-140  $\mu$ A for the AlSi7Mg foam samples. With a voxel size of 15  $\mu$ m the image acquisition process was performed at a rotational step of 0.19° over 360°. The 3D reconstruction of the samples was obtained through VG StudioMax 2.0 software.

### 3.6 In-vivo investigation

To analyse the biological reactions and biomechanical behaviour of the porous implants in the cancellous bone, they were implanted in rat, and sheep at the Justus-Liebig-Universität Gießen, Germany.

#### 3.6.1 Implantation of porous Ti-6Al-7Nb implants in rats

Rats were used to study the osseointegration process of the Ti67 implants in the cancellous bone at the femoral metaphysis (Figure 3.15a). In total 48 rats were operated and handled under the recommendation of the regional commission of Gießen with the file number V 54 - 19 c 20-15 (1) GI 20/14 Nr. 56/2010 under § 8 paragraph 1 of the animal's protection act approved on 24.05.2007.

Two rats didn't survive the operation and therefore were used as reference of bone-implant interface at zero days. After 30 days, distal femoral metaphysis of 12 rats with their respective implants (Figure 3.15b) were extracted and used for the in-vitro post-operative biomechanical test. The rest of the rats were used for histomorphometric analysis at the Labor für Experimentelle Unfallchirurgie, JLU Gießen.

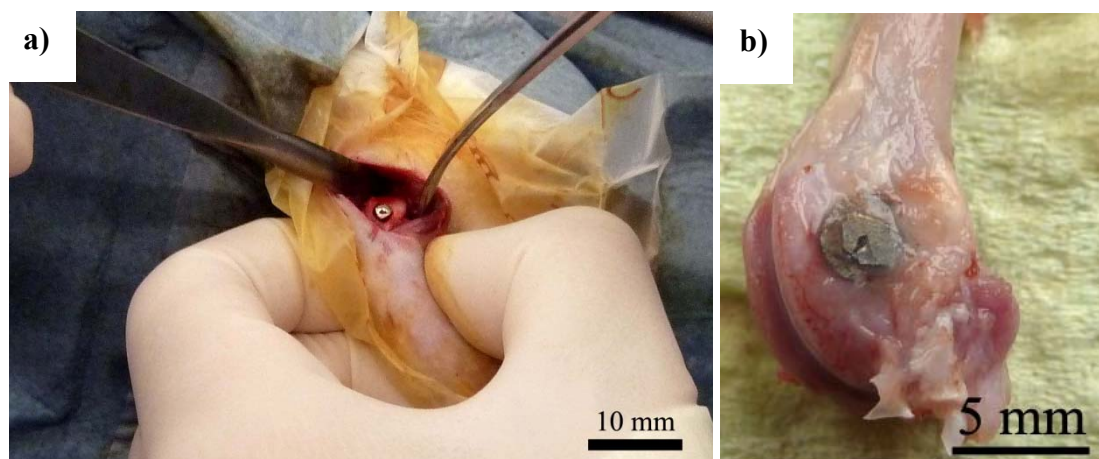


Figure 3.15: a) Implantation in a rat distal femoral metaphysis, b) extracted bone with implant after 30 days

### 3.6.2 Implantation of porous Ti-6Al-7Nb implants in sheep

Sheep were used to study the osseointegration process and the mechanical behavior of the Ti67 implants in the cancellous bone at the femoral metaphysis (Figure 3.16a) of big animals. In total 24 sheep were operated and handled under the recommendation of the regional commission of Darmstadt with the file number V 54 - 19 c 20/15 - F31/31 under § 8 paragraph 1 of the animal's protection act approved on 18.05.2006.

After 6 months, distal femoral metaphysis of 12 sheep (with ages between 49-95 months) with their respective implants (Figure 3.16b) were extracted and used for the in-vitro post-operative biomechanical test. The rest of the specimens were used for histomorphometric analysis at the Labor für Experimentelle Unfallchirurgie, JLU Gießen.

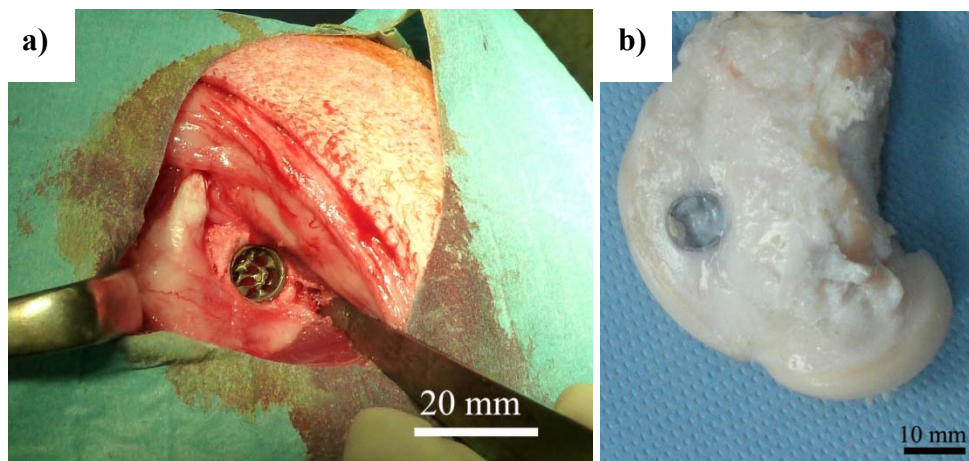


Figure 3.16: a) Implantation in an ovine distal femoral metaphysis, b) extracted bone with implant after 6 months

### 3.6.3 Post-operative biomechanical testing

To analyse the mechanical characteristics of the bone-implant interface of rats and sheep a push-out test was used. The samples used for the push-out test were carefully extracted from the femur of the rats and sheep and laterally cut with a diamond saw. In order to use the push-out system showed in Figure 3.17a the cut side of the rat bones was carefully ground with an abrasive SiC paper of grit size 220 until the lower side of the implant was visible. As a consequence, the flat lower surface of the rat bone was perpendicular to the implant axis. Finally, the rat implant was perfectly aligned to a push-out indenter which extracts the implant from the rat bone through the orifice of the holding system platform (Figure 3.17b).

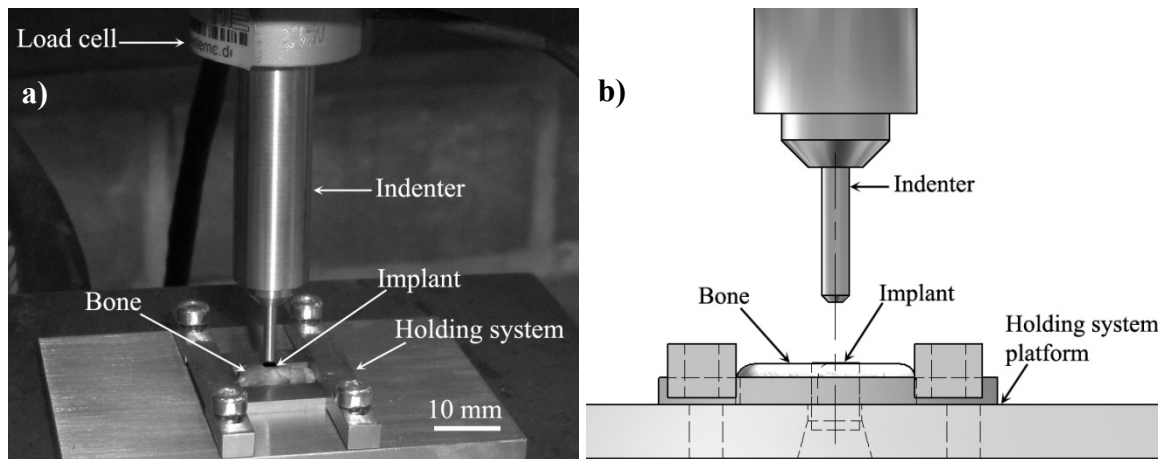


Figure 3.17: Push-out testing system used to analyse the bone-implant interface a) push-out system used for the rats, b) Frontal schematic of the push-out test

The push-out system used to study the bone-implant interface of sheep was modified from that used for the rat experiments. The size of the ovine implants and the manual procedure to position the implants into the bones resulted in misalignment of the implants inside the bones during the healing time. Therefore, X-ray analysis was done to observe the position of the implants in the ovine distal femoral metaphysis before to the push-out test in order to find the inclination angle of the implants. The X-ray analysis was carried out with a Comet MRX 320/26 equipment with X-ray settings of 50 kV, 5 mA and an exposure time of 3 min. The experiments were performed at the Ingenieurbüro F. Braun (Zerstörungsfreie Werkstoffprüfungen) Freudenberg, Germany. After measuring this angle in two directions P1 and P2, the samples were perfectly aligned in the direction of the push-out indenter by using a self made system. Figure 3.18 shows that the push-out system utilized three M5x1 (70 mm in length) screws to align the implant in the indenter direction.

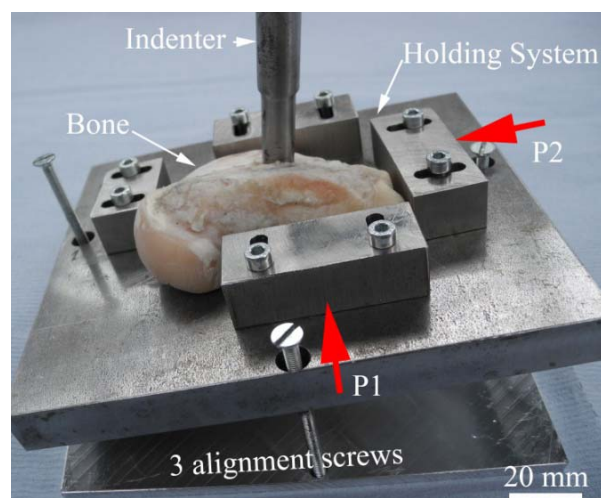


Figure 3.18: Push-out testing system used to analyse the ovine bone-implant interface (P1 and P2 are the directions used for the X-ray analysis)

Push-out test was performed on the MTS 810 system which was equipped with an indenter of 2.5 mm of diameter for the rat and an indenter of 9.3 mm in diameter for the ovine implant experiments. The push-out force of the rat-implants interface was measured with a 2 kN load cell while the push-out force of the ovine-implant interface was measured with a 50 kN load cell, at a displacement rate of 1 mm/min until the implant was completely removed from the bone. Force and absorbed energy of the bone-implant interface were registered and compared with the push-out test of the reference samples (specimens with 0 days of osseointegration).

After the push-out test, the external and the internal surface of the implants were studied with optical microscope and SEM to analyse the bone ingrowth and osseointegration with the implants. The extracted ovine implants were cut laterally with a diamond wire saw of type 5237 at a cutting rate of 1 mm/min.

### **3.7 Morphological and analytical studies**

Microstructure of the metallic and bone samples were analysed by using optical and scanning electron microscopy (SEM). SEM analysis was carried out with a Philips XL 30 equipment. Microstructure, failure analyses and changes in the surface topography were observed with secondary electron (SE) and back-scatter electron (BSE) detection in combination with energy-dispersive X-ray spectroscopy (EDS) and automated electron back-scattered diffraction (EBSD). A confocal laser microscope model Olympus LEXT OLS 4000 was utilized to measure the surface roughness of samples.

Prior to SEM analysis, bone samples were ultrasonically cleaned in ethanol at 50°C for 2 hr [250]. Bone marrow, fat and oil of bone samples were removed by compressed air. This process was repeated 5 times until the soft tissue of the bone was completely removed. The samples were washed with ethanol and dehydrated 24 hr in a desiccator [251]. In order to have a conductive surface the dried bone samples were sputtered with gold.

To analyse the organic material without damaging the bone-implant interface after the push-out test, the samples received a special treatment in the Justus-Liebig-Universität Gießen, Germany. The bone-implant samples were initially washed with a 0.1 M sodium phosphate buffer and fixed for 24 hr with 2.5% glutaraldehyde + 1% sucrose. The samples were again washed in 0.1 M sodium phosphate. Finally, the samples were dehydrated in ethanol until the critical drying point was reached with a CPD7501 (Thermo VG Scientific).

Metallic samples were ultrasonically cleaned with ethanol for 15 min and then for 5 min in distilled water. Finally, the samples were completely dried.

## 4 Results

This chapter presents the results obtained from the material analyses, as well as from the mechanical and biomechanical experiments. Section 4.1 shows the compression properties of the ovine and bovine cancellous bone. Bovine cancellous bone was used to complement the understanding of the deformation mechanism that occurs in cancellous bone during compressive loading conditions. These results are compared with the compression properties of a ductile metallic foam. The 45ppi open-cell AlSi7Mg foam was selected to be used as reference for the analysis of the mechanical behaviour of open-cell metallic foam. The mechanical properties and behaviour of the porous Ti-6Al-7Nb implants have not been studied until now, and therefore it is necessary to compare these results with a commercial metallic foam which has a porosity close to the cancellous bones used in this work.

The characterization of the cast Ti-6Al-7Nb material is described in section 4.2. In this section, special attention is given to the analysis of the microstructure and surface of the samples.  $\alpha$ -Case and other cast defects are analysed and solutions are introduced to improve the surface condition and mechanical properties of the Ti67 cast samples. In addition, this section presents the surface and mechanical properties of the Ti67 implants used for the rats and sheep experimentation. Section 4.3 exhibits the characterization of the calcium titanate reaction layer used to coat the implants prior to the implantation in the animals. Section 4.4 describes the biomechanical response of the bone-implant interface that was studied with push-out tests after the euthanasia of the animals.

### 4.1 Compression behaviour of the cancellous bones and open-cell foam

#### 4.1.1 Compression behaviour of the ovine cancellous bone

Figure 4.1 shows the compression behaviour of the ovine cancellous bone. This bone was tested in two directions: along the MTD and perpendicular to the MTD in order to observe the influence of the anisotropy in the mechanical properties of the ovine distal femoral metaphysis. Figure 4.1a and c exhibit CT analyses of the cancellous bone showing the orientation of the trabeculae during the compression test while Figure 4.1b and d show the compression behaviour of the ovine bone tested along and perpendicular to the MTD. The compressive behavior of the ovine cancellous bone was linear elastic at the beginning of the compression. The linear elastic behaviour was followed by a brief but significant hardening period, then by a prolonged softening with considerable reduction of stresses due to progressive failure of the trabeculae (at a strain between 2 to 4%). For large strains between 5-

## Results

7%, a slight increase in the stress was observed also, probably due to the densification process of the trabeculae.

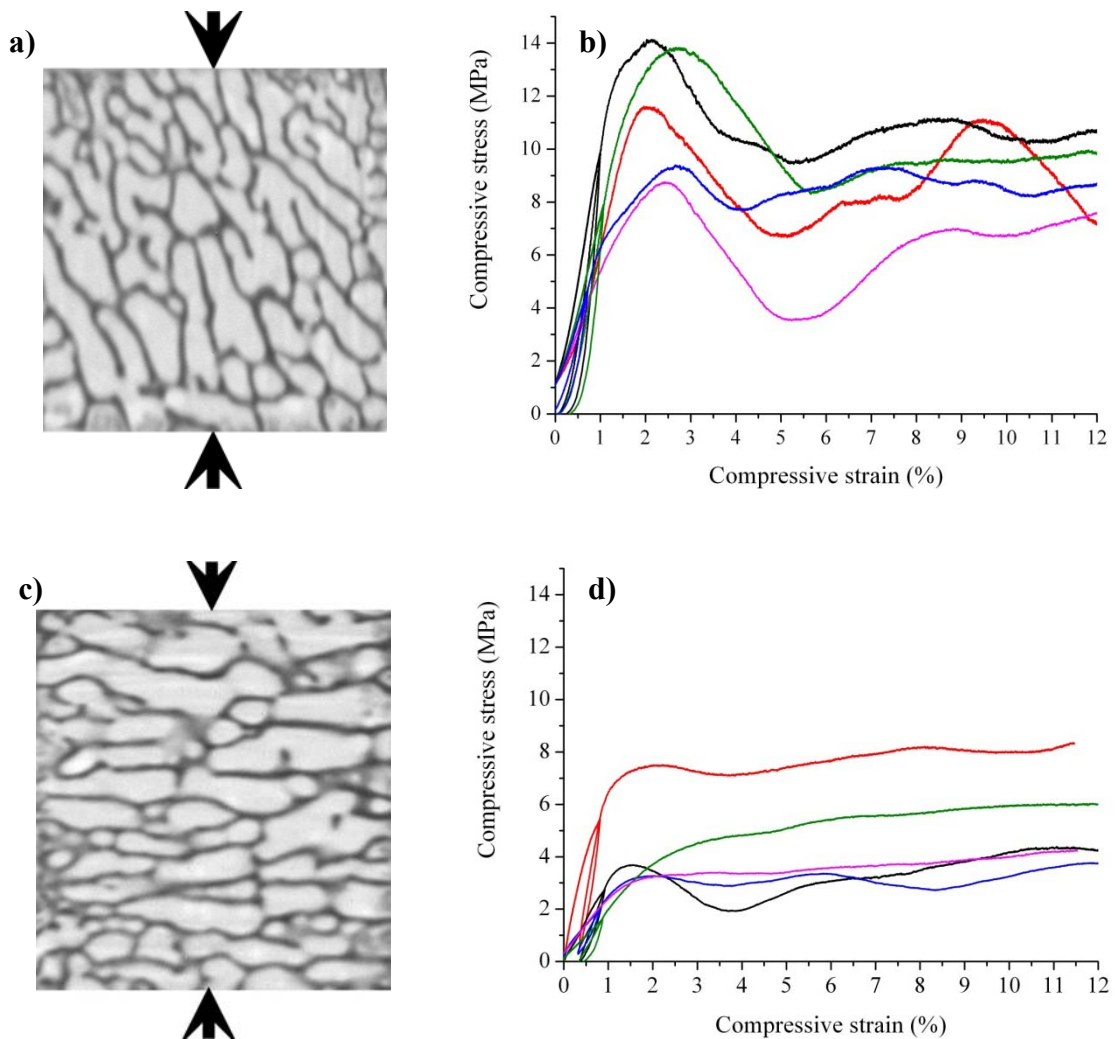


Figure 4.1: Ovine cancellous bone: a) orientation of the trabeculae along the MTD, b) compression behaviour along the MTD, c) orientation of the trabeculae perpendicular to the MTD, d) compression behaviour perpendicular to the MTD

The compressive strength and Young's modulus of the ovine bone tested along the MTD are about twice higher than those values of the bone tested perpendicular to the MTD. This high difference between the two tested directions shows the effect of the anisotropy in the distal femoral metaphysis. The samples used for these tests were manually extracted, therefore some deviation from the exact MTD are possible. However, the intention of this experiment was to show the effect of the bone orientation in the mechanical properties of the cancellous bone.

#### 4.1.2 Compression behaviour of the bovine cancellous bone

Figure 4.2a shows the 3D reconstruction of a section of the bovine bone used for the compression test while Figure 4.2b exhibits the compression behaviour of this bone. These bone samples were selected from iliac crest where no pronounced anisotropy exists in the trabecular network. Compressive behaviour and values of the bovine cancellous bone are very similar to that observed for the ovine bones tested along the MTD. Therefore, this bone was considered a good candidate to be used as bone model to observe the deformation mechanism during the in-situ  $\mu$ CT analysis.

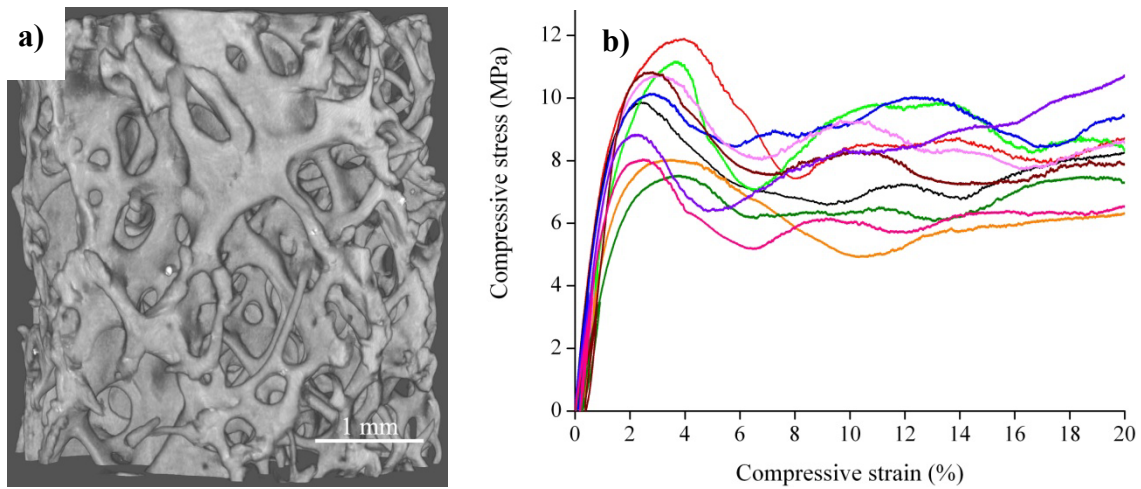


Figure 4.2: Bovine cancellous bone: a) 3D reconstruction of a part of the bone used for the compression test, b) compression behaviour of the cancellous bone

A summary of the mechanical properties of the ovine and bovine bone in term of the elastic modulus ( $E$ ), yield stress ( $\sigma_y$ ) and ultimate strength ( $\sigma_{ult}$ ) is presented in Table 4.1. There are significant higher scatters in the data obtained from the ovine bones, than those from the bovine bone. The high scatter of the compression values of the ovine bones can be explained due to the anisotropy of the cancellous bone at the distal femoral metaphysis.

Table 4.1: Mechanical properties of ovine and bovine cancellous bone

Mechanical properties	Bovine bone	Ovine bone (tested along the MTD)	Ovine bone (tested perpendicular to the MTD)
$\sigma_{ult}$ in MPa ( $\pm$ SD)	$9.36 \pm 1.45$	$10.45 \pm 3.46$	$4.56 \pm 2.22$
$\sigma_y$ in MPa ( $\pm$ SD)	$8.02 \pm 1.19$	$9.62 \pm 3.06$	$4.10 \pm 1.89$
$E$ in MPa ( $\pm$ SD)	$800 \pm 138$	$825.33 \pm 388.3$	$385 \pm 464$

## Results

The plate-like structure of the ovine cancellous bone differs from the structure of the bovine bone, although both bones show similar compressive values. Due to these similarities and to the limited ovine bone specimens, the deformation mechanism was analysed in the bovine bone with an in-situ load stage in a microfocus computed tomography.

Figure 4.3 shows the mechanical response of the bovine trabecular bone with the four deformation points tested in the in-situ loading stage: a) = 0%, b) = yield, c) =  $\sigma_{ult}$  and d) = plastically deformed (approx. 8% strain). The local deformation occurred at these steps on the trabeculae was examined using the CT 3D reconstructions (Figure 4.4).

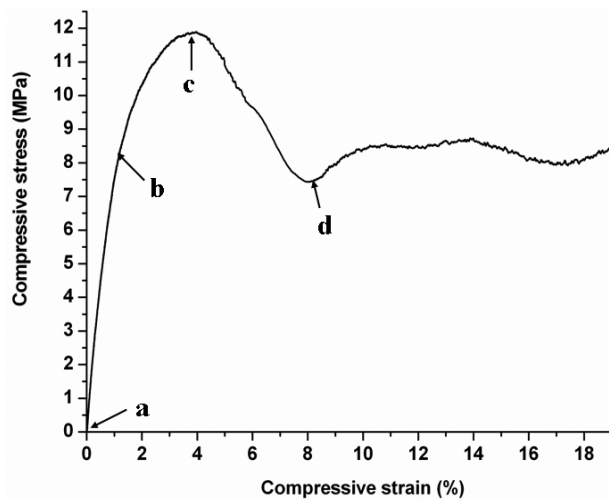


Figure 4.3: Mechanical response of the bovine trabecular bone with the four deformation points tested in the in-situ loading stage

$\mu$ CT analysis shows that bones deform principally due to bending and buckling (Figure 4.4). The arrows in Figure 4.4 show the evolution of the mechanical deformation of specific trabeculae at 0% deformation, yield,  $\sigma_{ult}$  and plastically deformed. As the strains within trabeculae approach the yield point (Figure 4.4b) of the trabecular structure, bending was principally observed (see arrows). The bending on the trabeculae was followed by buckling (Figure 4.4c) producing permanent deformation. During the collapse of the trabeculae a decrease of the global stress (softening) was observed. After the complete collapse of trabeculae due to inelastic buckling, the deformation propagated to a neighbouring trabeculae band producing again a stress increase.

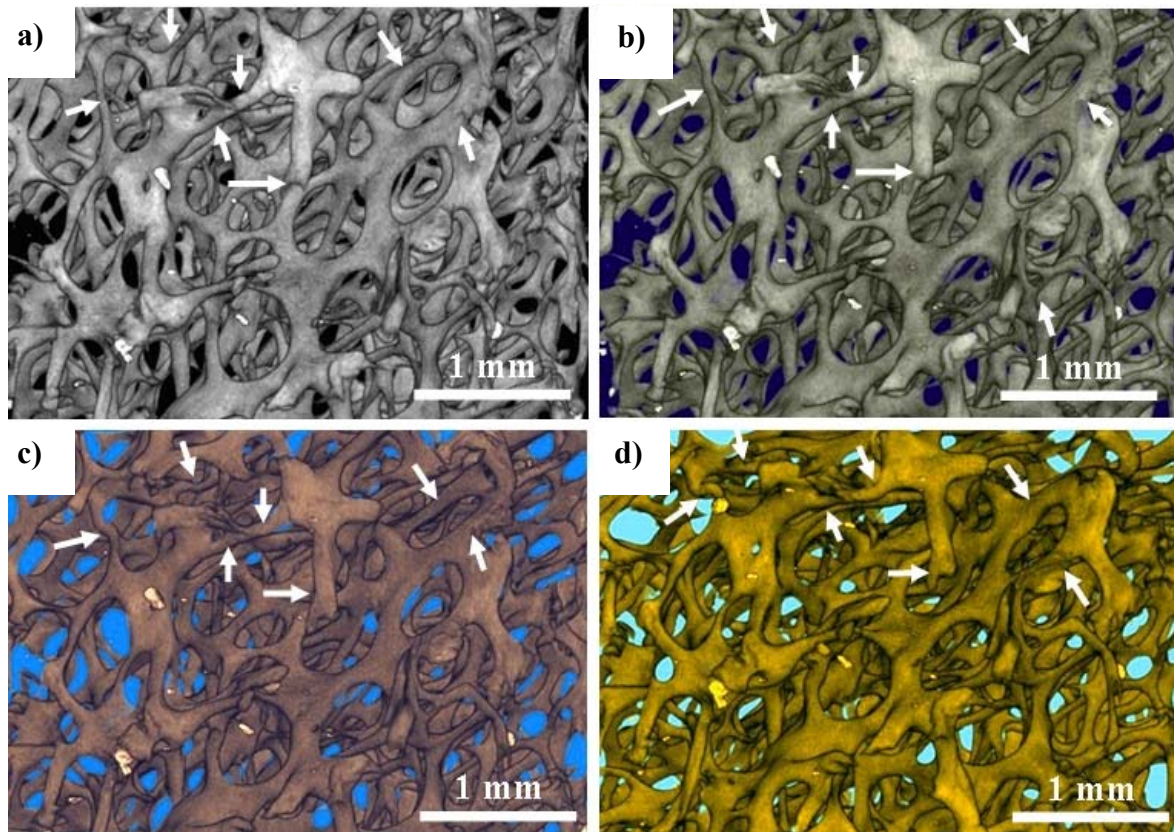


Figure 4.4:  $\mu$ CT-analysis of the deformation occurring during step-wise compression of the bovine cancellous bone: a) at 0% stress, b) at yield, c) at maximum stress, d) plastically deformed

#### 4.1.3 Compression behaviour of an open-cell metallic foam

Figure 4.5a shows the 3D reconstruction of a 45ppi open-cell AlSi7Mg foam used for the compression test, while Figure 4.5b exhibits the compression behaviour of the foam which possesses a  $\sigma_y$  of  $0.84 \pm 0.09$  MPa,  $\sigma_{ult}$  of  $1.19 \pm 0.09$  MPa, and a Young's modulus of  $314 \pm 63$  MPa.

The stress-strain behaviour of the AlSi7Mg foam (Figure 4.5) appears to be close to that of the cancellous bones, although the magnitudes of the yield and ultimate stresses are considerably lower for the foam. The mechanical response of the AlSi7Mg foam shows a significant range of hardening (up to 3% strain) following the initial elastic response, followed by “softening” till approx. 8-10% strain.

## Results

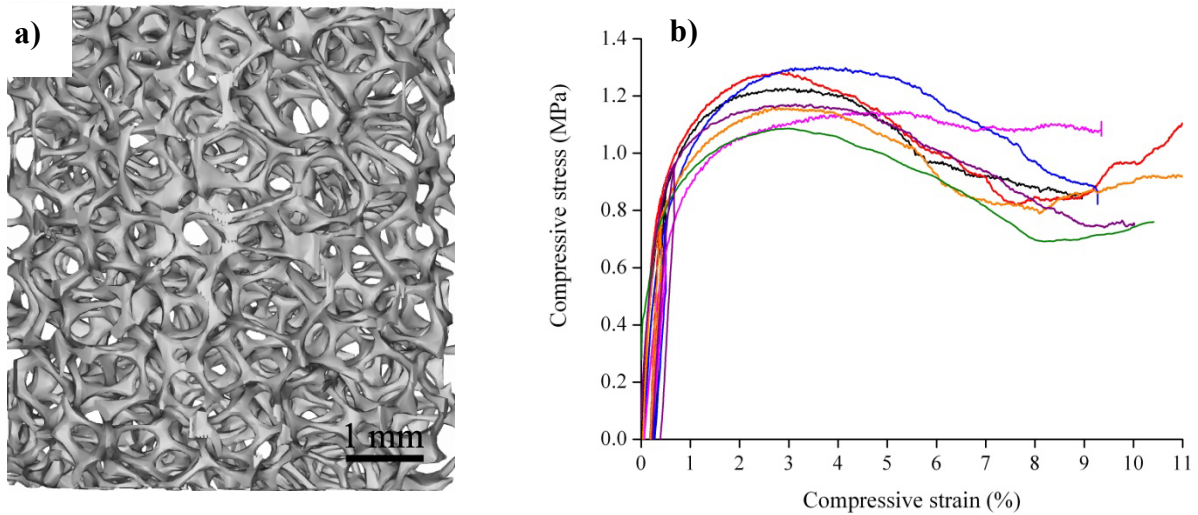


Figure 4.5: 45ppi open-cell AlSi7Mg foam: a) 3D reconstruction of a sample used for the compression test, b) compression behaviour of the foam

Similar to the bovine bones, the deformation mechanism of the AlSi7Mg foam was analysed with an in-situ loading stage. Figure 4.6 shows the mechanical response of the foam with the four deformation points tested in the in-situ loading stage: a) = 0%, b) = yield, c) =  $\sigma_{ult}$  and d) = plastically deformed (approx. 8% strain).

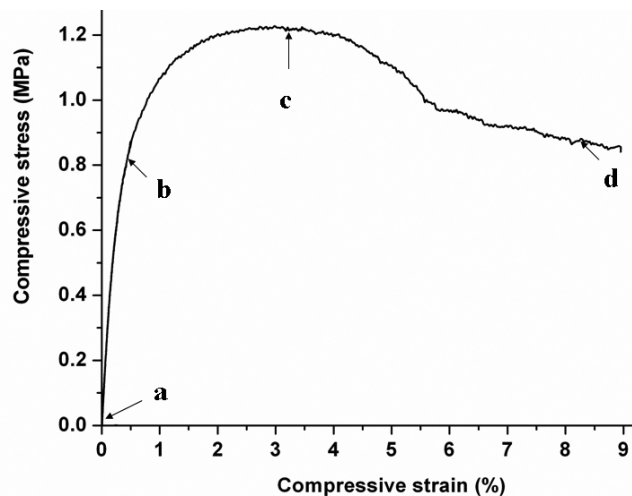


Figure 4.6: Mechanical response of the 45ppi open-cell AlSi7Mg foam with the four deformation points tested in the in-situ loading stage

$\mu$ CT reveals that foams deform by bending in the linear-elastic region and then collapsing by a combination of buckling and brittle fracture (Figure 4.7). The arrows in Figure 4.7 show the evolution of the mechanical deformation of specific cell struts at 0% deformation, yield,  $\sigma_{ult}$  and plastically deformed. Similar to the bones, AlSi7Mg deforms by bending and

buckling (arrows in Figure 4.7a-c). Nevertheless, CT reconstructions of the foam after the stress softening (Figure 4d) show that the cell struts failure is due to both (i) inelastic buckling and (ii) brittle fracture. That can be explained by the cast properties and the irregular strut thickness of the AlSi7Mg foam.

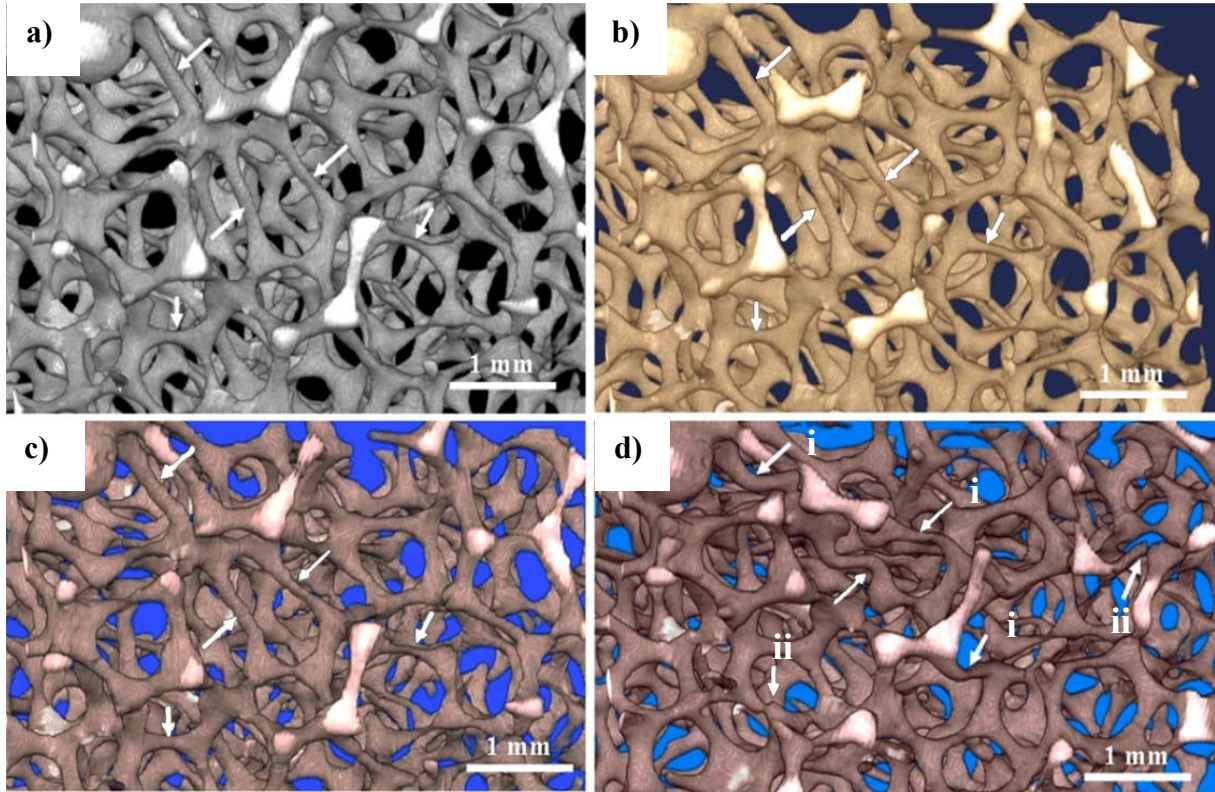


Figure 4.7:  $\mu$ CT-analysis of the deformation occurring during step-wise compression of the 45ppi AlSi7Mg foam: a) at 0% stress, b) at yield, c) at maximum stress, d) plastically deformed

The compressive values of the open-cell foam were lower than those of the cancellous bone; however both materials exhibit similarities in their compression behaviour and deformation mechanisms. The results obtained with the cancellous bone and foam samples are important to understand and compare the mechanical response of these materials with those of the cast Ti-6Al-7Nb porous implants.

## 4.2 Characterization of the cast Ti-6Al-7Nb material

Prior to the development and manufacturing of the porous cast Ti67 implants a characterization of the cast properties of this Ti-alloy was carried out. Small rectangular, grid-shaped and foam samples were used.

The study of the cast Ti67 rectangular and grid samples reveals various types of defects associated with the casting technique and material. Microporosity, inhomogeneous microstructure, entrapment of residues of the investment materials in the surface and  $\alpha$ -case

## Results

were the principal defects observed in the samples. These defects were undesirable as they could potentially affect the design life of implants. Therefore, careful analysis was carried out to understand and subsequently eliminate their influence on the mechanical properties of the samples as much as possible.

### 4.2.1 Microstructural analysis

Cross sectional analysis of the plates and grid-shaped samples reveals that the sample microstructures were formed of three layers: the inner bulk microstructure, a coarse acicular zone and an  $\alpha$ -case layer (Figure 4.8).

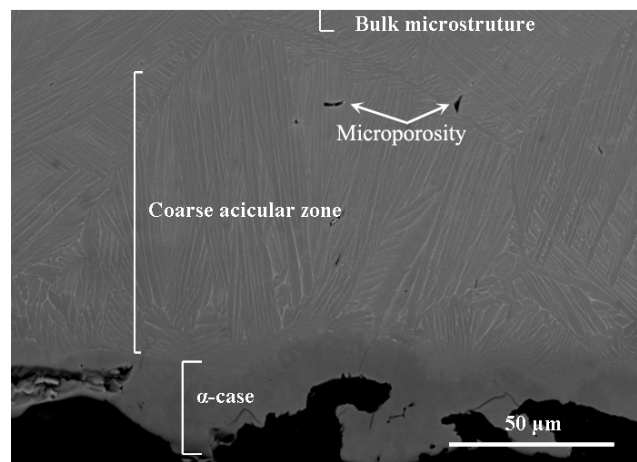


Figure 4.8: SEM micrograph of a Ti67 cast sample

The external layer was identified as to be  $\alpha$ -case with a thickness between 5  $\mu\text{m}$  and 30  $\mu\text{m}$ . This  $\alpha$ -case layer was mainly formed by a reaction between the Ti67 alloy and the aluminium from the investment mold material. To identify the nature of the  $\alpha$ -case layer of the cast TiAl6Nb7 specimen, energy-dispersive X-ray spectroscopy (EDS) and automated electron back-scattered diffraction (EBSD) studies were used. The EDS measurements revealed a chemical composition of the  $\alpha$ -case layer of approx. 74at.% Ti, 23at.% Al, and 3at.% Nb (Figure 4.9). Additionally, analysis of the crystallographic structure of the surface layer revealed a fine-grained outer zone of hexagonal  $\text{Ti}_3\text{Al}$  corresponding to the  $\alpha$ -case layer (Figure 4.10).

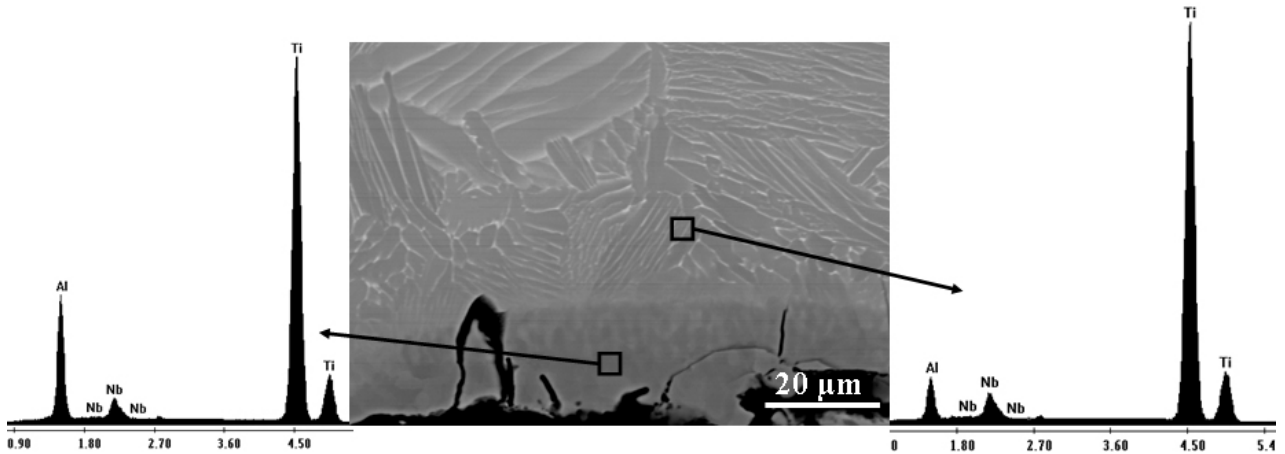


Figure 4.9: SEM micrograph with two EDS spot analyses of the chemical composition of the  $\alpha$ -case and the coarse acicular zone, respectively, revealing the high Al concentration in the outermost zone

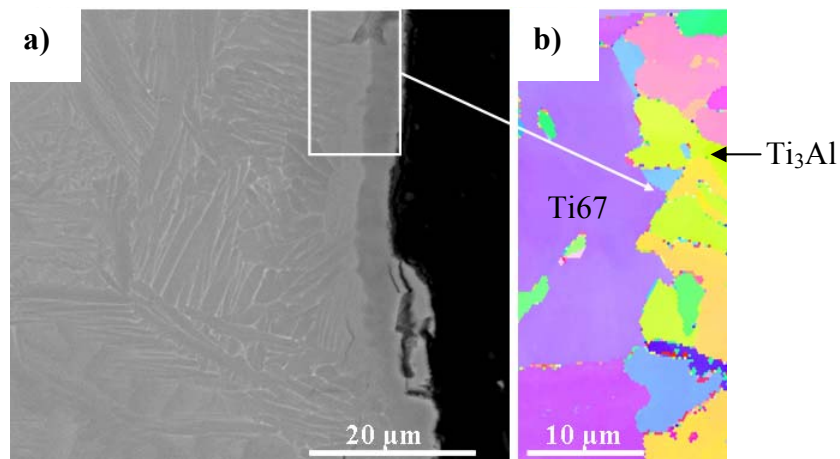


Figure 4.10: a) SEM micrograph of a cast Ti67 sample and b) corresponding EBSD orientation mapping of the interface between the fine grained  $\alpha$ -case layer and the coarse acicular  $\alpha+\beta$  Ti structure

Underneath the  $\alpha$ -case layer, a coarse acicular Widmanstätten microstructure was found. The acicular zone was having a thickness between 20 μm and 50 μm and consists of  $\alpha$ -Ti laths formed within a  $\beta$ -Ti matrix. The core of the samples which had bulk microstructure with fine plates follows the acicular layer. The grain size of the bulk microstructure was found to be  $163\pm 54$  μm in grid-shaped and plate samples. It was observed that the grain size of thinner samples was smaller than that of the thicker samples. Due to the reduced thickness of the grid-shape samples a clear distinction between the bulk microstructure and the acicular zone was not observable in every sample. That results in the formation of a highly heterogeneous microstructure in samples with just 2 or three grains in thickness.

The different properties of the  $\alpha$ -case layer, the coarse acicular layer and the bulk zone were confirmed by measuring the Vickers microhardness profile across the sample. The

## Results

results are shown in Figure 4.11. While the microhardness of the  $\alpha$ -case was determined to be about 800 HV, in the bulk microstructure the hardness drops down to about 350 HV.

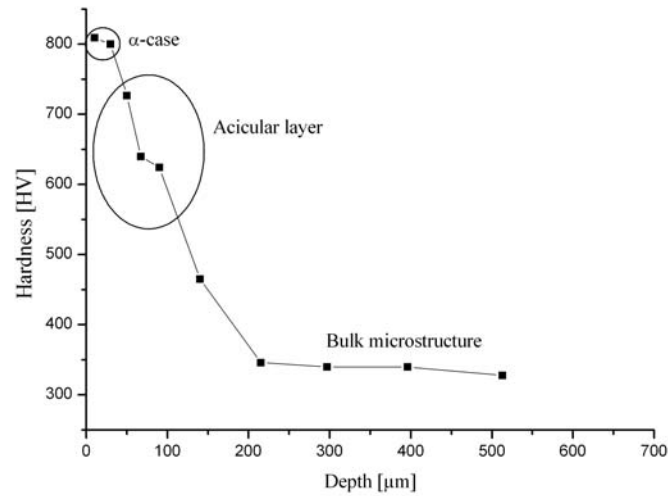


Figure 4.11: Vickers microhardness vs. distance from the surface in a cast Ti67 specimen

The coarse acicular layer exhibits intermediate hardness value of about 620 HV. This increase in hardness can be partially attributed to the rapid cooling at the mold surface during casting ("hardening layer", cf. [252]) or to an increase in the concentration of dissolved oxygen, which is known to strongly embrittle Ti alloys.

### 4.2.2 Removal of the $\alpha$ -case

From the measurements and analysis of the  $\alpha$ -case, it can be concluded that this layer comprises approx. 1-5% of the overall cross-sectional area of the specimens. Hence, the  $\alpha$ -case mass percentage to be eliminated was estimated as to be 5% of the sample gross mass.

Figure 4.12 exhibits the results of the gravimetric analysis of the mass loss during pickling of the cast Ti-6Al-7Nb samples in  $\text{HNO}_3$ +HF acid solution assisted by ultrasonic vibration. The initial cleaning behaviour can be considered as linear, but after 60-70 min of pickling the slope of the curve decreased. This reduction of the pickling speed can be considered as a signal of complete  $\alpha$ -case elimination. The percentage of mass loss at this point was around 10% of the sample mass. The unexpected high mass loss is due to the additional removal of investment residues from the casting process.

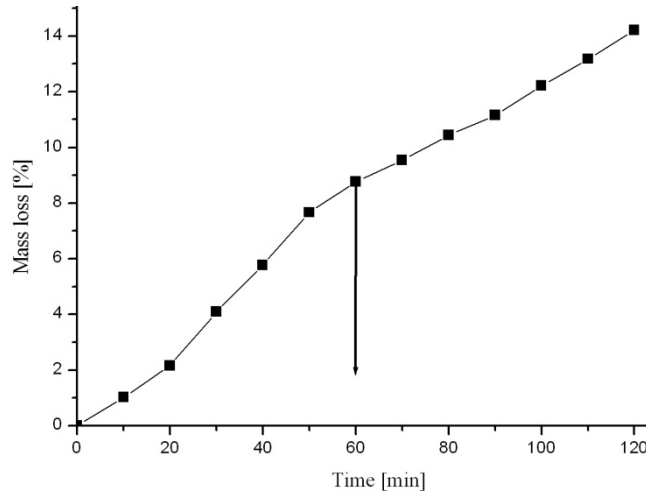


Figure 4.12: Gravimetrically measured mass loss during pickling

Surface examination by SEM was carried out in order to observe the progress of pickling attack. Figure 4.13 shows the specimen surface after four different times of pickling. Figure 4.13d reveals clearly that after 70 min the surface of the sample was completely cleaned. That supports the gravimetric measurements concerning the complete elimination of  $\alpha$ -case after around 60-70 min of pickling.

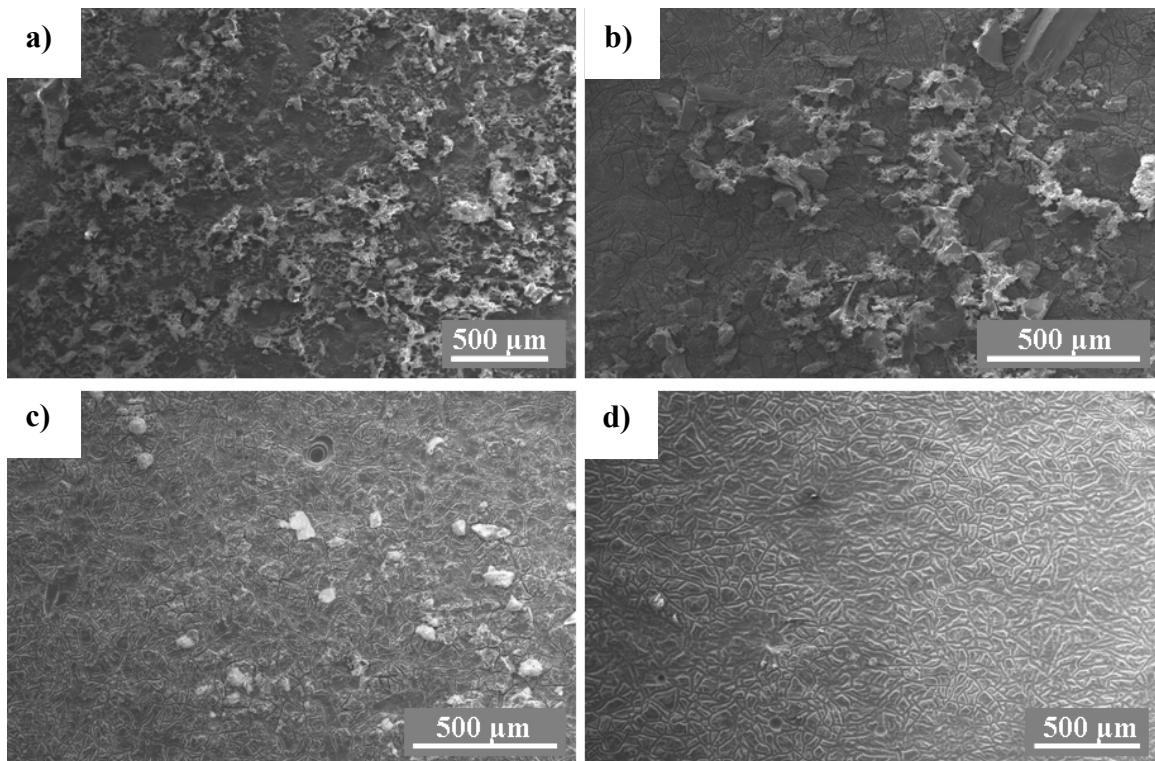


Figure 4.13: Specimen surface after: a) 0 min, b) 20 min, c) 40 min, d) 70 min of pickling

Figure 4.14 illustrates the pitting corrosion effect which was the predominant mechanism of material removal from the samples by pickling. However, one interesting phenomenon that occurred during pickling was the gradual reduction of the pitting corrosion effect on the

## Results

sample's surfaces with increasing pickling time. As Figure 4.14a shows, pitting corrosion is significantly high after 20 min of pickling. However, pitting corrosion marks and cracks are not acceptable since they act as nuclei for fatigue crack formation leading to premature failure of the structure. After 40 min in contact with the acid bath the specimen still was highly affected by pitting corrosion, but as Figure 4.14b shows, the loci of pitting corrosion marks are replaced by a kind of “worm marks”. These worm marks were growing during the progress of pickling until they cover the complete surface after around 60-70 min (cf. Figure 4.14c). Unlike to the pitting cracks, the worm marks do not exhibit sharp edges (see figure 4.14d) which can initiate cracks under mechanical loading conditions. Hence, the worm marks are of significant importance for the improvement of surface characteristics, i.e., reduction in surface roughness and elimination of the brittle surface layer.

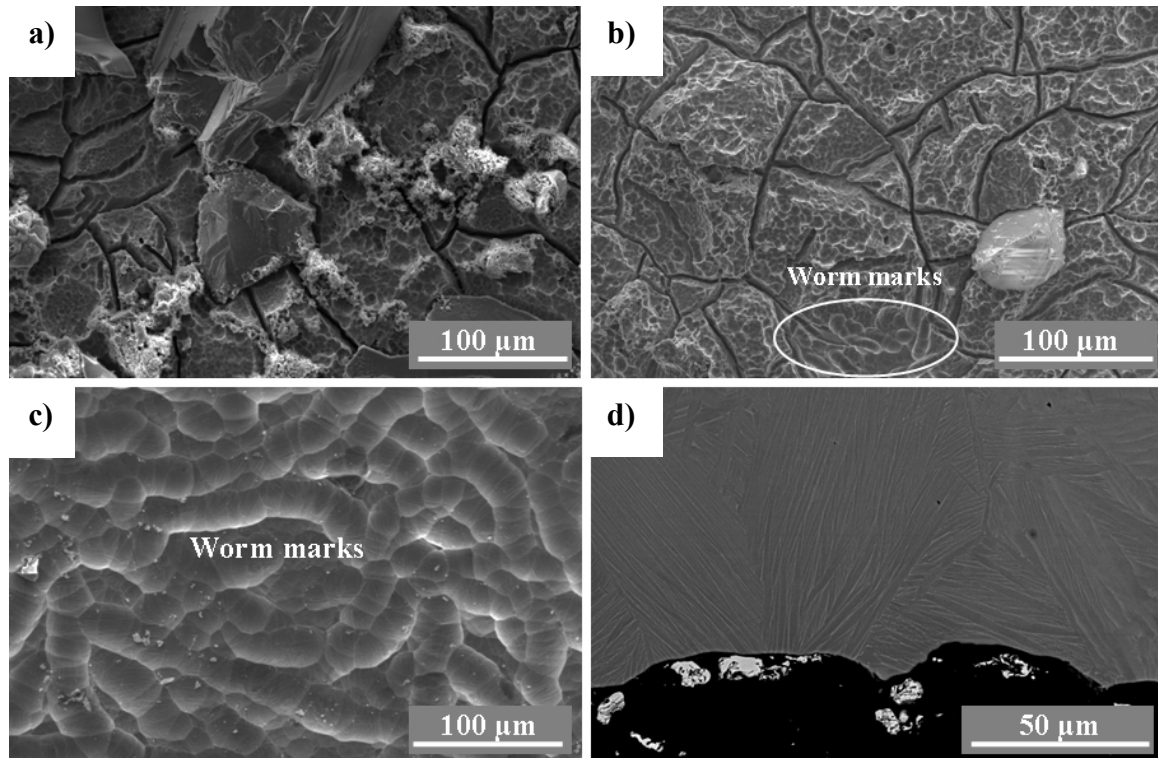


Figure 4.14: Pitting corrosion after: a) 20 min, b) 40 min, c) 60-70 min of pickling, and d) cross sectional SEM micrograph after 60-70 min of pickling

Surface roughness analysis was carried out before and after the acid attack. Not-pickled samples showed maximum roughness values of about  $R_{\max}=44.72 \mu\text{m}$  with an arithmetic average of the absolute roughness value of approx.  $R_a=5.47 \mu\text{m}$ . After 70 min of pickling, the values dropped to  $R_{\max}=8.84 \mu\text{m}$  with a  $R_a=1.01 \mu\text{m}$ .

### 4.2.3 Effect of heat treatment and pickling on the mechanical properties of the cast Ti-6Al-7Nb samples

Grid-shaped samples and Ti67 sponges were analysed before and after the homogenization of the microstructure by heat treatments. After the heat treatment, the  $\alpha$ -case was removed from the samples. The effect of the homogenization of the microstructure and the removal of the  $\alpha$ -case on the mechanical properties of the samples was characterized by compression and bending tests.

Figure 4.15 shows the compression behaviour of a cast Ti-6Al-7Nb sponge. Because of the very limited specimen dimensions, the compression test was not performed according to DIN 50134 [246]. Consequently, the results obtained cannot be considered as representative of the general compression behaviour of the Ti67 sponges. Nevertheless, with these results it was possible to recognize the critical brittleness of the sponges that needs to be analysed more in detail. Therefore, further compression-bending tests were focused on the grid-shaped samples.

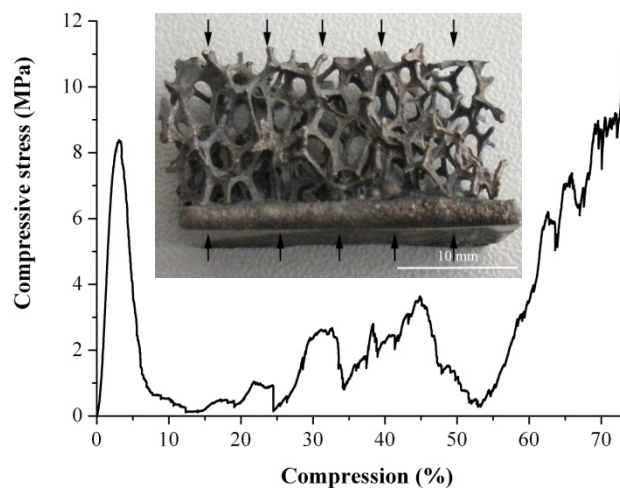


Figure 4.15: Stress vs. compression curve of Ti67 sponge

The stress vs. compression curve in Figure 4.15 shows that the ultimate compression strength of the Ti67 sponge is about 8.3 MPa, but once the compression strength is reached, the compression stress dropped to a value of almost 0 MPa. Subsequently, the stress increased again, but contrary to other ductile materials, e.g. open-cell AlSi7Mg foam (cf. section 4.1.3), an obvious stress plateau regime was not observed.

Fracture surface analyses support the observation of brittle behaviour of the Ti67 sponge. This behaviour was mainly observed in the sections of the cell struts containing  $\alpha$ -case. These sections exhibit cleavage-like fracture of the lamellar microstructure. Figure 4.16 shows a SEM micrograph representing the fracture surface of a cell strut after compression testing.

## Results

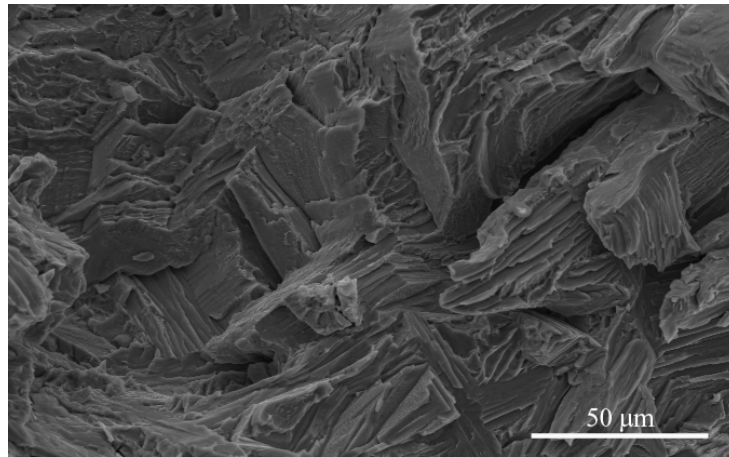


Figure 4.16: SEM micrograph of the fracture surface of a Ti67 sponge after compression testing

The combination of heat treatments to homogenise the microstructure with a removal process to dissolve the  $\alpha$ -case of the samples were considered as suitable means to improve the mechanical behaviour that was revealed during the compression tests. In order to eliminate the influence of geometry variations in sponge specimens, grid-shaped samples produced by an identical casting process were used to study the improvement of the mechanical properties by heat treatment and pickling processing.

The aim of the heat treatment was the improvement of ductility of the cast material. Heat treatment results were analysed using hardness tests and compared with the hardness of the samples without treatment which was approx. 370 HV. Samples after annealing above the  $\beta$ -transus (1060°C) for 1 hr and furnace cooling showed the worst results. Hardness of these samples was approx. 550 HV. These samples present very brittle behaviour which results in the failure of the samples during the mounting procedure, consequently the evaluation of the mechanical strength of the samples treated at 1060°C was impossible.

The brittle behaviour of the grid-shaped samples treated at high temperature can be explained due to the small thickness of the samples. This dimension may induce the precipitation of an  $\alpha$ -phase that extends through the thickness of the grid-shape and plate samples.  $\alpha$ -Phase forms principally on the grain boundaries that lead to the formation of  $\alpha$ -phase grains around the reduced  $\alpha+\beta$  colonies. One reason of the formation of this  $\alpha$ -phase is because of the oxygen content of the furnace chamber. Even if the treatment were performed under argon atmosphere, the system was not completely isolated. That allows small amount of incoming air that reacts with the Ti67 surface and produces this brittle microstructure. Figure 4.17 shows a cross sectional microstructure of a grid-shaped sample annealed at 1060°C for 1 hr. Samples annealed at 1060°C show a small grain size of  $105\pm 23$   $\mu\text{m}$ , perhaps due to the strong  $\alpha$ -phase formed around the grain boundaries.

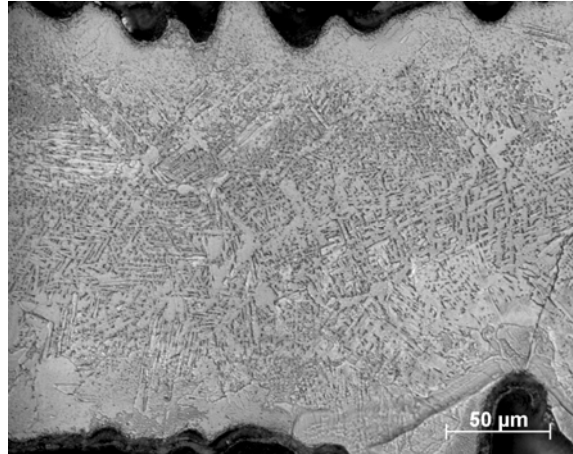


Figure 4.17: Cross section microstructure of a grid-shaped sample after annealing at 1060°C for 1 hr

Samples aged at 600°C for 4 hr and samples annealed at 870°C for 1 hr show the best results. Hardness of samples annealed at 870°C was about 320 HV. Aged samples present a hardness of approx. 340 HV and homogeneous microstructure. Figure 4.18 shows the cross sectional microstructure of a plate sample which exhibits a grain size of  $116 \pm 23 \mu\text{m}$ . The grain size of the aged samples shows low variation with respect to the grain size after the heat treatment at 870°C.

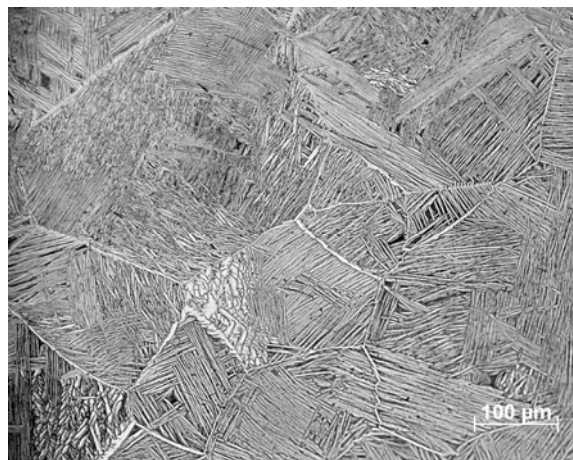


Figure 4.18: Microstructure of a cast Ti67 sample aged at 600°C for 4 hr

In order to complement the hardness test, a bending test was used to evaluate the improvement of the mechanical properties of the grid-shaped sample after the heat treatments. Before bending the samples were subdivided in two groups: samples of group 1 were aged at 600°C and samples of group 2 were annealed at 870°C. Finally both groups of samples were acid pickled in order to remove the brittle  $\alpha$ -case.

Results of the bending tests are presented in Figure 4.19. Although the samples annealed at 870°C for 1 hr showed the lowest hardness after heat treatment, bending tests showed that these samples exhibit poor mechanical strength. In Figure 4.19 one can observe that the

## Results

samples aged at 600°C exhibit the best combination of high strength and ductility. Additionally to the samples aged at 600°C for 4 hr, other samples were aged for 60 hr. Bending results of these samples show further ductility improvement with aging time, but a reduction of the strength of the samples was observed. This can be explained by the effect of oxide layer formation or by the increase of the  $\alpha$ -case layer thickness formed during the heat treatment. Samples with thicker  $\alpha$ -case layer suffer from a more pronounced reduction of thickness after acid cleaning and consequently, they show less strength compared to the samples aged for 4 hr during bending test.

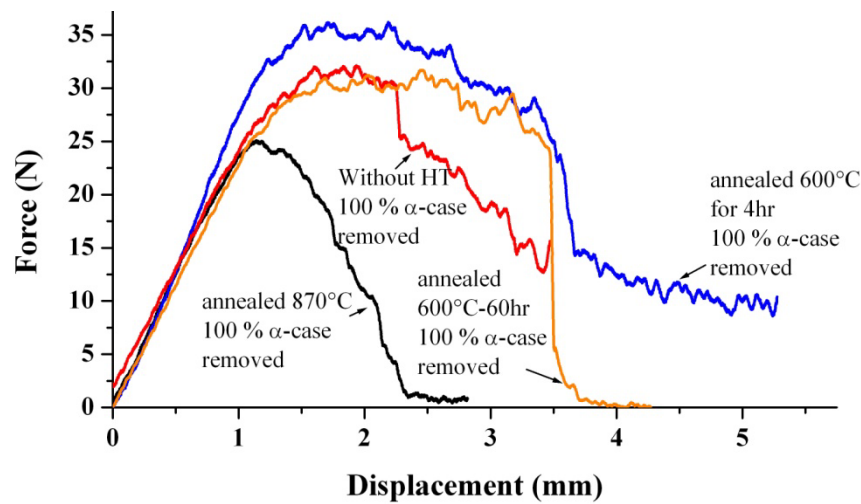


Figure 4.19: Uniaxial-bending test of heat-treated and acid-cleaned samples

### 4.2.4 Cast Ti-6Al-7Nb porous implants

Surface properties and morphology of the implants were analysed in detail to understand their role in the osseointegration process and in the amount of bone tissue growth inside the implants. The shape of the rat implants can be seen in Figure 4.20. The implants have various irregularities with respect to shape and surface. These imperfections can be attributed to the casting technique and to the subsequently pickling process applied to the implants.

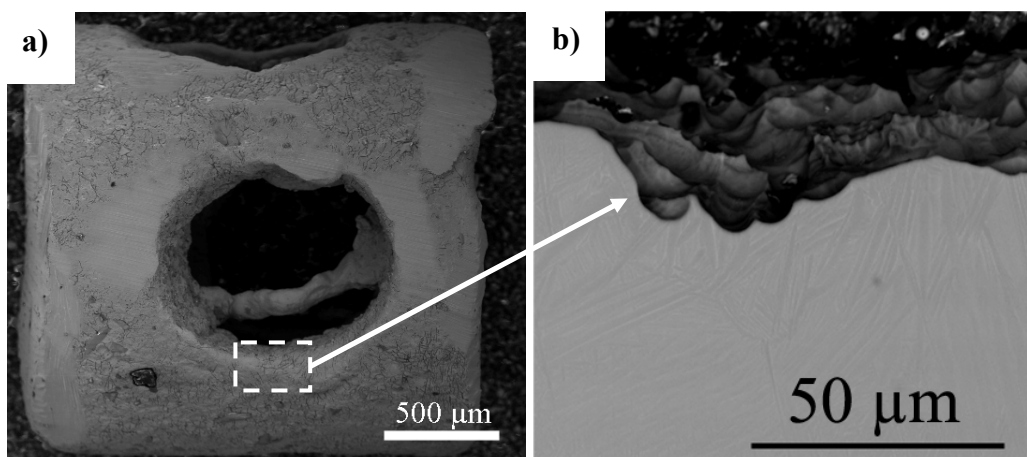


Figure 4.20: a) Pickled rat implant, b) surface details of the implant at the border of the implants holes

The surface of the rat implants show similar roughness as the grid-shape and plate samples after pickling ( $R_{\max}=8.84 \mu\text{m}$  with a  $R_a=1.01 \mu\text{m}$ ). However, the borders of the implant holes show roughnesses of approx.  $R_{\max}=26.55\pm 12 \mu\text{m}$  with a  $R_a=3.35\pm 1 \mu\text{m}$  (Figure 4.20b). The complete external and internal surfaces of the implants were covered by the worm marks discussed above. They are mainly responsible for the roughness found in the implants. It was noticed that some regions were mechanically milled or/and ground prior to the pickling process (Figure 4.20a). These regions did not show any change in the roughness before and after the chemical milling ( $R_{\max}=0.81\pm 0.20 \mu\text{m}$  with a  $R_a=0.19\pm 0.13 \mu\text{m}$ ). Therefore, it can be thought that the surface condition of a sample before pickling affects the final roughness results. This phenomenon was confirmed by a test in which two samples with different surface conditions were pickled applying the same procedure. Figure 4.21 shows that the sample with prior grinding exhibits lower mass loss than the cast sample without any prior mechanical milling. Additionally, no worm marks in regions that have previously been ground were found. This result validates the theory that the acid milling is more active in regions of the sample with  $\alpha$ -case than in regions without this layer, e.g. mechanical milled.

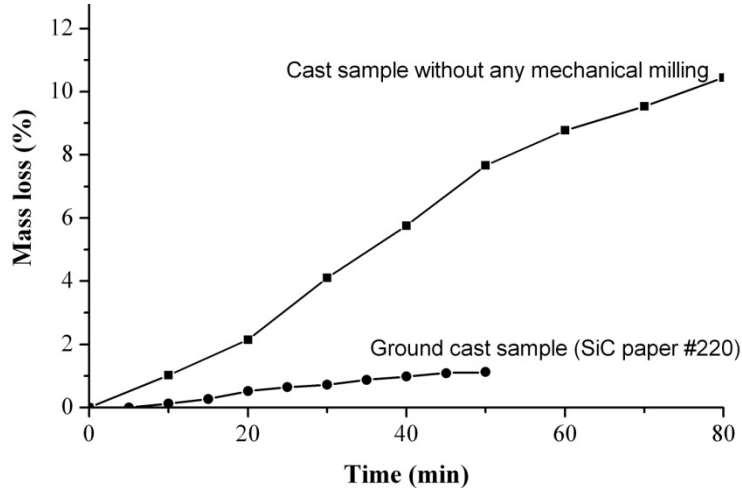


Figure 4.21: Gravimetric measurements of the mass loss during pickling of cast Ti67 samples without any prior mechanical milling and cast Ti67 samples ground with an abrasive paper

The rat implants show a relative density value of  $\rho_r=61\pm 4\%$  which is higher than the maximum  $\rho_r$  commonly accepted for a cellular material ( $\rho_r=30\%$ ) [209]. The porous implants exhibit interconnected holes of approx. 1 mm of diameter which are bigger than the dimensions suggested by Ryan et al. [6] for the optimum porosity in a cellular implant. The rat cell spacing (Tb.Sp.) of  $234\pm 131 \mu\text{m}$  and a strut thickness (Tb.Th.) of  $90\pm 78 \mu\text{m}$  are also much smaller than the holes of the implants. Therefore, attention was placed in the post-

## Results

operative biomechanical test to observe the influence of the pore sizes in the bone tissue ingrowth.

Mechanical tests reveal that rat implants failed at a compressive nominal strength of  $184.2 \pm 74.4$  MPa. This stress is much higher than the ultimate compressive strength found for the rat cancellous bones ( $\sigma_{ult} = 1.82 \pm 1.24$  MPa) [253]. Due to the small loads applied to the implants inside the rat femur, no deformation of the implants may be expected.

The Young's module values of the rat implants are  $21.26 \pm 5.82$  GPa. This value is 334 times higher than the values of the rat cancellous bones ( $E = 63.6 \pm 55.1$  MPa) [253]. This huge difference of the values of  $E$  between implant and cancellous bone can cause stress-shielding phenomena if the implants stay inside the bones for a long time [49]. However, the implants remained into the rat bones only for 30 days; therefore no stress-shielding was expected in the bone-implant interfaces.

This consideration was taken into account for the further design of the ovine implants. These implants must stay inside the bone for approx. 6 months. Therefore, the Young's modulus of the implants should be reduced by decreasing the relative density of the porous implants.

Figure 4.22 shows the ovine implant and its final surface condition prior to the coating process. These implants were mechanically milled to obtain a diameter of  $9.7 \pm 0.1$  mm. This implant accuracy was suggested by the Labor für Experimentelle Unfallchirurgie, JLU Gießen in order to reduce the influence of the diameter on the histomorphometric and biomechanical results. Internal micro-porosities in the surface were exposed after the mechanical milling. The implants were then pickled to remove the  $\alpha$ -case of the internal and struts surfaces. The external surface of the ovine implants shows no worm mark and consequently no change of the roughness before and after acid milling ( $R_{max} = 0.82 \pm 0.17$   $\mu\text{m}$  with a  $R_a = 0.17 \pm 0.13$   $\mu\text{m}$ ). The internal surface of the implants and the surface of the cells and struts show the presence of worm marks and a roughness similar to that found for the rat implants.

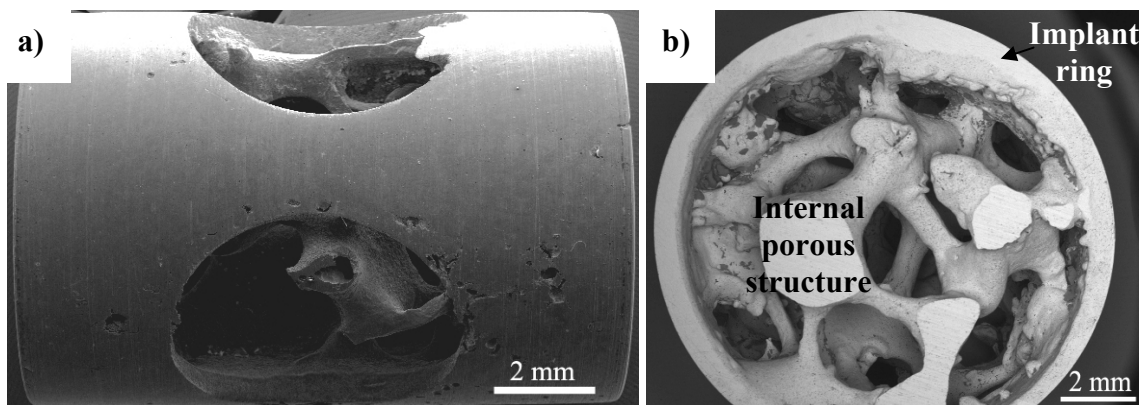


Figure 4.22: a) Ovine implant after mechanical and chemical milling, b) cross section of the implant

The internal cellular structure of the implants was developed to improve the bone tissue ingrowth and osseointegration of the implant. The ovine implants show a relative density value of  $\rho_r=30\pm 1\%$  which is the limit of the  $\rho_r$  commonly accepted for a cellular material ( $\rho_r=30\%$ ) [209]. The ovine implants show cell spacing of  $1674\pm 704\ \mu\text{m}$  and strut thickness of  $595\pm 205\ \mu\text{m}$  while the ovine cancellous bones exhibit a cell spacing of approx.  $520\text{-}7670\ \mu\text{m}$  and a plate thickness of  $163\pm 50\ \mu\text{m}$ .

The implants were compression tested horizontally (Figure 4.23) because this was the position that the implants occupied inside the distal femoral metaphyses. Inside the femur, the implants need to resist the main loads at this position. These results were compared to the compression analysis of the ovine cancellous bone tested in the MTD. The implants show a  $\sigma_{\text{ult}}=49\pm 6\ \text{MPa}$  and an  $E = 5010\pm 1098\ \text{MPa}$  (Figure 4.23). The value of the implant strength is satisfactory as it is high enough to resist the internal loads of the ovine cancellous bones ( $\sigma_{\text{ult}}=10.45\pm 3.46\ \text{MPa}$  and an  $E=825.33\pm 388.3\ \text{MPa}$ ). The Young's modulus of the implants is 23 times lower than the tensile Young's modulus of the Ti-6Al-7Nb ingot material (116 GPa). A considerable reduction of the stress-shielding phenomena in the implants-bone interface is therefore expected.

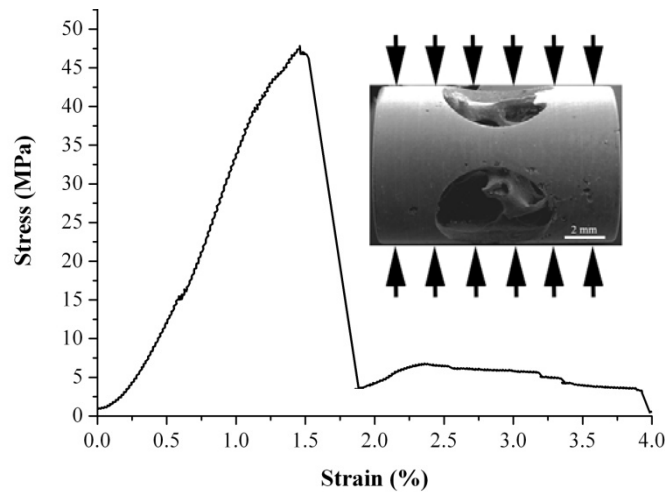


Figure 4.23: Compression behaviour of an ovine implant

During the compression test it was observed that the stresses were mainly carried by the external ring of the implants. However, the internal cellular structure of the implant may help in an internal distribution of the applied loads through the implant.

After the fabrication and properties optimization of the cast Ti67 implant, bioactive calcium titanate layers for coating the implant surfaces were applied and studied.

### 4.3 Characterization of calcium titanate reaction layer

A calcium titanate ( $\text{CaTiO}_3$ ) reaction layer was applied to the implant surface to alter the surface energy and surface composition with the aim of improving the bone-implant interface properties. In this work, a calcium salt-melt method was used by the BAM, Berlin, for changing the surface of the Ti67 samples to form a Ca containing surface.

This investigation was carried out with pickled plates and grid-shaped samples which were coated for 2 hr in a salt bath. Figure 4.24 shows the micrographs of the four coatings investigated in this work. Coating SBI formed at  $350^\circ\text{C}$  was hardly visible. Figure 4.24a exhibits a fissured layer over the worm marks which was recognized as the Ca-Ti layer by the EDS examination. The sample coated with SBII ( $410^\circ\text{C}$ ) shows small crystals (Ca-Ti) that cover discontinuously the surface of the sample (Figure 4.24b). Samples coated with the SBIII ( $450^\circ\text{C}$ ) show an evident increment in the amount in the Ca-Ti crystals (Figure 4.24c). These crystals grow in diameter and join with the neighbouring crystals until the complete surface of the samples was covered. The samples coated with SBIV ( $510^\circ\text{C}$ ) exhibit the highest concentration of Ca-Ti crystals which extend on the complete surface of the samples (Figure 4.24d). Some regions with the coating SBIV seem to be oversaturated with the Ca-Ti crystals.

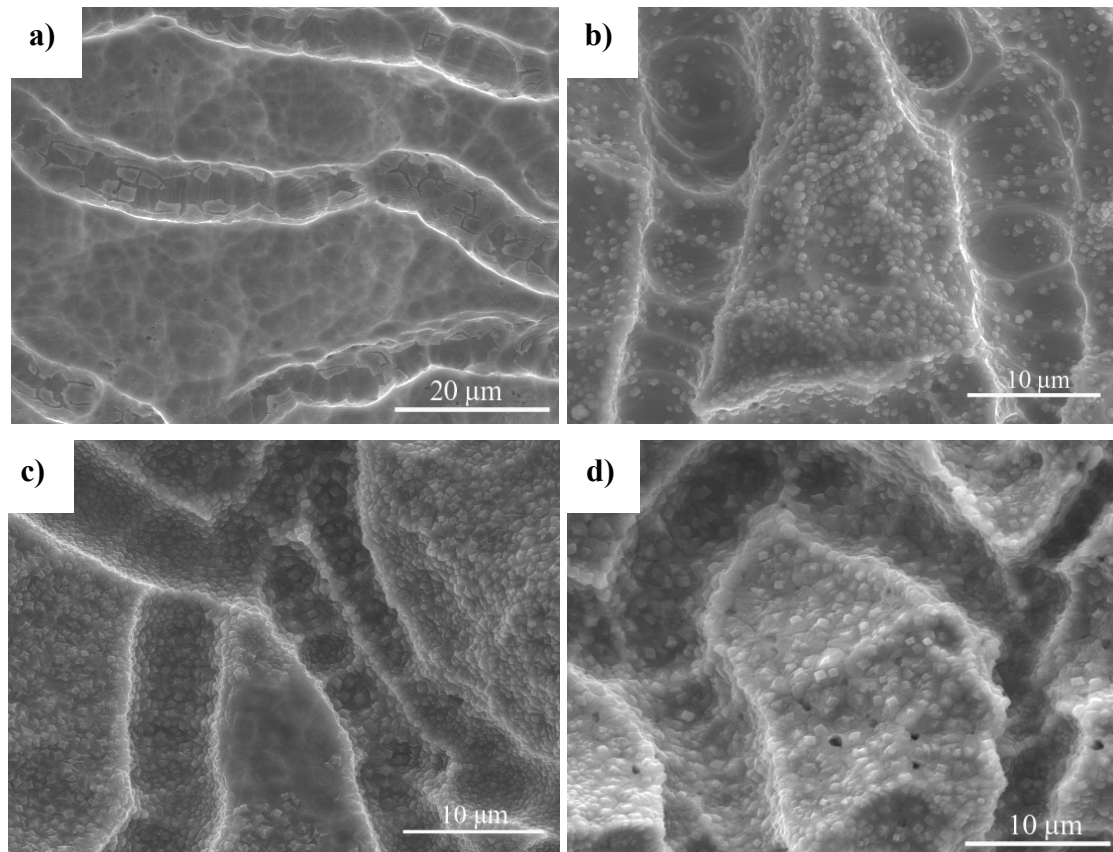


Figure 4.24: Sample surfaces coated with: a) SBI, b) SBII, c) SBIII and d) SBIV

Thicknesses of the reaction layers were analysed by a cross sectional examination in the SEM. To avoid coating spallation during the cross-sectional preparation, each sample was sputtered with gold, and subsequently a Ni layer was electrochemically deposited. Figure 4.25 shows the cross-sectional microstructures and thicknesses of the reaction layers. SBI shows a very thin thickness of approx. 5-20 nm. SBII shows a thickness of  $516 \pm 178$  nm. The layer thickness of the sample with coating SBIII is  $1000 \pm 420$  nm, while the SBIV shows a thickness of  $1200 \pm 395$  nm. The thicknesses of these coatings are very similar compared to those obtained in other work with the same procedure applied to Ti-6Al-4V [254].

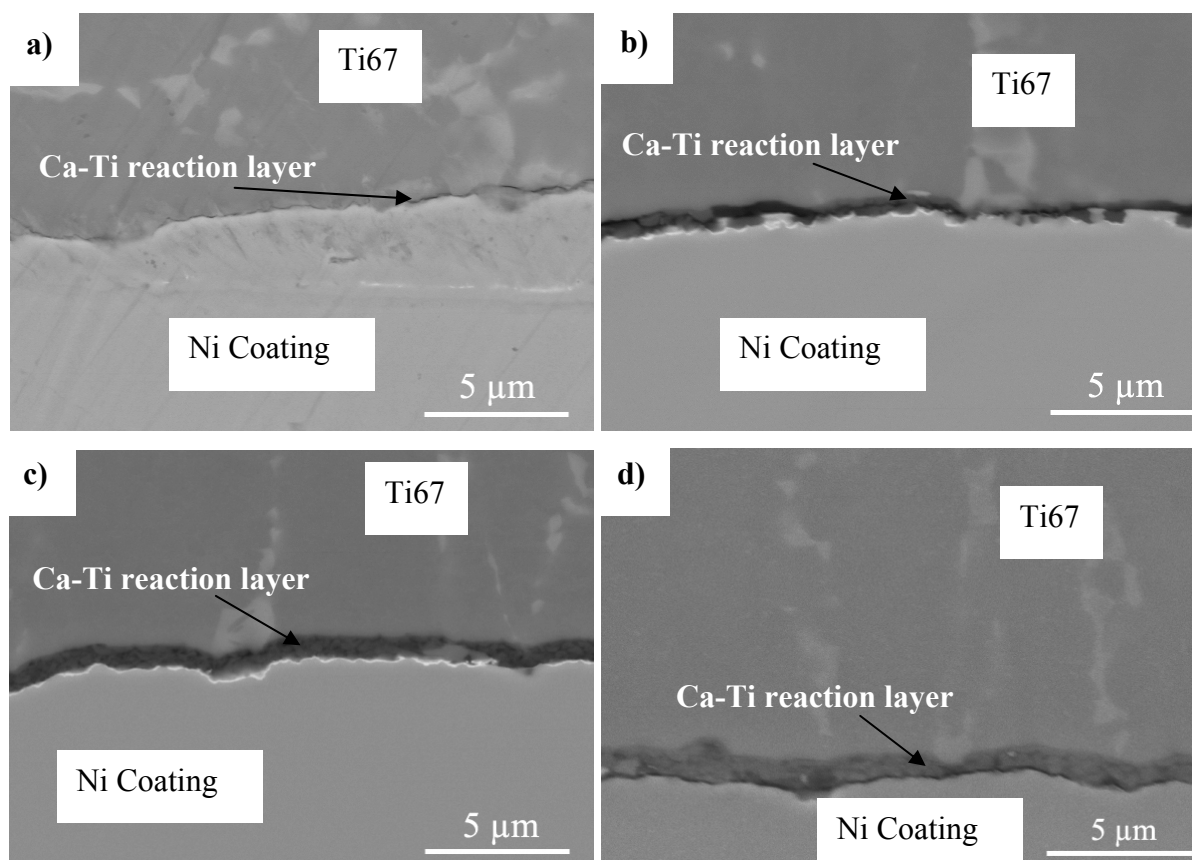


Figure 4.25: Cross-sectional micrograph of the Ca-Ti reaction layer: a) SBI, b) SBII, c) SBIII and d) SBIV

#### 4.3.1 Corrosion-bending behaviour of the reaction layer

To analyse the behaviour of the reaction layer under similar condition as in the body, coated grid-shape samples were mechanically tested in Ringer's solution which is usually utilized as simulated body fluid. Ringer's solution has similar corrosive properties than the blood in the body and therefore it was used as electrolyte for the corrosion test. Corrosion analysis that involves open-circuit potential (OCP) measurements was used to monitor possible microdamage in the reaction layers during the bending test.

## Results

Prior to the corrosion-bending test, the open-circuit potential of the uncoated cast Ti67 samples without any load was analysed (Figure 4.26). Voltage increased parabolically from -600 mV at time 0s to a steady state value due to oxidation. This steady-state was identified as the passivation of the samples by the formation of a TiO<sub>2</sub> layer.

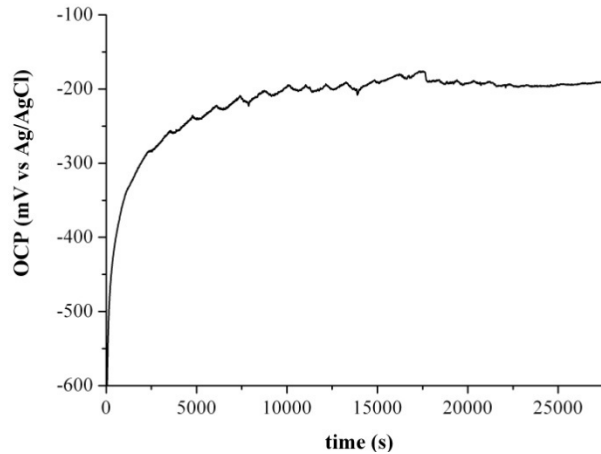


Figure 4.26: Open-circuit potential of a cast Ti67 uncoated sample

Under the discussed conditions, the OCP steady-state of the cast Ti67 samples was reached at a time of approx. 10 000 seconds with a constant voltage of approx -190 mV. For the coated samples the passivation voltage varied between -150 mV to -100 mV. This voltage variation can be attributed to the different chemical composition and amount of the coating on the surface of the samples.

After finding the passivation voltage and time for the coated samples, they were fixed in the cyclic bending system. This test was carried out between a maximum load of -2 N and a minimum load of -15 N at 5 Hz until the grid-shaped samples failed in order to perform the test under complete compressive loading conditions. Figure 4.27 shows the displacement response of the grid-shaped samples with a SBIII reaction layer (coated at 450°C for 2 hr). This behaviour was very similar to that found for the samples coated with the other coating layers. The results reveal cyclic creep of the sample during the first 200 cycles, and then the sample shows almost no change in the mechanical response until the failure at ~5000 cycles. On the basis of the mechanical deformation response, no indication of damage evolution could be detected.

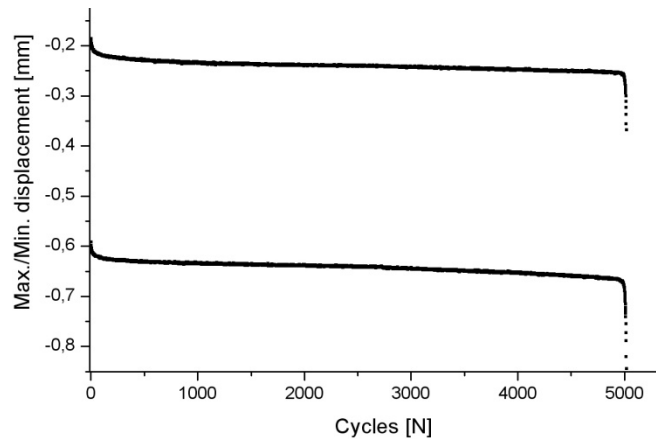
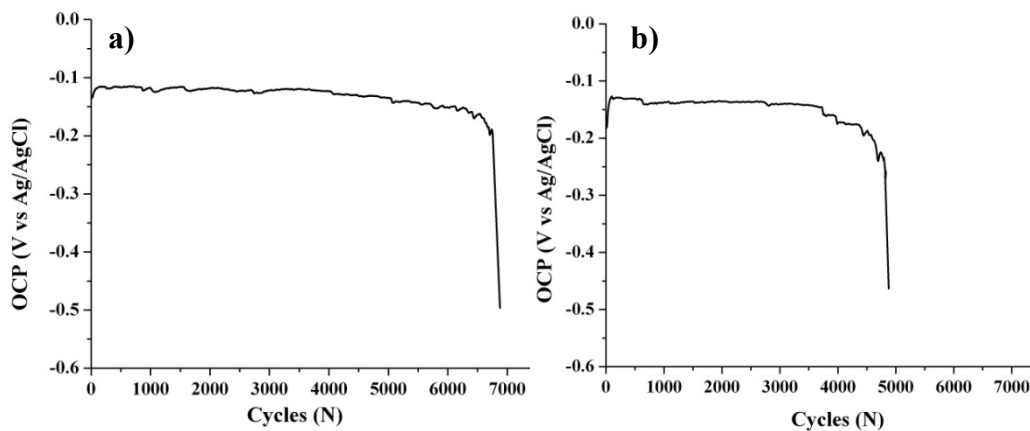


Figure 4.27: Cyclic displacement behaviour of a sample coated with SBIII

While the displacement response of the samples was unable to detect any surface damage e.g. delamination of the coatings, the OCP measurement was found to be more sensitive with respect to microchanges that occur on the coating layers. Figure 4.28 shows the OCP curves of the coated samples. Initially, the OCP reaches a steady-state after the passivation process and keeps this potential until the test was completed or an alteration of the electrochemical system occurs. A drastic drop of the OCP occurs at failure of the grid samples. That suggests that bending cracks on the sample surface were created and then they were exposed to the electrolyte which results in new oxidation at these regions. The drops of the OCP during the test were often observed in the analysis of the SBIII and SBIV coated samples. Taking into account that the samples being affected by this behaviour had the thickest and most homogeneous reaction layers, OCP drops were associated with a probable delamination or flaking of the reaction layer due the effect of bending load conditions. Consequently, microstructural examination of the surrounding areas of the bending cracks of all the tested coated samples were carried out.



Results

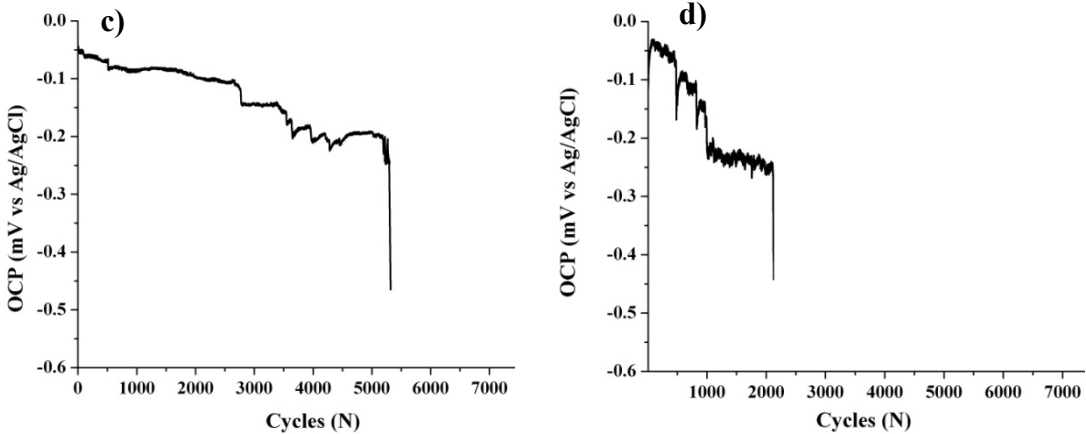


Figure 4.28: OCP curves of the coated samples: a) SBI, b) SBII, c) SBIII and d) SBIV

The fracture analysis of the cyclic-bending samples shown in Figure 4.29 was carried out in a SEM. While SBI and SBII coated samples exhibited very few delamination near the cracks, SBIV samples documented a significant loss of the coated layer. The coating spallation on these samples may be due to delamination of the coating crystals which was produced by the bending forces applied to the samples. On the other hand, it may be also possible that the cast Ti67 sample surface (not the coating) have loose small pieces of the material in the vicinity of the cracks. Consequently, the surrounding coating of these zones delaminated with these pieces.

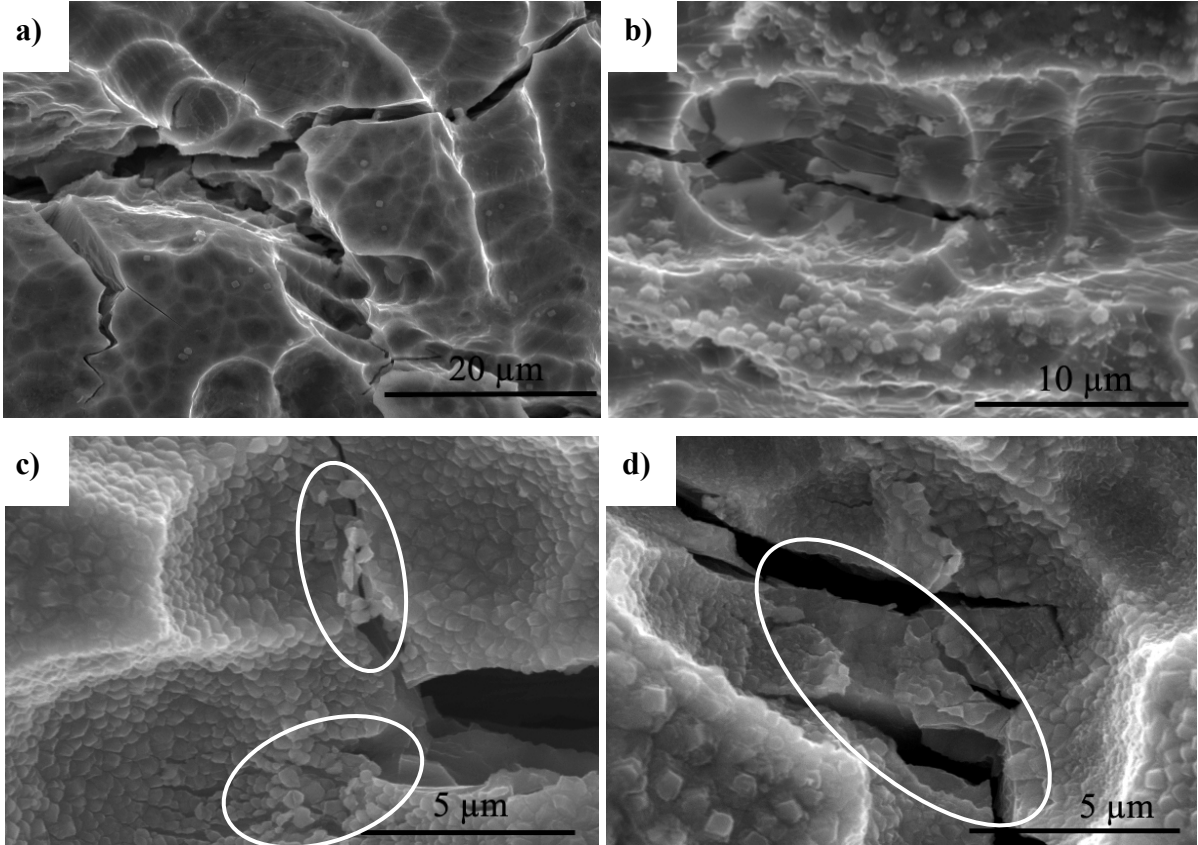


Figure 4.29: Micrograph of the coated samples after the cyclic bending test: a) SBI, b) SBII, c) SBIII and d) SBIV

### 4.3.2 Fretting behaviour of the reaction layer

In order to confirm the nature of the behaviour of the coatings during the bending analysis, fretting tests on the coated samples were carried out. A sphere of CP (commercially pure) Ti with a diameter of 3 mm was used to compress the coatings with a force of approx. 1.5 N. After adjusting the test force, the sphere was displaced cyclically with an amplitude of 4 mm. The aim of this test was to analyse the behaviour of the Ca-Ti crystals in contact with another surface at very small loads. Every sample was tested for approx. 200 cycles with a frequency of 3 Hz and then the coatings were analysed using SEM.

Figure 4.30 shows the micrographs of the coating after the friction test where the arrows represent the direction of the friction test and the discontinued lines correspond to the friction area. No delamination of the coatings or brittle-failure of the Ca-Ti crystals was observed after this test. Samples coated with SBII to SBIV exhibit flattened crystals, however no detachment of the crystal was observed.

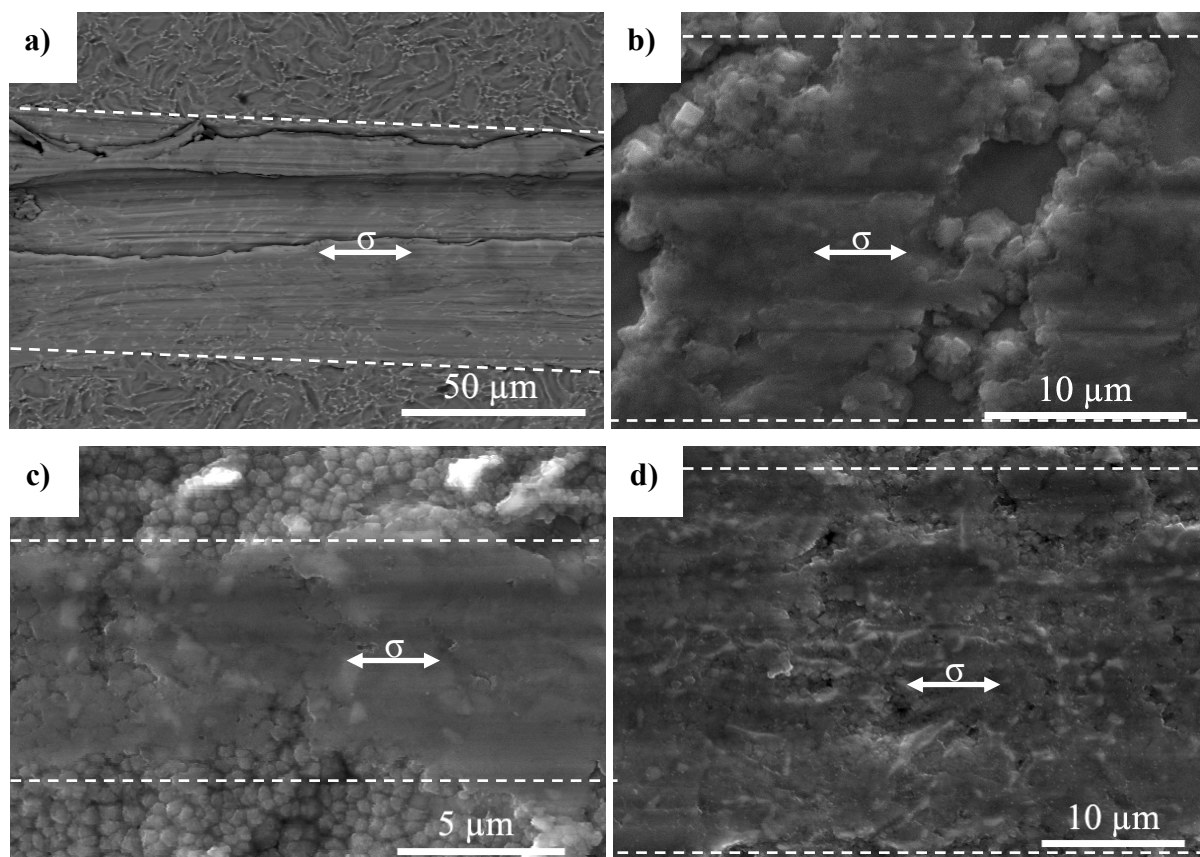


Figure 4.30: SEM micrograph of the coatings after the friction test: a) SBI, b) SBII, c) SBIII, d) SBIV

The absence of delamination or spallation during the friction test may support the theory that the delamination observed during the bending test occurs due to the loosening of small pieces of the cast Ti67 sample surface and not due to spallation of the reaction layer.

## Results

Because of the superior mechanical and corrosion behaviour of SBI coating and based on the previous clinical experiences [254], the coating SBI was selected to be used on the rat and ovine implants. This coating possesses a low thickness and good mechanical properties and is expected to provide an adequate surface energy and promote osseointegration of the implants. Additionally, the samples coated with SBI showed the best results during the cell culture analysis carried out at the Labor für Experimentelle Unfallchirurgie, JLU Gießen. Cell culture experiments reveal that the maintenance and proliferation of the animal cells on the samples coated with SBI was superior to that of the samples with other coatings.

### **4.4 Post-operative biomechanical analysis**

To test the biological and osseointegration behaviour of the porous cast Ti-6Al-7Nb implants, they were implanted in rats and sheep. The aim of these experiments was to analyse the biocompatibility properties of the cast Ti67 material, the influence of the porous implants on the osseointegration process and to compare the effect of the coated and the uncoated implants. For this work, the implants reside for a sufficient predetermined period in the animals, then they were sacrificed to analyse the osseointegration and the bone ingrowth with push-out tests and SEM analyses.

#### **4.4.1 Post-operative biomechanical analysis of the rat implants**

The implantation was carried out in 12 rats followed by a healing time of 30 days. These rats were divided in two groups: one group of 6 rats were operated with implants coated with SBI and the other group of 6 rats were operated with uncoated implants. One animal died directly after the implantation. Therefore, this specimen was taken as rat with 0 days after the operation (from now called specimen 0) and used as reference to compare its biomechanical behaviour with the behaviour of the other rats which recovered for 30 days (details of the rat operation procedure are presented in appendix A).

Figure 4.31 shows the cross sectional structure of a rat distal femoral metaphysis with the approximate position of the implants (discontinued line). During the operation, the implants were positioned in an area which was mostly formed of rod-like cancellous bone. It was expected that this type of bone will grow around and inside the implants.

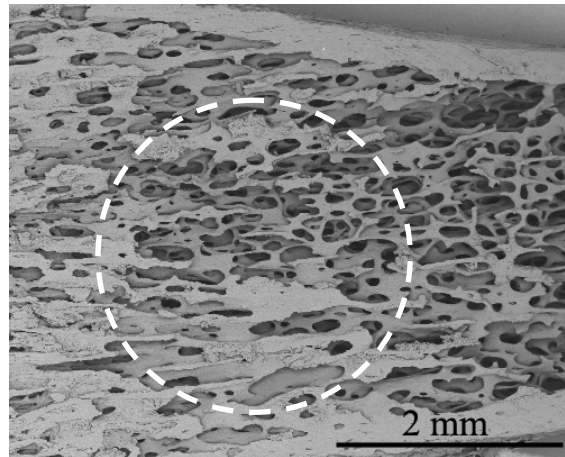


Figure 4.31: Cross sectional structure of a rat distal femoral metaphysis with the approximate position of the implants

After the euthanasia of the rats, the distal femoral metaphyses with the implants were extracted from the rats and prepared for the biomechanical test. To evaluate the osseointegration of the bone-implant a self-designed push-out system was utilized. Figure 4.32 shows the push-out force-displacement behaviour of the coated (Figure 4.32a) and uncoated implants (Figure 4.34b). The push-out behaviours of both specimen groups were compared with those of the specimen 0 (discontinued curve).

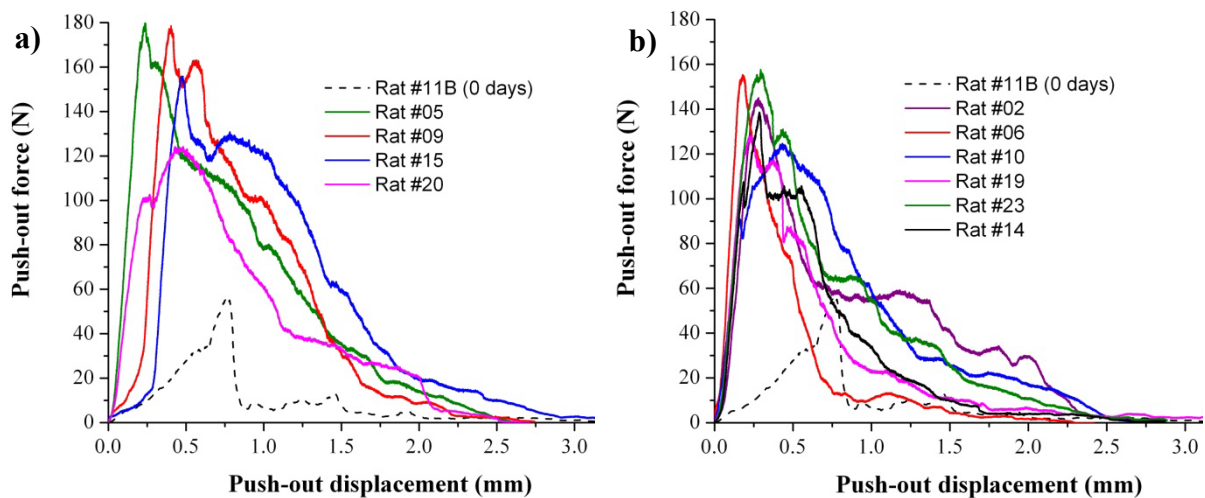


Figure 4.32: Push-out behaviour of the a) coated rat implants, b) uncoated rat implants

The maximum push-out force, which is the shear load necessary for the bone-implant interface failure, was analysed. Another value obtained from this test is the absorbed energy of the bone-implant interface which is measured as the integral of every push-out curve. The specimen 0 shows a push-out force of 57 N which was very low in comparison with those of the specimens after 30 healing days. The push-out force of the uncoated implants was 2.5 times higher compared to the specimen 0 ( $140 \pm 14$  N) while the push-out force for the coated implants was 2.8 times higher than the specimen 0 ( $160 \pm 26$  N). On the other hand, the

## Results

absorbed energy of the specimen 0 was 28.3 mJ. The absorbed energy of the uncoated implants was  $101 \pm 25$  mJ (3.6 times higher compared to the specimen 0) while the absorbed energy of the coated implants was  $147 \pm 17$  mJ (5.2 times higher compared to the specimen 0). The improvement in the mechanical behaviour of the implants with 30 healing days was associated to the osseointegration and new bone ingrowth effect. Push-out values of all the specimens are presented in appendix B.

The coated implants show slightly better biomechanical results than those of the uncoated implants. It was not clear if the reaction layer plays a relevant role of the improvement in the osseointegration and in the bone ingrowth. Therefore, SEM was used to analyse the bone ingrowth and the bone on the implant surfaces. Figure 4.33 shows the micrographs of a coated and of an uncoated rat implant after the push-out test. The bone marrow and bone fat were previously eliminated. SEM analysis reveals remains of cancellous bone, dried soft tissue and residues of amorphous tissue on the surface and inside the implants. Cancellous bone was principally found inside as well as surrounding the holes of the implants.

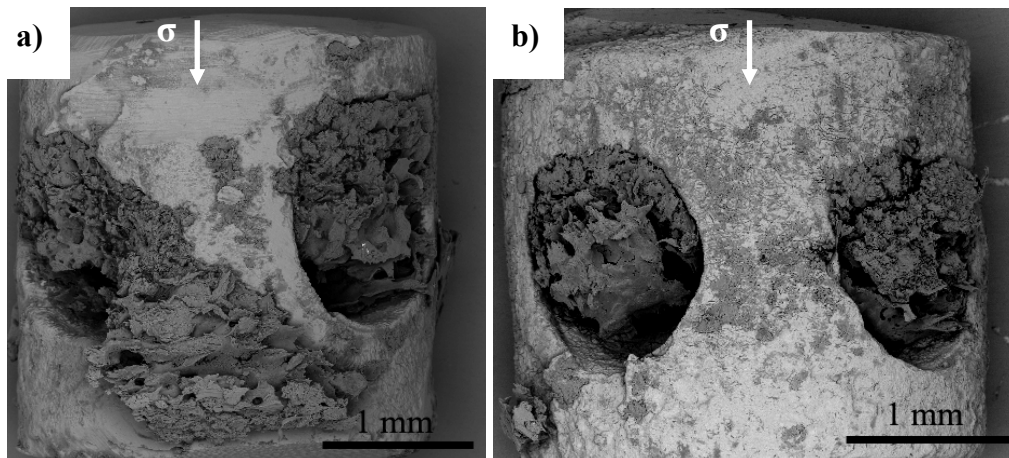


Figure 4.33: SEM micrograph of the rat implants after push-out test: a) coated implant, b) uncoated implant

SEM analysis of coated implants shows higher amount of bone tissue bonded to the implant surface compared to the uncoated implants. However, the bonded bone was observed in few regions surrounding the implant holes (Figure 4.33a). Uncoated implants show no presence of cancellous bone at its external surface, but residues of amorphous bone and granulation tissue were found in some surface regions (Figure 4.33b).

EDS analysis on the implant surfaces shows amorphous bone apposition which is a calcium-phosphate component of the mineral bone together with the crystalline apatitic bone [255]. This amorphous bone was only found in some regions of the implants. No evidence of bone material was found in the regions with a previous mechanical milling while regions with higher roughness show evidently higher amount of bone apposition. Interestingly, worm

marks provide a kind of grooves along which the deposition of amorphous bone follows and finally these marks help to form clusters of amorphous bone (Figure 4.34).

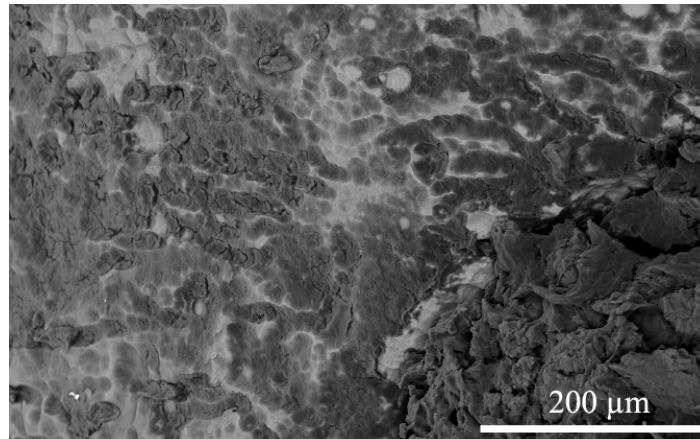


Figure 4.34: SEM micrograph of the amorphous bone deposited on the worm marks

Inside the holes of the implants, the trabeculae were found deformed in opposite direction of the push-out test. The trabeculae initially deform by bending and fail principally due to shear and rupture. Figure 4.35 shows a SEM micrograph of a failed bone trabecula that exhibits some curvature and damage in the central section of the rod. The end of this trabecula reveals a torn-like rupture similarly to other trabeculae surrounding it.

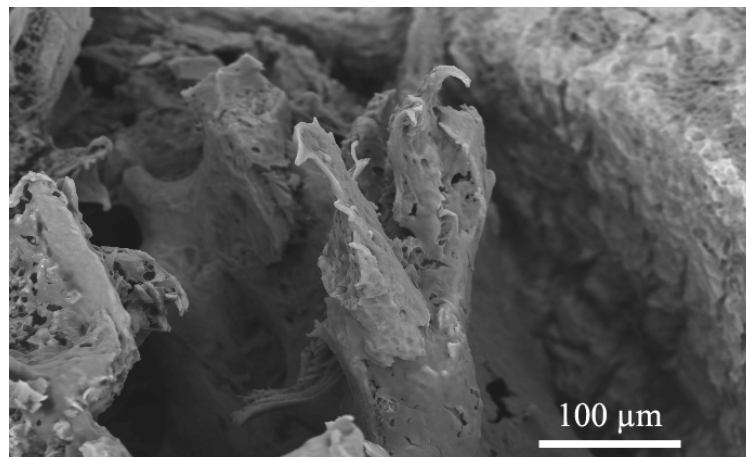


Figure 4.35: SEM micrograph of a failed trabeculae located in the holes of the implants

#### 4.4.2 Post-operative biomechanical analysis of the ovine implants

For this work, 12 sheep were operated and received the implants for six months (details in appendix C). 6 sheep received implants coated with the SBI and 6 sheep receive uncoated implants.

Similar to the rat experiments, the ovine implants were located in the distal femoral metaphysis.  $\mu$ -CT analysis in Figure 4.36 shows that the implants were surrounded by cancellous bone which has plate-shape structure. The implantation was carried out manually,

## Results

consequently the implants were found at different position of the distal femoral metaphysis. These positions differed in the amount of cancellous bone surrounding the implants. Additionally, the manual implantation results in misalignment of the implant. During the operation, the top side of the implant was positioned in the cortical bone side (external darkest area on Figure 4.36a and b but some implants were positioned below the cortical bone side. That permit that cortical bone grows and covers the top of the implant.

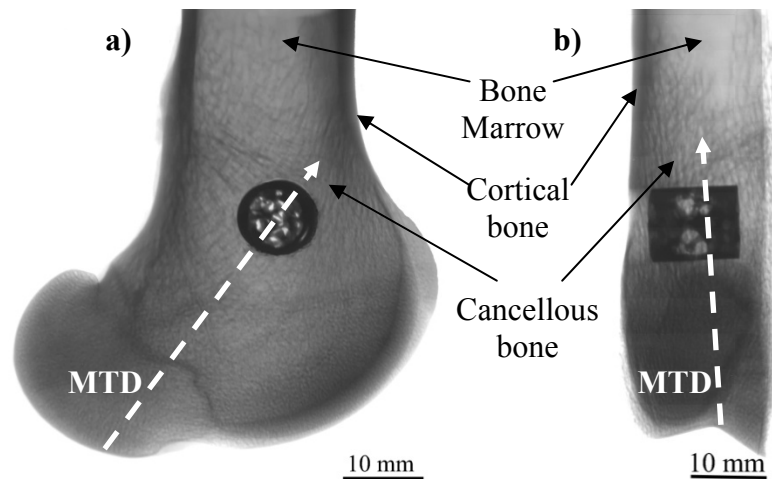


Figure 4.36:  $\mu$ -CT pictures of the ovine distal femoral metaphysis with implants a) frontal view, b) lateral view

After the euthanasia of the sheep and preparation of the distal femoral metaphysis with implants, they were analysed with X-rays in order to find the inclination angle of the implants. Both lateral and frontal view of each implant were analysed. Figure 4.37 shows an example of this procedure. After measuring the inclination angle, the samples were perfectly aligned in the direction of the push-out indenter by using a self made system.

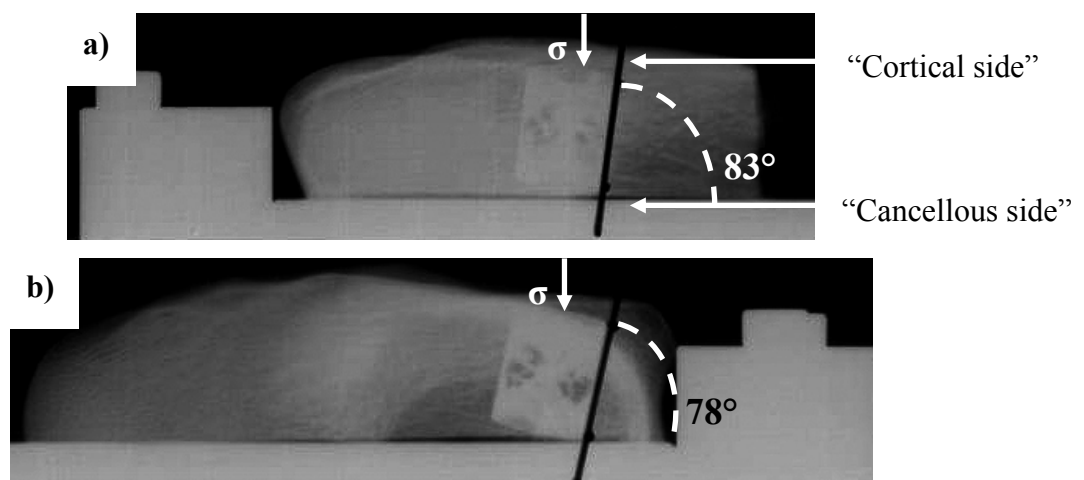


Figure 4.37: Example of the inclination angle of the ovine implant: a) lateral position, b) front position of the push-out system

All the sheep survived the operation and therefore no specimen “0” was available to study the improvement of the osseointegration and bone ingrowth with time. The push-out test results exhibit no considerable difference between the coated and uncoated implants (Figure 4.38). The coated samples show a push-out force of  $1419 \pm 494$  N and an absorbed energy of  $3993 \pm 2274$  mJ while the uncoated samples show similar values with a push-out force of  $1362 \pm 529$  N and an absorbed energy of  $3614 \pm 1556$  mJ.

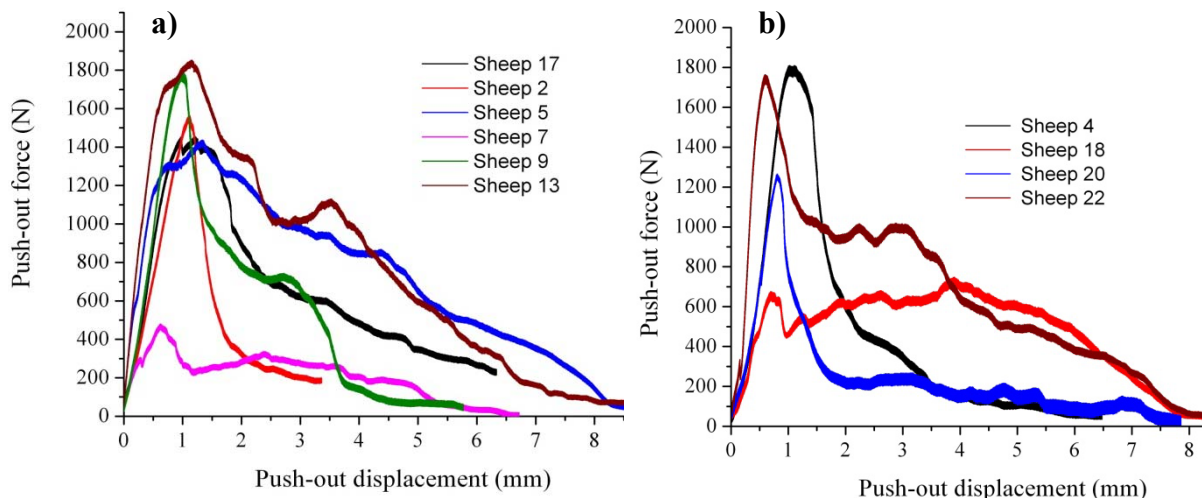


Figure 4.38: Push-out behaviour of the a) coated ovine implants, b) uncoated ovine implants

Coated and uncoated implants exhibit similar push-out values. However, both groups of implants show two push-out curves with very low values. Push-out result of sheep #7 (coated implants) and of sheep #18 (uncoated implants) reveal very low values. A possible explanation of these low values can be the age of these two animals. At the euthanasia, sheep #7 was 95 months old and sheep #18 was 86 months old. Both sheep were older than the other sheep (details in appendix D) and therefore the bone growth activity of the sheep #7 and sheep #18 might be lower. Another explanation may be that the implants of these animals occupied a position in the distal femoral metaphysis with reduced amount of cancellous bone. In this case, less cancellous growth inside the implants is expected and consequently that can reduce the push-out values.

After the push-out test, the implants were carefully cut along the length and then the fat and bone marrow were removed in order to examine the bone that grew inside the implants. Stereoscopy analysis shows no cancellous bone inside the implants of the older sheep (Figure 4.39a) while the implant of a younger sheep shows a high amount of cancellous bone in the holes and from the “cancellous side” to the top of the implant (Figure 4.39b). The lower side of the implant was in direct contact with the cancellous bone while the upper side was in direct contact with the cortical bone. The soft material found at the “cortical section” of the implant was identified as granulation tissue and rest of cartilaginous tissue (Figure 4.39).

## Results

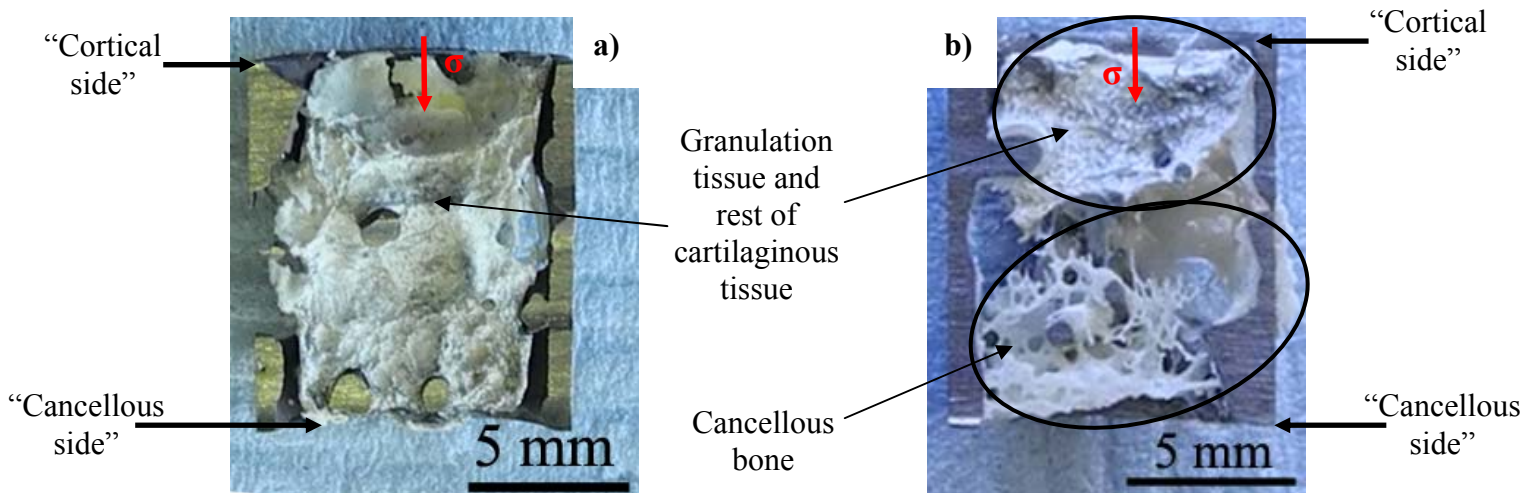
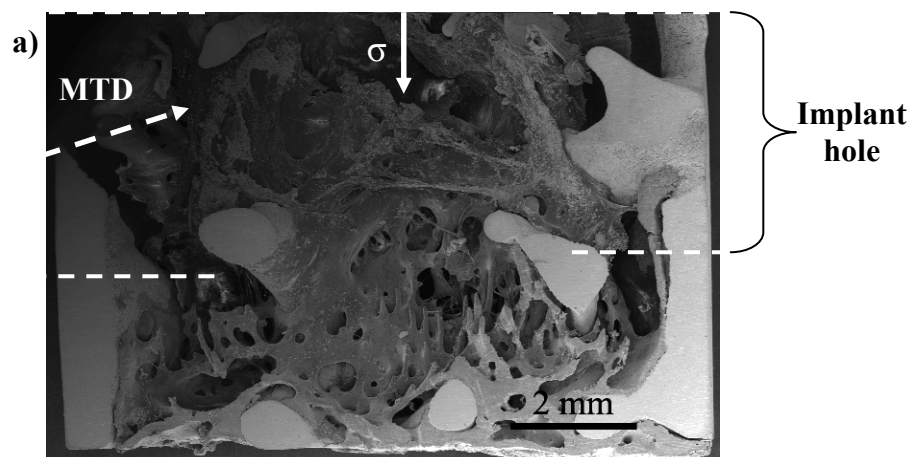


Figure 4.39: Bone ingrowth in the implants of the sheep a) old sheep #7 (95 months old), b) young sheep #22 (49 months old)

Figure 4.40 shows the SEM microstructure of the implants of the sheep #5 (58 months old) and sheep #22 (49 months old) and the main directions where the bone grows inside the implants. It was found that not only the bone grows from the “cancellous side” but also from the MTD and through the implant holes. The amount of cancellous bone found in the holes depends highly on their alignment with respect to the MTD. In the case of the implants with one of the holes perfectly aligned to the MTD, the highest amount of cancellous bone ingrowth from this hole through the diameter of the implants was observed. The cancellous bone found in the boundaries of the hole and in the border of the lower side (cancellous side) of the implant was thicker than those found inside the implants. Cancellous bone inside the implants shows a rod-like structure with a trabeculae spacing (Tb.Sp.) of  $532 \pm 232 \mu\text{m}$  and a trabeculae thickness (Tb.Th.) of  $120 \pm 50 \mu\text{m}$  (Figure 4.40b and c). These values are lower in comparison with those found for the plate-like cancellous bone that surrounded the implants. This indicated that the loads inside the implant are much lower than the loads found at its external surface.



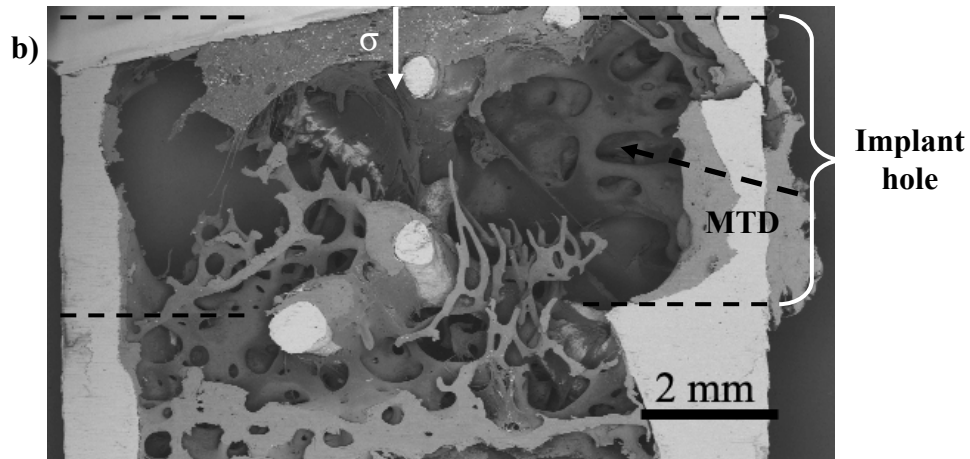


Figure 4.40: SEM internal micrograph of the implant: a) sheep #5 and b) sheep #22

The external surface of the implants shows a very limited osseointegration with the exception of the areas around the holes (Figure 4.41a). This limited osseointegration can be explained due to mechanical milling applied to these implants before the operation of the sheep. The consequently reduced roughness is considered prejudicial in the formation of the bone-implant interface. On the other hand, the internal surface of the implant show high osseointegration. In the vicinity of the implants, three forms of tissue were found: 1) cancellous bone, 2) granulation tissue and 3) cartilaginous tissue. Figure 4.41b shows that the bone with the forms 2 and 3 grows around the surface of the internal struts.

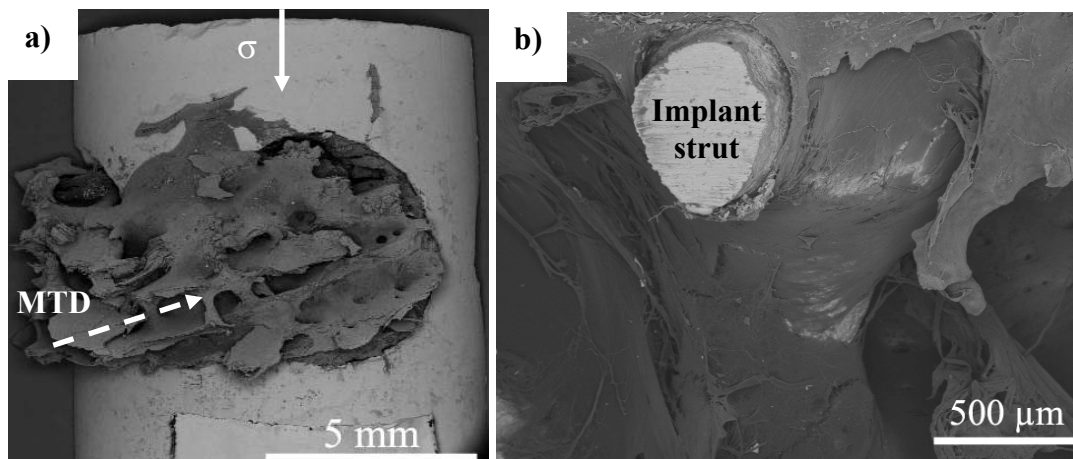


Figure 4.41: SEM micrograph of the ovine implants after the push-out test: a) external surface of the implant of the sheep #2, b) surface at the internal implant strut of the sheep #22

The failure mode of the cancellous bone showed in Figure 4.41a was typically found in all the cancellous bones that grow inside the holes of the implants. However, this cancellous bone ingrowth was not always found in all the implants. Cancellous bone deforms by bending and fails by shear at its weakest section and at the regions where the new cancellous bone was not completely mature. The MTD plays an important role in the cancellous bone ingrowth and

## Results

in the strength of this new cancellous bone. It was noticed that the new cancellous bone around the implants which grew in direction to the MTD (see Figure 4.36b and Figure 4.41a) were stronger than the bone located at the opposite site of the implants.

## 5 Discussion

This chapter discusses the results observed in chapter 4, with principal focus on:

- (1) The compression properties of the ovine and bovine cancellous bone as well as the behaviour of the 45ppi open-cell AlSi7Mg foam are considered. This section compares the compressive behaviour of cancellous bones, of the AlSi7Mg foam and the behaviour of the porous cast Ti-6Al-7Nb implants used in rat and sheep experiments.
- (2) the microstructure and surface properties of the Ti-6Al-7Nb material are analysed to understand their influence on the mechanical behaviour of the porous cast implants. The influence of the morphology and mechanical properties of the implants in the osseointegration process are evaluated.
- (3) the morphology and mechanical response of the CaTiO<sub>3</sub> reaction layer are discussed. The influence of the reaction layer in the osseointegration and in the formation of the bone-implant interface are analysed in detail.
- (4) the osseointegration and the cancellous bone ingrowth in the rat and ovine implants after the healing process are explained. Surface properties and morphologies of the implants used in rats and sheep and their effects in the osseointegration process are evaluated as the base of the results obtained during the push-out tests and morphological analysis.

### 5.1 Comparison of the mechanical properties of the cancellous bone and open-cell metallic foam

Cancellous bones and the AlSi7Mg foam exhibited the usual compressive deformation behaviour observed by Gibson and Ashby in cellular materials [49, 209]. The adoption of a compression test standard for cellular materials (DIN 50134 [246]) and an appropriate gripping arrangement (Figure 3.13) have reduced the testing variables, hence more consistent results in the measured elastic modulus, yield stress and ultimate strength are obtained. Particular attention was placed on the determination of the elastic modulus. At the initial loading stage of the test, an increase in stress was observed, which, at first sight, appeared to be elastic. However, previous works revealed that the stress was only partially reversible, and some irreversible deformation processes in the cellular structure occurred during the loading stage [256]. Therefore, the measurement of the elastic modulus was carried out based on the unloading linear stress–strain relationship between R<sub>70</sub> and R<sub>20</sub>. The use of this standard permits not only accurate measurements of the Young's modulus,  $\sigma_y$  and  $\sigma_{ult}$  but also an appropriate identification of the deformation mechanism occurring in these materials.

## Discussion

The stress–strain behaviour of the bone is shown in Figure 4.1 and 4.2, where linear behaviour was observed at the beginning of the compression. This was followed by a brief but significant hardening period, then by a prolonged softening with considerable reduction of stresses due to progressive failure of the trabeculae. For large strains between 9%–12%, a slight increase in the stress was observed, probably due to the densification process of the trabeculae. Similar results have been obtained in previous works [3, 257], in which it was observed that after the deformation of the first band of trabeculae a plateau of almost constant stress and a final increasingly steep region occurred.

Ovine cancellous bones at the distal femoral metaphysis present high anisotropy which was analysed with samples extracted along the MTD and perpendicular to the MTD. Bone grows in response to mechanical loading [27, 43] and there is substantial evidence that the trabeculae are oriented in the directions of the main stresses. That was confirmed after analysing the compression results. Figure 4.1 shows clearly the orientation of the trabeculae in two opposite directions and their different behaviour under compressive loads. Bones tested along the MTD show compression values about two times of those values obtained with bones tested perpendicular to the MTD (Table 4.1). It is well known that the bone regeneration around an implant is affected by the internal loads and anisotropy of the bone [34, 53, 85]. Therefore, it is necessary to take into account the position of the implants in the sheep femur during the implantation, because the main loads in the bone may influence the results of the bone ingrowth and the formation of the bone-implant interface.

Compression values obtained from the bovine bones were very close to those of the ovine bones tested at the MTD. The bovine bone samples extracted from the iliac crest show less anisotropy than the ovine bones at the distal femoral metaphysis. For these reasons and because of the limited number of ovine bone samples available, the bovine bones were used as bone model in the study of the deformation mechanism of the cancellous bone in the  $\mu$ CT. Additionally, the rod-like trabeculae and the homogeneity of the cancellous structure of the bovine bones provide a structure that is easier to analyse during the in-situ test.

Analysis of the compressive deformation behaviour of the bone samples in the in-situ device reveals that the trabeculae deform principally due to bending and buckling. Approaching the ultimate compression strength, the bending on the trabeculae was followed by buckling producing permanent deformation. Similar observations were made in previous works at tissue level [258] showing that the predominant deformation mode in bones is bending, where the trabeculae can be strained in tension even under apparent compressive loading. Brittle fracture due to the presence of minerals was observed to be dominant in bones

Comparison of the mechanical properties of the cancellous bone and open cell metallic foam [259] although the collagen network within the trabeculae may keep the mineral phase together even at large strains.

The stress–strain curves of the AlSi7Mg foam show a significant range of stress hardening (up to 3% strain) following the initial elastic response, then “softening” till about 8-10% strain. This “softening” or reduction of load may be characteristic for this type of alloy, which is influenced by the manufacturing process. It was observed previously [211] that in cast AlSi7Mg foams coarse Si and Mg<sub>2</sub>Si precipitates were present along the grain boundaries. These precipitates can drastically reduce the effective properties of cell struts and trigger “brittle” failure. Another factor that may affect the deformation behaviour is the homogeneity of the foam. Poor homogeneity introduces localised deformation by the formation of deformation bands leading to cells collapsing. With increasing homogeneity the deformation of the foam structure becomes more uniform due to the more uniform distribution of the stresses. The results of current compression tests show that the ductility of the AlSi7Mg foam studied in this work is superior to that used in a previous study [233]. A possible reason for this improvement may be the development of advanced casting techniques, which resulted in not only a more homogeneous foam structure but also better microstructural properties of the cell struts.

During the deformation analysis of the foam a general trend of buckling was observed. AlSi7Mg foam deforms by bending in the linear elastic region. When approaching the ultimate compression strength, the bending on the struts was followed by a combination of buckling and brittle fracture that results in permanent deformation. The deformation mechanism observed in the AlSi7Mg foam is very similar to that observed in the cancellous bone.

Despite the similarities in deformation mechanisms and morphology, the apparent mechanical responses differ considerably between the foam and the bones. That can be explained by the differences in the mechanical properties of the base materials as well as their micro-architecture details. However, the knowledge of these analyses permit to recognize that metal foams can mimic the mechanical behaviour of the cancellous bone. The processing route for open-cell metal foams allows the use of base materials with appropriated strength as well as the optimisation of cell architecture. That was the idea behind this project and therefore, the Ti-6Al-7Nb alloy which has outstanding biocompatible and mechanical properties was selected to develop a porous implant that can be used to substitute damaged or diseased cancellous bones. Compression values of the ovine bones and the deformation

## Discussion

behaviour exhibited by the bones and the foam reveal the desired values and deformation behaviours for the Ti67 porous implants in order to permit an optimal substitution of cancellous bone. The ideal open-cell implant should possess higher strength than the bone which it substitutes but with a similar Young's modulus to prevent stress shielding phenomena. The single pore dimensions should be controlled to stimulate both mineral and collagen osteointegration. Additionally, an adequate porosity to assure the proper interconnection between different pores and bone, high corrosion resistance under stress conditions and good biocompatibility are needed [8].

Previously it was explained that open-cell foams can be considered almost isotropic, meaning that their structure and their properties have no directionality. That can be considered as an advantage for the open-cell implants. It was observed in the ovine bone analysis that its structural anisotropy depends on the ratio and direction of the main stresses, and therefore the bone shows higher strength in the main trabecular direction (MTD) than perpendicular to that direction. Open-cell foams do not present this characteristic, permitting the use of foams as implant in different directions inside the bone without altering the Young's modulus and strength of the implant.

## **5.2 Cast Ti-6Al-7Nb as implant material**

### **5.2.1 Microstructure and mechanical properties of the cast Ti-6Al-7Nb material**

Nowadays, the necessity to use implants with very complicated shapes in restorative dentistry and orthopaedics has increased. In the fabrication of devices with complex shapes that require great accuracy, methods such as precision casting [164, 176], electron and laser beam melting [16, 177], powder metallurgy [13], etc. are used.

In this project a precision casting process for the manufacturing of the complex porous implants was selected. Precision casting has attracted an increasing interest due to the relative reduction of the overall cost and material. In addition, the mechanical properties of the cast Ti-alloy implants can be controlled by controlling their microstructures [175].

Titanium alloys are suitable for orthopaedic and load bearing implants. Their biocompatible and mechanical properties are superior to those of other biomedical alloys. Between the Ti-alloys, Ti-6Al-4V was the first option considered in this project for the production of the porous implants due to its excellent corrosion resistance and biocompatibility. The mechanical properties of this  $\alpha+\beta$  titanium alloy are superior to other materials and it is therefore one of the most studied and used alloys for orthopaedic implants. However, long-term performance of this alloy has raised some concerns due to release of

vanadium to the body. V ions released from the Ti64 alloy were found to create long-term health problems, such as neuropathy and osteomalacia [166]. Depending on the manufacturing process, vanadium can diffuse to the surface of the implant and carried by the blood [12, 167]. Taking into account that vanadium is toxic both in the elemental state and as oxide  $V_2O_5$  in this project it was avoided to use this element [168, 169]. Therefore, the Ti-6Al-7Nb alloy was selected for the production of the porous implants. The Ti67 alloy has similar biocompatible and mechanical properties compared to Ti64. Additionally, the Ti67 alloy has niobium instead to vanadium to stabilise the  $\beta$  phase which is considered as a vital class element [10]. Nb has a stabilizing effect on the oxide film of Ti based alloys [170]. The excellent corrosion resistance is due in part to the formation of Nb rich oxide which is very stable in the body environment [4].

During the development of the cast porous Ti67 implants it was necessary to investigate their microstructure and mechanical properties. Therefore, other samples with simple morphologies such as rectangular and grid-shaped specimens were manufactured and studied. The analysis of these samples helps in understanding of the microstructure and mechanical properties of thinner sectioned structures such as cell struts of the implants.

Microstructural analysis and mechanical testing of cast Ti67 samples revealed various defects associated with the casting process. Many Ti-alloys show defects in the final product that may be associated to the casting process, such as porosity due to poor filling, shrinkage, or dissolved gases, chemical segregation and hence non-uniform properties due to the physical chemistry of solidification, and contamination due to mould-casting interactions. Previous works have demonstrated that titanium investment casting defects are potentially affecting the design life of a structure [179, 200].

The microstructure of small cellular, grid-shaped and plate structures of cast Ti-6Al-7Nb show three different regions: a thin brittle  $\alpha$ -case layer, a coarse acicular layer, and the bulk microstructure consisting of  $\alpha$ -laths embedded in primary  $\beta$ -phase. Microhardness analysis confirmed strong dissimilarities between these three regions. The  $\alpha$ -case layer has a hardness more than twice as high as in the bulk Ti67 material. Therefore, the brittle behaviour exhibited by the samples during the mechanical testing was associated with the  $\alpha$ -case and to the inhomogeneous internal microstructure.

From several studies, (cf. [189, 260, 261]) it is known that depending on the kind of mold material the  $\alpha$ -case layer in cast Ti structures consists of  $TiO_2$  and  $Ti_3Al$ . EDS analysis reveals that the Al concentration in the  $\alpha$ -case was more than 2.5 times higher than in the bulk microstructure. Therefore, the higher amount of Al in the  $\alpha$ -case layer was attributed to the

## Discussion

formation of a very brittle intermetallic  $\text{Ti}_3\text{Al}$  surface layer resulting from the reaction of the melt with the mold material. That was confirmed with EBSD analysis (Figure 4.10) which shows that the  $\alpha$ -case layer possesses a fine-grained hexagonal  $\text{Ti}_3\text{Al}$  crystallographic structure. Unlike other reports, no tetragonal  $\text{TiO}_2$  was identified inside the  $\alpha$ -case (cf. [262-264]).

The  $\alpha$ -case strongly deteriorated the mechanical properties of the materials by promoting cracks formation under static and cyclic loading conditions. Therefore an aim of this project was the elimination of the  $\alpha$ -case to improve the ductility of the samples. Due to the morphology and lower thickness of the samples, mechanical milling methods were avoided in order to reduce risks of damage of the thinner sectioned structures. Hence, the optimal method to remove this outer layer was by acid milling.

The identification of the nature of the  $\alpha$ -case layer permits to select the possible acids which can react and dissolve it. According to earlier works [198, 265] on  $\alpha+\beta$  titanium alloys the  $\alpha$ -phase is preferentially attacked by  $\text{HNO}_3+\text{HF}$  acid solution, while the  $\beta$ -phase, on the other hand, remains stable. Sittig et al. [265] attributed this effect to a difference in the electrochemical potential, with the  $\alpha$ -phase being more anodic as compared with the  $\beta$ -phase. Previous reports [9, 17, 19], proposed that the  $\alpha$ -case layer is mainly formed by  $\alpha$ -phase components. Based on these considerations, it was expected that the  $\alpha$ -case is more rapidly attacked during pickling than the acicular region. Optimal  $\alpha$ -case elimination was obtained with a mixture of 70%  $\text{HNO}_3$  +10%  $\text{HF}$  and distilled water inside an ultrasonic cleaning device at a temperature between 30-40°C.

The effect of ultrasonic vibration was quantified by measuring the open circuit potential. Figure 5.1 shows that the voltage of the sample drops to values of -225 mV when the specimen was in contact with the pickling bath. This potential remains constant until onset of vibration. Then, the voltage drops to more negative values of around -300 mV. That gives the impression that the vibration acts like an activator, accelerating the pickling process. The effect of the vibration helped to eliminate non-metallic residues from the surface of the specimens and to generate a homogeneous bath acting on the sample's surfaces.

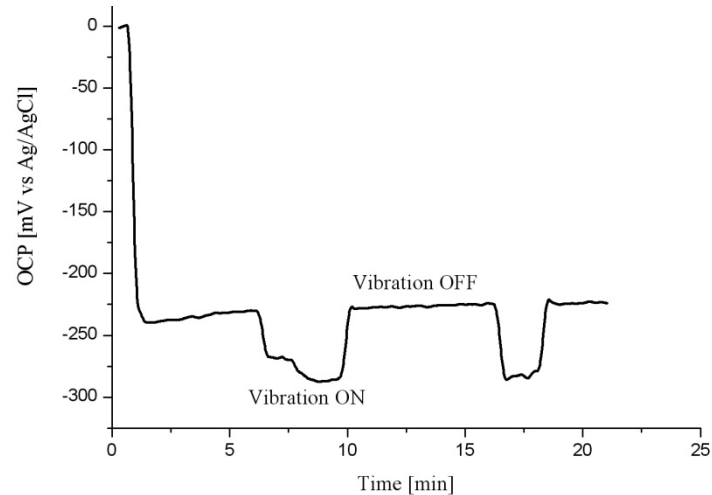


Figure 5.1: Open circuit potential of Ti67 submerged in the  $\text{HNO}_3 + \text{HF}$  bath

Elimination of the  $\alpha$ -case layer shows two principal advantages: improvement of the ductility and the formation of the worm marks on the surface of the samples. These worm marks provide the surface with an adequate roughness which was promising for the osseointegration process of the porous implants. Additionally, these rounded worm marks substitute sharp cracks on the surface produced in the  $\alpha$ -case layer and consequently reduce the risk of propagation of cracks during external loading.

Section 4.2.2 shows that the full  $\alpha$ -case elimination was obtained when the surface of the sample was completely covered by worm marks. Gravimetric measurement of the mass loss during pickling (Figure 4.12) shows a decrease of the slope after 60-70 min. The change in the slope of the mass-loss rate due to pickling as shown in Figure 4.12 can be explained by the formation of the worm marks: Figure 5.2a illustrates schematically in which way specimens with strong pitting corrosion exhibit more effective surface area to be attacked as compared to the specimens fully covered by worm marks (Figure 5.2b). In other words, samples highly affected by pitting corrosion will lose mass faster than the samples fully covered by worm marks. That can be explained by the higher surface energy associated with the sharp cracks of the samples with  $\alpha$ -case.

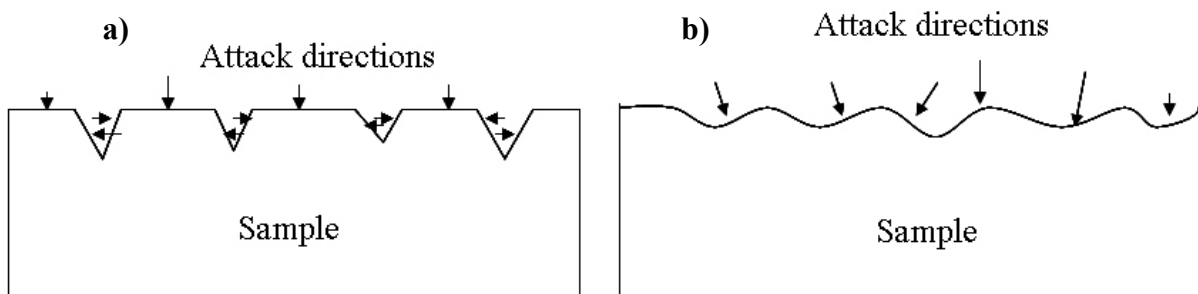


Figure 5.2: Schematic representation of the effective surface for acid attack with a) pitting corrosion marks and b) worm marks

## Discussion

The inhomogeneous microstructure of the cast Ti67 samples was analysed in details. Samples show two types of internal microstructures: (1) the acicular layer formed by colonies of coarse  $\alpha$  and  $\beta$  lamellae or also called Widmanstätten structure [9]. (2) Depending on the thickness of the samples, the acicular zones was sometimes followed by grains with colonies formed by fine  $\alpha$  and  $\beta$  lamellae or also called martensitic structure [9].

According to previous works [17, 185], the sizes of the acicular layer and bulk microstructure depend on the kind of investment material, the mold temperature and the casting volume. For instance, the higher the temperature of the mold and the larger the cast volume, the thicker is the acicular layer and the coarser are the acicular grains [185]. On the other hand, the bulk microstructure was found more often in thicker sectioned samples than in thinner sectioned samples. The grains of the bulk microstructure show similar shape like those of other cast Ti alloys e.g. Ti-6Al-4V, Ti-5Al-2.5Fe, near  $\alpha$ -Ti (IMI 685), etc. [9, 266]. The grain sizes of the thicker samples were bigger than in the thinner samples. That can be explained by considering the effect of the cooling rate, since samples with thinner section experience faster cooling rates than thicker samples.

Microstructures of conventional cast Ti-alloys are composed of parallel  $\alpha$  and  $\beta$  lamellae aligned within one colony which indicates that parallel plates belong to the same Burgers relationship [184]. The size and the density of  $\alpha$  and  $\beta$  lamellae in these colonies as well as the slip length affect the mechanical properties of the cast part [9, 175]. Additionally, it has been observed that samples with homogeneous sizes of colonies with fine  $\alpha$  and  $\beta$  lamellae are stronger than microstructures with coarse  $\alpha$  and  $\beta$  lamellae. Heat treatments were thought as the optimal solution to homogenize the microstructure with fine  $\alpha$  and  $\beta$  lamellae and consequently to obtain an improvement in the mechanical properties of the samples. Previous authors have shown that cooling rate after  $\beta$  heat treatments determinate the colony size [175]. With increasing cooling rate the colony size is decreased (decreasing slip length) and the yield stress  $\sigma_{0.2}$  is increased. A drastic increase in yield stress is observed when the colony structure is changed to a martensitic type of microstructure (slip length and "colony" size equal to the width of individual plates) [267]. From previous works [175, 267] it is known that the ductility, showing with increasing cooling rate first also a normal increasing behaviour (decrease in slip length), passes through a maximum and is then declining drastically at high cooling rates.

Three heat treatments were applied in his work with the aim to improve the ductility of the samples. Different from the literature [9], the heat treatment applied at the  $\beta$  phase shows a detrimental effect on strength and ductility. That can be attributed to the reduced thickness of

the samples and presence of a small amount of oxygen inside the furnace. The heat treatments were applied under protective Ar atmosphere, however, some small amount of O<sub>2</sub> may cause reactions with the surface and bulk microstructure of the samples. It has been found that at high temperatures the local increase in oxygen content in the metal near the surface promotes the formation of an oxygen-rich Ti hexagonal solid solution which additionally alters the  $\alpha/\beta$  structure near the surface during cooling to room temperature [190, 267]. This oxygen contaminated region ranges in thickness from 50 to 2000  $\mu\text{m}$ . Taking into account the small thickness of the grid-shaped sample (approx. 500  $\mu\text{m}$ ) and the cell struts of the Ti67 sponges (between 300-700  $\mu\text{m}$ ), the complete thickness will be consumed by this oxygen-rich microstructure. That was confirmed with the analysis of the cross sectional microstructure of a grid-shaped sample after a heat treatment at 1060°C applied for 1 hr (Figure 4.17).

An improvement of the homogenisation of the microstructure was found in the samples after the heat treatment at 870°C for 1 hr. Nevertheless, an oxygen-rich Ti layer with a thickness of approx. 30-70  $\mu\text{m}$  was observed. This layer was then removed by acid milling but the thickness of the samples was reduced considerably. Figure 4.19 shows the effect of reduced thickness on the sample in terms of lower bending force values than the samples with aging treatment. A homogeneous microstructure and an improvement of the ductility were reached by aging the samples at 600°C for 4 hr. The hardness and the bending tests revealed that the best mechanical response was acquired with samples which were aged for a prolonged period. Similar work [268] has shown that for  $\alpha+\beta$  titanium alloys, the strengthening effect of an aging heat treatment is caused by precipitation of fine  $\alpha$ -lamellae into homogenised colonies. Additionally, it was previously observed that homogenous colonies can induce an improvement of the ductility of cast Ti-alloy samples [267]. Optimal strength and ductility improvement can be achieved with a recrystallisation process which involves a combination of deformation and annealing [9]. However, the small dimensions and complex geometries of the samples do not allow any mechanical deformation of the samples.

The results observed during the microstructural and mechanical analyses reveal that the Ti-6Al-7Nb alloy is a difficult material to be used for casting of fine and complex structures such as sponges and porous implants. The production of an implant with a desired morphology requires experience and advanced casting techniques which include the use of sophisticated centrifugal casting machines. That limited the maximum volume of the cast, and therefore relatively small size implants were manufactured.

### 5.2.2 Cast Ti-6Al-7Nb porous implants

Porous Ti67 implants were produced with the aim to reduce the Young's modulus of the structure that is in contact with the bone and consequently reduce the stress-shielding effect on the bone-implant interface. Due to difficulties in the production of open-cell implants it was not possible to obtain an implant with fully cellular structure and with porosities above 20ppi (20 pores per inch). The implants studied in this work cannot be considered cellular structures because the relative density ( $\rho_r = \rho^*/\rho_s$ ) of the rat implants is  $\rho_r = 0.61 \pm 0.04$  while the relative density of the ovine implants is  $\rho_r = 0.30 \pm 0.01$ . That is in contrast with the definition of Gibson and Ashby [209] who considered a true cellular solid as a structure with a relative density below 0.3. If the relative density is above 0.3, the structure is better thought of as a solid containing pores. The density of bulk Ti-6Al-7Nb was considered to be  $4.52 \text{ g/cm}^3$  [269].

The mechanical properties of the porous implants show the effect of their morphology, exhibiting compression behaviours dissimilar to those found by the cancellous bones and the AlSi7Mg foam in section 4.1. The stress-strain curves during compression tests of the rat and ovine implants were linear elastic at the beginning of the compression. The linear elastic deformation was followed by a brief hardening period and then by a severe softening with a considerable reduction of the stresses due to drastic failure of the implant structure (at strains between 1 to 1.5%). Differently to the cancellous bone and aluminium foam, no recovery of the stress was observed after the softening period, consequently both compression test curves of rat and ovine implants show no plateau after reaching  $\sigma_{ult}$ .

The crushing suffered by the implants during the compression test follows the collapse behaviour of brittle cellular solids (Figure 2.29c) described by Gibson et al. in [3]. It can be thought that the crushing behaviour of the implant limits the loads that can be applied to them. On the other hand, the behaviour showed by the cancellous bone and AlSi7Mg can be described with the cell collapse behaviour that is exhibited by ductile cellular solids (Figure 2.29b) which deform by buckling and fail by plastic yielding. The deformation and failure mode of the ductile cellular solids was desirable for the cast Ti67 implants in order to mimic similar deformation behaviour of the cancellous bone under compressive loads.

The desired deformation behaviour during the compression test was not achieved; however the implants exhibit considerable reduction of their Young's modulus. Especially, the ovine implants show a Young's modulus 23 times lower than the  $E = 116 \text{ GPa}$  of bulk Ti67 [269]. That can be considered as an advantage of the ovine implants because its lower  $E$  may reduce

the biomechanical incompatibility that leads to death of bone cells and thus avoid the bone resorption around the implant that finally leads to implant loosening.

During the compression test it was observed that the main deformation and failure of the ovine implant occurs at its external ring. The dimensions and morphology of this ring permit to resist a high strength of  $49\pm 6$  MPa. The strength of the implant was superior to that observed by the cast Ti67 sponges in section 4.2.3 which exhibit a  $\sigma_{ult}$  of approx. 8.3 MPa. This cast Ti67 sponges had similar cell spacing and strut thickness to those showed by the internal porous structure of the implants. Therefore, one can suppose that the internal porous structure of the implant plays a limited role in the mechanical performance of the implant under compressive loading conditions. However, this internal structure can be useful in the osseointegration process and in the amount of trabeculae than can ingrow and interconnect with the implant structure.

The internal structure of the ovine implants shows a cell spacing of  $1674\pm 704$   $\mu\text{m}$  and a strut thickness of  $595\pm 205$   $\mu\text{m}$ . The dimensions of the cell spacing and strut thickness are not so far from those values of the ovine cancellous bone which exhibits a cell spacing of approx. 520-7670  $\mu\text{m}$  and a plate thickness of  $163\pm 50$   $\mu\text{m}$ . However, the porosity of the implants is not even close to the cell spacing in the range of 50-400  $\mu\text{m}$  suggested by Ryan et al. in order to optimize the bone ingrowth in the porous implant [6]. Therefore, attention was placed in the post-operative biomechanical test to observe the influence of the pore sizes in the bone tissue ingrowth.

The significant features of the rat implants were their pores size and surface properties in order to test the osseointegration and bone ingrowth at the implants in small animals. Due to the small dimension of the rat bones it was not possible to generate implants with porosities close to the cell spacing ( $234\pm 131$   $\mu\text{m}$ ) and strut thickness ( $90\pm 78$   $\mu\text{m}$ ) found for the rat cancellous bone. The pores sizes (1 mm) of the rat implants were considered too big, and therefore a detailed examination was done during the post-operative analysis to observe if the small rat trabeculae are able to grow inside the pores of the rat implants.

The surface properties of the implants were important in this work for the improvement of osseointegration process. After the elimination of the  $\alpha$ -case and the formation of the worm marks on the implant surfaces, it was shown that an appropriate roughness may help in the formation of bony tissue around the implants. Roughness of the rat implant surface was much better than the surface roughness observed in the ovine implants. Prior to the acid attack the ovine implants were mechanically milled to obtain an exact cylindrical diameter. Section 4.2.4 describes that previous mechanical milling decreases the effect of pickling process on

## Discussion

the implant surface and, therefore, reduced the roughness of the surface. The influence of the surface roughness of an implant in the osseointegration process has not been clearly defined until now. Therefore, the different roughness of the rat and ovine implants were compared after the bio-mechanical test.

Titanium and its alloys are considered biotolerant materials which means that their surfaces have excellent interaction with the surrounding bone tissue and induce the formation of a thin connective tissue capsule [101]. However, previous authors [4] highly preferred bioactive materials as they give rise to high integration with surrounding bone. Therefore, the surface of the implants used in this project was coated with a bioactive material based on  $\text{CaTiO}_3$ .

### **5.3 Properties of $\text{CaTiO}_3$ reaction layer on cast Ti-6Al-7Nb material**

The attachment of orthopaedic implants by bone ingrowth or bone apposition has become increasingly popular as the problem with aseptic loosening of hip and knee arthroplasties has remained significant. Therefore, cemented (with e.g. PMMA) and uncemented techniques have been developed to improve the fixation between bone and implants [270]. Amongst the uncemented techniques, application of coatings on implants was introduced in an effort to achieve earlier and stronger fixation as compared with uncoated implants.

Implants make the first contact in the bone with their surface, and the specific interactions between bone and implant surface determine the path and speed of the healing process and the long-term integration of the bone-implant interface. It is known that the nature of the initial interface that is developed between an artificial material and the attached tissue determines the ultimate success or failure of the materials [4]. Tissue-biomaterial compatibility is the most important issue to be considered for the implant success. In order to achieve high osseointegration, the surface chemistry, surface topography, surface roughness and mainly the surface energy of the implants must be improved because they regulate the type and degree of the interactions that take place at the bone-implant interface [4, 144].

In this project, the surface chemistry of the implants was modified by using calcium titanate reaction layer. Ca-Ti coating was formed on the surface by immersing the implants in a salt-bath containing  $\text{Ca}(\text{NO}_3)_2 + \text{NaNO}_3$  and  $\text{KNO}_3$ . The modification of the surface occurs through partial conversion of the  $\text{TiO}_2$  surface layer into calcium titanate by reaction with the calcium ion of the melt. This technique is suitable for implant with complex shapes which shall remain in the body till death.

The selection of the  $\text{CaTiO}_3$  coating over a common coating such as hydroxyapatite was important. Previous authors had shown that thick HA coatings exhibit poor mechanical

behaviour under cyclic loads producing pores and microcracks inside the coating [157]. As a result, delamination or loosening of coating fragments occurs which migrate into the joint space between bone and implant causing third-body wear of the implants surfaces [271-273]. It has been also reported that the delamination of these coatings may generate progressive inflammatory reactions and bone loss [270, 273] decreasing the pH in this body section until an acidic level [4]. Acid environments may produce dehydroxylation of the entire HA reaction layer reducing the coating durability in terms of chemical stability [274].

The performance of calcium titanate coatings has previously been analysed on Ti-6Al-4V samples [254]. These coatings with thickness between 0.02 to 1.5 µm showed good apposition in complex geometries and good mechanical properties under cyclic loads.

In order to characterize the coating properties on the implants used in this work, four different coatings were analysed in grid-shaped and rectangular samples. SBI, SBII, SBIII and SBIV coatings described in section 4.3 show different morphologies and thickness. The SBI coating show the lowest thickness and therefore was the most attractive to be used on the implants. Some researchers have found that thick coatings with inadequate bonding may induce relative movement of the interfacial zone between the tissue and the implant which eventually leads to deterioration in function of the reaction layer [275]. On the other hand, thin reaction layers of several nanometers on titanium alloy surface can give rise to osteoinduction by proliferation of cells and their differentiation towards bone cells, revascularisation and eventual gap closing. Ideally, a strong bond is formed between implant and tissue [276].

The clear dependency of the coating thickness and the Ca-Ti crystals amount with the temperature of the salt melt follows similar pattern observed in previous work. Ploska et al. [254] have described that the reaction layer thickness and the calcium content varied with salt melt composition, temperature and storing time. The layer thickness growth accelerates primarily with increasing salt melt temperature; however, above 500-510°C it diminished due to the higher corrosive effect of the salt melt. On the other hand, the effect of the time in the increase of the calcium content reaches a maximum at 100 to 120 min and then the calcium content shows no variation.

To select a coating for the rat and ovine implants the four coatings were used in grid-shaped and rectangular samples which were then mechanically tested under Ringer's solution. The microdamage of the coatings during the cyclic-bending test was monitored with a corrosion system that measured the open-circuit potential (OCP) using a circuit with three electrodes. It has been shown that the corrosion potential measurements during mechanical

## Discussion

testing in quasi-physiological media can reliably indicate the microstructural damage on the specimen surface [140-142].

In the galvanic series of metals, titanium has a standard potential of -1.63 V which is close to that of aluminium [9]. Therefore, titanium cannot be considered as intrinsically noble. Yet, the excellent resistance of titanium to general corrosion in most environments is the result of the formation of a stable protective surface film, which consists basically of  $\text{TiO}_2$ . This thin oxide film passivates titanium as long as the integrity of the film is maintained. It has been observed that even in solutions with low oxygen contents, the  $\text{TiO}_2$  layer can rebuilt spontaneously after being damaged [277, 278]. Following the suggestion of previous authors [141-143], the oxidation was defined as a drop of the OCP while the passivation was defined as a steady-state of the OCP curve (Figure 4.26).

During the cyclic-bending test, the grid-shaped samples show that the OCP curve suffers drops from the steady-state condition. These drops were associated with the formation of cracks and consequently new exposed areas that react immediately with the Ringer's solution producing oxidation of these areas. It was expected that a drastic drop appears only at failure of the samples but in some coated samples alteration of the OCP curve was observed before the sample failure. These alterations of the OCP were associated with loosening of coating fragments that leads to oxidation of the exposed areas previously covered by the coating fragments. Figure 4.28 shows that the samples coated with SBIII and SBIV present more alterations of OCP than the samples coated with SBI and SBII. Although the meaning of the drops of the OCP was clear, samples coated with SBIII and SBIV needed to be analysed in details with other methods.

After the cyclic-bending test, SEM analysis carried out at the areas surrounding the bending cracks show delamination of some coating fragments (Figure 4.29). This phenomenon was often observed on the samples coated with SBIII and SBIV. Therefore, one can link the delaminations observed in the SEM to the drops of the OCP during the cyclic bending test. The frequent OCP drops and the delamination observed on the coatings SBIII and SBIV may be explained due to higher stress development in thicker coating that lead to crack formation. The samples with these coatings exhibit a higher amount of Ca-Ti crystals on the surface resulting in thicker coatings than that observed on the samples coated with SBI and SBII. Consequently, delamination of Ca-Ti crystals was more probable on these coating than on the samples coated with SBI and SBII.

Cyclic bending test and SEM analysis reveal loosening of coating fragments; however, the nature of these loosening was not clear: On one hand, it is possible that a weak bond between

the coating and the sample surface generates brittle delaminations of the thicker coating layers under cyclic loads. On the other hand, the formation of bending cracks could provoke loosening of pieces of the cast Ti67 material surrounding the bending cracks including the coatings on the cast Ti67 pieces. A fretting test was used to understand the nature of the coating loosening observed in the cyclic bending test. This test was used since tribology and abrasive resistance of a reaction layer used in orthopaedic implants is a very important criteria for the selection of a biomaterial in artificial joints [279]. It is necessary to avoid flaking or spallation of the implant surface in order to reduce the risk of inflammatory reactions in the body.

The deformation of the coatings produced by fretting was analysed to observe possible surface damage and loosening of the coating material. The fretting test was carried out for a reduced number of cycles and with a small load (1.5 N) in order to avoid higher load that may cause the formation of fragments of metals (from the sphere or from the cast Ti67 samples) that brake off and become trapped between the mating surface causing unwanted wear and scoring.

The SEM analysis of fretted samples revealed that all the coatings were flattened by the Ti sphere but no loosening of the coating was observed. That can be considered as a ductile behaviour of the Ca-Ti coating and as a strong bond between coating and sample. Consequently, the loosening of the coating fragments during the cyclic bending test was produced due to the loosening of cast Ti67 pieces in the surrounding areas of the bending cracks.

Ploska et al. [254] have shown that salt melt temperatures up to 350°C have no significant influence on the fatigue strength of Ti-6Al-4V which has similar mechanical properties as that of the Ti-6Al-7Nb. Additionally, cell culture analysis was carried out at the JLU Gießen to study the in-vitro behaviour of animal cells which were deposited under controlled conditions on the surface of grid-shaped samples coated with SBI, SBII, SBIII and SBIV. This analysis shows that the animal cells proliferation and maintenance on the samples coated with SBI was better than those observed on the samples with other coatings.

Some authors consider that the failure of an implant occurs often at the metal/coating interface [158, 160], for this reason a reaction layer on a implant must possess not only excellent long-term biocompatibility and chemical stability but also outstanding bond with the implant to assure the success of the implant in the body [159]. As per the mechanical and corrosion behaviour of the studied coatings, the coating SBI was selected to be used in the rat and ovine implants. The low thickness and excellent mechanical properties of the reaction

## Discussion

layer SBI may contribute to long-term stability of the Ti-6Al-7Nb reducing the risk of inflammatory reaction by avoiding debonding of the reaction layer. Additionally, is expected that this coating provides an adequate surface energy and promotes osseointegration with the implants.

### **5.4 Biomechanical response of porous Ti-6Al-7Nb implants in animal experiments**

Numerous animal models have become a reliable basis for research on aetiology and pathogenesis, and they enable scientists to develop new treatment strategies. So far, there has been no animal model available which can satisfactorily answer the orthopaedic and surgical questions related to osteosynthesis materials and fracture healing treatments for bones. In this project rat and sheep were used as models to (1) analyse the biocompatibility properties of the cast Ti67 implants, (2) to study the influence of the porous structures in the attachment of implants by bone ingrowth or bone apposition and (3) to evaluate the effect of coatings in the osseointegration process.

Push-out [117], push-in [116], pull-out [115], and removal torque tests [114] are the most common methods to evaluate the biomechanical characteristics of osseointegrated implants. These tests can give an indication of resistance of a bone-implant interface to applied load. To accomplish the aims of the biomechanical analysis a push-out test was used in this work. The push-out test was selected, because it permits an uni-axial strength evaluation and a control of the deformation rate of the bone-implant interface. This test allows an optimal evaluation of the bone-implant interface considering the morphology of the implant and its anatomical position in the animal bones. Finally, an accurate analysis of the shear strength without the interference of the tensile component is possible by using a push-out test. Consequently, it produces more reliable stress analysis generated at the bone-implant interface [118].

Morphological analyses with optical and scanning electron microscopy were used to obtain information about the type and extent of osseointegration, the quality of the bone/implant interface and the structure of the tissue surrounding the implants. It has been seen previously that the morphological studies together with biomechanical testing can provide complete information not only about the quality of osseointegration in relation to the different implant treatments [280, 281] but also the biomechanical characteristics of the bone-implant interface [116].

#### **5.4.1 Biomechanical response of porous Ti-6Al-7Nb implants in rats**

Rats were chosen as animal model because they are inexpensive and easy to handle. Particularly their metabolism and healing process are faster than the ones of big animals e.g. sheep, which permits the use of rats to study the effect of aging on the bone in short periods [282, 283].

Coated (n=6) and uncoated (n=6) implants were positioned at the distal femoral metaphysis during the operation of the rats. One rat did not survive the implantation and its bone with the implant was used as specimen with 0 days of osseointegration. The other 11 specimens recovered for 30 days and then they were sacrificed. The complete distal femoral metaphysis with its respective implant was extracted and prepared for the push-out test.

Load-displacement curves of the push-out tests exhibited an initial linear behaviour which corresponds to a quasi-elastic resistance of the bone-implant interface under shear loads. After the linear elastic behaviour, the push-out curve reached the maximum load (push-out load) prior to a decrease in the load-displacement curve until the implant was completely removed. The push-out load was defined as the maximum shear load needed to break the bond between the implant and the newly formed bone around and inside the implant. After reaching the push-out load, the decrease of the push-out force was not abrupt and in some cases the stress decreases very slowly. Abrupt decrease of the push-out load after reaching the maximum load would indicate a weak bond between bone and implant. In contrast, slow decrease of the push-out load can be attributed to a strong bond between bone and implant which included growth of cancellous bone inside the implants. The bone inside the implant deforms by buckling and fails by combination of shear and rupture.

Previous works conducted with full cylindrical implants in rabbit's femurs exhibited a quick decrease of the push-out load after reaching the maximum push-out force [117, 284]. In these works, bone attachment occurs only on the implant surface and no bone tissue could grow inside the implants. The maximum push-out load found in these studies is only influenced by the bone fixed around the implant. In contrast, our test revealed that the push-out values were influenced by the bone fixed around the implants and by the bone that grows inside the implants.

The area under the push-out curve was considered as the energy absorbed during the push-out test by the bone fixed around and inside the implant. The maximum push-out load and absorbed energy were the most important values obtained to analyse the biomechanical characteristics of the bone-implant interface.

## Discussion

The implant with 0 healing days shows a maximum push-out load of approx. 57 N and an absorbed energy of 28.3 mJ. The push-out load and absorbed energy were considered as the minimum values which are related to no osseointegration of the implants. These values correspond to the friction between the implant and the tight drilling hole generated during the operation of the rat.

The biomechanical results on the implants of the rats recovered for 30 days were superior to those of the specimen with 0 days. These results were associated to the osseointegration and to the new bone that grows inside the implant. The maximum push-out force of specimens after 30 healing days was about 2.5-2.8 times higher than that of specimen 0, while the absorbed energy of the specimens after 30 healing days was approx. 3.6-5.2 times higher than the absorbed energy of the specimen with 0 healing days.

The push-out values obtained for the coated implants was slightly better than those of the uncoated implants. Despite the enhanced push-out results of the coated implants in comparison with those of the uncoated implants, it was not possible to associate this improvement of the push-out values to the coating influence on the implants. The difference between the biomechanical values of the coated and uncoated implants was not high enough to conclude that the  $\text{CaTiO}_3$  coating on the implant results in an improvement of the osseointegration process. The values of the push-out tests could be influenced by other factors such as the roughness, dimensions and the position of the implants inside the distal femoral metaphysis.

During the analysis of the implants in sections 3.3.2 and 4.2.4 it was observed that the rat implants used for the biomechanical test had various irregularities in shape and surface. For example, the variation of the rat implant diameter was  $3.0 \pm 0.2$  mm which was 6.7% of the average diameter. This value is high considering the small dimension of the rat cancellous bone (Tb.Sp. of  $234 \pm 131$   $\mu\text{m}$  and Tb.Th. of  $90 \pm 78$   $\mu\text{m}$ ). Therefore, this variation of diameter may be due to the fact that some implants were closer to the bone tissue than others implants during the operation and consequently the bond between the implant and bone surrounding might have varied.

Another factor that could influence the biomechanical test results was the different roughnesses observed on the implant surface. Section 4.2.4 describes that the rat implants were acid milled prior to the operation and consequently the surface of the implants was covered by worm marks that results in a surface roughness of  $R_{\text{max}}=8.84$   $\mu\text{m}$  with a  $R_a=1.01$   $\mu\text{m}$ . Morphological analysis shows the evidence that this roughness is positive for the osseointegration process, but unfortunately the roughness was not always controllable. The

effect of pickling is different depending on previous surface treatment (e.g. grinding) and on different sections of the implant. For example, the roughness near the hole was higher than at the external surface. Additionally, previous to the pickling process some surface regions received mechanical milling which decreases the roughness of these areas ( $R_{\max}=0.81\pm 0.20 \mu\text{m}$  with a  $R_a=0.19\pm 0.13 \mu\text{m}$ ) and therefore the bone apposition on these areas was reduced. Similar studies confirm that an appropriated roughness (higher than  $R_a=0.3 \mu\text{m}$ ) increases the osseointegration of Ti-alloys [115, 285]. The authors of these works concluded that the roughness of machined surfaces shows the worse osseointegration results while implants which were sand blasted and fluoride acid etched exhibited the best bone-implants attachments.

The anatomical position of the implant inside the femur during the operation is another factor that may contribute in the variation of the push-out results. Figure 4.31 shows the distal femoral metaphysis with the position of the rat implant (discontinued line) which varied depending on the manual skills of the surgeon that inserted the implants. The heterogeneous cancellous bone structure in the distal femoral metaphysis perhaps affected the bone growth rate around and inside the implants. It can be thought that the thicker trabeculae around the implant may grow with more difficulty inside holes than the thinner trabeculae. On the other hand, thicker trabeculae are stronger than thinner trabeculae and therefore it is expected that the thicker trabeculae that would grow inside the implant holes may improve the bond between implant and bone, and consequently increase the push-out results.

In order to analyse the osseointegration around and inside the implants, morphological analyses were carried out. SEM examination after the extraction of the implants revealed bone apposition on the surface and cancellous bone that grows inside the implants. Figure 4.33 shows that both coated and uncoated implants exhibit residues of bone tissue on the surface and inside the implant holes. During the preparation of the implants for the SEM analysis, some bone component such as bone marrow and bone fat were removed from the bone attached to the implants. Therefore, morphological analysis was focused on the mineral bone and bony tissue.

Mineral bone consists of two calcium phosphate phases, amorphous and crystalline apatitic components. The non-apatitic component represents about 40% of the total mineral in mature bone and an even higher percentage in younger bone [255]. The external surface of the implants was mostly covered by the remnant of amorphous bone, especially at the regions with worm marks. Figure 4.34 shows that these marks provide a favourable surface

## Discussion

morphology for the formation of amorphous bone clusters that may grow and improve the fixation of the bone-implant interface.

Cancellous bone was observed around the implants and inside their holes. The thickness of the trabeculae inside the implants varied depending on the anatomical position of the implant inside the distal femoral metaphysis. Similar results were observed during the histomorphometric analysis of the internal structure of the rat implants. The histomorphometric analysis carried out at the Laboratorium für Experimentelle Unfallchirurgie, JLU Gießen consists of a biopsy of the bone tissue that surrounds and grows inside the implants. This biopsy was done with a fully automatic computer-linked image analysis equipment that performs a quantitative measurement and characterization of the bone tissue surrounding the implants. Figure 5.3a shows the structure of the bone tissue around and inside a rat implant (black areas) in the distal femoral metaphysis.

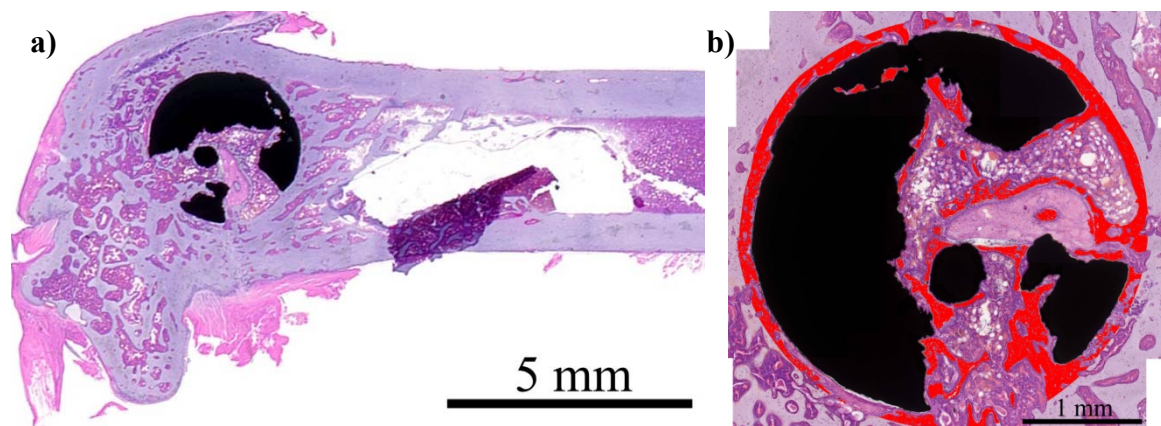


Figure 5.3: Histomorphometric analysis of the rat bone-implant: a) position of the rat implant inside the rat femur, b) selection of an area of interest (these results are reproduced with permission of the Laboratorium für Experimentelle Unfallchirurgie, Universität Gießen)

For the histomorphometric analysis an area of interest (red coloured area) which was 100  $\mu\text{m}$  bigger than the external diameter of the implant was selected (Figure 5.3b) in order to measure the bony tissue percentage. From the total bone material in this area of interest,  $26\pm 9.4\%$  correspond to the new bone tissue which grows inside and around the coated implants, while the new bony tissue percentage of uncoated implants was of  $25\pm 3.6\%$ .

The histomorphometric measurements support the results observed during the biomechanical tests which revealed that the coated implants exhibit a slight improvement in the push-out results in comparison to the uncoated implants. However, from this small difference in the values it cannot be assured that the  $\text{CaTiO}_3$  reaction layer was responsible for the high osseointegration observed at the coated implants.

Rat experiments carried out in this works showed that this animal permits faster and reliable examinations of the osseointegration process that occurs at the cast Ti-6Al-7Nb porous implants. However, in order to evaluate the biological-mechanical behaviour of Ti67 implants at loads closer to those found in human bones, a large animal model was needed.

#### 5.4.2 Biomechanical response of porous Ti-6Al-7Nb implants in sheep

In order to evaluate the behaviour of the cast Ti67 implants in big animals, sheep were used because they are docile, easy to handle and house, relatively inexpensive and they are available in large number [281]. Additionally, previous authors have observed resemblance between some bones in sheep and human [286, 287].

Coated (n=6) and uncoated (n=6) implants were positioned at the distal femoral metaphysis during the operation of the sheep. In this study, no animal died during the implantation, therefore no specimen 0 was available to compare the osseointegration process. The 12 animals recovered for 6 months and then they were sacrificed. The complete distal femoral metaphysis with its respective implant was extracted and prepared for the push-out test.

Before the push-out test, X-ray analysis was carried out at the extracted bones to determine the inclination angle of the implants inside the ovine femurs. Factors such as the manual implant positioning and the movement of the animal during the recovery could influence the alignment of the implant. After the measurement of the inclination angle at two positions of the bones (P1-lateral view and P2-back view in Figure 3.18), they were fixed and perfectly aligned with a self designed system. This system permits an accurate test eliminating the longitudinal and lateral force ( $F_x$  and  $F_y$  in Figure 5.4) of the push-out load during the test at the implants.

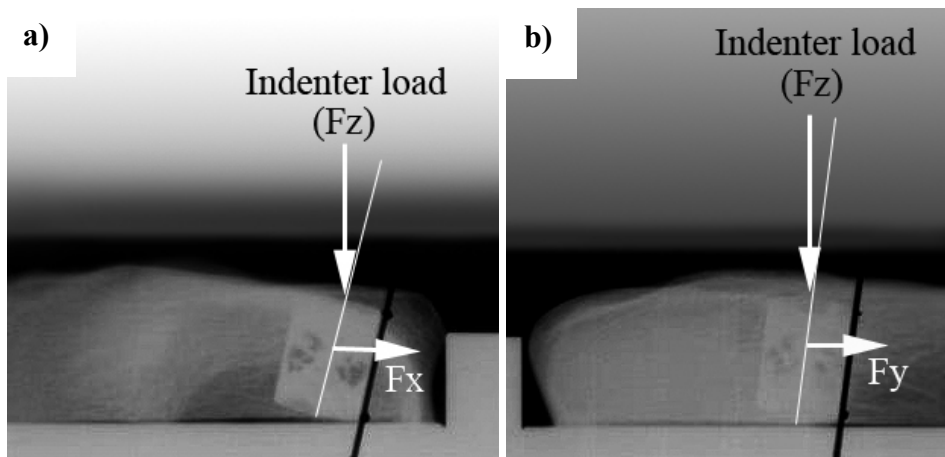


Figure 5.4: Eliminated force components during the push-out test: a) longitudinal force  $F_x$  and b) lateral force  $F_y$

## Discussion

Load-displacement curves from push-out analyses of the ovine implant-bone interface exhibited similar behaviour to that observed during the push-out tests on rat implants. An initial quasi-elastic response was followed by a maximum push-out load prior to a decrease in the load-displacement curve until the implants were completely removed. Despite the similar behaviour, the push-out values obtained on the ovine implants were much higher than those observed on the rat implants. The higher values observed by the ovine examination are because of the higher contact area of the ovine implants compared to the rat implant and because the ovine bone around and inside the implants was stronger than the rat bone.

Coated ovine implants showed slightly higher push-out values in comparison to the uncoated implants. The slight difference between the values obtained during the push-out tests cannot be attributed to the effect of the reaction layer in the osseointegration process. The values of the push-out tests could be influenced by other factors such as sheep age, the position of the implants inside the distal femoral metaphysis and the amount of cancellous bone surrounding the implants.

At the euthanasia, the age of the sheep varied from 49 to 95 months. This high variation could have affected the osseointegration rate and consequently influenced the push-out values. It is usually considered that in sheep a bone age of one month correspond approximately to that of one year in human [63]. Additionally, a sheep older than 40 months possesses mature bones [85] and it might have a reduced capacity to regenerate bone after a failure. Figure 4.38 shows two specimens with not-satisfactory push-out results. The sheep #7 (95 months old) that received a coated implant showed a maximum load of 473.6 N, while the sheep #18 (86 months old) that received an uncoated implant showed a maximum push-out load of 657.5 N. The lower values during the push-out tests were associated with less osseointegration and bone ingrowth. On the other hand, the highest push-out values were found in the youngest animals e.g. the push-out on the implant of the sheep #22 (49 months old) exhibited maximum load of 1752 N while a maximum push-out load of 1845 N was found for the implant of the sheep #13 (59 months old).

The influence of the age in the osseointegration process is high but it is not the unique factor that must be considered. The sheep with coated implants #2 (83 months) and #17 (86 months) as well as the sheep with uncoated implant #20 (85 months) reveal push-out forces close to the average value. The values found on these old animals were considered as satisfactory. That may indicate that the age was not the only factor that influences the push-out results of the implant in sheep #7 and #18. Other factors that play relevant roles in the osseointegration is the position of the implant and the amount of cancellous bone surrounding

the implants. Implant in the sheep #18 was found to be located very close to the bone marrow and cortical bone region. It is believed that implants located in regions with minimal quantity of surrounding cancellous bone result in reduced bone ingrowth and consequently low values in the push-out test can be expected.

Similar studies have been performed in semi-circular disc implants coated with different titanium porous coatings (porosities of approx. 50-62%) with pore size of about 200-220  $\mu\text{m}$  [288]. The implants resided in the sheep for 26 weeks, and then they were removed using a push-out test. The average maximum push-out load of their implants were very similar (1000 to 2000 N) to those observed in our work. The authors of this work interpreted that the high values of the push-out forces are related to high amount of osseointegration and bone ingrowth.

Optical and electron microscopy were used to analyse the morphology of the bone fixed to the implant and to evaluate the role of the internal porous structure of the implants in the osseointegration process. In order to observe the bone that grows inside the implants, they were cut along the length, and the bone fat and bone marrow were removed. Morphological analysis focused on the bone tissue and in the mineral bone revealed remnant of bone material around and inside the implants. As expected, the extracted implants of the youngest sheep show a higher amount of mature bone material than in the case of the implants of the oldest sheep. Figure 4.39b and Figure 4.40 reveal higher amount of cancellous bone on the implants of the sheep #5 (56 months old) and #22 (49 months old). No cancellous bone was observed inside and around the implants in the sheep #7 and #18. These implants showed that the dominant material that grew inside was a soft tissue which was identified as granulation tissue and rest of cartilage tissue that is a connective tissue which can be found in joint between bones and that could migrate from articulations to the inner side of the implants. The kind of bone material found in the implants depends principally of the anatomical position that the implant occupied inside the distal femoral metaphysis. In others words, the implants surrounded by a high amount of cancellous bone show more of this bony tissue inside the implants than the implants located in regions with a small amount of cancellous bone. Additionally, remnant of amorphous bone was found on the internal surface of the implants and on the struts. Figures 4.40 and 4.41b show that the mineral bone on implants struts was in direct interaction with the cancellous and granulation tissue.

Cancellous bone grows inside the implants principally from two directions: (1) from the underneath side of the implants, which was named cancellous side (Figure 4.37), and (2) from the implants holes which were aligned to the main trabecular direction (Figure 4.40 and

## Discussion

4.41a). Figure 4.40 shows that the trabeculae located at the underneath side grow almost to the middle of the implant with a strut thickness and cell diameter smaller than the cancellous bone surrounding the implants. Cancellous bone inside the implants shows a rod-like structure with a trabeculae spacing (Tb.Sp.) of  $532 \pm 232 \mu\text{m}$  and a trabeculae thickness (Tb.Th.) of  $120 \pm 50 \mu\text{m}$  while the surrounding cancellous bone exhibits a plate like structure with Tb.Sp. varying from 520 to 7670  $\mu\text{m}$  and a plate thickness of  $163 \pm 50 \mu\text{m}$ . Furthermore, the cancellous bone inside the implants shows random orientation differently to the structure of the external cancellous bone which was oriented along the MTD. The dissimilarities between the structure and dimension of the cancellous bone inside and outside the implants may indicate that the load transfer along the external bone was higher than the load transfer at the interior of the implant. It is generally accepted that the density of cancellous bone depends on the magnitude of the stresses that it experiences while the microstructural anisotropy depends on the ratio and direction of the main stresses [3].

In order to achieve a successful replacement of a bone lost by diseases, an implant must dissipate forces resulting from load on the prosthesis supported by the implant to underlying bone [289]. Therefore, the presence of a higher amount of the cancellous bone inside the implants was unexpected because no load transfer was expected inside the implants. In section 4.2.4 and 5.2.2 it was described that the deformation of the implants occurs principally at the implant ring, and the internal porous structure plays a small role in the internal load distribution. However, the evidence of cancellous bone inside the implants can be interpreted as the presences of load distribution by the internal structure which promotes the cancellous bone growth inside the implants. Another explanation of the presence of internal cancellous bone can be attributed to the presence of the porous structure of the implants which was used as supporting structure when the trabeculae grow and attach to the implants struts. As consequence, the newly formed trabeculae use the struts as platform to form other trabeculae.

The external surface of the ovine implants was mechanically milled in order to obtain an accurate diameter of approximately  $9.7 \pm 0.1 \text{ mm}$ . That was done after analysis of the rat biomechanical results which reveal that the different diameter of the implants could affect the push-out results and therefore a high scatter in the values could occur. The mechanical milling was useful to reduce the scatter in the push-out values. However, morphological analysis shows that the external surface of the implants possessed a limited roughness this resulted in poor osseointegration. No bone material was found on the external surface after the extraction of the implants by using push-out test with the exception of the regions surrounding the implants holes that show residues of cancellous bone.

It is believed that cancellous bone that grows inside the implant's holes was principally responsible for the high push-out values obtained in this work. During the push-out test the trabeculae fixed to the implant's holes deform by bending and fail by shear at the weakest sections and in the regions, where the newly formed bone was not completely mature (Figure 4.41 a). Previous work observed high concentration of von Mises stresses during a push-out test in the border between bone and external surface of the implants [284]. The bone surrounding the implant surface yields when the maximum bond strength of the bone-implant interface is reached following to shear at this section. It is expected that the border of the holes may create a "guillotine" effect on the surrounding bone during the extraction of the implants creating high concentration of stresses in this regions.

In addition to the cancellous bone and mineral bone fixed to the implants, cortical bone was found present at the top of the implants (in the cortical side at the Figure 4.37). During the preparation of the bone-implant specimens for the biomechanical tests it was necessary to remove a part of cortical bone that grows above the implants in order to reach the implant. That was considered as an evidence of the cortical bone growth around and above the implants. The fast growth of the cortical bone was unexpected taking into account that the sheep were considered old and that some authors [24] describe the growth of cortical bone as less active than the cancellous bone.

The results obtained during the biomechanical testing of rats and sheep revealed outstanding biocompatibility properties of the cast Ti-6Al-7Nb implants. High amount of mineral and cancellous bone observed on the surface and inside the implants were evidence that the morphology of the implant plays an important role in the osseointegration process. It is believed that the amount of bone ingrowth can be enhanced by improving the porosity and internal morphology of the implants. The cell spacing or pore size and the strut thickness of the implants were bigger than those of the cancellous bone. Reducing these dimension may contribute to higher osseointegration especially in bones which suffer a bone disease such as osteoporosis. Osteoporotic bones have a reduced bone mass which results in a reduced bone growth rate. Therefore, porous implants with higher porosity may contribute to stimulate more bone ingrowth than implants with lower and inhomogeneous porosities.

## Discussion

## Summary

This thesis presents the development, the characterization and the application of cast Ti-6Al-7Nb porous implants with respect to repair defects in cancellous bone of rats and sheep. In the framework of this project, it was aimed at fabricating porous implants with high mechanical strength to resist the internal loads of both animal cancellous bones. Additionally the implants should have a relatively low Young's modulus to prevent stress shielding phenomena which means a reduction in stress in the remaining bone that usually lead to bone resorption and a subsequently loosening of the implant. Other important properties of the porous implants are a controlled cell dimensions to stimulate both mineral and collagen osseointegration, high porosity to guarantee interconnection between different pores, corrosion resistance under stress conditions and good biocompatibility.

To identify the mechanical stresses and deformation behaviour that a porous implant should fulfil in order to substitute cancellous bone, bovine and ovine cancellous bone samples were compression tested. Ovine and bovine cancellous bone samples were used as model to understand their mechanical behaviours and the relationship between morphology and mechanical properties of the bone. In addition, a 45ppi open-cell AlSi7Mg foam was studied to understand the deformation mechanisms occurring in compression tests of metallic foams in comparison with those of the cancellous bones and of the Ti-6Al-7Nb porous implants. MicroCT characterisation and compressive mechanical testing of ovine and bovine cancellous bone as well as the AlSi7Mg foam indicate that despite the apparent differences in their respective microstructures and mechanical properties, the deformation behaviour is very similar in foam and bones, particularly at small strains. This analysis was useful to compare and to understand the deformation behaviour of the Ti-6Al-7Nb porous implants.

The Ti-6Al-7Nb alloy was selected because of its excellent mechanical and biocompatible properties which were confirmed by means of in-vivo and in-vitro analysis in rats and sheep. However, before the use of the cast Ti-6Al-7Nb implants, defects associated to the casting process such as  $\alpha$ -case and heterogeneous microstructure had to be solved to improve the mechanical properties of the implants.

The cross sectional microstructure of grid-shaped, small cellular and plate structures of cast Ti-6Al-7Nb show three different regions: a thin brittle  $\alpha$ -case layer, a coarse acicular layer, and the bulk Widmannstätten-type microstructure consisting of  $\alpha$ -laths embedded in primary  $\beta$ -phase. Microhardness analysis confirmed strong dissimilarities between these three regions. The  $\alpha$ -case layer exhibits a more than twice higher hardness than the bulk Ti67

## Summary

material. This can be one of the reasons of the relatively brittle response of the cast structures to mechanical loading.

It was shown that the  $\alpha$ -case layer can completely be removed by using a pickling process in a  $\text{HNO}_3$ +HF solution supported by ultrasonic vibration. Surface analysis and roughness measurements confirmed that for Ti-6Al-7Nb alloy 60-70 min pickling periods led to a strong improving of the surface properties not only by removing the brittle  $\alpha$ -case layer, but also by a cleaning effect and by improvement of the surface roughness. These effects are considered as beneficial for the applicability of cast Ti-6Al-7Nb cellular structures as tailored biomedical implants since they seem to promote the osseointegration process.

Cast Ti-6Al-7Nb samples show homogeneous microstructures as well as improvement of the ductility and strength after aging treatment and acid cleaning. Bending test results reveal that after heat treatment and pickling process grid-shaped samples showed an excellent combination of strength and ductility.

The surface and porosity of the rat and ovine implants were analysed to understand their role in the osseointegration process and in the amount of bones tissue that grows inside the implants. After pickling, rat implants show an optimal roughness that turned out to lead outstanding osseointegration observed during the biomechanical analysis. Another factor that affects the osseointegration on the rat implants was their porosity. The porosity of the rat implant was very low affecting the cancellous bone ingrowth. From the results can be deduced the recommendations to increase the porosity in order to stimulate higher amount of cancellous bone ingrowth.

The ovine implants show higher porosity than the rat implants, and it was observed that the porosity of the ovine implants facilitate the cancellous bone ingrowth. However, improvement of the porosity is required to improve the osseointegration. Ovine implants exhibit poor surface roughness produced by mechanical milling which was done to obtain an accurate external diameter. The low surface roughness of the ovine implants affects the osseointegration in terms of a low amount of bone attached to the surface of the implants.

Ovine implants were compression tested and the results were compared with those of cancellous bone and AlSi7Mg foam. The implants show  $\sigma_{\text{ult}}=49\pm 6$  MPa and a Young's modulus of  $5010\pm 1098$  MPa. The value of the implant strength is satisfactory as it is high enough to resist the internal loads of the ovine cancellous bones. Moreover, ovine implants show a Young's modulus 23 lower than the tensile Young's modulus of the Ti-6Al-7Nb ingot material. The deformation behaviour of the ovine implants is different to the deformation behaviour of the bone and the AlSi7Mg foam. The implants did not show the typical

deformation behaviour for cellular solids. This can be attributed to the implants design which consists of a cylindrical ring with lateral holes and an internal open-cell structure. The implant ring is much stiffer than the inner structure and, therefore, during compression the maximum stress is carried by the implant ring. After the collapse of the ring, the complete implant fails resulting in a fast decrease of the stress.

In this project, the surface chemistry of the implants was modified by using calcium titanate reaction layer with the aim to achieve high osseointegration.  $\text{CaTiO}_3$  coating was formed on the surface by immersing the implants in a salt-bath containing  $\text{Ca}(\text{NO}_3)_2 + \text{NaNO}_3$  and  $\text{KNO}_3$  for 2 hr. In order to characterize the coating properties on the implants, four different coatings ( $350^\circ\text{C}$ ,  $410^\circ\text{C}$ ,  $450^\circ\text{C}$ , and  $510^\circ\text{C}$ ) were analysed in grid-shaped and rectangular samples. The coated samples were tested by fretting and cyclic bending in a corrosive environment.

Open circuit potential measurements of coated grid-shaped samples revealed small delamination-like phenomena during monotonic and cyclic bending tests. In particular, the samples coated at higher temperature were more affected by this delamination of the reaction layer. Material loss was observed by the drop of the corrosion potential and by SEM surface examination near to the bending cracks. However, fretting test with a Ti sphere and subsequently SEM analysis show no evidence of loosening of the coatings on any sample. That was considered a consequence of the ductile behaviour of the Ca-Ti coating and a strong bond between coating and sample. Consequently, the loosening of the coating fragments during the cyclic bending test was attributed to the loosening of cast Ti-6Al-7Nb pieces in the surrounding areas of the bending cracks. Considering the mechanical behaviour of the four coatings and the results of previous investigations, the coating formed at  $350^\circ\text{C}$  was selected for the rat and ovine implants.

The osseointegration process and cancellous bone ingrowth was studied in rats and sheep with coated and uncoated implants. The cast porous implants remained in the femoral metaphyses of the animals for a defined healing period: 30 days in rats and 6 months in sheep. After the period of healing, the implants were extracted by using push-out test. Coated and uncoated implants showed outstanding biomechanical results in rats and sheep confirming the excellent biocompatible properties of the Ti-6Al-7Nb alloy and the positive effect of porosity of these implants in the osseointegration process.

Biomechanical analyses in rats reveal that the osseointegration on the coated implants was slightly higher than that observed in the uncoated implants. However, the high push-out values found on the coated implants could not directly be associated to the coating effect. The

## Summary

scatter in push-out values might be affected by the position of the implants inside the femoral metaphyses, scatter in the rat implant diameter and differences in the surface roughness of the implants.

No difference between the push-out values of the coated and uncoated ovine implants was found. The  $\text{CaTiO}_3$  reaction layer plays a minor role during the osseointegration process. Push-out values of the coated and uncoated implants show high scatter which was associated to a combination of factors such as the age differences between the sheep, the inaccurate positioning of the implants inside the ovine femurs and the different amount of cancellous bone surrounding the implants.

SEM analysis revealed high amount of cancellous bone inside the implants, particularly inside the ovine implants. Cancellous bone found inside the ovine implant exhibited smaller trabeculae spacing and lower trabeculae thickness than the cancellous bone surrounding the implants. The high amount of cancellous bone inside of some ovine implants was associated to the internal porous structure of the implants.

The results presented in this thesis are intended to contribute to future selection and improvement of porous implants based on Ti-6Al-7Nb alloy. In order to improve osseointegration at the implants and high amount of bone ingrowth, it is recommended to use implants with higher porosity and to reach a more homogeneous cellular structure.

## Appendices

### Appendix A: Information of the rats used for the biomechanical test

Rat-Nr.	ZTL-number	Implantation date	Weight (g)	Kind of implant	Time stand of the implant (days)	Euthanasia-date
1	2820	04.10.2010	479	coated	30	03.11.2010
2	2821	04.10.2010	477	uncoated	30	03.11.2010
5	2824	04.10.2010	440	coated	30	03.11.2010
6	2825	04.10.2010	525	uncoated	30	03.11.2010
9	2828	04.10.2010	475	coated	30	03.11.2010
10	2829	04.10.2010	443	uncoated	30	03.11.2010
11	2830	04.10.2010	483	coated	0	Deceased during the implantation
14	2841	04.10.2010	508	uncoated	30	03.11.2010
15	2842	05.10.2010	445	coated	30	04.11.2010
19	2838	05.10.2010	541	uncoated	30	04.11.2010
20	2839	05.10.2010	533	coated	30	04.11.2010
23	2834	05.10.2010	453	uncoated	30	04.11.2010

## Appendices

### Appendix B: Push-out results of the rat implants

Rat-Nr.	Kind of implant	Push-out force (N)	Absorbed energy (mJ)
1	coated	Damaged during mounting	Damaged during mounting
2	uncoated	143.5	125.1
5	coated	180.4	156.4
6	uncoated	154.5	64.9
9	coated	178.9	145.4
10	uncoated	123.2	124.7
11	coated	57	28.3
14	uncoated	137.6	88.9
15	coated	155.7	161.1
19	uncoated	126.4	84.7
20	coated	124	123.8
23	uncoated	156.3	119.6

**Appendix C:** Information of the sheep used for the biomechanical test

Sheep-Nr.	Implant	Implantation date	Birthday	Weight before implantation (kg)	Kind of implant	Standing time of the implant (days)	Euthanasia-date	Weight at euthanasia (kg)
22	G15	15.07.2011	01.01.2008	87	uncoated	192	23.01.2012	91
9	B1	12.07.2011	23.12.2005	100	coated	195	23.01.2012	107
2	B7	11.07.2011	28.02.2005	95.5	coated	196	23.01.2012	99
7	B8	12.07.2011	02.03.2004	90	coated	195	23.01.2012	97
4	G2	11.07.2011	16.02.2007	87	uncoated	196	23.01.2012	91
1	G14	11.07.2011	06.01.2005	90	uncoated	197	24.01.2012	88
18	G8	14.07.2011	11.12.2004	101	uncoated	194	24.01.2012	104
17	B9	14.07.2011	14.12.2004	111	coated	194	24.01.2012	108
20	G16	14.07.2011	29.12.2004	88	uncoated	194	24.01.2012	86
5	B12	11.07.2011	04.04.2007	87	coated	197	24.01.2012	80
13	B6	13.07.2011	14.02.2007	118	coated	195	24.01.2012	114

## Appendices

### Appendix D: Push-out results of the ovine implants

Sheep-Nr.	Kind of implant	Inclination 1 of the implant before the push-out test	Inclination 2 of the implant before the push-out test	Push-out force (N)	Absorbed energy (mJ)
2	coated	12°	4°	1548	1865
5	coated	1°	0°	1430	6393
7	coated	15°	0°	473.6	1387
9	coated	7°	12°	1774	3269
13	coated	0°	1°	1845	6858
17	coated	9°	9°	1445	4186
4	uncoated	7°	6°	1784	2970
18	uncoated	0°	5°	657.5	4012
20	uncoated	6°	14°	1255	1913
22	uncoated	5°	0°	1752	5562
1 Damaged during the preparation	uncoated	0°	0°	Approx. 1800 N but the cortical bone failed before the bone-implant interface	No data

## References

- [1] Long M., Rack H.J.: Titanium alloys in total joint replacement - A materials science perspective. *Biomaterials*, **19** (1998) 1621-1639.
- [2] Wang K.: The use of titanium for medical applications in the USA. *Materials Science and Engineering A: Structural Materials Properties Microstructure and Processing*, **213** (1996) 134-137.
- [3] Gibson L.J., Ashby M.F., Harley B.A.: *Cellular materials in nature and medicine*. Cambridge University Press, Cambridge, 2010.
- [4] Geetha M., Singh A.K., Asokamani R., Gogia A.K.: Ti based biomaterials, the ultimate choice for orthopaedic implants - A review. *Progress in Materials Science*, **54** (2009) 397-425.
- [5] Hulbert S.F., Morrison S.J., Klawitte J.J.: Tissue reaction to 3 ceramics of porous and non-porous structures. *Journal of Biomedical Materials Research*, **6** (1972) 347-374.
- [6] Ryan G., Pandit A., Apatsidis D.P.: Fabrication methods of porous metals for use in orthopaedic applications. *Biomaterials*, **27** (2006) 2651-2670.
- [7] Weber J.N., White E.W.: Carbon-Metal graded composites for permanent osseous attachment of non-porous metals. *Materials Research Bulletin*, **7** (1972) 1005-1016.
- [8] Marin E., Fusi S., Pressacco M., Paussa L., Fearizzi L.: Characterization of cellular solids in Ti6Al4V for orthopaedic implant applications: Trabecular titanium. *Journal of the Mechanical Behavior of Biomedical Materials*, **3** (2010) 373-381.
- [9] Lütjering G., Williams J.C.: *Titanium*, Springer-Verlag, Berlin, 2003.
- [10] Oliveira V., Chaves R.R., Bertazzoli R., Caram R.: Preparation and characterization of Ti-Al-Nb alloys for orthopedic implants. *Brazilian Journal of Chemical Engineering*, **15** (1998) 326-333.
- [11] Okazaki Y., Ito Y., Ito A., Tateishi T.: Effect of alloying elements on mechanical-properties of titanium-alloys for medical implants. *Materials Transactions, JIM*, **34** (1993) 1217-1222.
- [12] Ito A., Okazaki Y., Tateishi T., Ito Y.: In-vitro biocompatibility, mechanical-properties, and corrosion-resistance of Ti-Zr-Nb-Ta-Pd and Ti-Sn-Nb-Ta-Pd alloys. *Journal of Biomedical Materials Research*, **29** (1995) 893-899.
- [13] Oh I.H., Nomura N., Masahashi N., Hanada S.: Mechanical properties of porous titanium compacts prepared by powder sintering. *Scripta Materialia*, **49** (2003) 1197-1202.
- [14] Davis N.G., Teisen J., Schuh C., Dunand D.C.: Solid-state foaming of titanium by superplastic expansion of argon-filled pores. *Journal of Materials Research*, **16** (2001) 1508-1519.
- [15] Li J.P., Li S.H., de Groot K., Layrolle P.: Preparation and characterization of porous titanium, *Key Engineering Materials*, **218-220** (2002) 51-54.
- [16] Heinel P., Mueller L., Koerner C., Singer R.F., Mueller F.A.: Cellular Ti-6Al-4V structures with interconnected macro porosity for bone implants fabricated by selective electron beam melting. *Acta Biomaterialia*, **4** (2008) 1536-1544.
- [17] Miyakawa O., Watanabe K., Okawa S., Nakano S., Kobayashi M., Shiokawa N.: Layered structure of cast titanium surface. *Dent Mater J*, **8** (1989) 175-185.
- [18] Takahashi J., Kimura H., Lautenschlager E.P., Lin J.H.C., Moser J.B., Greener E.H.: Casting pure titanium into commercial phosphate-bonded SiO<sub>2</sub> investment molds. *Journal of Dental Research*, **69** (1990) 1800-1805.
- [19] Victorin L., EI-Mahallawy N., Taha M. A., Fredriksson H.: Metallographic studies of cast titanium - an experimental study of metal/mould reaction. *Cast Metals*, **4** (1992) 182-187.

## References

- [20] Rosenberg K.R.: The anatomy and biology of the human skeleton. *American Journal of Physical Anthropology*, **82** (1990) 236-237.
- [21] Wintermantel E., Ha S.-W.: *Medizintechnik-Life science engineering*. Springer, Berlin, 2008.
- [22] Stedman T. L.: *The American Heritage Stedman's medical dictionary*. Mass.: Houghton Mifflin, Boston, 2005.
- [23] Weiner S., Traub W.: Bone structure: From angstroms to microns. *Faseb Journal*, **6** (1992) 879-885.
- [24] Rho J.Y., Kuhn-Spearing L., Zioupos P.: Mechanical properties and the hierarchical structure of bone. *Medical Engineering & Physics*, **20** (1998) 92-102.
- [25] Landis W.J.: The strength of a calcified tissue depends in part on the molecular-structure and organization of its constituent mineral crystal in their organic matrix. *Bone*, **16** (1995) 533-544.
- [26] Weiner S., Wagner H.D.: The material bone: Structure mechanical function relations. *Annual Review of Materials Science*, **28** (1998) 271-298.
- [27] Currey J.D.: *Bones: Structure and Mechanics*. Princeton University Press, New Jersey, 2002.
- [28] Glanze W.D., Anderson K., Myers T.: *Mosby's Medical Dictionary*. Mosby, St. Louis-Missouri, 2009.
- [29] Reilly D.T., Burstein A.H., Frankel V.H.: Elastic modulus for bone. *Journal of Biomechanics*, **7** (1974) 271-275.
- [30] Choi K., Kuhn J.L., Ciarelli M.J., Goldstein S.A.: The elastic moduli of human subchondral, trabecular, and cortical bone tissue and the size-dependency of cortical bone modulus. *Journal of Biomechanics*, **23** (1990) 1103-1113.
- [31] Rho J.Y., Roy M.E., Tsui T.Y., Pharr G.M.: Elastic properties of microstructural components of human bone tissue as measured by nanoindentation. *Journal of Biomedical Materials Research*, **45** (1999) 48-54.
- [32] Dendorfer S.: *Cyclic Deformation and Fatigue Behaviour in Cancellous Bone*, Dissertation, Universität Paderborn, 2008.
- [33] Carter D.R., Hayes W.C.: Compressive behaviour of bone as a 2-phase porous structure. *Journal of Bone and Joint Surgery - American Volume*, **59** (1977) 954-962.
- [34] Gibson L.J.: The mechanical behaviour of cancellous bone. *Journal of Biomechanics*, **18** (1985) 317-328.
- [35] Jurist J.M.: In-vivo determination of the elastic response of bone: II. Ulnar resonant frequency in osteoporotic, diabetic and normal subjects. *Physics in Medicine and Biology*, **15** (1970) 427-434.
- [36] Christensen A.B., Ammitzboll F., Dyrbye C., Cornelissen M., Cornelissen P., Vanderperre G.: Assessment of tibial stiffness by vibration testing in situ - I. Identification of mode shapes in different supporting conditions. *Journal of Biomechanics*, **19** (1986) 53-60.
- [37] Rho J.Y., Hobatho M.C., Ashman R.B.: Relations of mechanical properties to density and CT numbers in human bone. *Medical Engineering & Physics*, **17** (1995) 347-355.
- [38] Goldstein S.A.: The mechanical properties of trabecular bone: Dependence on anatomic location and function. *Journal of Biomechanics*, **20** (1987) 1055-1061.
- [39] Singh I.: Architecture of cancellous bone. *Journal of Anatomy*, **127** (1978) 305-310.
- [40] Ohman C., Baleani M., Perilli E., Dall'Ara E., Tassani S., Baruffaldi F., Viceconti M.: Mechanical testing of cancellous bone from the femoral head: Experimental errors due to off-axis measurements. *Journal of Biomechanics*, **40** (2007) 2426-2433.
- [41] Keaveny T.M., Morgan E.F., Niebur G.L., Yeh O.C.: Biomechanics of trabecular bone. *Annual Review of Biomedical Engineering*, **3** (2001) 307-333.

- [42] Lozupone E., Favia A.: The structure of the trabeculae of cancellous bone. 2. Long bones and mastoid. *Calcified Tissue International*, **46** (1990) 367-372.
- [43] Carter D.R., Beaupré G.S.: *Skeletal function and form: Mechanobiology of skeletal development, aging, and regeneration*. Cambridge University Press, Cambridge, 2001.
- [44] Silva M.J., Gibson L.J.: Modeling the mechanical behavior of vertebral trabecular bone: Effects of age-related changes in microstructure. *Bone*, **21** (1997) 191-199.
- [45] Rho J.Y., Ashman R.B., Turner C.H.: Young's modulus of trabecular and cortical bone material: ultrasonic and microtensile measurements. *Journal of Biomechanics*, **26** (1993) 111-119.
- [46] Wolff J.: *Das Gesetz der Transformation der Knochen*. Pro Business, Berlin, 1892.
- [47] Ashman R.B., Rho J.Y.: Elastic modulus of trabecular bone material. *Journal of Biomechanics*, **21** (1988) 177-181.
- [48] Feldkamp L.A., Goldstein S.A., Parfitt A.M., Jesion G., Kleerekoper M.: The direct examination of three-dimensional bone architecture in vitro by computed tomography. *Journal of Bone and Mineral Research*, **4** (1989) 3-11.
- [49] Gibson L.J.: Biomechanics of cellular solids, *Journal of Biomechanics*, **38** (2005) 377-399.
- [50] Majumdar S., Kothari M., Augat P., Newitt D.C., Link T.M., Lin J.C., Lang T., Lu Y., Genant H.K.: High-resolution magnetic resonance imaging: Three-dimensional trabecular bone architecture and biomechanical properties. *Bone*, **22** (1998) 445-454.
- [51] Mosekilde L.: Sex differences in age-related loss of vertebral trabecular bone mass and structure - biomechanical consequences. *Bone*, **10** (1989) 425-432.
- [52] Parfitt A.M.: Implications of architecture for the pathogenesis and prevention of vertebral fracture. *Bone*, **13** (1992) S41-S47.
- [53] Silva M.J., Gibson L.J.: The effects of non-periodic microstructure and defects on the compressive strength of two-dimensional cellular solids. *International Journal of Mechanical Sciences*, **39** (1997) 549-563.
- [54] Guo X., Kim C.: Effects of age-related bone loss: A 3D microstructural simulation. In: *Proceedings of Bioengineering Conference, ASME BED vol. 42*. 1999. p. 327-328.
- [55] Vajjhala S., Kraynik A.M., Gibson L.J.: A cellular solid model for modulus reduction due to resorption of trabeculae in bone. *Journal of Biomechanical Engineering - Transactions of the ASME*, **122** (2000) 511-515.
- [56] Schumacher S.: *Biochemische Marker des Knochenstoffwechsels nach Osteotomie Das Schaf als Osteoporosemodell*, Dissertation, Ludwig-Maximilians-Universität München, 2007.
- [57] Michel M.C., Guo X.D.E., Gibson L.J., McMahon T.A., Hayes W.C.: Compressive fatigue behavior of bovine trabecular bone. *Journal of Biomechanics*, **26** (1993) 453-463.
- [58] Bowman S.M., Keaveny T.M., Gibson L.J., Hayes W.C., McMahon T.A.: Compressive creep behavior of bovine trabecular bone. *Journal of Biomechanics*, **27** (1994) 301-310.
- [59] Bowman S.M., Guo X.E., Cheng D.W., Keaveny T.M., Gibson L.J., Hayes W.C., McMahon T.A.: Creep contributes to the fatigue behavior of bovine trabecular bone. *Journal of Biomechanical Engineering - Transactions of the ASME*, **120** (1998) 647-654.
- [60] Moore T.L.A., Gibson L.J.: Fatigue of bovine trabecular bone, *Journal of Biomechanical Engineering - Transactions of the ASME*, **125** (2003) 761-768.
- [61] Moore T.L.A., O'Brien F.J., Gibson L.J.: Creep does not contribute to fatigue in bovine trabecular bone. *Journal of Biomechanical Engineering - Transactions of the ASME*, **126** (2004) 321-329.

## References

- [62] Mc Donnell P., Harrison N., Lohfeld S., Kennedy O., Zhang Y., Mc Hugh P.E.: Investigation of the mechanical interaction of the trabecular core with an external shell using rapid prototype and finite element models. *Journal of the Mechanical Behavior of Biomedical Materials*, **3** (2010) 63-76.
- [63] Nafei A., Danielsen C.C., Linde F., Hvid I.: Properties of growing trabecular ovine bone - Part I: Mechanical and physical properties. *Journal of Bone and Joint Surgery - British Volume*, **82B** (2000) 910-920.
- [64] Bergmann G., Graichen F., Rohlmann A.: Hip joint forces in sheep. *Journal of Biomechanics*, **32** (1999) 769-777.
- [65] Mosekilde L., Danielsen C.C.: Biomechanical competence of vertebral trabecular bone in relation to ash density and age in normal individuals. *Bone*, **8** (1987) 79-85.
- [66] Linde F., Hvid I.: The effect of constraint on the mechanical behavior of trabecular bone specimens. *Journal of Biomechanics*, **22** (1989) 485-490.
- [67] Rohlmann A., Zilch H., Bergmann G., Kolbel R.: Material properties of femoral cancellous bone in axial loading. 1. Time independent properties. *Archives of Orthopaedic and Trauma Surgery*, **97** (1980) 95-102.
- [68] Keaveny T.M., Wachtel E.F., Ford C.M., Hayes W.C.: Differences between the tensile and compressive strengths of bovine tibial trabecular bone depend on modulus. *Journal of Biomechanics*, **27** (1994) 1137-1146.
- [69] Folgado J., Fernandes P.R., Guedes J.M., Rodrigues H.C.: Evaluation of osteoporotic bone quality by a computational model for bone remodeling. *Computers & Structures*, **82** (2004) 1381-1388.
- [70] Swartz D.E., Wittenberg R.H., Shea M., White A.A., Hayes W.C.: Physical and mechanical properties of calf lumbosacral trabecular bone. *Journal of Biomechanics*, **24** (1991) 1059-1068.
- [71] Geusens P., Boonen S., Nijs J., Jiang Y., Lowet G., VanAuderkercke R., Huyghe C., Caulin F., Very J.M., Dequeker J., VanderPerre G.: Effect of salmon calcitonin on femoral bone quality in adult ovariectomized ewes. *Calcified Tissue International*, **59** (1996) 315-320.
- [72] Keaveny T.M., Pinilla T.P., Crawford R.P., Kopperdahl D.L., Lou A.: Systematic and random errors in compression testing of trabecular bone. *Journal of Orthopaedic Research*, **15** (1997) 101-110.
- [73] Cowin S.C., Turner C.H.: On the relationship between the orthotropic Young's moduli and fabric. *Journal of Biomechanics*, **25** (1992) 1493-1494.
- [74] Zysset P.K., Curnier A.: An alternative model for anisotropic elasticity based on fabric tensors. *Mechanics of Materials*, **21** (1995) 243-250.
- [75] Linde F., Hvid I., Madsen F.: The effect of specimen geometry on the mechanical behavior of trabecular bone specimens. *Journal of Biomechanics*, **25** (1992) 359-368.
- [76] Pugh J.W., Rose R.M., Radin E.L.: Structural model for mechanical behavior of trabecular bone. *Journal of Biomechanics*, **6** (1973) 657-670.
- [77] Williams J.L., Lewis J.L.: Properties and an anisotropic model of cancellous bone from the proximal tibial epiphysis. *Journal of Biomechanical Engineering - Transactions of the Asme*, **104** (1982) 50-56.
- [78] Townsend P.R., Rose R.M., Radin E.L.: Buckling studies of single human trabeculae. *Journal of Biomechanics*, **8** (1975) 199-201.
- [79] Dendorfer S., Maier H.J., Hammer J.: Fatigue damage in cancellous bone: An experimental approach from continuum to micro scale. *Journal of the Mechanical Behavior of Biomedical Materials*, **2** (2009) 113-119.
- [80] Moore T.L.A., Gibson L.J.: Fatigue microdamage in bovine trabecular bone. *Journal of Biomechanical Engineering - Transactions of the Asme*, **125** (2003) 769-776.

- [81] Schoenfeld C.M., Lautenschlager E.P., Meyer P.R.: Mechanical properties of human cancellous bone in the femoral head. *Medical & Biological Engineering*, **12** (1974) 313-317.
- [82] Zilch H., Rohlmann A., Bergmann G., Kolbel R.: Material properties of femoral cancellous bone in axial loading. 2. Time dependent properties. *Archives of Orthopaedic and Trauma Surgery*, **97** (1980) 257-262.
- [83] Keller T.S., Spengler D.M., Hansson T.H.: Mechanical behavior of the human lumbar spine. 1. Creep analysis during static compressive loading. *Journal of Orthopaedic Research*, **5** (1987) 467-478.
- [84] Hansson T.H., Keller T.S., Spengler D.M.: Mechanical behavior of the human lumbar spine. 2. Fatigue strength during dynamic compressive loading. *Journal of Orthopaedic Research*, **5** (1987) 479-487.
- [85] Royle G.J., Farquharson M., Speller R., Kidane G.: Applications of X-ray diffraction analysis in crystalline and amorphous body tissues. *Radiation Physics and Chemistry*, **56** (1999) 247-258.
- [86] Riggs B.L., Melton L.J.: Involutional osteoporosis. *New England Journal of Medicine*, **314** (1986) 1676-1686.
- [87] Mazess R.B.: On aging bone loss. *Clinical Orthopaedics and Related Research*, **165** (1982) 239-252.
- [88] Smith D.M., Khairi M.R.A., Johnston C.C.: Loss of bone mineral with aging and its relationship to risk of fracture. *Journal of Clinical Investigation*, **56** (1975) 311-318.
- [89] Chien K.R., Karsenty G.: Longevity and lineages: Toward the integrative biology of degenerative diseases in heart, muscle, and bone. *Cell*, **120** (2005) 533-544.
- [90] Cooper C., Melton L.J.I.: Magnitude and impact of osteoporosis and fractures. Kelsey J. (Ed.) *Osteoporosis*. San Diego, 1996. p. 419-434.
- [91] Thurner P.J., Erikson B., Schriock Z., Langan J., Scott J., Zhao M., Fantner G.E., Turner P., Kindt J.H., Schitter G., Hansma P.K.: High-speed photography of human trabecular bone during compression. In: *Materials Research Society Symposium*, 2005. p. L1.2.1-L1.2.6.
- [92] Kleerekoper M.: Osteoporosis prevention and therapy: preserving and building strength through bone quality. *Osteoporosis International*, **17** (2006) 1707-1715.
- [93] Dao T.T., Anderson J.D., Zarb G.A.: Is osteoporosis a risk factor for osseointegration of dental implants? *The International Journal of Oral & Maxillofacial Implants*, **8** (1993) 137-144.
- [94] Cheng S.L., Toivanen J.A., Suominen H., Toivanen J.T., Timonen J.: Estimation of structural and geometrical properties of cortical bone by computerized tomography in 78-year-old women. *Journal of Bone and Mineral Research*, **10** (1995) 139-148.
- [95] Ruff C.B., Hayes W.C.: Sex differences in age-related remodeling of the femur and tibia. *Journal of Orthopaedic Research*, **6** (1988) 886-896.
- [96] Fini M., Giavaresi G., Rimondini L., Giardino R.: Titanium alloy osseointegration in cancellous and cortical bone of ovariectomized animals: Histomorphometric and bone hardness measurements. *International Journal of Oral & Maxillofacial Implants*, **17** (2002) 28-37.
- [97] Mitra E., Rubin C., Gruber B., Qin Y.X.: Evaluation of trabecular mechanical and microstructural properties in human calcaneal bone of advanced age using mechanical testing, micro-CT, and DXA. *Journal of Biomechanics*, **41** (2008) 368-375.
- [98] Ramakrishna S., Mayer J., Wintermantel E., Leong K.W.: Biomedical applications of polymer-composite materials: a review. *Composites Science and Technology*, **61** (2001) 1189-1224.
- [99] Alvarez K., Nakajima H.: Metallic scaffolds for bone regeneration. *Materials*, **2** (2009) 790-832.

## References

- [100] Ikada Y.: Tissue engineering: fundamentals and applications. Elsevier Academic press, Amsterdam, 2006.
- [101] Williams D.F.: On the mechanisms of biocompatibility. *Biomaterials*, **29** (2008) 2941-2953.
- [102] Sumner D.R., Turner T.M., Igloria R., Urban R.M., Galante J.O.: Functional adaptation and ingrowth of bone vary as a function of hip implant stiffness. *Journal of Biomechanics*, **31** (1998) 909-917.
- [103] Wintermantel E., Ha S.-W.: *Biokompatible Werkstoffe und Bauweisen*, Springer, Berlin, 1996.
- [104] Huiskes R., Hollister S.J.: From structure to process, from organ to cell - recent developments of Fe-analysis in orthopedic biomechanics. *Journal of Biomechanical Engineering - Transactions of the Asme*, **115** (1993) 520-527.
- [105] Oka M.: Biomechanics of natural and artificial joints. *Nihon Seikeigeka Gakkai Zasshi*, **67** (1993) 535-547.
- [106] Puleo D.A., Nanci A.: Understanding and controlling the bone-implant interface. *Biomaterials*, **20** (1999) 2311-2321.
- [107] Black J.: *Biological performance of materials: fundamentals of biocompatibility*. CRC Press, New York, 3<sup>rd</sup> ed, 1999.
- [108] Horbett T.A., Brash J.L.: Proteins at interfaces – current issues and future-prospects, *Acs Symposium Series*, **343** (1987) 1-33.
- [109] Andrade J.D., Hlady V.: Protein adsorption and materials biocompatibility - a tutorial review and suggested hypotheses. *Advances in Polymer Science*, **79** (1986) 1-63.
- [110] Brunski J.B.: Biomechanical factors affecting the bone-dental implant interface. *Clinical materials*, **10** (1992) 153-201.
- [111] Pilliar R.M., Davies J.E., Smith D.C.: The bone-biomaterial interface for load-bearing implants. *MRS Bulletin*, **16** (1991) 55-61.
- [112] Szmukler-Moncler S., Salama H., Reingewirtz Y., Dubruille J.H.: Timing of loading and effect of micromotion on bone-dental implant interface: review of experimental literature. *Journal of Biomedical Materials Research*, **43** (1998) 192-203.
- [113] Carter D.R., Hayes W.C.: Compact bone fatigue damage: a microscopic examination. *Clinical Orthopaedics and Related Research*, **127** (1977) 265-274.
- [114] Favero L.G., Pisoni A., Paganelli C.: Removal torque of osseointegrated mini-implants: an in vivo evaluation. *European Journal of Orthodontics*, **29** (2007) 443-448.
- [115] Pedrolli Renz R., Cunha A., Wantowski G., Blando E., Hübler R.: Osseointegration evaluation of treated surfaces of titanium implants applying tensile pull out test. *Rev. de Clín. Pesq. Odontol.*, **3** (2007) 149-157.
- [116] Zaffe D., Baena R.R.Y., Rizzo S., Brusotti C., Soncini M., Pietrabissa R., Cavani F., Quaglioni V.: Behavior of the bone-titanium interface after push-in testing: a morphological study. *Journal of Biomedical Materials Research Part A*, **64A** (2003) 365-371.
- [117] Brandt J., Bierogel C., Holweg K., Hein W., Grellmann W.: Extended push-out test to characterize the failure of bone-implant interface. *Biomedizinische Technik*, **50** (2005) 201-206.
- [118] Teixeira C.S., Alfredo E., de Camargo Thome L.H., Gariba-Silva R., Correa Silva-Sousa Y.T., Sousa-Neto M.D.: Adhesion of an endodontic sealer to dentin and gutta-percha: shear and push-out bond strength measurements and SEM analysis. *Journal of Applied Oral Science*, **17** (2009) 129-135.
- [119] Sundgren J.E., Bodo P., Lundstrom I., Berggren A., Hellem S.: Auger electron spectroscopic studies of stainless-steel implants. *Journal of Biomedical Materials Research*, **19** (1985) 663-671.

- [120] Lausmaa J., Kasemo B., Mattsson H.: Surface spectroscopic characterization of titanium implant materials. *Applied Surface Science*, **44** (1990) 133-146.
- [121] Sundgren J.E., Bodo P., Lundstrom I.: Auger electron spectroscopic studies of the interface between human tissue and implants of titanium and stainless steel. *Journal of Colloid and Interface Science*, **110** (1986) 9-20.
- [122] Kuroda D., Niinomi M., Morinaga M., Kato Y., Yashiro T.: Design and mechanical properties of new beta type titanium alloys for implant materials. *Materials Science and Engineering a-Structural Materials Properties Microstructure and Processing*, **243** (1998) 244-249.
- [123] Williams D.F.: *Biocompatibility of Orthopedic Implants*. FL: CRC Press, Boca Raon, 1982.
- [124] Hennig F.F., Raithel H.J., Schaller K.H., Dohler J.R.: Nickel-concentrations, chrom-concentrations and cobalt-concentrations in human tissue and body fluids of hip prosthesis patients. *Journal of Trace Elements and Electrolytes in Health and Disease*, **6** (1992) 239-243.
- [125] Dorr L.D., Bloebaum R., Emmanuel J., Meldrum R.: Histologic, Biochemical, and Ion Analysis of Tissue and Fluids Retrieved During Total Hip Arthroplasty. *Clinical Orthopaedics and Related Research*, **261** (1990) 82-95.
- [126] Bartolozzi A., Black J.: Chromium concentrations in serum, blood clot and urine from patients following total hip arthroplasty. *Biomaterials*, **6** (1985) 2-8.
- [127] Jacobs J.J., Skipor A.K., Patteson L.M., Hallab N.J., Paprosky W.G., Black J., Galante J.O.: Metal release in patients who have has a primary total hip arthroplasty - A prospective, controlled, longitudinal study. *Journal of Bone and Joint Surgery-American Volume*, **80A** (1998) 1447-1458.
- [128] Nordberg G.F., Fowler B.A., Nordberg M., Friberg L.T.: *Handbook on the Toxicology of Metals*, 3rd ed.. Elsevier, Amsterdam, 2007.
- [129] Merritt K., Brown S.A.: Distribution of cobalt chromium wear and corrosion products and biologic reactions. *Clinical Orthopaedics and Related Research*, **329** (1996) 233-243.
- [130] Thompson G.J., Puleo D.A.: Effects of sublethal metal ion concentrations on osteogenic cells derived from bone marrow stromal cells. *Journal of Applied Biomaterials*, **6** (1995) 249-258.
- [131] Thompson G.J., Puleo D.A.: Ti-6Al-4V ion solution inhibition of osteogenic cell phenotype as a function of differentiation timecourse in vitro. *Biomaterials*, **17** (1996) 1949-1954.
- [132] Nichols K.G., Puleo D.A.: Effect of metal ions on the formation and function of osteoclastic cells in vitro. *Journal of Biomedical Materials Research*, **35** (1997) 265-271.
- [133] Reclaru L., Lerf R., Eschler P.Y., Blatter A., Meyer J.M.: Pitting, crevice and galvanic corrosion of REX stainless-steel/CoCr orthopedic implant material. *Biomaterials*, **23** (2002) 3479-3485.
- [134] Blackwood D.J.: Biomaterials: Past successes and future problems. *Corrosion Reviews*, **21** (2003) 97-124.
- [135] Yu J., Zhao Z.J., Li L.X.: Corrosion fatigue resistance of surgical implant stainless steels and titanium alloy. *Corrosion Science*, **35** (1993) 587-597.
- [136] Reclaru L., Lerf R., Peschler.Y., Meyer J.M.: Corrosion behavior of a welded stainless-steel orthopedic implant. *Biomaterials*, **22** (2001) 269-279.
- [137] Brown S.A., Flemming C.A.C., Kawalec J.S., Placko H.E., Vassaux C., Merritt K., Payer J.H., Kraay M.J.: Fretting corrosion accelerates crevice corrosion of modular hip tapers. *Journal of Applied Biomaterials*, **6** (1995) 19-26.

## References

- [138] Gusmano G., Marchioni F., Montesperelli G.: A crevice corrosion study by electrochemical noise analysis. *Materials and Corrosion / Werkstoffe und Korrosion*, **51** (2000) 537-544.
- [139] Li Y.F., Farrington G.C., Laird C.: Cyclic response-electrochemical interaction in mono- and polycrystalline AISI 316L stainless steel in H<sub>2</sub>SO<sub>4</sub> solution – 3. Potential dependence of the mechanical behavior during corrosion fatigue. *Acta Metallurgica Et Materialia*, **41** (1993) 723-737.
- [140] Fleck C., Eifler D.: Characterization of the cyclic deformation behaviour of the implant alloy TiAl6V4 in air and Ringer's solution by temperature and corrosion potential measurements. *Advanced Engineering Materials*, **3** (2001) 500-503.
- [141] Leinenbach C., Fleck C., Eifler D.: The cyclic deformation behaviour and fatigue induced damage of the implant alloy TiAl6Nb7 in simulated physiological media. *International Journal of Fatigue*, **26** (2004) 857-864.
- [142] Schwilling B., Fleck C., Eifler D.: Cyclic deformation behaviour of TiAl6V4 and TiAl6Nb7 in different quasi-physiological media. *Materialwissenschaft und Werkstofftechnik*, **33** (2002) 453-458.
- [143] Robin A., Carvalho O.A.S., Schneider S.G., Schneider S.: Corrosion behavior of Ti-xNb-13Zr alloys in Ringer's solution. *Materials and Corrosion / Werkstoffe und Korrosion*, **59** (2008) 929-933.
- [144] Babu N.R., Manwatkar S., Rao K.P., Kumar T.S.S.: Bioactive coatings on 316L stainless steel implants. *Trends in Biomaterials & Artificial Organs*, **17** (2004) 43-47.
- [145] Baier R.E., Meyer A.E.: Implant surface preparation. *The International Journal of Oral & Maxillofacial Implants*, **3** (1988) 9-20.
- [146] Hamamoto N., Hamamoto Y., Nakajima T., Ozawa H.: Histological, histochemical and ultrastructural study on the effects of surface charge on bone formation in the rabbit mandible. *Archives of Oral Biology*, **40** (1995) 97-106.
- [147] Jarcho M.: Calcium phosphate ceramics as hard tissue prosthetics. *Clinical Orthopaedics and Related Research*, **157** (1981) 259-278.
- [148] Schreckenbach J.P., Marx G., Schlottig F., Textor M., Spencer N.D.: Characterization of anodic spark-converted titanium surfaces for biomedical applications. *Journal of Materials Science: Materials in Medicine*, **10** (1999) 453-457.
- [149] Buser D., Schenk R.K., Steinemann S., Fiorellini J.P., Fox C.H., Stich H.: Influence of surface characteristics on bone integration of titanium implants. A histomorphometric study in miniature pigs. *Journal of Biomedical Materials Research*, **25** (1991) 889-902.
- [150] Lowery P., Roll D.: Comparing the characteristics of surface-passivated and electropolished 316L stainless steel. *Micro*, **16** (1998) 43-49.
- [151] Casaletto M.P., Ingo G.M., Kaciulis S., Mattogno G., Pandolfi L., Scavia G.: Surface studies of in vitro biocompatibility of titanium oxide coatings. *Applied Surface Science*, **172** (2001) 167-177.
- [152] Zinger O., Anselme K., Denzer A., Habersetzer P., Wieland M., Jeanfils J., Hardouin P., Landolt D.: Time-dependent morphology and adhesion of osteoblastic cells on titanium model surfaces featuring scale-resolved topography. *Biomaterials*, **25** (2004) 2695-2711.
- [153] Gross U., Muller-Mai C., Voigt C., Mesgarian M., Berger G., Ploska U.: Tissue response in the femur of rabbits after implantation of a new calcium titanium phosphate composition. In: S.M.A. Giannini (Ed.) *Bioceramics*, **192** (2000) 383-386.
- [154] Fukumoto S., Tsubakino H., Inoue S., Liu L., Terasawa M., Mitamura T.: Surface modification of titanium by nitrogen ion implantation. *Materials Science and Engineering A: Structural Materials: Properties, Microstructure and Processing*, **263** (1999) 205-209.

- [155] Liu X.Y., Chu P.K., Ding C.X.: Surface modification of titanium, titanium alloys, and related materials for biomedical applications. *Materials Science and Engineering: R: Reports*, **47** (2004) 49-121.
- [156] Cheang P., Khor K.A.: Addressing processing problems associated with plasma spraying of hydroxyapatite coatings. *Biomaterials*, **17** (1996) 537-544.
- [157] Tsui Y.C., Doyle C., Clyne T.W.: Plasma sprayed hydroxyapatite coatings on titanium substrates. Part 1: Mechanical properties and residual stress levels. *Biomaterials*, **19** (1998) 2015-2029.
- [158] Geesink R.G.T., Degroot K., Klein C.: Bonding of bone to apatite-coated implants. *Journal of Bone and Joint Surgery-British Volume*, **70** (1988) 17-22.
- [159] Klein C., Patka P., Wolke J.G.C., Deblieckhogervorst J.M.A., Degroot K.: Long-term in vivo study of plasma-sprayed coatings on titanium alloys of tetracalcium phosphate, hydroxyapatite and alpha-tricalcium phosphate. *Biomaterials*, **15** (1994) 146-150.
- [160] Inadome T., Hayashi K., Nakashima Y., Tsumura H., Sugioka Y.: Comparison of bone-implant interface shear strength of hydroxyapatite-coated and alumina-coated metal implants. *Journal of Biomedical Materials Research*, **29** (1995) 19-24.
- [161] Berndt C.C.: Tensile adhesion testing methodology for thermally sprayed coatings. *Journal of Materials Engineering*, **12** (1990) 151-158.
- [162] Niinomi M.: Recent metallic materials for biomedical applications. *Metallurgical and Materials Transactions A: Physical Metallurgy and Materials Science*, **33** (2002) 477-486.
- [163] Niinomi M., Kuroda D., Fukunaga K., Morinaga M., Kato Y., Yashiro T., Suzuki A.: Corrosion wear fracture of new beta type biomedical titanium alloys. *Materials Science and Engineering A: Structural Materials Properties Microstructure and Processing*, **263** (1999) 193-199.
- [164] Watanabe K., Miyakawa O., Takada Y., Okuno O., Okabe T.: Casting behavior of titanium alloys in a centrifugal casting machine, *Biomaterials*, **24** (2003) 1737-1743.
- [165] Tang X., Ahmed T., Rack H.J.: Phase transformations in Ti-Nb-Ta and Ti-Nb-Ta-Zr alloys. *Journal of Materials Science*, **35** (2000) 1805-1811.
- [166] Nag S., Banerjee R., Fraser H.L.: Microstructural evolution and strengthening mechanisms in Ti-Nb-Zr-Ta, Ti-Mo-Zr-Fe and Ti-15Mo biocompatible alloys. *Materials Science and Engineering C: Biomimetic and Supramolecular Systems*, **25** (2005) 357-362.
- [167] Okazaki Y., Ito Y., Kyo K., Tateishi T.: Corrosion resistance and corrosion fatigue strength of new titanium alloys for medical implants without V and Al. *Materials Science and Engineering A: Structural Materials Properties Microstructure and Processing*, **213** (1996) 138-147.
- [168] Wapner K.L.: Implications of metallic corrosion in total knee arthroplasty. *Clinical Orthopaedics and Related Research*, **271** (1991) 12-20.
- [169] Eisenbarth E., Velten D., Muller M., Thull R., Breme J.: Biocompatibility of beta-stabilizing elements of titanium alloys, *Biomaterials*, **25** (2004) 5705-5713.
- [170] Kobayashi E., Wang T.J., Doi H., Yoneyama T., Hamanaka H.: Mechanical properties and corrosion resistance of Ti-6Al-7Nb alloy dental castings. *Journal of Materials Science: Materials in Medicine*, **9** (1998) 567-574.
- [171] Niinomi M.: Mechanical biocompatibilities of titanium alloys for biomedical applications. *Journal of the Mechanical Behavior of Biomedical Materials*, **1** (2008) 30-42.
- [172] Song Y., Xu D.S., Yang R., Li D., Wu W.T., Guo Z.X.: Theoretical study of the effects of alloying elements on the strength and modulus of beta-type bio-titanium alloys. *Materials Science and Engineering A: Structural Materials Properties Microstructure and Processing*, **260** (1999) 269-274.

## References

- [173] Sakaguchi N., Niinomi M., Akahori T., Takeda J., Toda H.: Relationships between tensile deformation behavior and microstructure in Ti-Nb-Ta-Zr system alloys. *Materials Science and Engineering C: Biomimetic and Supramolecular Systems*, **25** (2005) 363-369.
- [174] Niinomi M.: Mechanical properties of biomedical titanium alloys. *Materials Science and Engineering A: Structural Materials Properties Microstructure and Processing*, **243** (1998) 231-236.
- [175] Wegmann G., Albrecht J., Lutjering G., Folkers K.D., Liesner C.: Microstructure and mechanical properties of titanium castings. *Zeitschrift Fur Metallkunde*, **88** (1997) 764-773.
- [176] Mohammadi S., Esposito M., Victorin L., Aronsson B.O., Thomsen P.: Bone response to machined cast titanium implants. *Journal of Materials Science*, **36** (2001) 1987-1993.
- [177] Murr L.E., Esquivel E.V., Quinones S.A., Gaytan S.M., Lopez M.I., Martinez E.Y., Medina F., Hernandez D.H., Martinez E., Martinez J.L., Stafford S.W., Brown D.K., Hoppe T., Meyers W., Lindhe U., Wicker R.B.: Microstructures and mechanical properties of electron beam-rapid manufactured Ti-6Al-4V biomedical prototypes compared to wrought Ti-6Al-4V. *Materials Characterization*, **60** (2009) 96-105.
- [178] Jovanović M., Bobić I., Mišković Z., Zec S.: Precision cast of Ti-based alloys - microstructure and mechanical properties. *Metalurgija - Journal of Metallurgy*, **15** (2009) 53-69.
- [179] Suzuki K.: The high quality precision casting of titanium alloys. *Jom: Journal of the Minerals, Metals and Materials Society*, **50** (1998) 20-23.
- [180] Watanabe I., Woldu M., Watanabe K., Okabe T.: Effect of casting method on castability of titanium and dental alloys. *Journal of Materials Science: Materials in Medicine*, **11** (2000) 547-553.
- [181] Jovanović M., Lukić B., Misković Z., Bobić I., Cvijović I., Dimčić B.: Processing and some applications of nickel, cobalt and titanium-based alloys. *Metalurgija - Journal of Metallurgy*, **13** (2007) 91-106.
- [182] Suzuki K., Nishikawa K., Watakabe S.: Stability of yttria for titanium alloy precision casting mold. *Materials Transactions, JIM*, **38** (1997) 54-62.
- [183] Watakabe S., Suzuki K., Nishikawa K.: Control of chemical compositions of Ti-6AL-4V alloy during melting by electron beam furnace. *ISIJ International*, **32** (1992) 625-629.
- [184] Peters M., Lutjering G., Ziegler G.: Control of microstructures of (alpha+beta) - titanium alloys. *Zeitschrift Fur Metallkunde*, **74** (1983) 274-282.
- [185] Watanabe I., Watkins J.H., Nakajima H., Atsuta M., Okabe T.: Effect of pressure difference on the quality of titanium casting. *Journal of Dental Research*, **76** (1997) 773-779.
- [186] Kar S., Searles T., Lee E., Viswanathan G.B., Tiley J., Banerjee R., Fraser H.L.: Modeling the tensile properties in beta-processed alpha/beta Ti alloys. *Metallurgical and Materials Transactions A: Physical Metallurgy and Materials Science*, **37A** (2006) 559-566.
- [187] Ducheyne P., Kohn D., Smith T.S.: Fatigue properties of cast and heat treated Ti-6Al-4V alloy for anatomic hip prostheses. *Biomaterials*, **8** (1987) 223-227.
- [188] Okabe T., Hero H.: The use of titanium in dentistry. *Cells and Materials*, **5** (1995) 211-230.
- [189] Sung S.Y., Choi B.J., Han B.S., Oh H.J., Kim Y.J.: Evaluation of alpha-case in titanium castings. *Journal of Materials Science & Technology*, **24** (2008) 70-74.

- [190] Boettinger W.J., Williams M.E., Coriell S.R., Kattner U.R., Mueller B.A.: Alpha case thickness modeling in investment castings. *Metallurgical and Materials Transactions B: Process Metallurgy and Materials Processing Science*, **31** (2000) 1419-1427.
- [191] Chen G.Z., Fray D.J., Farthing T.W.: Cathodic deoxygenation of the alpha case on titanium and alloys in molten calcium chloride. *Metallurgical and Materials Transactions B: Process Metallurgy and Materials Processing Science*, **32** (2001) 1041-1052.
- [192] Koike M., Guo Q., Brezner M., Fujii H., Okabe T.: Mechanical properties of cast Ti-Fe-0-N alloys. In: Zardiackas L.D., Freese H.L., Kraay M.J.: (Eds.) *Titanium, Niobium, Zirconium, and Tantalum for Medical and Surgical Applications*, ASTM International, 2006.
- [193] Donachie Matthew J.: *Titanium: A Technical Guide*, 2nd ed., ASM International, 2000.
- [194] Atwood R.C., Lee P.D., Curtis R.V.: Modeling the surface contamination of dental titanium investment castings. *Dental Materials*, **21** (2005) 178-186.
- [195] Kikuchi H., Onouchi M., Miyanaga K., Wakashima M., Okuno O., Nishiyama M.: The thickness effects of titanium castings on the surface reaction layer. *Dental Materials*, **23** (2004) 387-394.
- [196] Chan K.S., Koike M., Johnson B.W., Okabe T.: Modeling of alpha-case formation and its effects on the mechanical properties of titanium alloy castings. *Metallurgical and Materials Transactions A: Physical Metallurgy and Materials Science*, **39A** (2008) 171-180.
- [197] Saha R.L., Nandy T.K., Misra R.D.K., Jacob K.T.: On the evaluation of stability of rare earth oxides as face coats for investment casting of titanium. *Metallurgical Transactions B: Process Metallurgy*, **21** (1990) 559-566.
- [198] Takahashi K.: Change of morphology of titanium surface by pickling in nitric-hydrofluoric acid solutions. In: Matsushashi Ryo (Eds.), *Nippon Steel Technical Report*, **375** (2002) 64-70.
- [199] Ohkubo C., Watanabe I., Ford J.P., Nakajima H., Hosoi T., Okabe T.: The machinability of cast titanium and Ti-6Al-4V. *Biomaterials*, **21** (2000) 421-428.
- [200] Cotton J.D., Clark L.P., Phelps H.R.: Titanium investment casting defects: A metallographic overview. *JOM*, **58** (2006) 13-16.
- [201] Al-Mesmar H.S., Morgano S.M., Mark L.E.: Investigation of the effect of three sprue designs on the porosity and the completeness of titanium cast removable partial denture frameworks. *Journal of Prosthetic Dentistry*, **82** (1999) 15-21.
- [202] Watanabe K., Okawa S., Miyakawa O., Nakano S., Shiokawa N., Kobayashi M.: Molten titanium flow in a mesh cavity by the flow visualization technique. *Dental Materials*, **10** (1991) 128-137.
- [203] Hero H., Syverud M., Waarli M.: Porosity and mold filling of titanium castings. *Journal of Materials Science: Materials in Medicine*, **4** (1993) 296-299.
- [204] Mitchell A.: Melting, casting and forging problems in titanium alloys. *Materials Science and Engineering A: Structural Materials: Properties, Microstructure and Processing*, **243** (1998) 257-262.
- [205] Levine B.: A new era in porous metals: applications in orthopaedics. *Advanced Engineering Materials*, **10** (2008) 788-792.
- [206] Ajdari A.: Mechanical behavior of cellular structures: A finite element study. In: Department of Mechanical and Industrial Engineering, Northeastern University, Boston, Massachusetts, 2008.
- [207] Krupp U., Altindis M., Guillén T., Ohrndorf A., Christ H.-J., Hagemann K., Bührig-Polaczek A., Ploska U., Berger G., Ursula S., Wenisch S., Schnettler R.: Development and characterization of open-cell Ti-6Al-7Nb structures to be used as biomedical

## References

- implants: In: 6th international conference of porous metals and metallic foams - Metfoam 2009, Bratislava, Slovakia, 2009.
- [208] Ashby M.F.: The mechanical properties of cellular solids. *Metallurgical Transactions A: Physical Metallurgy and Materials Science*, **14** (1983) 1755-1769.
- [209] Gibson L.J., Ashby M.F.: *Cellular Solids: Structure and Properties*. Cambridge University Press, Cambridge, 1997.
- [210] Paul A., Ramamurty U.: Strain rate sensitivity of a closed-cell aluminum foam. *Materials Science and Engineering A: Structural Materials: Properties, Microstructure and Processing*, **281** (2000) 1-7.
- [211] Krupp U., Ohrndorf A., Guillen T., Christ H.J., Demiray S., Becker W., Hohe J.: Isothermal and thermomechanical fatigue behavior of open-cell metal sponges. *Advanced Engineering Materials*, **8** (2006) 821-827.
- [212] Sarkar S.K., Kim Y.H., Kim M.S., Min Y.K., Yang H.M., Song H.-Y., Lee B.-T.: Fabrication and characterization of porous TCP coated Al<sub>2</sub>O<sub>3</sub> scaffold by polymeric sponge method. *Journal of the Korean Ceramic Society*, **45** (2008) 579-583.
- [213] White E.W., Weber J.N., Roy D.M., Owen E.L., Chiroff R.T., White R.A.: Replaminiform porous biomaterials for hard tissue implant applications. *Journal of Biomedical Materials Research*, **9** (1975) 23-27.
- [214] Stephenson P.K., Freeman M.A., Revell P.A., Germain J., Tuke M., Pirie C.J.: The effect of hydroxyapatite coating on ingrowth of bone into cavities in an implant. *The Journal of Arthroplasty*, **6** (1991) 51-58.
- [215] Kim H.W., Lee S.Y., Bae C.J., Noh Y.J., Kim H.E., Kim H.M., Ko J.S.: Porous ZrO<sub>2</sub> bone scaffold coated with hydroxyapatite with fluorapatite intermediate layer. *Biomaterials*, **24** (2003) 3277-3284.
- [216] He X., Zhang Y.Z., Mansell J.P., Su B.: Zirconia toughened alumina ceramic foams for potential bone graft applications: Fabrication, bioactivation, and cellular responses. *Journal of Materials Science-Materials in Medicine*, **19** (2008) 2743-2749.
- [217] Holy C.E., Fialkov J.A., Davies J.E., Shoichet M.S.: Use of a biomimetic strategy to engineer bone. *Journal of Biomedical Materials Research Part A*, **65A** (2003) 447-453.
- [218] Mikos A.G., Sarakinos G., Leite S.M., Vacanti J.P., Langer R.: Laminated three-dimensional biodegradable foams for use in tissue engineering. *Biomaterials*, **14** (1993) 323-330.
- [219] Singh L., Kumar V., Ratner B.D.: Generation of porous microcellular 85/15 poly ((DL)-lactide-co-glycolide) foams for biomedical applications. *Biomaterials*, **25** (2004) 2611-2617.
- [220] Levine B.R., Sporer S., Poggie R.A., Della Valle C.J., Jacobs J.J.: Experimental and clinical performance of porous tantalum in orthopedic surgery. *Biomaterials*, **27** (2006) 4671-4681.
- [221] Zardiackas L.D., Parsell D.E., Dillon L.D., Mitchell D.W., Nunnery L.A., Poggie R.: Structure, metallurgy, and mechanical properties of a porous tantalum foam. *Journal of Biomedical Materials Research*, **58** (2001) 180-187.
- [222] Imwinkelried T.: Mechanical properties of open-pore titanium foam, *Journal of Biomedical Materials Research Part A*, **81A** (2007) 964-970.
- [223] Banhart J.: Manufacture, characterisation and application of cellular metals and metal foams, *Progress in Materials Science*, **46** (2001) 559-U553.
- [224] Ashby F.M., Evans A., Fleck N.A., Gibson L.J., Hutchinson J.W., Wadley H.N.G.: *Metal Foams: A Design Guide*. Butterworth Heinemann, Oxford, UK, 2000.
- [225] Girlich D., Franzke U.: Open pore metal foams for heat exchange in ventilation and refrigeration. *Advanced Engineering Materials*, **3** (2001) 351-352.

- [226] Wagner I., Hintz C., Sahn P.R.: Precision cast near net shape components based on cellular metal materials. In: B. Jouffrey (Ed.) *Microstructural Investigation and Analysis*. Wiley - VCH Verlag GmbH & Co. KGaA, Weinheim, 2006.
- [227] Krupp U., Ohrndorf A., Hipke T., Hohlfeld J., Danninger A., Reinfried M., Aegerter J.: Development of a standard for compression testing of cellular metals. In: *MetFoam 2007, Fifth International Conference on Porous Metals and Metallic Foams*, Montreal, Canada, 2007, p. 407-410.
- [228] Warren W.E., Kraynik A.M.: Linear elastic behavior of a low-density Kelvin foam with open cells. *Journal of Applied Mechanics - Transactions of the Asme*, **64** (1997) 787-794.
- [229] Gibson L.J., Ashby M.F., Schajer G.S., Robertson C.I.: The mechanics of two-dimensional cellular materials. *Proceedings of the Royal Society of London Series A: Mathematical Physical and Engineering Sciences*, **382** (1982) 25-42.
- [230] Zhu H.X., Mills N.J., Knott J.F.: Analysis of the high strain compression of open-cell foams. *Journal of the Mechanics and Physics of Solids*, **45** (1997) 1875-1904.
- [231] Rusch K.C.: Energy-absorbing characteristics of foamed polymers. *Journal of Applied Polymer Science*, **14** (1970) 1433-1447.
- [232] Guillén T., Zhang Q.-H., Tozzi G., Ohrndorf A., Christ H.-J., Tong J.: Compressive behaviour of bovine cancellous bone and bone analogous materials, microCT characterisation and FE analysis. *Journal of the Mechanical Behavior of Biomedical Materials*, **4** (2011) 1452-1461.
- [233] Ohrndorf A., Krupp U., Christ H.J.: Metallic open-cell foams - a promising approach to fabricating good medical implants. *Technol Health Care*, **14** (2006) 201-208.
- [234] Ohrndorf A., Krupp U., Christ H.J.: Mechanical properties of aluminium foams, *Materialprüfung*, **44** (2002) 78-82.
- [235] Banhart J., Brinkers W.: Fatigue behavior of aluminum foams. *Journal of Materials Science Letters*, **18** (1999) 617-619.
- [236] Harte A.M., Fleck N.A., Ashby M.F.: Fatigue failure of an open cell and a closed cell aluminium alloy foam. *Acta Materialia*, **47** (1999) 2511-2524.
- [237] Sugimura Y., Rabiei A., Evans A.G., Harte A.M., Fleck N.A.: Compression fatigue of a cellular Al alloy. *Materials Science and Engineering A: Structural Materials Properties Microstructure and Processing*, **269** (1999) 38-48.
- [238] Zhou J., Soboyejo W.O.: Compression - compression fatigue of open cell aluminum foams: macro-/micro-mechanisms and the effects of heat treatment. *Materials Science and Engineering A: Structural Materials Properties Microstructure and Processing*, **369** (2004) 23-35.
- [239] Seiler C.: *Collateral circulation of the heart*. Springer-Verlag, London, 2009.
- [240] Nuss K., Auer J.A., Boos A., von Rechenberg B.: An animal model in sheep for biocompatibility testing of biomaterials in cancellous bones. *BMC Musculoskeletal Disorders*, **7** (2006) 67-81.
- [241] Linde F., Sorensen H.C.F.: The effect of different storage methods on the mechanical properties of trabecular bone. *Journal of Biomechanics*, **26** (1993) 1249-1252.
- [242] Mittra E., Rubin C., Qin Y.X.: Interrelationship of trabecular mechanical and microstructural properties in sheep trabecular bone. *Journal of Biomechanics*, **38** (2005) 1229-1237.
- [243] Perilli E., Baleani M., Ohman C., Fognani R., Baruffaldi F., Viceconti M.: Dependence of mechanical compressive strength on local variations in micro architecture in cancellous bone of proximal human femur. *Journal of Biomechanics*, **41** (2008) 438-446.

## References

- [244] Guglielmi G., Muscarella S., Bazzocchi A.: Integrated Imaging Approach to Osteoporosis: State-of-the-Art Review and Update. *Radiographics*, **31** (2011) 1343-1364.
- [245] Budras K.-D., Habel R.E., Wünsche A., Budas S.: *Bovine anatomy*. Schlütersche, Hannover, 2011.
- [246] DIN 50134, Testing of metallic materials - Compression test of metallic cellular materials. In: Deutsches Institut für Normung, 2008.
- [247] Keaveny T.M., Borchers R.E., Gibson L.J., Hayes W.C.: Trabecular bone modulus and strength can depend on specimen geometry. *Journal of Biomechanics*, **26** (1993) 991-1000.
- [248] Ciarelli T.E., Fyhrie D.P., Schaffler M.B., Goldstein S.A.: Variations in three-dimensional cancellous bone architecture of the proximal femur in female hip fractures and in controls. *Journal of Bone and Mineral Research*, **15** (2000) 32-40.
- [249] Li B.H., Aspden R.M.: Composition and mechanical properties of cancellous bone from the femoral head of patients with osteoporosis or osteoarthritis. *Journal of Bone and Mineral Research*, **12** (1997) 641-651.
- [250] Hobdell M.H., Boyde A.: Microradiography and Scanning Electron Microscopy of Bone Sections. *Zeitschrift Fur Zellforschung Und Mikroskopische Anatomie*, **94** (1969) 487-494.
- [251] Boyde A.: Improved digital SEM of cancellous bone: scanning direction of detection, through focus for in-focus and sample orientation. *Journal of Anatomy*, **202** (2003) 183-194.
- [252] Guilin Y., Nan L., Yousheng L., Yining W.: The effects of different types of investments on the alpha-case layer of titanium castings. *The Journal of Prosthetic Dentistry*, **97** (2007) 157-164.
- [253] Hogan H.A., Ruhmann S.P., Sampson H.W.: The mechanical properties of cancellous bone in the proximal tibia of ovariectomized rats. *Journal of Bone and Mineral Research*, **15** (2000) 284-292.
- [254] Ploska U., Berger G., Jörn D., Willfahrt M., Hackbarth A.: Calcium titanate reaction layer on TiAl6V4 implants. *Key Engineering Materials*, **361-363** (2008) 657-660.
- [255] Baud C.A., Pouezat J.A., Tochondanguy H.J.: Quantitative analysis of amorphous and crystalline bone tissue mineral in women with osteoporosis. *Calcified Tissue Research*, **21** (1976) 452-456.
- [256] Banhart J., Baumeister J.: Deformation characteristics of metal foams. *Journal of Materials Science*, **33** (1998) 1431-1440.
- [257] Muller R., Gerber S.C., Hayes W.C.: Micro-compression: a novel technique for the nondestructive assessment of local bone failure. *Technology and Health Care : Official Journal of the European Society for Engineering and Medicine*, **6** (1998) 433-444.
- [258] Vanrietbergen B., Weinans H., Huiskes R., Odgaard A.: A new method to determine trabecular bone elastic properties and loading using micromechanical finite-element models. *Journal of Biomechanics*, **28** (1995) 69-81.
- [259] Nazarian A., Muller R.: Time-lapsed microstructural imaging of bone failure behavior. *Journal of Biomechanics*, **37** (2004) 55-65.
- [260] Sung S.Y., Kim Y.J.: Alpha-case formation mechanism on titanium investment castings. *Materials Science and Engineering A: Structural Materials Properties Microstructure and Processing*, **405** (2005) 173-177.
- [261] Sung S.Y., Kim Y.J.: Influence of Al contents on alpha-case formation of Ti-xAl alloys. *Journal of Alloys and Compounds*, **415** (2006) 93-98.
- [262] Martin P.L., Lipsitt H.A., Nuhfer N.T., Williams J.C.: The effects of allowing on the microstructure and properties of Ti<sub>3</sub>Al and TiAl. In: H.I.a.O. Izumi (Ed.) *Titanium 80*, The American Society of Metals, 1980, p. 1245-1254.

- [263] Ehrhart I., Thomas M., Vassel A., Veyssiere P.: Surface defects in as-grown Ti<sub>3</sub>AlV. *Revue De Physique Appliquee*, **24** (1989) 699-709.
- [264] Simons P.Y., Dachille F.: The structure of TiO<sub>2</sub>II, a high-pressure phase of TiO<sub>2</sub>. *Acta Crystallographica*, **23** (1967) 334-336.
- [265] Sittig C., Textor M., Spencer N.D., Wieland M., Vallotton P.H.: Surface characterization of implant materials cp Ti, Ti-6Al-7Nb and Ti-6Al-4V with different pretreatments. *Journal of Materials Science - Materials in Medicine*, **10** (1999) 35-46.
- [266] Leyens C., Peters M.: Titanium and titanium alloys. Wiley - VCH Verlag GmbH & Co. KGaA, Cologne, Germany, 2003.
- [267] Li J.C.M.: Microstructure and mechanical properties of materials. University of Rochester, New York, 2000.
- [268] Meyer L.W., Krueger L., Sommer K., Halle T., Hockauf M.: Dynamic strength and failure behavior of titanium alloy Ti-6Al-4V for a variation of heat treatments. *Mechanics of Time - Dependent Materials*, **12** (2008) 237-247.
- [269] Streicher R.M., Weber H., Schon R., Semlitsch M.: New surface modification for Ti-6Al-7Nb alloy: oxygen diffusion hardening (ODH). *Biomaterials*, **12** (1991) 125-129.
- [270] Carlsson A.S., Gentz C.F.: Mechanical loosening of the femoral head prosthesis in the Charnley total hip arthroplasty. *Clinical Orthopaedics and Related Research*, **147** (1980) 262-270.
- [271] Bloebaum R.D., Dupont J.A.: Osteolysis from a press-fit hydroxyapatite-coated implant. A case study. *The Journal of Arthroplasty*, **8** (1993) 195-202.
- [272] Morscher E.W., Hefti A., Aebi U.: Severe osteolysis after third-body wear due to hydroxyapatite particles from acetabular cup coating. *Journal of Bone and Joint Surgery -British Volume*, **80B** (1998) 267-272.
- [273] Campbell P., McKellop H., Park S.H., Malcom A.: Evidence of abrasive wear by particles from a hydroxyapatite coated hip prosthesis. *Transactions of Orthopaedic Research Society* **18** (1993) 224.
- [274] Nie X., Leyland A., Matthews A., Jiang J.C., Meletis E.I.: Effects of solution pH and electrical parameters on hydroxyapatite coatings deposited by a plasma-assisted electrophoresis technique. *Journal of Biomedical Materials Research*, **57** (2001) 612-618.
- [275] Hench L.L.: Bioceramics- From concept to clinic. *Journal of the American Ceramic Society*, **74** (1991) 1487-1510.
- [276] Heimann R.B.: Thermal spraying of biomaterials. *Surface & Coatings Technology*, **201** (2006) 2012-2019.
- [277] Ellingsen J.E.: A study on the mechanism of protein adsorption to TiO<sub>2</sub>. *Biomaterials*, **12** (1991) 593-596.
- [278] Effah E.A.B., Bianco P.D., Ducheyne P.: Crystal structure of the surface oxide layer on titanium and its changes arising from immersion. *Journal of Biomedical Materials Research*, **29** (1995) 73-80.
- [279] Watari F., Yokoyama A., Omori M., Hirai T., Kondo H., Uo M., Kawasaki T.: Biocompatibility of materials and development to functionally graded implant for biomedical application. *Composites Science and Technology*, **64** (2004) 893-908.
- [280] Li J.G., Liao H.H., Fartash B., Hermansson L., Johnsson T.: Surface-dimpled commercially pure titanium implant and bone ingrowth. *Biomaterials*, **18** (1997) 691-696.
- [281] Vercaigne S., Wolke J.G.C., Naert I., Jansen J.A.: Histomorphometrical and mechanical evaluation of titanium plasma-spray-coated implants placed in the cortical bone of goats. *Journal of Biomedical Materials Research*, **41** (1998) 41-48.

## References

- [282] Newman E., Turner A.S., Wark J.D.: The potential of sheep for the study of osteopenia - current status and comparison with other animal-models. *Bone*, **16** (1995) 277-284.
- [283] Ogawa T., Ozawa S., Shih J.H., Ryu K.H., Sukotjo C., Yang J.M., Nishimura I.: Biomechanical evaluation of osseous implants having different surface topographies in rats. *Journal of Dental Research*, **79** (2000) 1857-1863.
- [284] Holweg K.: Bestimmung der Eigenschaft der Grenzfläche zwischen Knochen und Implantat. In: Zentrum für Ingenieurwissenschaften Martin-Luther-Universität Halle-Wittenberg, Halle (Saale), 2010.
- [285] Ronold H.J., Lyngstadaas S.P., Ellingsen J.E.: Analysing the optimal value for titanium implant roughness in bone attachment using a tensile test. *Biomaterials*, **24** (2003) 4559-4564.
- [286] Pastoureau P., Arlot M.E., Caulin F., Barlet J.P., Meunier P.J., Delmas P.D.: Effects of oophorectomy on biochemical and histological indices of bone turnover in ewes. *Journal of Bone and Mineral Research*, **4** (1989) 237.
- [287] Turner A.S., Villanueva A.R.: Static and dynamic histomorphometric data in 9-year-old to 11-year-old ewes. *Veterinary and Comparative Orthopaedics and Traumatology*, **7** (1994) 101-109.
- [288] Heuer D.A., Williams M., Moss R., Butcher K., Anderson M., Milner R., Alley C., Gilmour L., Scott M.: Biologic fixation of an asymmetric titanium particle porous coating in a load-bearing animal model. *Journal of Bone Joint Surgery - British Version*, **93-B** (2011) 419.
- [289] Legeros R.Z., Craig R.G.: Strategies to affect bone remodeling - Osteointegration. *Journal of Bone and Mineral Research*, **8** (1993) 583-596.